

Studies of Ionospheric Structures and Their Effects on Systems

**Cesar A. Valladares
M. Patricia Hagan
Robert Sheehan
Eileen MacKenzie**

**Boston College
Institute for Scientific Research
140 Commonwealth Avenue
Chestnut Hill, MA 02467**

16 September 2002

Final Report

Approved for Public Release; Distribution Unlimited



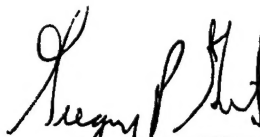
**AIR FORCE RESEARCH LABORATORY
Space Vehicles Directorate
29 Randolph Rd
AIR FORCE MATERIEL COMMAND
HANSCOM AFB, MA 01731-3010**

20030623 018

This Technical Report has been reviewed and is approved for publication.



Todd Pedersen
Contract Manager



GREGORY P. GINET, Chief
Space Weather Center of Excellence

This report has been reviewed by the ESC Public Affairs Office (PA) and is releasable to the National Technical Information Service.

Qualified requestors may obtain additional copies from the Defense Technical Information Center (DTIC). All others should apply to the National Technical Information Service (NTIS).

If your address has changed, if you wish to be removed from the mailing list, or if the address is no longer employed by your organization, please notify AFRL/VSIM, 29 Randolph Rd., Hanscom AFB, MA 01731-3010. This will assist us in maintaining a current mailing list.

Do not return copies of this report unless contractual obligations or notices on a specific document require that it be returned.

REPORT DOCUMENTATION PAGEForm Approved
OMB NO. 0704-0188

Public Reporting burden for this collection of information is estimated to average 1 hour per response, including the time for reviewing instructions, searching existing data sources, gathering and maintaining the data needed, and completing and reviewing the collection of information. Send comment regarding this burden estimate or any other aspect of this collection of information, including suggestions for reducing this burden, to Washington Headquarters Services, Directorate for Information Operations and Reports, 1215 Jefferson Davis Highway, Suite 1204, Arlington, VA 22202-4302, and to the Office of Management and Budget, Paperwork Reduction Project (0704-0188), Washington, DC 20503.

1. AGENCY USE ONLY (Leave Blank)		2. REPORT DATE 16 September 2002	3. REPORT TYPE AND DATES COVERED Final - (18 Aug 97 - 17 Aug 2002)
4. TITLE AND SUBTITLE STUDIES OF IONOSPHERIC STRUCTURES AND THEIR EFFECTS ON SYSTEMS			5. FUNDING NUMBERS Contract No. F19628-97-C-0094 PE 63434F PR 1010 TA IM WU AC
6. AUTHOR(S) Cesar E. Valladares Robert Sheehan M. Patricia Hagan Eileen MacKenzie			
7. PERFORMING ORGANIZATION NAME(S) AND ADDRESS(ES) Boston College Institute for Scientific Research 140 Commonwealth Avenue Chestnut Hill MA 02467			8. PERFORMING ORGANIZATION REPORT NUMBER
9. SPONSORING / MONITORING AGENCY NAME(S) AND ADDRESS(ES) Air Force Research Laboratory 29 Randolph Road Hanscom AFB MA 01731 Contract Manager: Todd Pedersen / VSBX			10. SPONSORING / MONITORING AGENCY REPORT NUMBER AFRL-VS-TR-2002-1668
11. SUPPLEMENTARY NOTES			
12 a. DISTRIBUTION / AVAILABILITY STATEMENT Approved for public release; distribution unlimited.			12 b. DISTRIBUTION CODE
13. ABSTRACT (Maximum 200 words) This is a comprehensive investigation of the basic ionospheric processes which produce plasma density structuring. The emphasis of the research efforts was on understanding the formation and evolution of large-scale structures and the embedded km-scale irregularities that disrupt world-wide Air Force communication and navigation systems. Measurement of the temporal variability of a Sun-aligned arc electrodynamics was conducted with the Sondrestrom radar. It was demonstrated experimentally that traveling convection vortices and large plasma jets are able to form large-scale polar cap patches. The analysis of latitudinal profiles of TEC, obtained between 1800 and 2000 LT, indicated that equatorial spread-F develops when there is a sharp increase of TEC in the crests of the anomaly and a decrease near the trough. We have conducted a correlative study using the neutral winds and the irregularity drifts measured near the magnetic equator to show that most of the time drift and wind are closely coupled. On days when the coupling was not perfect there existed large wind gradients. Using two imagers displaced in longitude by ~800 km we were able to perform the first simultaneous observations of the cusp aurora and to determine the response of the whole aurora to changes of the IMF.			
14. SUBJECT TERMS polar cap patches, sun-aligned arcs, interplanetary magnetic field (IMF), cusp/cleft region, auroral oval, plasma density structures, total electron content (TEC), equatorial spread-F, <i>in situ</i> density structures, GPS observations, VHF/UHF scintillations, equatorial latitudes			15. NUMBER OF PAGES 203
			16. PRICE CODE
17. SECURITY CLASSIFICATION OR REPORT UNCLASSIFIED	18. SECURITY CLASSIFICATION ON THIS PAGE UNCLASSIFIED	19. SECURITY CLASSIFICATION OF ABSTRACT UNCLASSIFIED	20. LIMITATION OF ABSTRACT UL

NSN 7540-01-280-5500

Standard Form 298 (Rev.2-89)
Prescribed by ANSI Std. Z39-18
298-102

TABLE OF CONTENTS

1.	INTRODUCTION	1
2.	POLAR CAP ARC PHENOMENA	1
2.1	Temporal variability of the electrodynamics of sun-aligned arcs	1
2.2	Global aspects of polar cap patches	1
3.	POLAR CAP PATCH PHENOMENA	1
3.1	Observations of plasma density structures in association with large-scale transients	3
3.2	Characteristics of plasma structuring in the cusp/cleft region	3
3.3	Simultaneous observations of polar cap patches and polar cap arcs	3
3.4	Observations of the dayside aurora using two imagers	4
3.5	Observations in the cusp polar cap during a south-eastward IMF	4
4.	COMPUTER SIMULATIONS OF POLAR CAP PATCHES	4
5.	PLASMA STRUCTURES IN THE EQUATORIAL REGIONS	7
5.1	Latitudinal distributions of TEC during equatorial spread-F	7
5.2	Ionospheric effects during major magnetic storms	7
5.3	Statistics of scintillations	7
5.4	Neutral wind and drift coupling	8
6.	SCINTILLATION DATA ACQUISITION SYSTEM	8
7.	REPRINTS OF SELECTED JOURNAL ARTICLES	13
	Simultaneous Observations of Polar-cap Patches and Sun-aligned Arcs during Transitions of the IMF	13
	Characteristics of Plasma Structuring in the Cusp/Cleft Region at Svalbard	31
	Observations of Plasma Density Structures in Association with the Passage of Traveling Convection Vortices and the Occurrence of Large Plasma Jets	47
	Global Aspects of Plasma Structures	67
	Measurement of the Latitudinal Distributions of Total Electron Content during Equatorial Spread-F Events	81
	Ionospheric Effects of Major Magnetic Storms during the International Space Weather Period of September and October 1999; GPS Observations, VHF/UHF Scintillations, and In-situ Density Structures at Middle and Equatorial Latitudes	101
	Statistics of Scintillations, TEC Depletions, and Radar Plumes Observed at Equatorial Latitudes	127
	Correlative Study of Neutral Winds and Scintillation Drifts Measured near the Equator	135
	Simultaneous Observations of Dayside Aurora from Heiss Island and NyAlesund	149
	Multi-site Ground-based Aurora and Plasma Convection in the Cusp Polar Cap during a South-eastward ($B_y \equiv B_z $) IMF Orientation	153

Studies of ionospheric structures and their effect on systems

1. Introduction

The main goals of this investigation are to understand the basic ionospheric processes which produce the large-scale plasma density structures at high latitudes, and to identify the drivers of the equatorial spread-F phenomena. The principal areas where significant progress has been obtained are: 1) Polar cap arc phenomena, 2) Polar cap patch phenomena, 3) Computer simulations of polar cap patches, 4) Plasma structures in the equatorial regions, and 5) Scintillation data acquisition system.

2. Polar cap arc phenomena

The study of polar cap arc phenomena has been greatly benefited by the acquisition of a unique experimental dataset consisting of images collected at Sondrestrom and Qaanaaq, concurrent measurements of the plasma characteristics by the Sondrestrom radar, and global convection patterns acquired by the SuperDARN radars. These measurements were conducted during a high latitude campaign carried out in January 2001.

2.1 Temporal variability of the electrodynamics of sun-aligned arcs

Figure 1 shows images which were measured at Sondrestrom and Qaanaaq and merged in a common geographic system. The images on the top panel of Figure 1 correspond to 0226 and the images on the bottom to 0232 UT. The line-of-sight (LOS) velocities, measured by the Sondrestrom IS radar during two antenna scans, are superimposed and placed at the projected distance from the radar site. The top panel shows the LOS velocities reversing from an antisunward direction within and on the east (dawn) side of the arc to a sunward direction at the west (dusk) side of the aurora. This sharp reversal has been observed quite typically in association with energetic or transpolar polar cap auroras. The bottom panel also displays a drift reversal but occurring outside the arc, about ~200 km dawnward from the dawn edge of the arc in a region void of auroral emissions. This example indicates that there exist rapid temporal changes (5 min scale time) in the relative location of the arc and the region of the velocity reversal. It also suggests that the closeness of the midnight side of the auroral oval produces additional changes in the drift pattern.

2.2 Global aspects of polar cap arcs

A review paper summarized recent advances on the global aspects of polar cap, sun-aligned and transpolar arcs. This publication describes the type of magnetosphere-ionosphere coupling that exists within polar cap arcs and the mapping characteristics of 10 polar cap arcs observed at Qaanaaq. This work is described in the paper entitled "Global aspects of plasma structures" by Su. Basu and C.E. Valladares. A copy of this paper is included in this report.

3. Polar cap patch phenomena

Significant progress has been achieved in the understanding of the formation and the fate of polar cap patches. The main focus in these studies was to investigate the relationship between the large scale (hundreds of km) structures and the km-scale size irregularities that grow embedded within them.

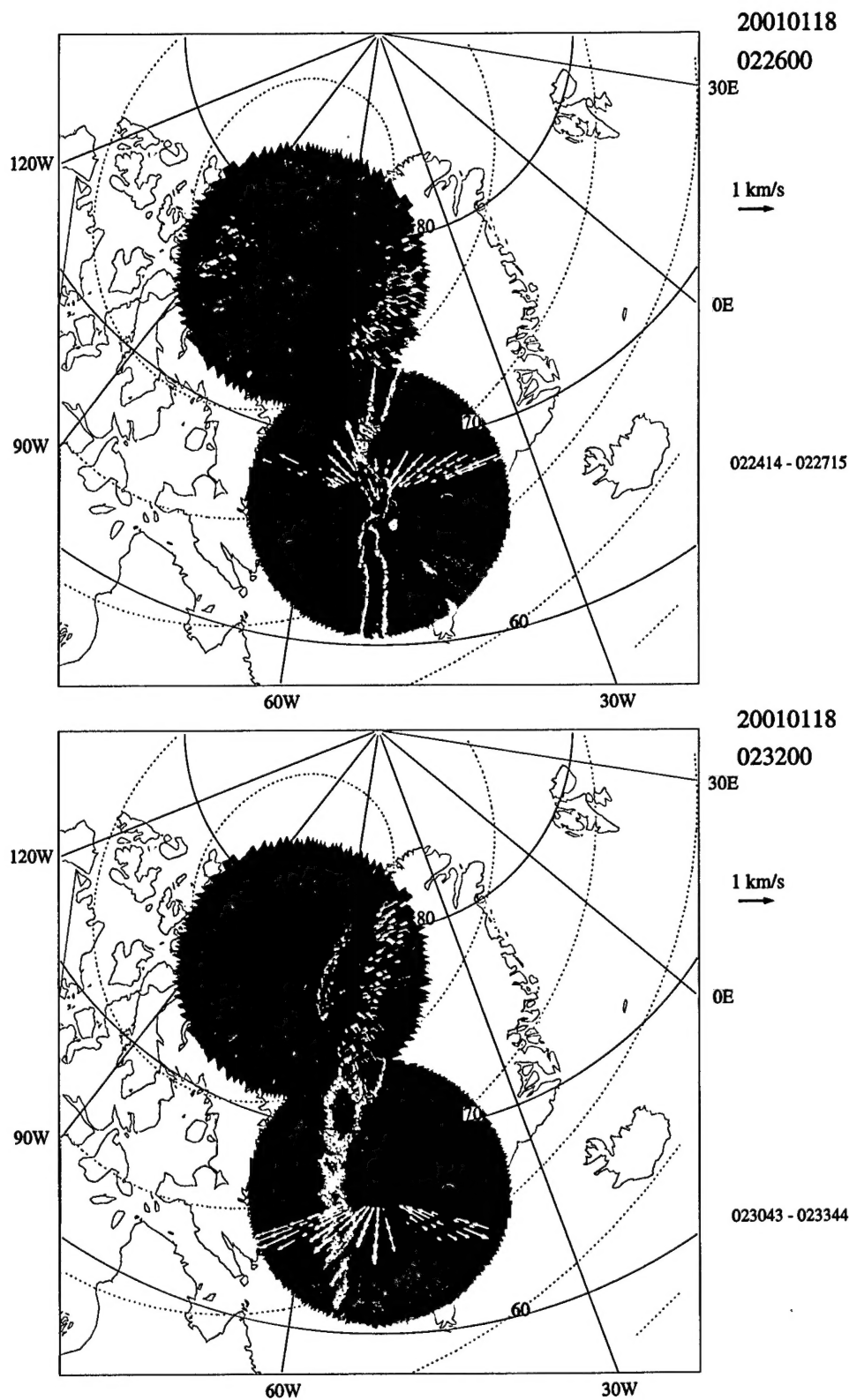


Figure 1 Images measured at Sondrestrom and Qaanaaq, Greenland on January 18, 2001. Line-of-sight velocities measured by the Sondrestrom ISR have been plotted on top of the images. Note that the reversal of the velocities are nearly collocated with the Sun-aligned arc in the top panel.

3.1 Observations of plasma density structures in association with large scale transients.

Two events in which the Sondrestrom radar registered the formation of large-scale density structures occurred on February 18, 1996. The first event consisted of the passage of traveling convection vortices (TCVs). The other event occurred in association with the development of a large plasma jet (LPJ). It was found that when the magnetic perturbations associated with the TCVs were larger than 100 nT, a section of the high-latitude plasma density was eroded by a factor of 2. It was suggested that the number density reduction was caused by an enhancement in the O^+ recombination due to an elevated T_i , which was produced by the much higher frictional heating inside the vortex. The LPJ had a considerable (> 1000 km) longitudinal extension and was 200-300 km in width. Enhanced T_i was observed by the Sondrestrom and EISCAT radars. The channels of high T_i were exactly collocated with the LPJ and some of them with regions of eroded plasma number density. It was suggested that the LPJs bring less dense plasma from later local times. It was also indicated that two different plasma structuring mechanisms (TCVs and LPJs) can act tens of minutes apart to provide increased levels of density structures in the near noon F-region ionosphere. This work is described in "Observations of plasma density structures in association with the passage of traveling convection vortices and the occurrence of large plasma jets" by C.E. Valladares, D. Alcayde, J.V. Rodriguez, J.M. Ruohoniemi, and A.P. Van Eyken. A copy of this paper is included in this report.

3.2 Characteristics of plasma structuring in the cusp/cleft region.

Scintillation data and GPS phase data along with all-sky optical imager and digisonde data were used to study the distribution of electron density irregularities in the dayside region, poleward of the cusp region. Amplitude scintillations obtained at NyAlesund, Svalbard were utilized in conjunction with GPS phase data from the same station obtained through the IGS network to provide total electron content measurements. Weak amplitude scintillations indicating sub-kilometer electron density irregularities were seen over much of the dayside auroral region in the period of study, while patches coordinated with TEC enhancements were only seen during the occurrence of a magnetic storm. A description of this work is contained in the paper "Characteristics of plasma structuring in the cusp/cleft region at Svalbard" by S. Basu, E.J. Weber, T.W. Bullett, M.J. Keskinen, E. MacKenzie, P. Doherty, R. Sheehan, H. Kuenzler, P. Ning, and J. Bongioliatti. A copy of this paper is included in this report.

3.3 Simultaneous observations of polar cap patches and polar cap arcs.

Simultaneous observations of polar cap patches and sun-aligned arcs were investigated using data from the Qaanaaq imager. After scanning images taken between 1989 and 1994, it was found that on few occasions, when B_z changed from a south to a north orientation, the patches and the arcs co-existed inside the polar cap. No similar pattern was found during north-to-south IMF transitions. The co-existence of patches and arcs is due to a slower response of the patches in exiting the polar cap, and the relatively sudden appearance of polar cap arcs presumably driven by dayside reconnection between the IMF and open flux initially drawn equatorward toward the cusp. This investigation is described in the paper entitled "Simultaneous observations of polar cap patches and Sun-aligned arcs during transitions of the IMF", by C.E. Valladares, K. Fukui, R. Sheehan, H.C. Carlson, and T. Bullett. A copy of this paper is included in this report.

3.4 Observations of the dayside aurora using two imagers.

The first simultaneous observation of the cusp aurora using two overlapping imagers displaced in longitude by several hundreds of kilometers was conducted to relate changes in the whole aurora and the values of the IMF. It was found that during a short period of dominant $B_x < 0$ and a solar wind phase front tilted toward the northern hemisphere the whole cusp-related aurora responded rapidly to the new solar wind configuration. A complete description of this research is contained in the paper entitled "Simultaneous observations of dayside aurora from Heiss Island and Ny Alesund" by C.E. Valladares, J. Moen, P.E. Sandholt, W.F. Denig, and O. Troshichev. A copy of this paper, which has been accepted for publication in the Journal of Geophysical Research Letters, is included in this report.

3.5 Observations in the cusp polar cap during a south-eastward IMF.

A combination of optical auroral emissions and ionospheric plasma convection measurements was utilized to diagnose the ionospheric response to an IMF $B_z < 0$ and $B_y \approx |B_z|$. A ~30 min long sequence of four brightening events was found, each of which consisted of latitudinally and longitudinally separated forms associated with pulsed ionospheric flows in merging and lobe convection cells. These events may be separated into two different phases. The initial phase consists of a brightening in the post-noon sector (~1200-1400 MLT) at ~73° MLAT, accompanied by a pulse of enhanced westward convection in the post-noon merging cell. Thereafter, the event evolution comprise a westward expansion of the auroral brightening into the prenoon sector, and auroral brightenings at higher latitudes (~75° MLAT). These types of events recur at ~5-10 min intervals. This study is summarized in the publication entitled "Multi-site Ground-based Aurora and Plasma Convection in the Cusp Polar Cap during a South-eastward ($B_y \approx |B_z|$) IMF Orientation" by P.E. Sandholt, J. Moen, C.J. Farrugia, S.W.H. Cowley, M. Lester, S.E. Milan, and C.E. Valladares. A copy of this paper is included in this report.

4. Computer simulations of polar cap patches

During the present contract we have continued improving the GTIM model and included a parameterization of the production rates of soft particles using the model developed by Strickland [1976]. Figures 2 and 3 show results from a typical run of our latest version of the GTIM model. The top panel of Figure 2 shows a convection trajectory that starts near dusk (0119 UT), traverses a region of dayside cusp precipitation from 0210 to 0220 UT, and convects antisunward across the polar cap (0300 UT). The color panels are altitude profiles of the ion production rate and electron density along the convection trajectory. The densities, in the lower panel, increase as the flux tube crosses the region of enhanced production and persist to the end of the convection path. Figure 3 shows the temporal evolution of the peak density of 3000 flux tubes convecting across the high latitude region. In this example, cusp-type fluxes were present for 15 minutes from 0215 to 0230 UT, between 78° and 80° CGLAT and between 10.5° and 12.5° CGLT. At 0220 UT some flux tubes have entered the enhanced cusp sector, while others, which were in the sector when precipitation started, have just moved into the polar cap. At 0300 UT the region of increased density has detached from the source region in the cusp because enhanced production no longer was present when the grid of flux tubes convected through the cusp sector. More than an hour after it was produced in the dayside cusp, the patch is still visible but degraded at 0330 UT in the night side polar cap.

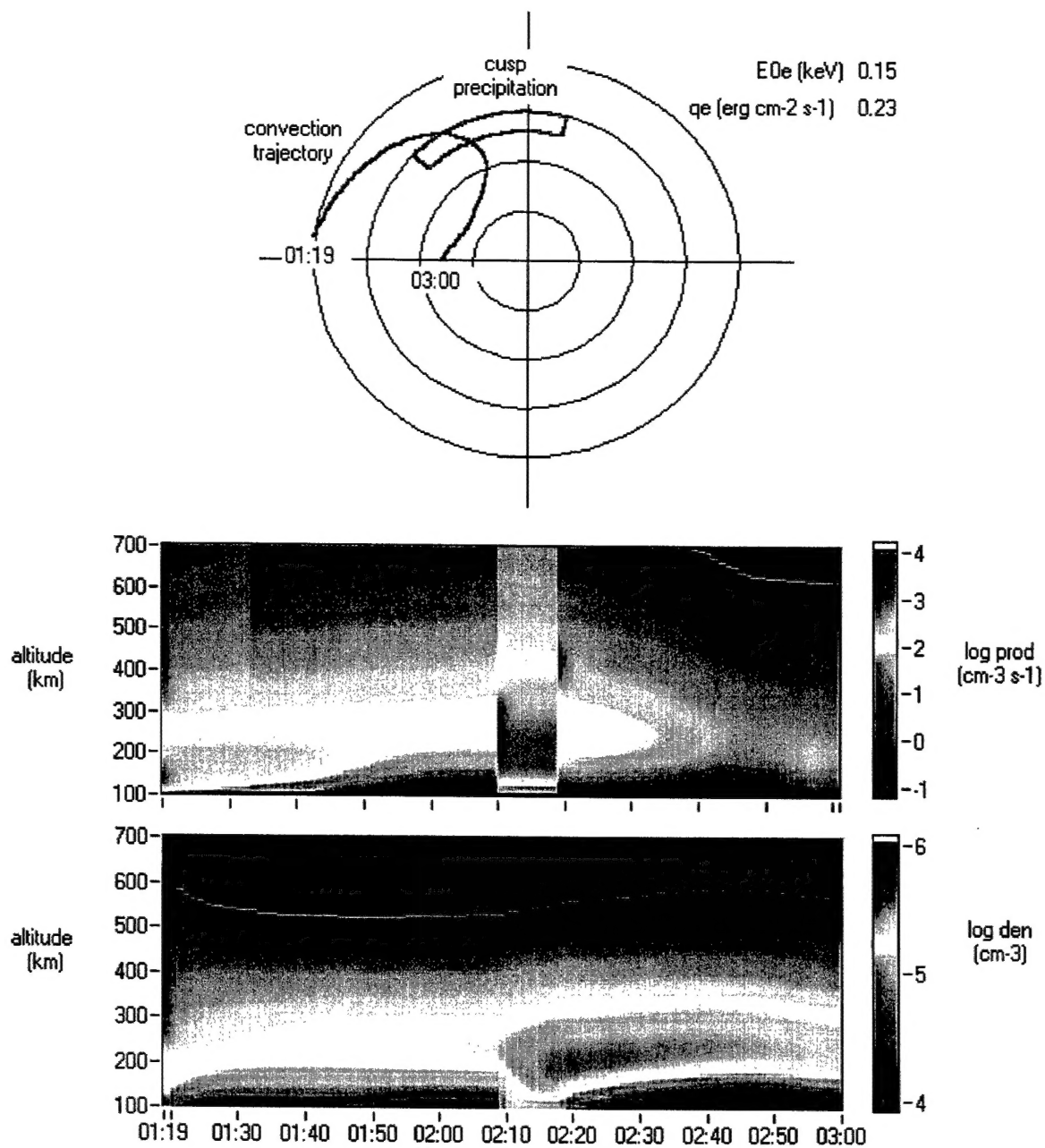


Figure 2 Model example showing the effects of enhanced electron precipitation in the cusp. Top panel is a plot of a convection path (blue trace) that starts near dusk at 0119 UT, and ends near the midnight side of the polar cap at 0300 UT. Middle panel displays production rate and bottom panel electron density altitude profiles.

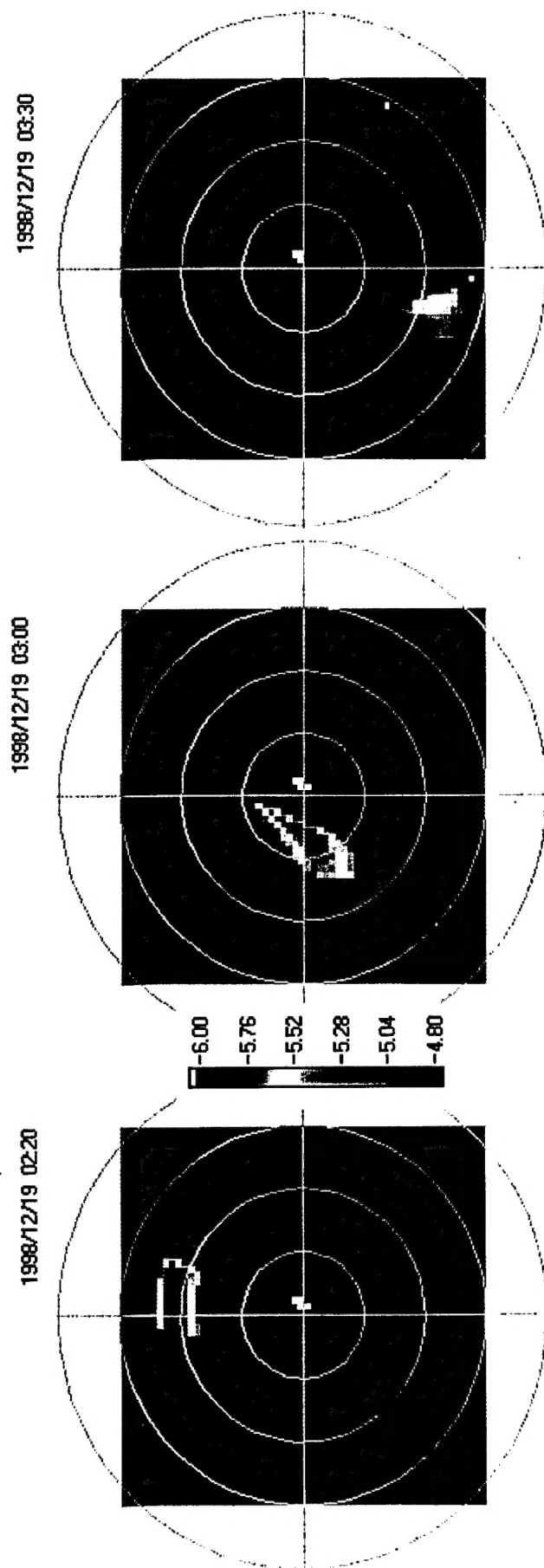


Figure 3 Model results showing a patch of ionization produced by cusp precipitation (left panel), its transport across the polar cap (middle panel), and decay at the night side (right panel). Each panel is a 60x60 grid of model runs like Figure 2 with the same end time. The cusp sector of enhanced precipitation (78 - 80 CGLAT, 10.5 - 12.5 CGLT) is on for 15 min. The electron flux parameters are $E = 0.08$ KeV, $q = 4$ erg cm⁻² s⁻¹.

5. Plasma structures in the equatorial regions.

We have performed several studies aimed at understanding the coupling between ions and neutrals for cases of Equatorial Spread F (ESF) and cases when ESF was not produced, and investigating the background ionospheric conditions favorable for the initiation of ESF. We have also completed statistical studies of the occurrence of ESF. These research efforts are described in the following section.

5.1 Latitudinal distributions of TEC during equatorial spread-F

Latitudinal profiles of TEC were constructed using measurements from 6 GPS receivers. These profiles showed the typical distribution of TEC seen at equatorial latitudes. During the equinoxes the crests of anomaly were located between 12° and 20° away from the magnetic equator with a trough in between. The characteristics of these profiles were correlated with the occurrence or absence of ESF. There were quite drastic increases of the crest values and sharp decreases near the trough during ESF days. In contrast, during days of no ESF there exist almost uniform TEC decreases at all latitudes. Also found were a high (>2) crest/trough ratio, small TEC values at the trough and large latitudinal integrated values during ESF events. This investigation is described in the paper entitled "Measurements of the latitudinal distribution of total electron content during equatorial spread-F events" by C.E. Valladares, S. Basu, K. Groves, M.P. Hagan, D. Hysell, A.J. Mazzella, and R.E. Sheehan. A copy of this paper is included in this report.

5.2 Ionospheric effects during major magnetic storms

During large magnetic storms, the TEC and plasma density irregularity structure of the mid- and low-latitude ionosphere can be affected. Amplitude scintillation data in conjunction with TEC data from the International Geodynamics Service (IGS) has been used to examine the penetration of storm induced electric fields during two large magnetic events. The first storm analyzed here occurred on September 22, 1999. On this day a sudden onset of amplitude scintillation recorded at Hanscom AFB, MA coordinated with DMSP F13 measurements indicate a penetration of electric field at this mid-latitude station. At the same time, the GPS TEC data at Westford showed large fluctuations. The effects extended to the equatorial altitudes within the $15 - 73^\circ$ W longitude region. During the October 1999 magnetic storm, amplitude scintillation again was observed at Hanscom AFB along with GPS TEC fluctuations at Westford, indicating a penetration of the electric field. The effects extended to a larger longitudinal swath within the equatorial region. It is postulated that the equatorial longitudes affected are those for which the sunset times coincide with the times of storm intensifications. This work is described in the paper entitled "Ionospheric effects of major magnetic storms during the International Space Weather period of September and October 1999; GPS observations, VHF/UHF scintillations, and in-situ density structures at middle and equatorial latitudes" by Su. Basu, S. Basu, and C.E. Valladares. A copy of this paper is included in this report.

5.3 Statistics of scintillations

The spaced-antenna scintillation system at Ancon was used to provide a complete characterization of the scintillation signal and the zonal drift of the irregularities. The seasonal occurrence of scintillations shows the well-known maximum during the equinoxes and the December solstice. While the equinoctial maximum is almost constant as a function of solar cycle, the December solstice occurrence increases from 50% at solar minimum to almost 100%

during solar maximum. For the June solstice, the occurrence of scintillations varies in the opposite direction, decreasing from 20% during solar minimum to almost 0% at solar max conditions. Daily TEC files from 6 GPS receivers, located also on the west coast of South America, have been used to determine the development of plasma bubbles and the production of TEC depletions in the GPS data. A computer algorithm to automatically identify and locate the boundaries of TEC depletions was also developed. The statistics of these TEC depletions were compared with similar statistics of scintillations and radar plumes recorded by the JULIA radar. The earliest appearance of scintillations agrees well with the earliest appearance of TEC depletions. However, the decay time of scintillations occurs at least one hour after TEC depletions disappear. In very few cases (less than 10 per year), it was observed a pattern of scintillations containing a high power law spectra (> 3) with no TEC depletions and no radar plumes. This work effort is described in the paper entitled "Statistics of Scintillations, TEC Depletions, and Radar Plumes Observed at Equatorial Latitudes" by C.E. Valladares and R. Sheehan. A copy of this paper is included in this report.

5.4 Neutral wind and drift coupling

Measurements of the thermospheric neutral wind at Arequipa and observations of the drift at Ancon were used to study the coupling that exists between ions and neutrals at equatorial latitudes and the variability of this coupling as a function of the occurrence of scintillations. This comparative analysis indicated that the relative wind-drift values vary depending on season and the solar flux level. It was found that during the equinoxes and low solar flux values, the averaged zonal drift is larger than the wind by 15 m s^{-1} , but for solar flux values above 130 units, the average wind exceeds the drift values by 10 to 20 m s^{-1} . Based on this fact, it was suggested that the occurrence of larger equinoctial drifts was due to the existence of altitude gradients in the zonal wind during that season. During the June solstice, the zonal wind seemed to exceed the irregularity drift by about $10\text{-}20 \text{ m s}^{-1}$ independent of the solar flux. This work is summarized in the paper "Correlative Study of Neutral Winds and Scintillation Drifts Measured near the Magnetic Equator" by C.E. Valladares, J.W. Meriwether, R. Sheehan, and M.A. Biondi. A copy of this paper is included in this report.

6. Scintillation Data Acquisition System

The system for recording and processing UHF and L-Band scintillation data has evolved from a functional system that stretched the limits of early PCs running DOS to a multi-windowed program that takes advantage of modern, relatively inexpensive Pentium machines. Only two field sites, Thule and Sondrestom, Greenland, still run the original DOS program. Two equatorial sites, Ascension Is, and Ancon, Peru, have early Windows programs running under version 3.11, while the newest sites (Bahrain, Diego Garcia, Guam, Longyearbyen, and Ny Alesund) use Windows 98, the latest version when they were installed.

The Windows application was written with the National Instruments LabVIEW program. This development software is a graphical programming environment where icons are used instead of operators or sub-routines written in text, and nodes along the edges of an icon represent input and output arguments. There is a set of icons for standard mathematical and logical operators from which icons for higher level functions can be constructed, much like a wiring diagram. LabVIEW readily supports data acquisition in the background, supplies many statistical and data analysis tools (e.g., FFT, digital filters), and provides reasonably flexible data display capabilities.

The new SDRS software can be configured as a campaign "high-speed" system or as a "normal" system for continuous monitoring at field sites or during campaigns. Data can be recorded locally, as before, or be made available over a network as part of a SCINDA system. The new software was designed to take data from RACAL UHF receivers modified with the RSSI linear detector board. This board directly detects the receiver's IF at 455 kHz and outputs a linear dB response over a wide dynamic range and bandwidth.

An experiment at Ascension Island with the scintillation system required a high-speed acquisition data rate of 5 KHz for three channels monitoring a geo-stationary satellite at UHF frequencies separated by 1 to 10 MHz. The raw data in memory was then digitally low-pass filtered to yield an effective data rate of 1.25 KHz. This involved a major upgrade of the low-level routines controlling the storage of the digital data in temporary arrays. Because only a 200 MHz machine was available at short notice, most of the on-line processing was disabled so that full-waveform data at 1.25 KHz could be recorded on the hard disk. The high-speed scintillation data acquisition program was completed and shipped with the PC to Ascension Island for the March 2001 campaign. A program to read the high-speed full waveform files was also developed to plot raw data off-line and write selected intervals as ASCII text files suitable for input to analysis software. Of particular interest were significant delays, ~.5 seconds, seen in signal fluctuations at the different frequencies, suggesting that different ray paths produced shifted phase screens at a single antenna location.

Two of the new RSSI scintillation systems were set up in August 2001 at two nearby polar sites, NyaAlesund and Longyearbyen on Spitzbergen Island, north of Scandinavia. Secure shell software for telnet and ftp was configured to access and download data files from the Linux servers at the sites. This allows us to monitor the status of the systems and download files containing S4 and signal level data.

The Spitzbergen sites are particularly interesting because they are separated by about 100 km and traverse the cusp region approximately between 07 and 10 UT. Figures 4 and 5 are survey plots of data recorded by the two systems shortly after they were installed (the velocity panel is for equatorial spaced-receiver systems where drift can be calculated). The S4, spectral power, and de-correlation times are roughly similar but show differences when examined in detail. Note, however, that both sites show a slight broadening of the spectra between 0830 and 1030 UT, more so at Longyearbyen. This may be an indication of increased convection speeds in the polar cusp, which shifts the spectrum of interference patterns caused by drifting irregularities to higher frequencies.

Reference

Strickland, D.J., D.L. Book, T.P. Coffey, and J.A. Fedder, Transport equation techniques for the deposition of auroral electrons, *J. Geophys. Res.*, 81, 2755, 1976.

lv1128d2.h00

NyAalesund UHF
2001/08/21

channel 1

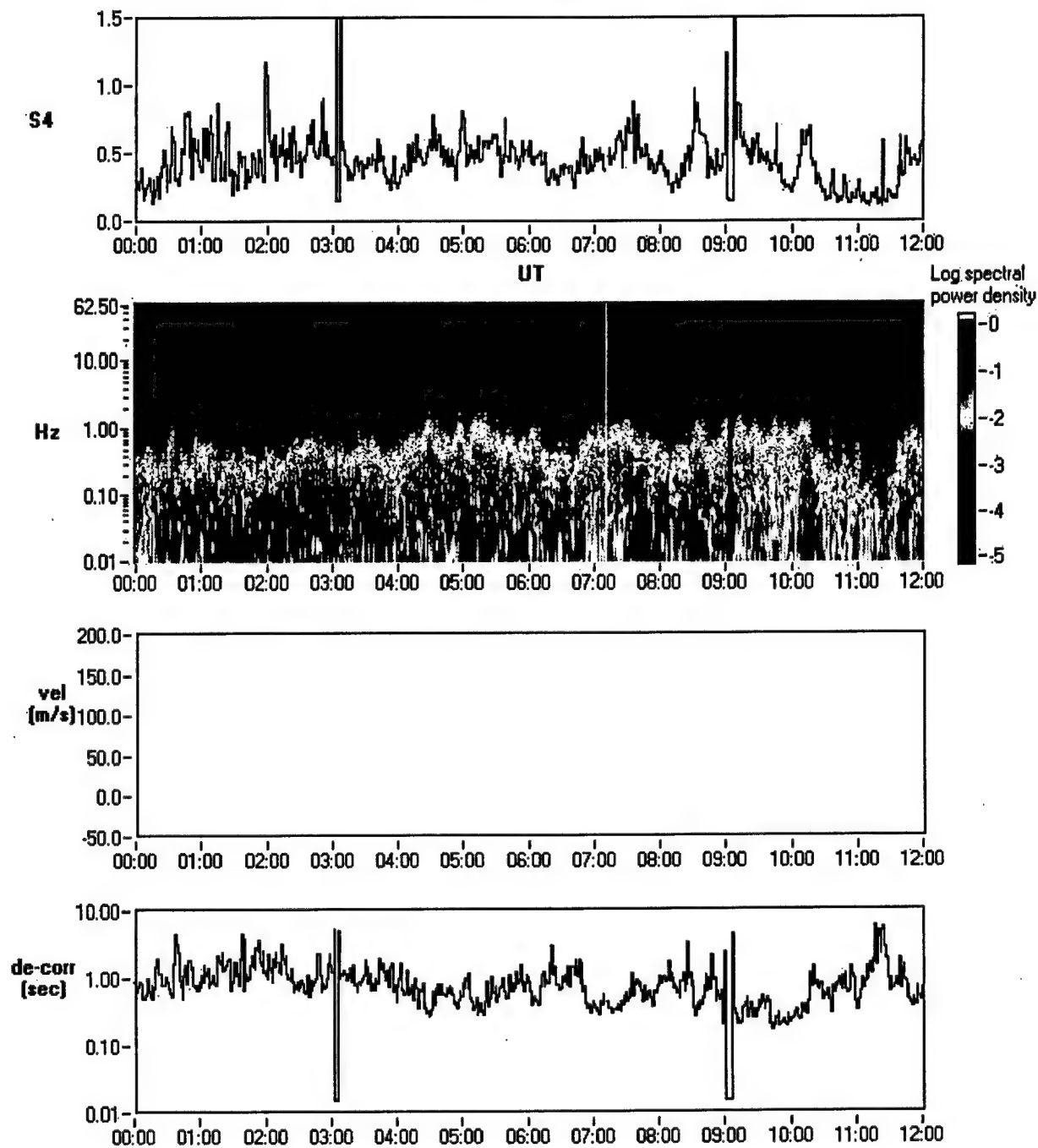


Figure 4 Survey plot of data recorded by the system at NyAalesund shortly after installation

lv1128d2.h00

Longyearbyen UHF
2001/08/21

channel 1

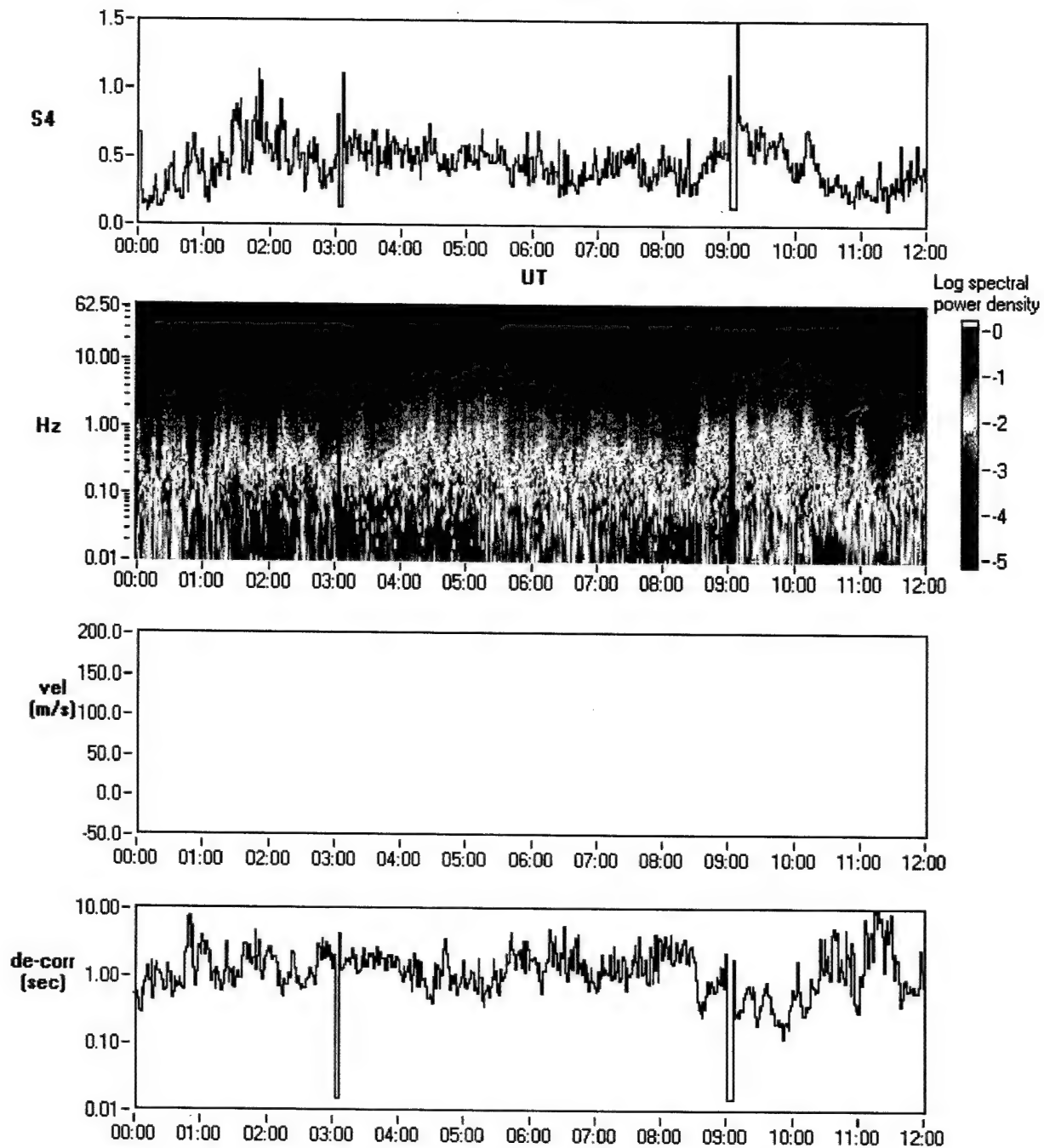


Figure 5 Survey plot of data recorded by the system at Longyearbyen shortly after installation

Simultaneous observations of polar cap patches and Sun-aligned arcs during transitions of the IMF

C. E. Valladares, K. Fukui, and R. Sheehan

Institute for Scientific Research, Boston College, Chestnut Hill, Massachusetts

H. C. Carlson Jr. and T. Bullett

Air Force Research Laboratory, Hanscom Air Force Base, Massachusetts

Abstract. This paper presents the first observations of simultaneous polar cap patches and polar cap arcs in a single common 1000-km field of view, and identifies a model that explains the interplanetary magnetic field (IMF) dependencies of the observed phenomenology. To study the characteristics of the polar cap optical emissions in the 630.0 nm line during transitions of the IMF B_z , we have scanned images taken at Qaanaaq, Greenland, between 1989 and 1994. We found that on a few occasions, when B_z changed from a south to a north orientation, a particular pattern of polar cap patches and Sun-aligned arcs coexisted. No similar pattern of coexisting arcs and patches was found during north-to-south IMF transitions. The detailed analyses of three of these events are presented here in which patches and polar cap arcs are clearly identified to reside simultaneously within the Qaanaaq imager field of view. The digisonde located also at Qaanaaq is used to confirm that the optical patches correspond to enhancements in the number density and a simultaneous decrease of the $h_m F_2$ value. These two factors increase the capability of the imager to differentiate between patches and the background airglow. Data collected by the DMSP F8 satellite during one of the events reaffirm the appearance of polar cap precipitation during the B_z positive period. The J4 sensor on board DMSP F8 detected typical electron fluxes commonly associated with polar cap arcs. The coexistence of patches and arcs is due to a slower response of the patches in exiting the polar cap, and then the relatively sudden appearance of polar cap arcs presumably driven by dayside reconnection between the IMF and open flux drawn initially equatorward toward the cusp. This model, of dayside reconnection switching from equatorward of the cusp for B_z south to poleward of the cusp for B_z north, likewise explains why arcs and patches are seen by the imager to coexist for rapid B_z reversals only from south to north and not from north to south.

1. Introduction

The polar cap ionosphere is a disturbed environment where large-, medium-, and small-scale density structures are likely always present. During disturbed magnetic conditions, F region plasma density enhancements, called polar cap patches, drift antisunward across the polar cap [Buchau *et al.*, 1983; Weber *et al.*, 1984, 1986]. During quiescent periods,

Sun-aligned F region arcs appear in the polar cap moving toward dawn or dusk [Weber and Buchau, 1981; Carlson *et al.*, 1984]. In other instances, still under quiet conditions, a low-density polar hole has been observed to occupy a large portion of the polar cap [Crowley *et al.*, 1993].

The B_z component of the interplanetary magnetic field (IMF) dictates, in general terms, the level of magnetic activity prevailing at high latitudes and consequently the type of large-scale structure populating the polar cap [Basu *et al.*, 1990]. Polar cap Sun-aligned F region arcs develop when B_z is directed north [Berkey *et al.*, 1976; Lassen and Danielsen, 1978], and circular, "cigar" shaped or amorphous

Copyright 1998 by the American Geophysical Union.

Paper number 98RS02187.

0048-6604/98/98RS-02187\$11.00

patches are observed when B_z is pointing south [Buchau *et al.*, 1983]. The Qaanaaq station (77.5° N, 69.2° W, 86° invariant latitude) is located deep inside the polar cap and is equipped with an all-sky intensified photometer (ASIP) and a state-of-the-art digisonde. This instrumentation allows us to detect and identify the type of density structure prevailing inside the polar cap. In fact, images from the ASIP at Qaanaaq have recently been used to address, in much detail, important morphological characteristics of polar cap patches and Sun-aligned arcs [Fukui *et al.*, 1994; Valladares *et al.*, 1994a; Rodriguez *et al.*, 1997]. In addition, continuous records of auroral emissions together with IMP 8 solar wind measurements can and have been used to learn more about the control that the IMF, through merging on the dayside and reconnection on the nightside, exerts on the arcs' growth, transit, and decay.

Since the early observations of large-scale structures inside the polar cap [Weber and Buchau, 1981; Buchau *et al.*, 1983], it became evident that the plasma density enhancements seen within the polar cap were transported from the subcusp/cusp ionosphere. In fact, incoherent scatter radars had observed high-density plasma convecting through the dayside throat region toward and into the polar cap [Foster and Doupnik, 1984; Kelly and Vickrey, 1984]. While time-averaged densities showed a continuous and an elongated tongue of ionization (TOI), optical and radio observations indicated that the plasma enhancements within the polar cap were always patchy. This fact suggested the existence of one or more physical processes able to split the continuous TOI into smaller entities or to produce intermittent intrusions of subcusp plasma into the polar cap [Lockwood and Carlson, 1992].

Tsunoda [1988], in his very complete treatise about patches and blobs, enumerated several potential mechanisms for patch formation. He suggested that consecutive reversals of B_y or B_z could indeed produce oval detached, confined regions containing high-density plasma. In spite of the early suggestions, not until recently have numerical simulations of the B_y switching mechanism, which included repetitious changes in the global convection pattern and the presence of localized velocity structures, been able to reproduce patches with the correct sizes and morphology [Sojka *et al.*, 1993, 1994; Decker *et al.*, 1994; Valladares *et al.*, 1994b, 1996]. The B_y switching mechanism makes the TOI break off into discrete entities of high density, presenting a variety of shapes and sizes. Numerical simulations have also demonstrated that elliptical

vortices moving poleward could generate more elongated patches [Valladares *et al.*, 1996]. These authors suggested that a large flow channel velocity, also named a plasma jet, can create a plasma depletion along a sectional cut of the TOI due to two factors: an enhancement of the O^+ recombination coefficient and transport of less dense plasma from regions away from noon.

In spite of recent progress in studies of patches and arcs, our knowledge of the high-latitude plasma structures is still incomplete, particularly in that we do not have a clear view of the density features and/or the velocity structures that populate the polar cap when transitions in the IMF occur. When the B_z component of the IMF changes sign, the temporal evolution of images of optical emissions seen within the polar cap provides valuable information to investigate the time delays that are required for the establishment of the new pattern of polar plasma velocities and the new order of plasma structures. In this paper we report observations of optical emissions gathered with the Qaanaaq ASIP during IMF B_z south-to-north transitions. We show the polar cap structure transition from a patch-dominated to an arc-dominated pattern. We studied 19 cases in which both patches and arcs were simultaneously present between 1989 and 1994. We present data here for three of these days, selected in part to show variability of the configurations in the images, while illustrating recurrence of simultaneous presence within the polar cap. Until now, study has largely focused on either patch or arc conditions. No data have appeared to address the question of whether " B_z south patches" and " B_z north arcs" can coexist, and if so under what conditions. This paper addresses these issues using concurrent measurements from an ASIP, a digisonde, and the IMP 8 and DMSP F8 satellites.

2. Observations

An all-sky intensified photometer (ASIP) was deployed at Qaanaaq in 1983. Since then this imager has been instrumental in several important studies of the morphology and dynamics of Sun-aligned arcs and polar cap patches [Valladares *et al.*, 1994a; Fukui *et al.*, 1994; Zhu *et al.*, 1996; Rodriguez *et al.*, 1997]. Details about the instrument sensitivity and calibration, as well as the data analysis, have been described in previous publications [Weber *et al.*, 1984; Buchau *et al.*, 1985; Fukui *et al.*, 1994; Valladares *et al.*, 1994a]. We present images in which polar cap patches and Sun-

aligned arcs coexisted for a short interval after transitions of the IMF B_z component. These images were found after scanning all the red line (630.0 nm) and the blue band (427.8 nm) images recorded between 1989 and 1994. During the search process, special attention was paid to the occasions when the imager display changed from a patch-dominated scenario to a Sun-aligned arc pattern and vice versa. We note that observations of "simultaneous occurrence of patches and arcs" have been previously reported in one publication by Buchau *et al.* [1983, Figure 1], although without reference to the IMF conditions. Buchau *et al.* [1983] observed, on a few occasions, small patches developing adjacent to a Sun-aligned arc and then drifting along the arc in the antisunward direction. Buchau *et al.* [1983] stated, that the small patches (<100 km) seemed to peel off from the larger arc structures. Accepting their hypothesis, we would suggest that their "simultaneous patches" would be better described as structured density within arcs, presumed to be for ongoing B_z north. In the present paper, our observations correspond to residual patches and newly formed arcs coexisting inside the polar cap due to proximity of flux tubes extended from within the patches to downstream magnetic field topology, while arcs reflect prompt

response to abrupt changes of the IMF and consequently prompt intrusion of flux tubes associated with electron currents and soft precipitation associated with the newly established convection.

We found 19 cases in which both patchy and arc structures were identified to occur simultaneously. All these cases correspond to south-to-north transitions of the IMF. However, no similar coexistence was found during north-to-south transitions. We present images from four periods to indicate the variability of the details of the process and the constancy of the nature of the process. Three of the four case events are fully described here by presenting the IMF data collected by the IMP 8 satellite, 630.0 nm images taken by the Qaanaaq ASIP; f_oF_2 values recorded by the digisonde; and in one of the events, particle and velocity information acquired by the DMSP F8 satellite. In the fourth case event, described in section 2.1, we present only Qaanaaq ASIP images.

In a recent study, Sojka *et al.* [1997] have pointed out the ambiguity that exists in the optical measurement of patches. These authors concluded that enhancements in the 630.0-nm airglow are not always one-to-one correlated with increases in N_mF_2 , but depend strongly upon h_mF_2 and more weakly on the neutral atmosphere.

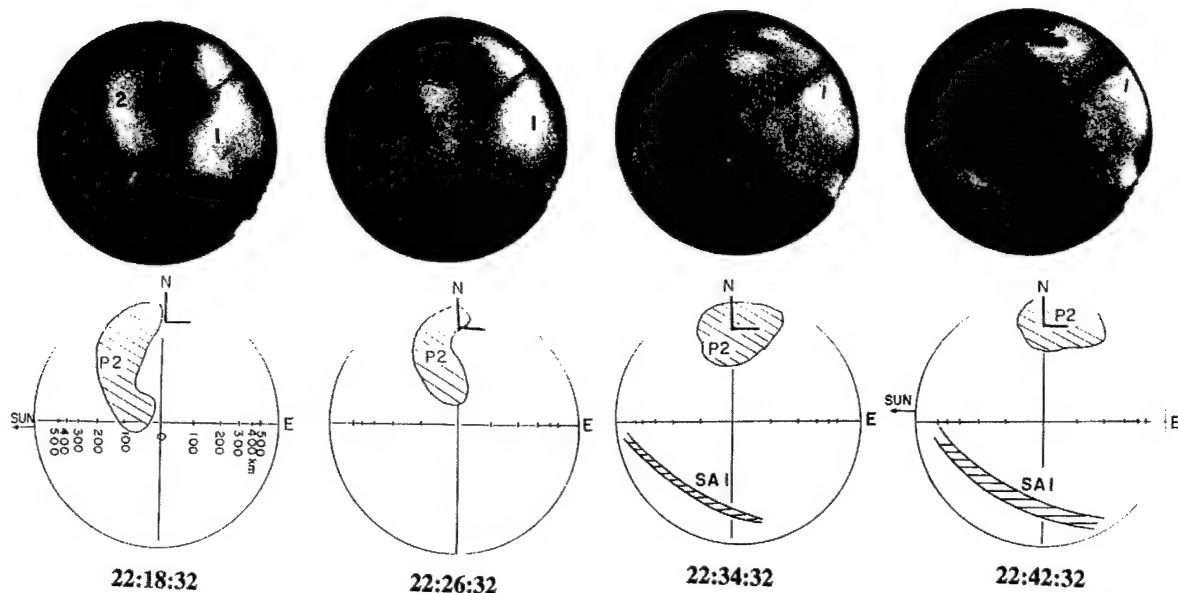


Figure 1. Sequence of four images measured at Qaanaaq, Greenland, during the transit of polar cap patches through the all-sky intensified photometer's field of view and the concurrent development of polar cap arcs. The four panels in the bottom row represent a schematic representation of the patches and arcs seen in the four images of the top row.

To overcome this inherent difficulty of the airglow images, we have used $h_m F_2$ values and plasma frequency profiles of the F region bottomside measured simultaneously by the Qaanaaq's digisonde.

2.1. December 28, 1991

The top row of Figure 1 displays four images obtained between 2218:32 and 2242:32 UT on December 18, 1991. The bottom row shows an artist's representation of the airglow and the auroral emissions recorded in the four images of the top row. The motion of patch 2 is in the antisunward direction (toward geographic east). This patch almost disappears near the northern edge of the imager field of view (FOV) in the image corresponding to 2242:32 UT. The image of 2234:32 UT shows the first clear view of a polar cap arc near the southwestern horizon (duskside). The arc is Sun-aligned and drifts toward the dawnside of the image. We have also indicated in the schematics of the bottom row the approximate horizontal distances in the

east-west direction. Note that the spatial distortion produced by the camera fish-eye lens is axially symmetric.

2.2. October 29, 1989

On this day the IMP 8 satellite was in a favorable position for the observation of the solar wind magnetic field. At the time of the B_z reversal the satellite was located in front of the magnetopause, at +24.5, -20.0, and +17.0 Earth radii (R_E), corresponding to the X , Y , and Z GSM coordinates, respectively. Figure 2 shows a B_z negative value until 0520 UT, when a sharp transition from -5 to 0.5 nT occurred. Afterward, B_z was positive for the following 7 hours, but it remained below +1 nT between 0520 and 0707 UT. Figure 3 shows a sequence of 630.0-nm images on October 29, 1989, at 6-min intervals. On this day, patches started transiting through the Qaanaaq field of view (FOV) at 0509 UT (image not shown). The image at 0525:26 UT shows two patches: one through the zenith, labeled 1,

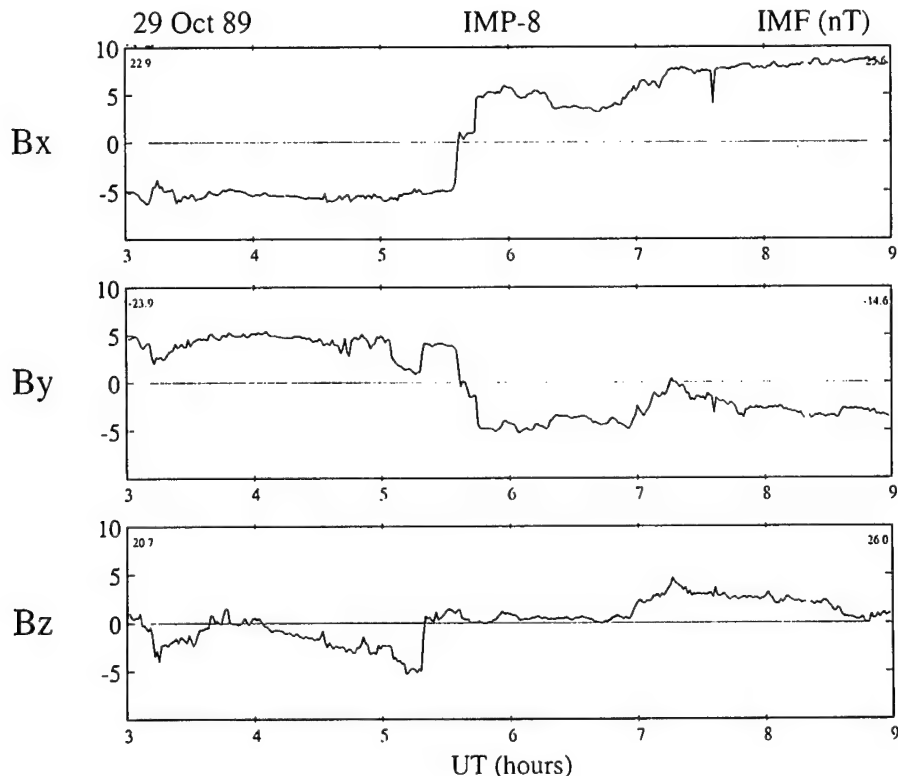


Figure 2. Interplanetary magnetic field (IMF) measured by the IMP 8 satellite at $22.9 R_E$, well within the solar wind. All three IMF components are shown in GSM coordinates. Units for all three quantities are nanoteslas. Note the south-to-north reversal of the B_z component at 0520 UT.

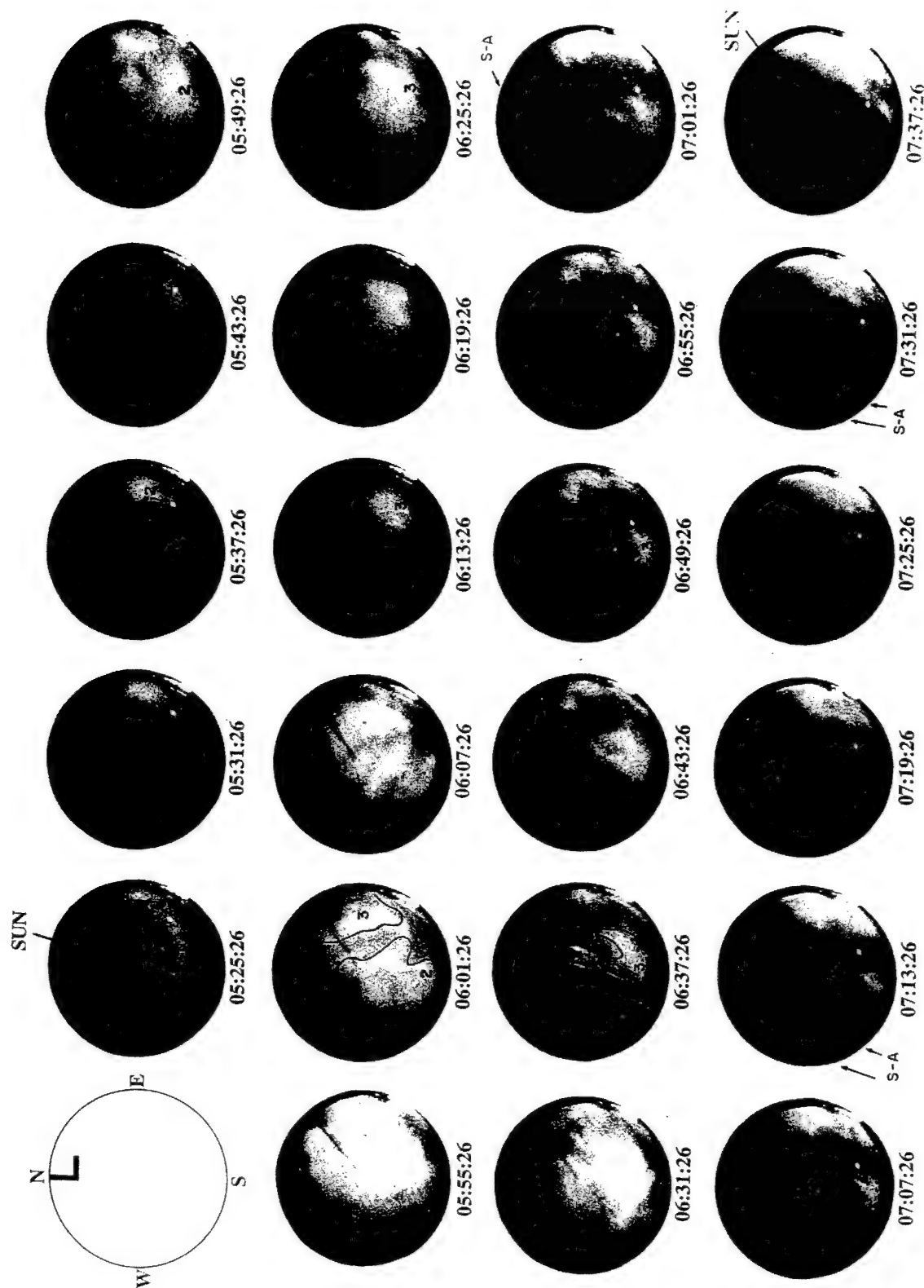


Figure 3. Sequence of all-sky images at 630.0 nm from Qaanaaq, October 29, 1989. Geographic north is at the top of each image, and geographic west is to the left. The direction toward the Sun is also displayed in the second and last frames to indicate the direction of motion of the patches and the orientation of the polar cap arcs.

and the other along the northeast horizon, labeled 2. Patch 1 is cigar-shaped, with the major axis aligned in the dawn-dusk direction. Patch 2 is more rounded and not yet fully within the ASIP FOV, at 0537:26 UT. The leading edge of patch 2 drifted through the zenith at 0543 UT. Both patches move antisunward between 0525 and 0549 UT. A third patch, labeled 3, entered the FOV near 0555:26 UT and crossed the zenith direction at 0619:26 UT. The situation is more complex while B_z is approximately zero, but as soon as B_z north intensifies, just before 0700 UT, Sun-aligned arcs become clear at the dusk horizon. (See arrows labeled S-A at the image of 0701:26 UT and successive images.) These arcs slowly moved downward in the subsequent images.

Figure 4 shows the f_oF_2 values measured by the digisonde. The four peak values labeled 1-4 correspond to the passage of the optical patches across the sounder zenith direction. These four f_oF_2 enhancements occur at 0520, 0550, 0615, and 0650 UT, when f_oF_2 values increase by at least a factor of 2. Figure 4 proves that the density enhancements detected by the digisonde correlate well with the timing of the appearance of the airglow patches of Figure 3.

Figure 5 shows digisonde density contours in a more proper format to reaffirm our conjecture that the airglow patches indeed correspond to patches of

enhanced density that convect across the station according to the antisunward plasma flow. *Sojka et al.* [1997] used the USU TDIM theoretical model to demonstrate that 630.0-nm airglow patches not only depend upon the ionospheric N_mF_2 values, but knowledge of h_mF_2 was necessary to evaluate quantitatively the level of airglow enhancement. Figure 5 displays the h_mF_2 (solid line with diamonds) and several isodensity contours. These contours start at 1 MHz ($0.12 \times 10^5 \text{ cm}^{-3}$) and increase in steps of 1 MHz. Contours corresponding to 6 ($4.4 \times 10^5 \text{ cm}^{-3}$) and 7 MHz ($6 \times 10^5 \text{ cm}^{-3}$) have been traced with bolder lines. We observe that, in fact, patches 1 and 3 occur at times when f_oF_2 increases to 7 and 8 MHz ($8 \times 10^5 \text{ cm}^{-3}$) and h_mF_2 lowers to 350- and 330-km altitude. The level of 630.0-nm airglow enhancement produced by these N_mF_2 and h_mF_2 values can be calculated using Figure 6 of *Sojka et al.* [1997] to demonstrate that the transit of the airglow patches can be explained by variations of the ionospheric plasma and do not correspond to the presence of auroral emissions. Using Figure 6 of *Sojka et al.* [1997], we obtained airglow intensities of 120 and 250 Rayleighs for the values of patches 1 and 3. These airglow values are indeed detectable and much higher than the 70-R sensitivity threshold of the Qaanaaq imager.

We used the expression given by *Lockwood et al.*

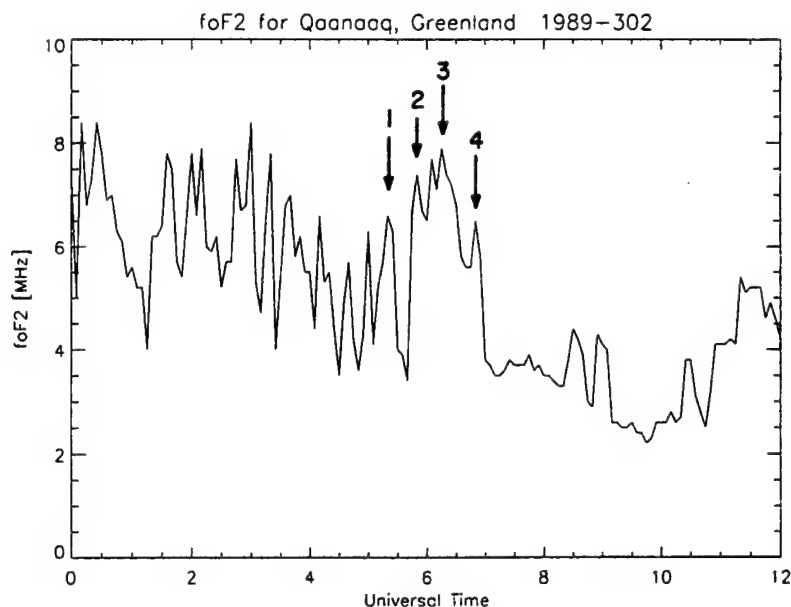


Figure 4. Variations of f_oF_2 as a function of UT on October 29, 1989 recorded at the Qaanaaq station (77.5° N, 69.2°W). Note the transit of the four patches indicated with arrows and labeled 1-4.

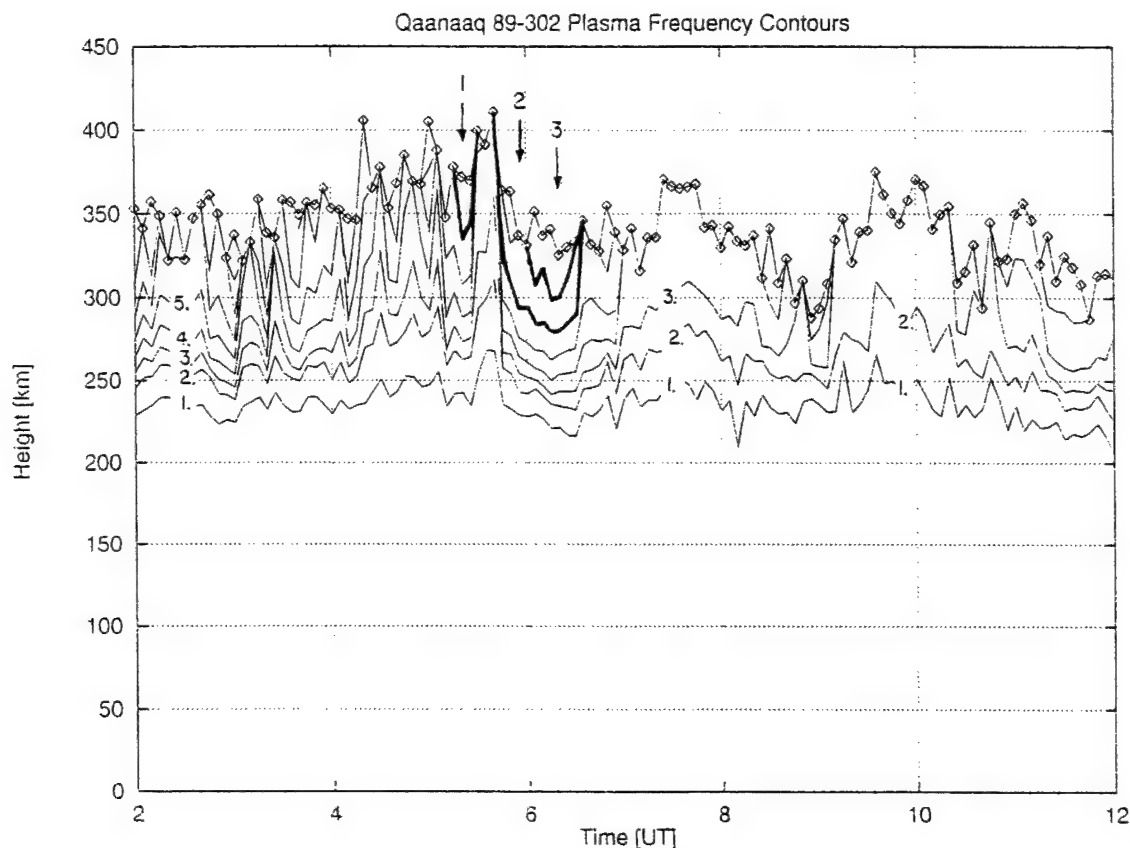


Figure 5. Plasma frequency contours and h_mF_2 (F layer peak altitude) measured by the Qaanaaq digisonde on October 29, 1989. Contours corresponding to 6 and 7 MHz have been traced with a bold line to point out the increase in the number density and the lowering of the vertical profiles associated with the passage of the patches. The contour with diamonds denotes the h_mF_2 values.

[1989] to calculate that the time delay for the effect of the IMF B_z transition to reach the ionosphere was 7.5 min. After considering this time delay, we concluded that the arc appeared inside the Qaanaaq FOV 80 min after the effect of the IMF south-to-north transition reached the ionosphere. Nevertheless, polar cap arcs may have appeared earlier at other places of the polar cap. Thus the 80 min may represent only an upper limit of the delay time for the arcs to appear.

2.3. October 17, 1990

Figure 6 displays the IMF values measured by the IMP 8 satellite on October 17, 1990. During this day the IMP 8 satellite was located at 16.2, -20.1, and 20.8 R_E , corresponding to the X , Y , and Z components, respectively, of the IMF. Several reversals of the B_z component of the IMF occurred between 0130 and 0243

UT. However, it is the last south-to-north reversal, the one at 0243 UT, that is probably associated with the appearance of Sun-aligned arcs at Qaanaaq.

Figure 7 shows 630.0-nm images at 6-min intervals from 0110 to 0328 UT on October 17, 1990. At 0110:37 UT, patch 1 is elongated in the dawn-dusk direction and located overhead; patch 2 is placed along the sunward horizon. Between 0110:37 and 0134:37 UT, both patches are seen moving antisunwardly. At 0134:37 UT the leading edge of patch 1 reaches the southern horizon, and patch 2 is nontypically aligned in the sunward-antisunward direction. Subsequent images show patch 2 moving toward dusk. A new patch, labeled 3, enters the imager FOV at 0146:37 UT, moves parallel to patch 2, and crosses the zenith at 0204:37 UT. Patch 3 possesses a nontypical velocity directed duskward. Plasma drift velocities (not presented here)

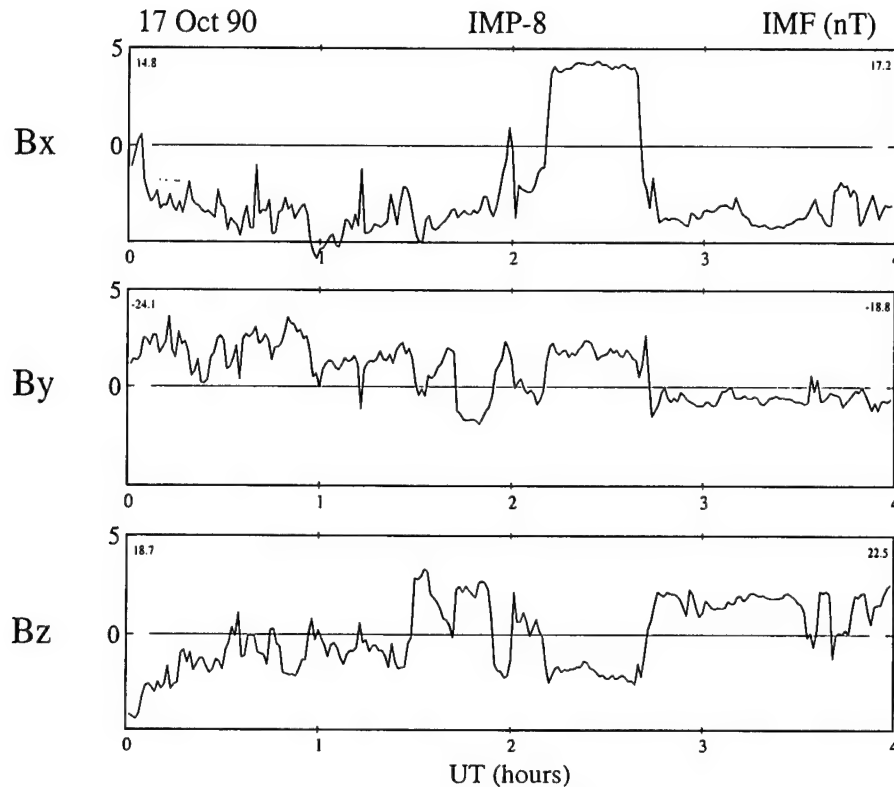


Figure 6. Interplanetary magnetic field on October 17, 1990, measured by the IMP 8 satellite at $14.8 R_E$, in front of the magnetopause. The format is similar to Figure 2. Note the series of B_z reversals between 0130 and 0245 UT.

measured with the digisonde show that, in fact, the velocity changed from an antisunward to a more duskward orientation at ~ 0130 UT. This corroborates that the motion of the airglow patches, observed with the ASIP, is in the same direction as the plasma velocity. At 0258:37 UT, patch 3 was observed near the dusk horizon coexisting with a faint Sun-aligned arc feature located near zenith. This corresponds to the first sight of the S-A arc during this event. Twelve minutes later another arc grows sunwardly from midnight and intensifies at 0322:37 UT. Sudden intensification and decays are quite typical of polar cap arcs, while the airglow emissions associated with patches are generally unchanged. This particular characteristic confirms the presence of a Sun-aligned arc in the southern region of the imager FOV.

Figure 8 shows that the f_oF_2 values reach a value equal to 9.5 MHz ($1.1 \times 10^6 \text{ cm}^{-3}$) during the transit of patches 1 and 3. Note also that the 630.0-nm images indicate that patch 2 did not cross the overhead location

due to a combined distortion and a westward (duskward) motion of the patch soon after it appeared within the FOV. Patches 1 and 3 did transit over the digisonde. Their h_mF_2 (Figure 9) are 315 and 335 km. Using these values and the parameterized model of *Sojka et al.* [1997], we obtained values of 400 and 300 R for patches 1 and 3, respectively.

Figure 10 shows the satellite trajectory of the DMSP F8 satellite projected from 840 km, along field lines, down to 300-km altitude. The satellite enters the dawnside of the Qaanaaq's FOV at 0258:30 UT and exits at 0303:30 UT. The spectrogram of Figure 11 shows a strong beam of electrons and ions being deposited within the polar cap at 0300:15 UT. Another much weaker electron precipitation, without ions, occurs at 0259:57 UT. From Figure 10 we can deduce that the strong electron beam occurred a few hundred kilometers east of Qaanaaq. Thus we conclude that this beam of precipitating particles is well collocated with the polar cap arc seen near the east horizon at 0304:37

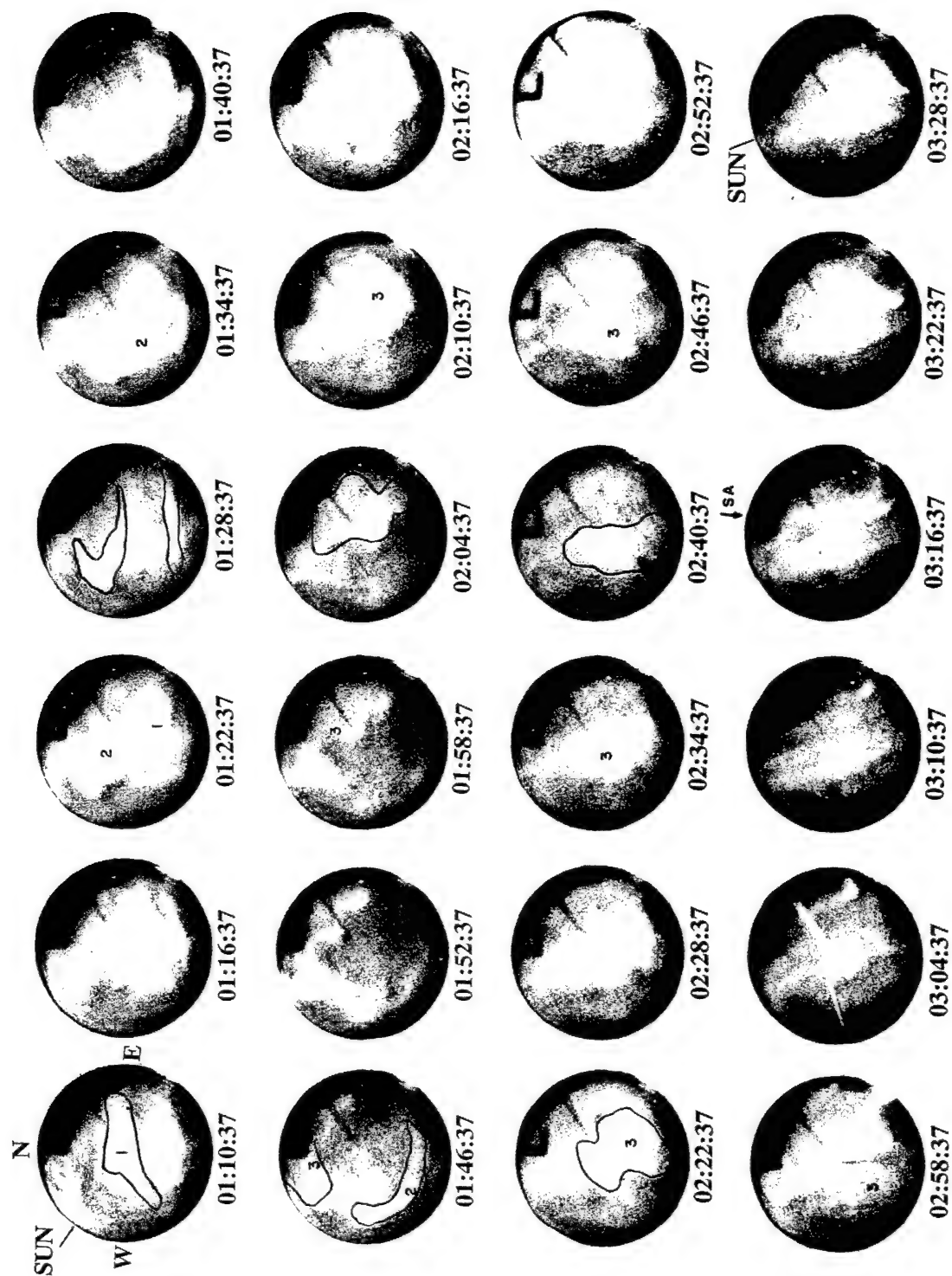


Figure 7. Similar to Figure 3, but for October 17, 1990.

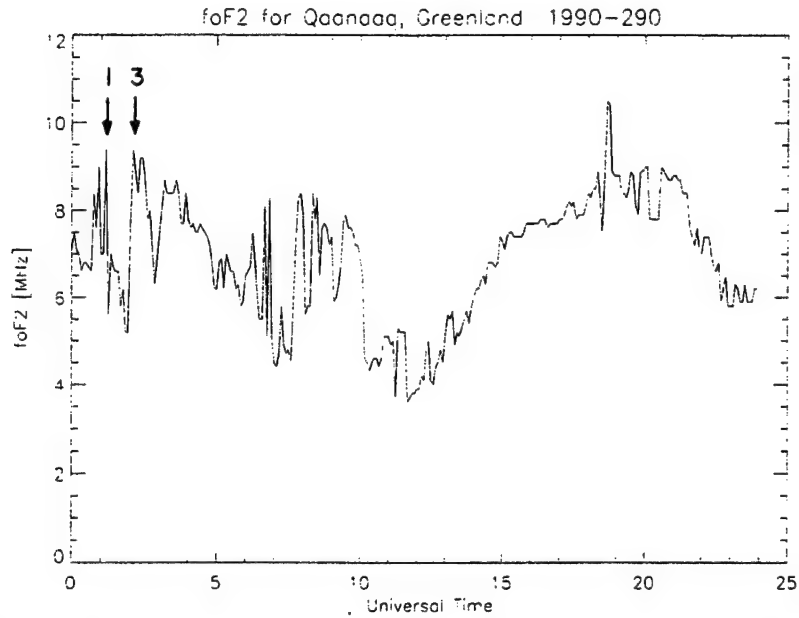


Figure 8. Values of f_oF_2 corresponding to October 17, 1990. The format is similar to that of Figure 4.

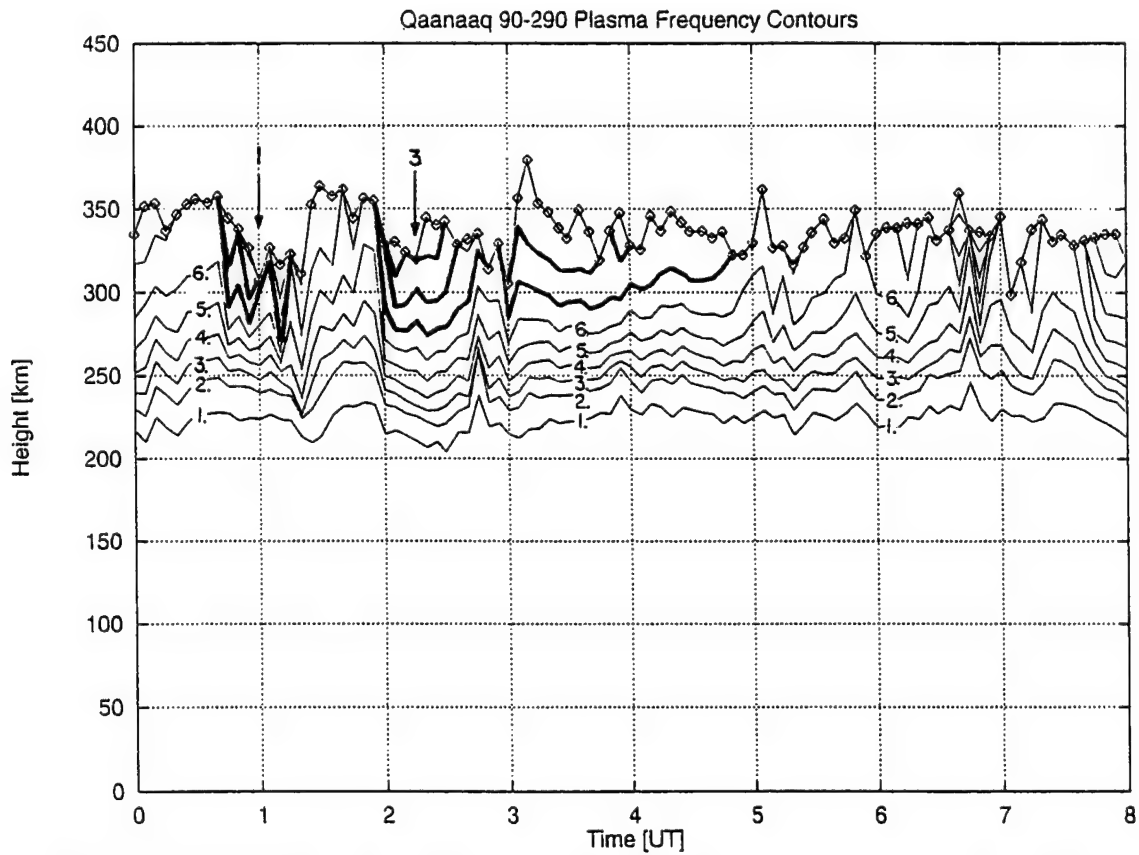


Figure 9. Plasma frequency contours and h_mF_2 measured by the Qaanaaq digisonde on October 17, 1990. The format is similar to Figure 5. The bold contours correspond to 7, 8, and 9 MHz.

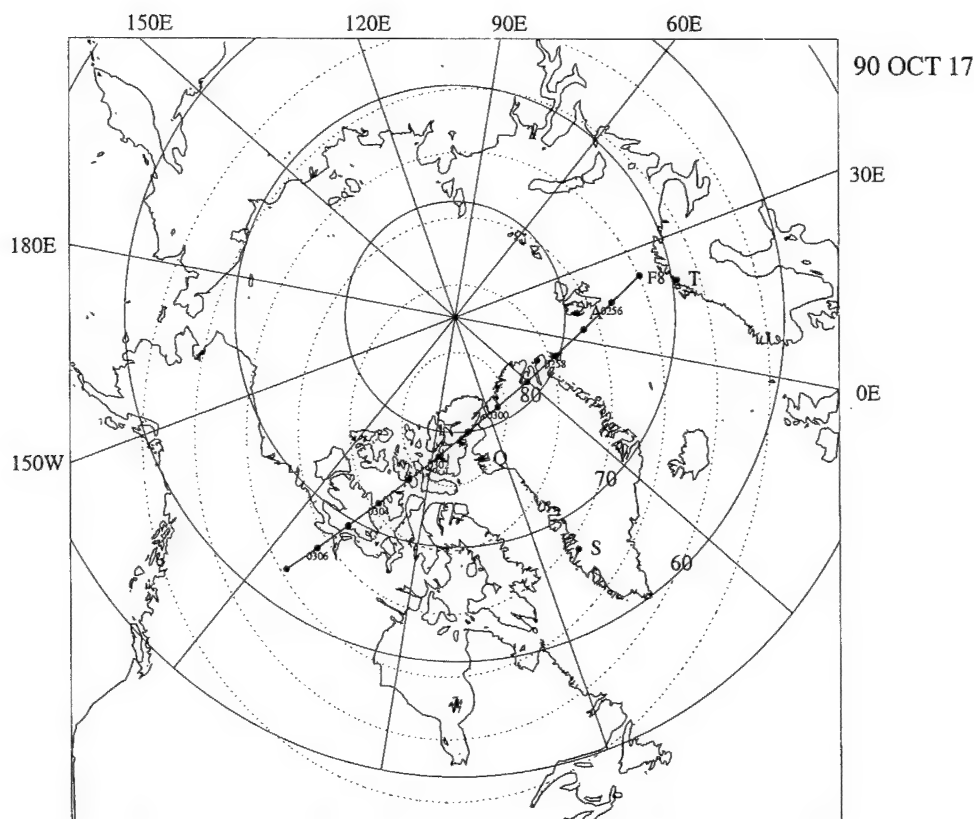


Figure 10. Illustration of the satellite trajectory projected along magnetic field lines to 250 km altitude, October 17, 1990. The location of the Qaanaaq station is indicated by the letter Q. The DMSP F8 pass was between 0256 and 0306 UT.

UT. This arc later moved almost overhead and clearly intensified at 0316:37 UT. In a summary, concurrent ASIP, digisonde, and DMSP observations demonstrate that during a few minutes polar cap patches (density enhancements) and S-A arcs (electron beams) existed simultaneously inside the Qaanaaq's FOV.

On the basis of the location of the IMP 8 satellite and the expression provided by Lockwood *et al.* (1989), we obtained a time delay equal to -3 min. On October 17, 1990, the appearance of the polar cap arcs lagged the B_z IMF transition by 18 min. However, close inspection of the Z component of the IMF shows a series of positive excursions before the reversal of 0243 UT. Consequently, it is quite likely that the polar cap arcs developed earlier in response to a previous positive B_z period.

2.4. December 3, 1992

On this day, the IMP 8 satellite was probably inside the magnetosheath on the dawn flank of the Earth. The

X , Y , and Z coordinates of the spacecraft in the GSM system were -14.7 , -20.6 and $17.0 R_E$, respectively. The time delay, computed following the method described above, is equal to 5 min. Figure 12 shows the three components of the IMF that were measured in a 4-hour segment centered near the time of the reversal of B_z . At 0542 UT, B_z reverses abruptly almost simultaneously with a B_y reversal from negative to positive. The images gathered by the Qaanaaq's ASIP (Figure 13) show a clear case in which a display of patches changed to an arc-dominated scenario. Patch 1 appeared at the northern part of the imager at 0533:53 UT. It crossed overhead at 0541:53 UT and then exited through the southern horizon at 0549:53 UT. On this day, f_oF_2 values were obtained with a 15-min time resolution. Owing to this coarse temporal resolution and the narrow width of patch 1, no measurement of the peak density within patch 1 was attained. Patch 2 was larger and more rounded. It crossed the overhead location between 0557:53 and 0609:53 UT. At 0600 UT, the

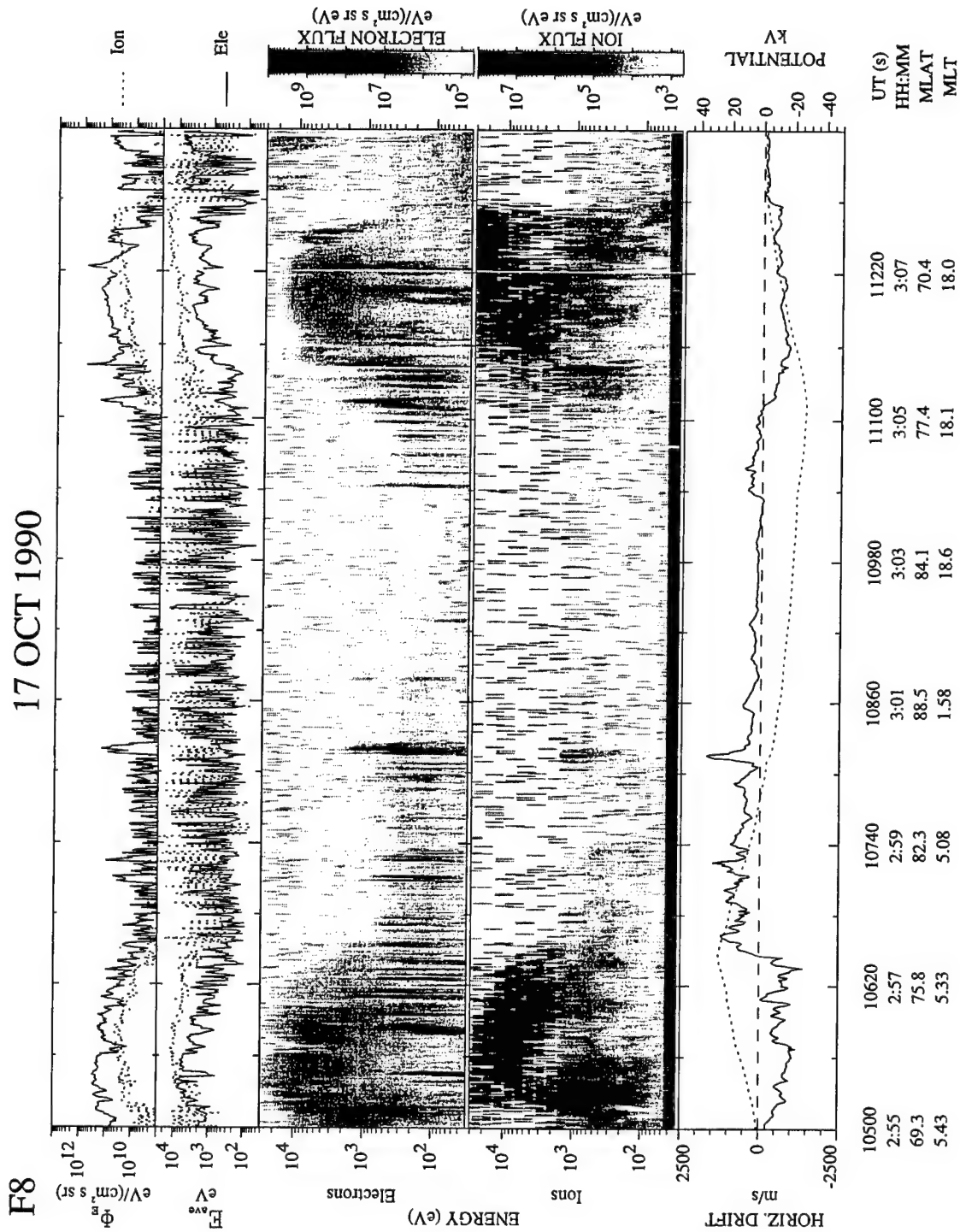


Figure 11. Integral electron and ion fluxes, energy-time spectrograms of precipitating electrons and ions, horizontal cross-track ion drift velocity observed by DMSP F8, and derived polar cap potential pattern for October 17, 1990.

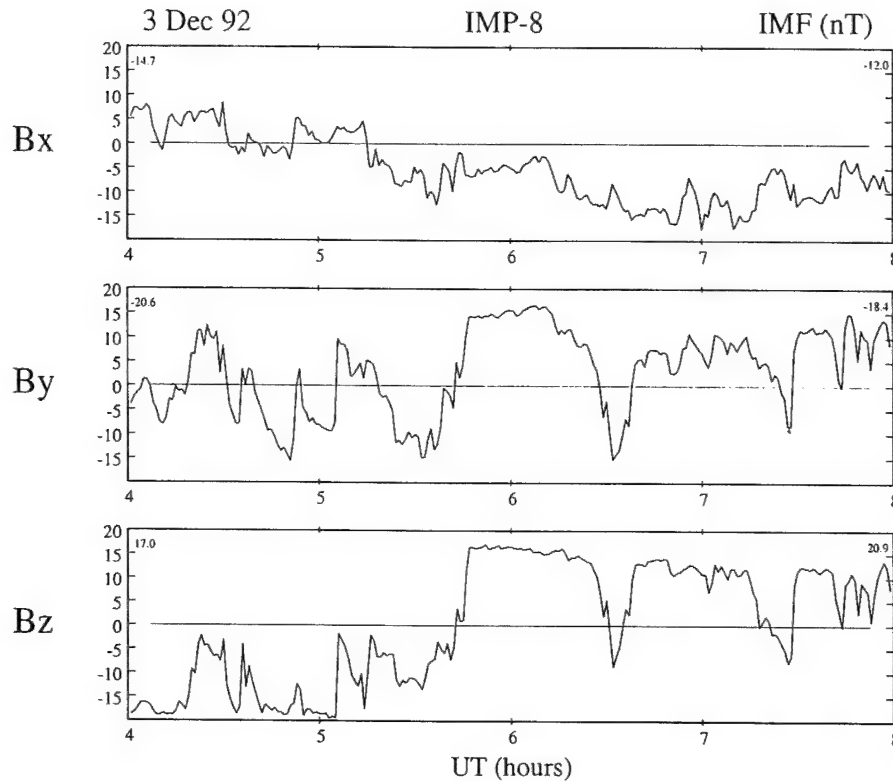


Figure 12. Interplanetary magnetic field measured by the IMP 8 satellite at $-14.7 R_E$ in the dawnside magnetosheath. The format is similar to Figure 2. Note the south-to-north B_z reversals at 0542 UT.

Qaanaaq's digisonde observed an enhancement of f_oF_2 , reaching a value of 5 MHz (see Figure 14). The density enhancement, similar to other patches presented here, was accompanied by a decrease in the h_mF_2 . Figure 15 shows that when the patch was transiting overhead the station, the h_mF_2 value decreased to 280 km. Patch 2 continues moving antisunwardly until 0621:53 UT, when it exits the FOV. At 0625:53 UT, there appears a faint arc extending from north to south and closely aligned with the Sun direction. This arc is seen in subsequent images. Later, at 0633:53 UT, the arc brightens starting from the arc end closest to the Sun and progressing in an antisunward manner. The arc becomes fully developed at 0637:53 UT and splits in two at 0641:53 UT. Again using the parameterized model of *Sojka et al.* [1997], we computed that the airglow enhancement due to the patch transit was equal to 200 R. On this day, the polar cap arcs were observed at Qaanaaq 48 min (adjusted by the IMF time delay) after the effect of the B_z IMF transition reached the ionosphere.

3. Discussion and Conclusions

This paper has provided the first experimental evidence that polar cap patches and Sun-aligned arcs can exist simultaneously inside the FOV of an ASIP that is located deep within the polar cap. It also interprets these observations in the context of a model that explains the IMF and time dependencies of the conditions under which coexistence is observed. The area covered by the imager is roughly equal to a circle of 1000 km in diameter. Our interpretation of the driving mechanism leads to the expectation that if we were able to observe the whole polar cap with the same instrumental sensitivity that was used at Qaanaaq, then many more cases of patches and arcs coexisting would have been found. Notable is that all these patch-arc sightings were restricted to near and shortly after the time the IMF B_z changed from a negative to a positive orientation.

We have seen that on two cases, October 29, 1989, and December 3, 1992, the patches continued moving antisunwardly apparently unaffected by the occurrence

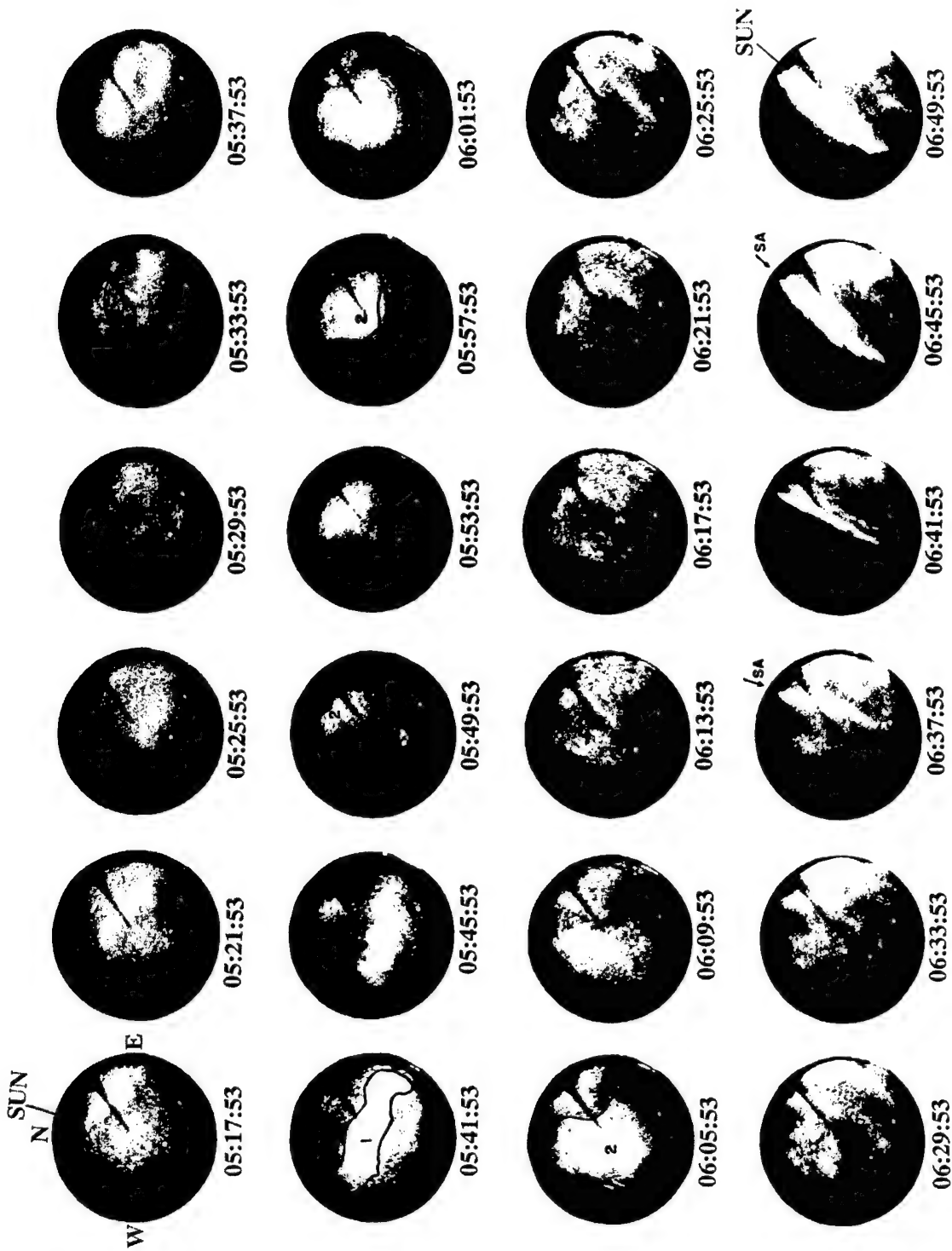


Figure 13. Similar to Figure 3, but for December 3, 1992.

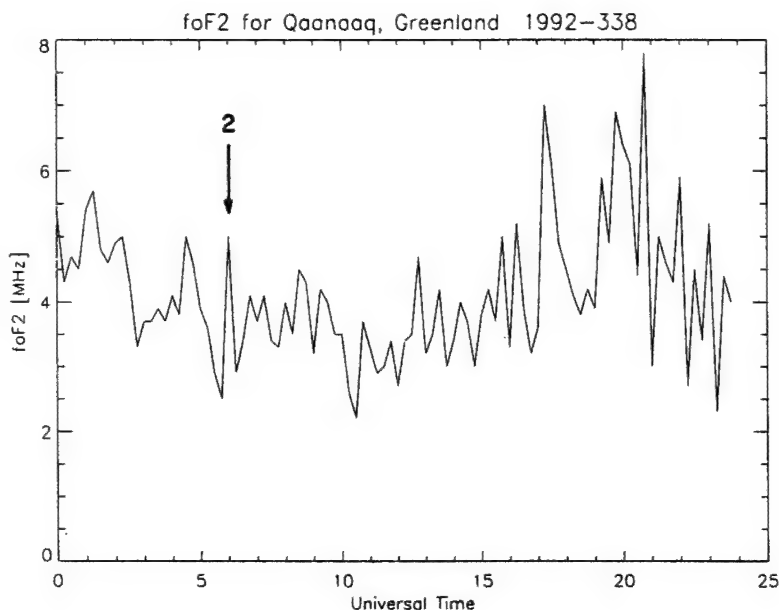


Figure 14. Values of f_oF_2 corresponding to December 3, 1992. The format is similar to that of Figure 4.

and the motion of the polar cap arcs. On October 17, 1990, several B_z reversals complicated the geophysical conditions beyond the scope of this paper between 0135 and 0240 UT. Before this time interval the patch motion is consistently oriented in the antisunward direction [Fukui *et al.*, 1994].

In all three cases presented here the last patches observed had progressed to near the midnight sector by the time the first arc was seen. Considering that it may take up to 1 hour for the patches to transit from the dayside to the midnight oval, this is consistent with the suggestion that all the patches presented here were created well before the arcs appeared within the Qaanaaq FOV. The patches in these three events did not have time to exit the polar cap before the time the arcs had developed. These patches were not peeled off from the arc structures, as suggested by Buchau *et al.* [1983].

The digisonde data have revealed that the plasma density enhancements, which constitute the patches, are also accompanied by a corresponding decrease in the value of the h_mF_2 . This property of the patches facilitates its detection using 630.0-nm airglow measurements.

We obtained arc delays equal to 80, 18, and 48 min; however, as seen in Figure 6, the second case was affected by multiple reversals of B_z . Thus we concluded that the more reliable delays were 80 and 48 min. As

expressed before, these numbers are only upper limits of the time delay between IMF B_z transitions and the arc appearance. This is borne out by the limited coverage that a single camera can provide. On the basis of DMSP overpasses above the poles, Hairston and Heelis [1995] obtained a time lag between 28 and 44 min for the establishment of a new polar convection signature in the ionosphere after the IMF turned from southward to northward. The numbers that we are reporting here clearly constitute an upper limit.

Cowley and Lockwood [1992] have discussed how the polar convection is maintained by the combined action of two reconnection-driven components. One occurs at the dayside, probably at the nose of the magnetopause, and the second occurs at the tail. During B_z northward conditions the plasma convection may occur by a combined action of two components, namely, lobe stirring due to reconnection between the northward IMF and open tail lobe lines, and continuing tail reconnection. Considering that the polar cap arcs are powered by any of these reconnection processes, then the field lines that end in the polar cap arcs will map to regions in the tail. The field lines that end in the polar cap patches are also on open field lines extending toward the magnetotail.

This study leads us to the following conclusions:

1. All the airglow patches were associated with enhancements of N_mF_2 and decreases of h_mF_2 . These

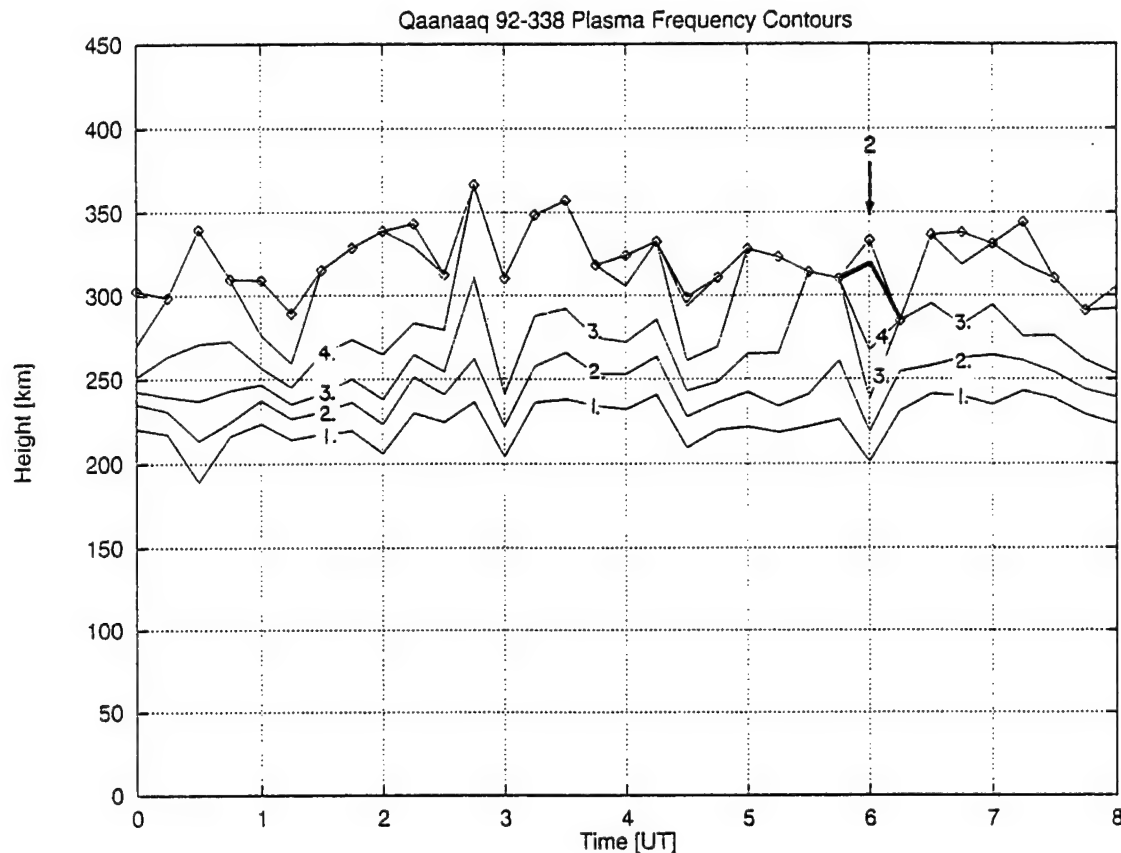


Figure 15. Plasma frequency contours and $h_m F_2$ measured by the Qaanaaq digisonde on December 3, 1992. The format is similar to Figure 5. The bold contour corresponds to 5 MHz.

two factors increase the amount of 630.0-nm airglow emissions detected on the ground, consequently improving the detection of the patches when only 630.0-nm airglow measurement is available.

2. Polar cap arcs embedded within the polar cap were seen by the DMSP F8 satellite and were well collocated with the auroral emissions detected by the Qaanaaq imager.

3. Polar cap patches and arcs can exist simultaneously even in a small region of the polar cap (1000 km diameter).

4. If we were able to combine images from several different ASIPs already deployed at or near the polar cap, we should be able to find many more cases of patches and arcs existing simultaneously. Covering a larger area of the polar cap, with several imagers, should allow tracing the progression of the arcs when they are formed.

Acknowledgments. The work at Boston College was partially supported by NSF grants INT-9603362, ATM-9404088, and ATM-9613925 and by Air Force Research Laboratory contract F19628-97-C-0094. One of us (H.C.C.) was supported by grant AFOSR 231069. We thank the Danish Commission for Scientific Research in Greenland for permission to conduct ground experiments at Sondrestrom under continuing project A16-91.

References

- Basu, Su., S. Basu, E.J. Weber, and G.J. Bishop, Plasma structuring in the polar cap, *J. Geomagn. Geoelectr.*, **42**, 763, 1990.
- Berkey, T., L.L. Cogger, S. Ismail, and Y. Kamide, Evidence for a correlation between Sun-aligned arcs and the interplanetary magnetic field direction, *Geophys. Res. Lett.*, **3**, 145, 1976.
- Buchau, J., B.W. Reinisch, E.J. Weber, and J.G. Moore, Structure and dynamics of the winter polar cap *F* region, *Radio Sci.*, **18**, 995, 1983.
- Buchau, J., E.J. Weber, D.N. Anderson, H.C. Carlson Jr., J.G.

- Moore, B.W. Reinisch, and R.C. Livingston, Ionospheric structures in the polar cap: Their origin and relation to 250-MHz scintillation, *Radio Sci.*, **20**, 325, 1985.
- Carlson, H.C., V.B. Wickwar, E.J. Weber, J. Buchau, J.G. Moore, and W. Whiting, Plasma characteristics of polar cap *F* layer arcs, *Geophys. Res. Lett.*, **11**, 895, 1984.
- Cowley, S.W.H. and M. Lockwood, Excitation and decay of solar wind-driven flows in the magnetosphere-ionosphere system, *Ann. Geophys.*, **10**, 103, 1992.
- Crowley, G., H.C. Carlson, S. Basu, W.F. Denig, J. Buchau, and B.W. Reinisch, The dynamic ionospheric polar hole, *Radio Sci.*, **28**, 401, 1993.
- Decker, D.T., C.E. Valladares, R. Sheehan, S. Basu, D.N. Anderson, and R.A. Heelis, Modeling daytime *F*-layer patches over Sondrestrom, *Radio Sci.*, **29**, 249, 1994.
- Foster, J.C., and J.R. Doupnik, Plasma convection in the vicinity of the dayside cleft, *J. Geophys. Res.*, **89**, 9107, 1984.
- Fukui, K., J. Buchau, and C.E. Valladares, Convection of polar cap patches observed at Qaanaaq, Greenland, during the winter of 1989-1990, *Radio Sci.*, **29**, 231, 1994.
- Hairston, M.R., and R. A. Heelis, Response time of the polar ionospheric convection pattern to changes in the north-south direction of the IMF, *Geophys. Res. Lett.*, **22**, 631, 1995.
- Kelly, J.D., and J.F. Vickrey, *F* region ionospheric structure associated with antisunward flow near the dayside polar cusp, *Geophys. Res. Lett.*, **11**, 907, 1984.
- Lassen, K., and C. Danielsen, Quiet time pattern of auroral arcs for different directions of the interplanetary magnetic field in the *Y-Z* plane, *J. Geophys. Res.*, **83**, 5277, 1978.
- Lockwood, M., and H.C. Carlson, Production of polar cap electron density patches by transient magnetopause reconnection, *Geophys. Res. Lett.*, **19**, 1731, 1992.
- Lockwood, M., P.E. Sandholt, S.W.H. Cowley, and T. Oguni, Interplanetary magnetic field control of dayside auroral activity and the transfer of momentum across the dayside magnetopause, *Planet. Space Sci.*, **37**, 1347, 1989.
- Rodriguez, J. V., C.E. Valladares, K. Fukui, and H.A. Gallagher, Antisunward decay of polar cap arcs, *J. Geophys. Res.*, **102**, 27,227, 1997.
- Sojka, J.J., M.D. Bowline, R.W. Schunk, D.T. Decker, C.E. Valladares, R. Sheehan, D.N. Anderson, and R.A. Heelis, Modeling polar cap *F* region patches using time varying convection, *Geophys. Res. Lett.*, **20**, 1783, 1993.
- Sojka, J.J., M.D. Bowline, and R.W. Schunk, Patches in the polar ionosphere: UT and seasonal dependence, *J. Geophys. Res.*, **99**, 14,959, 1994.
- Sojka, J.J., R.W. Schunk, M.D. Bowline, and D.J. Crain, Ambiguity in identification of polar cap *F*-region patches, *J. Atmos. Sol. Terr. Phys.*, **59**, 101, 1997.
- Tsunoda, R.T., High-latitude *F* region irregularities: a review and synthesis, *Rev. Geophys.*, **26**, 719, 1988.
- Valladares, C.E., Su. Basu, J. Buchau, and E. Friis-Christensen, Experimental evidence for the formation and entry of patches into the polar cap, *Radio Sci.*, **29**, 167, 1994a.
- Valladares, C.E., H.C. Carlson Jr., and K. Fukui, Interplanetary magnetic field dependency of stable Sun-aligned polar cap arcs, *J. Geophys. Res.*, **99**, 6247, 1994b.
- Valladares, C.E., D.T. Decker, R. Sheehan, and D.N. Anderson, Modeling the formation of polar cap patches using large plasma flows, *Radio Sci.*, **31**, 573, 1996.
- Weber, E.J., and J. Buchau, Polar cap *F*-layer auroras, *Geophys. Res. Lett.*, **8**, 125, 1981.
- Weber, E.J., J. Buchau, J.G. Moore, J.R. Sharber, R.C. Livingston, J.D. Winningham, and B.W. Reinisch, *F* layer ionization patches in the polar cap, *J. Geophys. Res.*, **89**, 1683, 1984.
- Weber, E.J., J.A. Klobuchar, J. Buchau, H.C. Carlson, Jr., R. C. Livingston O. de la Beaujardiere, M. McCready, J.G. Moore, and G.J. Bishop, Polar cap *F* layer patches: structure and dynamics, *J. Geophys. Res.*, **91**, 12, 121, 1986.
- Zhu, L., C.E. Valladares, J.J. Sojka, R.W. Schunk, and D.J. Crain, Model-observation comparison study of multiple polar cap arcs, *J. Geophys. Res.*, **101**, 323, 1996.

T. Bullett and H. C. Carlson Jr., Air Force Research Laboratory, Hanscom Air Force Base, MA 01731, (e-mail: drcarls@ibm.net)

K. Fukui, R. Sheehan, and C. E. Valladares, Institute for Scientific Research, Boston College, Chestnut Hill, MA 02167. (e-mail: sheehanr@plh.af.mil; cesar@dl5000.bc.edu)

(Received March 19, 1998; revised June 25, 1998; accepted June 29, 1998.)

2
17

2
17

2
17
2
17

Characteristics of plasma structuring in the cusp/cleft region at Svalbard

S. Basu,¹ E. J. Weber,¹ T. W. Bullett,¹ M. J. Keskinen,² E. MacKenzie,³
P. Doherty,³ R. Sheehan,³ H. Kuenzler,¹ P. Ning,⁴ and J. Bongioliatti¹

Abstract. Satellite scintillation, all-sky optical imager, and digisonde observations were coordinated during a cusp campaign conducted at Ny Alesund, Svalbard (78.9°N, 11.8°E; 75.7°N corrected geomagnetic latitude, over the period January 4–15, 1997. This paper is focused on a study of the distribution and dynamics of mesoscale (tens of kilometers to tens of meters) electron density irregularities in the dayside auroral region. This study has been performed at Ny Alesund, Svalbard, by measuring the effects of these irregularities on the amplitude scintillation of 250-MHz transmissions from a quasi-stationary polar satellite as well as the amplitude and phase scintillation of 1.6-GHz signals from Global Positioning System (GPS) satellites. These GPS scintillation measurements were augmented by the use of dual-frequency (1.2 and 1.6 GHz) GPS phase data acquired at the same station by the Jet Propulsion Laboratory for the International GPS Geodynamic Service (IGS). The continuous 250-MHz scintillation observations explored the daytime auroral ionosphere 2° poleward of Ny Alesund and showed that the scintillation spectra are often broad, as may be expected for irregularities in a turbulent flow region. Such irregularity dynamics were detected poleward of the nominal cusp region over the interval of 0600–1500 magnetic local time. The period of observations included the magnetic storm of January 10–11, 1997, when GPS observations of the IGS detected polar cap patches with total electron contents of $3 \times 10^{16} \text{ m}^{-2}$ and large-scale (tens of kilometers) phase variations at the GPS frequency of 1.6 GHz that corresponded to temporal gradients of $2 \times 10^{16} \text{ m}^{-2} \text{ min}^{-1}$. However, amplitude scintillations at the GPS frequency of 1.6 GHz could not be detected in association with these large-scale phase variations, indicating that the irregularities with wavelengths less than the Fresnel dimension of 400 m were below the detectable limit. This is shown to be consistent in the context of enhanced ionospheric convection determined by digisonde and scintillation spectra.

1. Introduction

The cusp/cleft region [Newell and Meng, 1992] in the dayside auroral oval is recognized to be the seat of structured electric fields, soft particle precipitation, large plasma flows, and auroral break-up events [Sandholt *et al.*, 1990; Smith and Lockwood, 1990]. These dayside auroral signatures are probed by multitechnique observations to investigate the coupling processes within the solar wind–magnetosphere–ion-

osphere system. From the standpoint of plasma structuring, the dayside auroral oval may be considered as the source region and gateway of major irregularity structures in the high-latitude ionosphere.

It is well established that the dayside auroral oval plays a major role in the formation of large-scale ionization structures, called patches, in the polar ionosphere [Buchau *et al.*, 1983; Weber *et al.*, 1984]. A great deal of research has revealed that under active magnetic conditions, the eastward electric field in the dayside auroral oval directs a “tongue of ionization” from the subauroral region into the polar cap which is sliced off into discrete structures by high plasma flows [Tsunoda, 1988; Valladares *et al.*, 1994, and references therein]. The convecting patches develop intermediate scale (tens of kilometers to tens of meters) irregularities by the action of the gradient drift instability mechanism [Chaturvedi and Huba, 1987; Tsunoda, 1988, and references therein]. This was confirmed experimentally by showing that patches are

¹ Air Force Research Laboratory, Hanscom Air Force Base, Massachusetts.

² Plasma Physics Division, Naval Research Laboratory, Washington, D. C.

³ Institute for Scientific Research, Boston College, Newton, Massachusetts.

⁴ KEO Consultants, Brookline, Massachusetts.

associated with scintillations of satellite signals which arise from the scattering of radio waves from intermediate scale irregularities [Weber *et al.*, 1986]. Indeed, after weak scintillation events due to polar cap arcs are excluded, the statistics of the remaining strong scintillation events in the polar cap [Aarons *et al.*, 1981; Basu *et al.*, 1985; Kersley *et al.*, 1995] may be used as the statistics of polar cap patches.

In addition to patches which convect into the polar cap, the sheared electric field in the cusp/cleft region is a viable source of localized intermediate scale (tens of meters to tens of kilometers) irregularities. Basu *et al.* [1988] first identified irregularities in velocity shear regions associated with nightside auroral arcs and provided a comprehensive description of the density and electric field fluctuation spectra. This stimulated theoretical development of instabilities driven by velocity shears parallel and perpendicular to the magnetic field [Keskinen *et al.*, 1988; Basu and Coppi, 1990; Ganguli *et al.*, 1989]. Compared with convective instabilities at high latitudes, the irregularities generated in velocity shear regions exhibit strikingly enhanced electric field fluctuations for given relative density fluctuations. Scintillations of satellite signals due to irregularities in the velocity shear region are expected to be weaker than patch-induced scintillations since patches are associated with high plasma density. However, the enhanced electric field fluctuations are expected to broaden the frequency spectra of scintillations as well as the Doppler spectra of HF backscatter.

In this paper we present the results of 250-MHz scintillation observations made from Ny Alesund, Svalbard (78.9°N, 11.9°E; corrected geomagnetic latitude (CGMLAT) 75.7°N, 113.8°E), during the period January 5–15, 1997. The station latitude corresponds to the nominal cusp location, and the station crosses local magnetic noon at 0850 UT. We focus our attention on dayside auroral observations made during 0500–1300 UT. During these hours the propagation path to the satellite explored the ionospheric *F* region about 2° poleward of the station. Spectral studies of 250-MHz scintillation are performed to determine the dynamics of 1-km to 100-m scale irregularities. These scintillation observations are supported by all-sky imager and digisonde observations, as well as scintillation and total electron measurements by the use of Global Positioning System (GPS) satellites. This paper also discusses the plasma structures at various scales encountered during the major magnetic storm of January 10–11, 1997.

2. Experimental Observations

Scintillation measurements were performed at Ny Alesund by the use of 250-MHz transmissions from quasi-stationary beacon satellites. The receivers sample signal intensity at 50 Hz and process the signals on-line to determine the scintillation index (S_4), defined as the normalized second moment of the signal intensity, the frequency spectra, and the distribution function. These parameters are obtained every 82 s and are then averaged to provide values at 5-min intervals. A GPS receiver at L1 (1.575 GHz), manufactured by Novatel, was deployed which acquires amplitude and phase at 50 Hz and obtains phase and amplitude scintillation at 82-s intervals. Dual-frequency GPS data were obtained from the Ny Alesund station of the International GPS Geodynamic Service (IGS), managed by the Jet Propulsion Laboratory. The IGS data provide 30-s values of carrier phase and group delay at both the GPS L1 (1.6 GHz) and L2 (1.2 GHz) frequencies. The data are processed to obtain the total electron content and the rate of change of the total electron content at 30-s intervals [Doherty *et al.*, 1994]. The all-sky imager mapped the dayside aurora at 630.0 nm and defined the optical auroral conditions at the subionospheric location which was probed by continuous 250-MHz scintillation measurements. The study is focused on daytime observations between 0800 and 1500 MLT, when the subionospheric location remained at about 78° CGMLAT, 2.3° poleward of Ny Alesund. Since Ny Alesund corresponds nominally to the dayside cusp region, this poleward position of scintillation observations during the daytime may be identified with the mantle region [Newell *et al.*, 1991].

3. Results and Discussions

Figure 1 shows the geometry of 250-MHz scintillation observations from Ny Alesund. The location of the station (75.7° CGMLAT) at magnetic noon (0850 UT) is indicated by a cross. The loci of the 350-km subionospheric position of scintillation observations with quasi-stationary satellites at different universal times (UT) are indicated at hourly intervals by asterisks and diamonds, which correspond to the two satellites. During this period the station will, of course, trace out a circular path, which is not shown in order to ensure clarity of the diagram; instead, its position at one particular time (0845 UT) corresponding to magnetic noon has been illustrated. Observations with each satellite are made for about 6

January 6, 1997

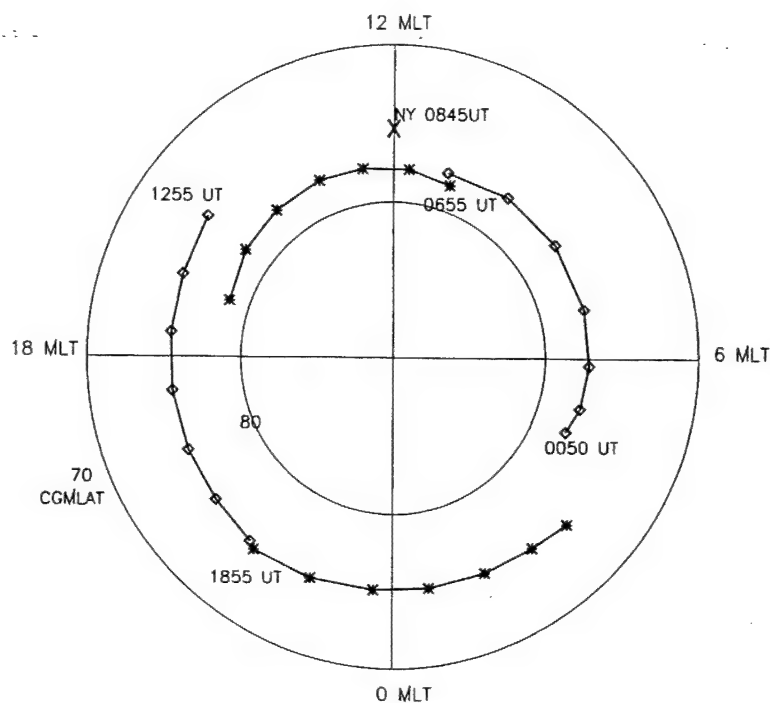


Figure 1. Shown is the geometry of 250-MHz scintillation observations in magnetic local time and the corrected geomagnetic latitude (CGMLAT) coordinate system. The measurements were made from Ny Alesund, Svalbard (CGMLAT 75.7°N) by using quasi-stationary beacon satellites. The position of the station is only shown at magnetic noon and is indicated by a cross. The 350-km subionospheric intersections of scintillation measurements at hourly universal time intervals are shown by crosses and diamonds.

hours, after which they are switched to the next available satellite. Although scintillation observations were performed around the clock, we shall focus in this paper on the results obtained during about 4 hours on either side of magnetic noon. Figure 1 shows that during this period, namely, 0500–1300 UT, scintillation observations probed the ionosphere at 78° CGMLAT, which, as mentioned above, is approximately 2° poleward of Ny Alesund.

We shall now discuss the characteristics of 250-MHz scintillation in the dayside auroral region with the typical example of January 6, 1997. It was a magnetically quiet day, as were most of the days during the campaign period. The Wind satellite data indicated that over the study period of 0500–1300 UT, the interplanetary magnetic field (IMF) B_z was southward, with $B_z = -2$ nT for only 1 hour between 0900 and 1000 UT, and remained northward for the

rest of the period with values ranging between +2 and +3 nT. Figure 2 shows the 630.0-nm images obtained by the all-sky imager at Ny Alesund at 1-min intervals between 0954 and 0958 UT. The 180° field-of-view images are presented in all-sky lens coordinates, with a linear change in elevation angle from 90° at the center to 0° at the edge of the image. The top, bottom, right and left of each image represent the four cardinal directions, north, south, east and west, respectively. The images show the stable cusp aurora, which are characterized by a rather sharp equatorward edge and a markedly diffuse poleward edge [Maynard *et al.*, 1997]. The asterisks in these images represent the directions of the propagation path of satellite scintillation observations. These images indicate that the propagation path intersected the cusp plume poleward of the cusp [Newell *et al.*, 1991]. At this time, no optical emission at 427.8 nm was ob-

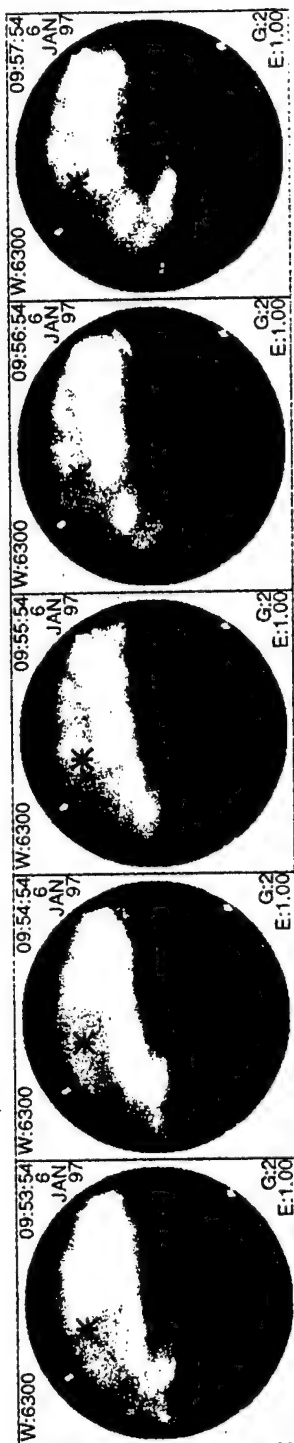


Figure 2. All-sky imager observations of the emissions at 630.0-nm wavelengths at each minute. The four cardinal directions, north, south, east, and west, correspond to the top, bottom, right, and left edges of the images. The observations are from Ny Alesund, Svalbard, on January 6, 1997. The elevation and azimuth of scintillation observations are indicated by asterisks in the images.

served, indicating that only soft particle precipitation was associated with the 630.0-nm images.

Figure 3 illustrates the variation of the S_4 index of amplitude scintillation with UT as recorded on January 6, 1997. The S_4 index, obtained from the ratio of the standard deviation of signal intensity fluctuation normalized to the average signal intensity, quantifies the strength of amplitude scintillation. In view of the prevailing solar minimum condition, scintillations were weak and did not exceed the weak scatter limit of $S_4 = 0.5$. Figure 3 clearly illustrates the daytime scintillation activity between 0500 and 1300 UT, with minimum S_4 values increasing to 0.2 and individual events increasing to 0.4. It establishes the presence of subkilometer scale irregularities during daytime at 78° CGMLAT over an extended magnetic local time interval of 0845–1645 MLT. Considering the optical images shown in Figure 2, the narrow scintillation structure around 1000 UT in Figure 3 is to be associated with the cusp plume. Scintillations, however, are continuously observed over most of the daytime at locations poleward of the dayside auroral oval corresponding to the mantle region. Kersley *et al.* [1995] obtained the occurrence statistics of phase scintillation from Ny Alesund and showed that large-scale (>10 km) irregularities occur during much of the daytime and are distributed in a belt extending from the south to the north of the station.

We now illustrate that the frequency spectra of daytime amplitude scintillations observed slightly poleward of the cusp have very special characteristics. Figure 4 shows a set of four successive spectra at 5-min intervals. Each of these spectra is obtained by using the fast Fourier transform (FFT) algorithm averaged over four successive 82-s data segments. These samples were obtained near magnetic noon, and the spectra show the variation of the power spectral density (psd) in decibels with log frequency. Each spectrum is characterized by a flat low-frequency portion and then a linear roll-off at higher frequencies, indicating a power law variation of psd with frequency. It is to be noted that the scintillation index of all the samples conforms to weak scatter limit ($S_4 < 0.5$). Under these conditions the power spectrum is expected to show a maximum at the Fresnel frequency (f_F), above which the spectrum should roll off rapidly and below which the spectrum should again roll off but at a much shallower slope [Basu *et al.*, 1994]. The Fresnel frequency is given by $f_F = \nu/(2\lambda z)^{1/2}$, where ν is the irregularity drift perpendicular to the propagation path, λ is the radio

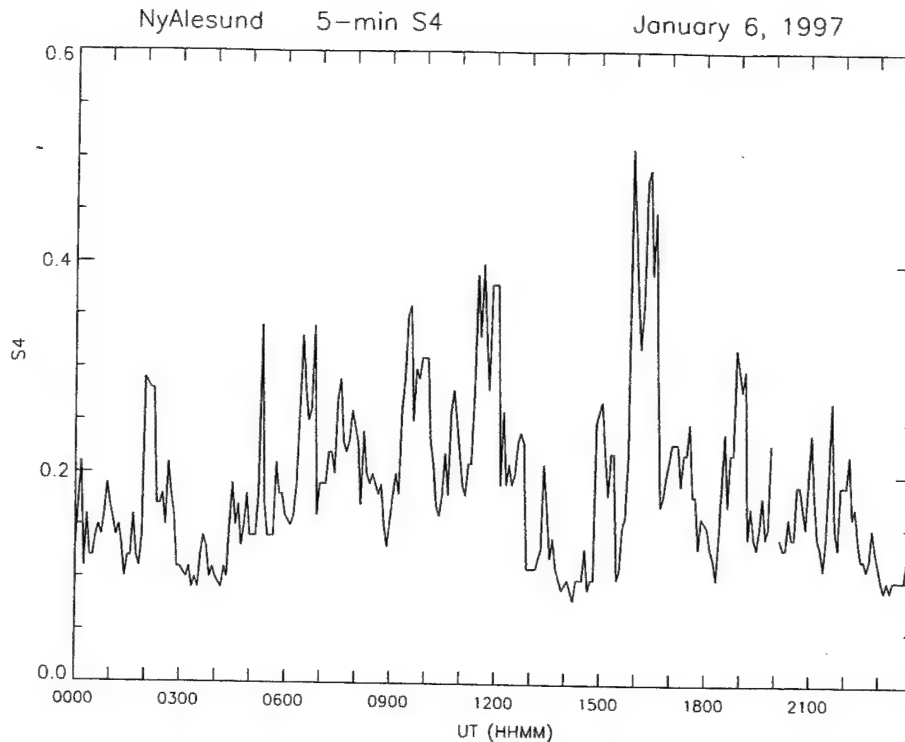


Figure 3. Shown is the observed variation of the S_4 index of scintillation at 250 MHz with universal time as observed on January 6, 1997. The S_4 index of scintillation is defined as the normalized second moment of signal intensity. The measurements were performed from Ny Alesund, Svalbard. The observing period of 0400–1400 UT corresponds to dayside auroral measurements.

wavelength, and z is the slant range to the irregularity layer. The spectral set in Figure 4 does not conform to the weak scatter spectral specifications for uniform flow speed. Instead, the flat-topped low-frequency spectral form may be a result of the irregularities moving with a distributed velocity rather than a uniform flow speed [Lotova, 1981]. The corner frequencies of the spectra shown in Figure 4 vary from one spectra to another, indicating that the velocity dispersion is a function of space and time. Figure 5 illustrates two spectra from the early morning period that indicate the shape of a weak scintillation spectrum in a uniform flow region. In this case, the spectra have narrower bandwidths and exhibit spectral maximum, particularly noticeable in the left-hand (0204:54 UT) spectrum, and have steeper high-frequency roll-off, with power law spectral indices of about 3 as compared with power law indices of 2 in Figure 4. Finally, it is to be emphasized that the broadband spectra shown in Figure 4 are observed just poleward of the cusp, not only at magnetic noon

but over an extended period during the daytime. However, the signature of velocity dispersion is most enhanced around magnetic noon. In a recent comprehensive study of the cusp, Baker *et al.* [1995] have established that HF radar backscatter from the cusp exhibits wide and complex Doppler spectra. This result implies that the cusp is a region of high electric field turbulence which is in agreement with the DE 1 and DE 2 satellite data [Maynard *et al.*, 1991; Basinska *et al.*, 1992].

Another example of daytime scintillation at 250 MHz is shown in Figure 6. A clear commencement of a scintillation event at 0500 UT and the decay at 1200 UT may be noted. The campaign ended at 1200 UT, which caused the abrupt end of the data. The daytime scintillation event again corresponded to the poleward location of about 78° CGMLAT and covered the time interval of about 0900–1600 MLT. The magnitude of scintillation was weak and remained below the S_4 level of 0.3. The scintillation spectra for this event are illustrated in Figure 7. As discussed earlier, the

SDRS Nyalesund

01/06/97 244 MHz

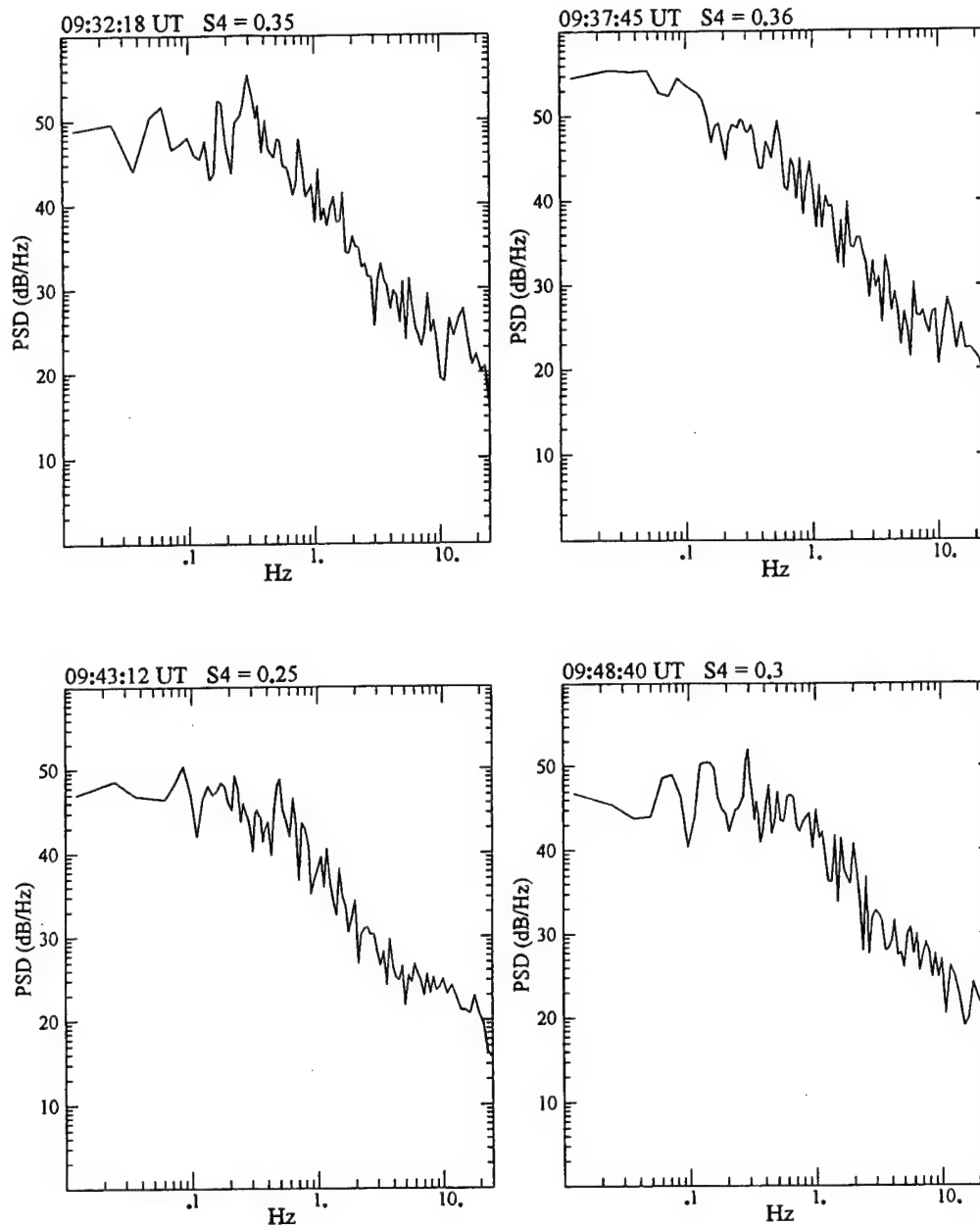


Figure 4. The frequency spectra of 250-MHz scintillations recorded on January 6, 1997, at Ny Alesund, Svalbard, are illustrated at 5-min intervals near magnetic noon. Broad spectra are illustrated.

flat-topped spectra indicate that the irregularities have turbulent velocities. The spectral width is considerably larger compared with the January 6, 1997, spectra, indicating larger velocity dispersion.

During the campaign period a major magnetic

storm occurred during January 9–11, 1997. To show the effect of the storm on amplitude scintillations at 250 MHz, the diurnal variations of S_4 with UT during January 10–12, 1997, are shown in Figure 8. The quiet-day pattern of scintillations with enhanced ac-

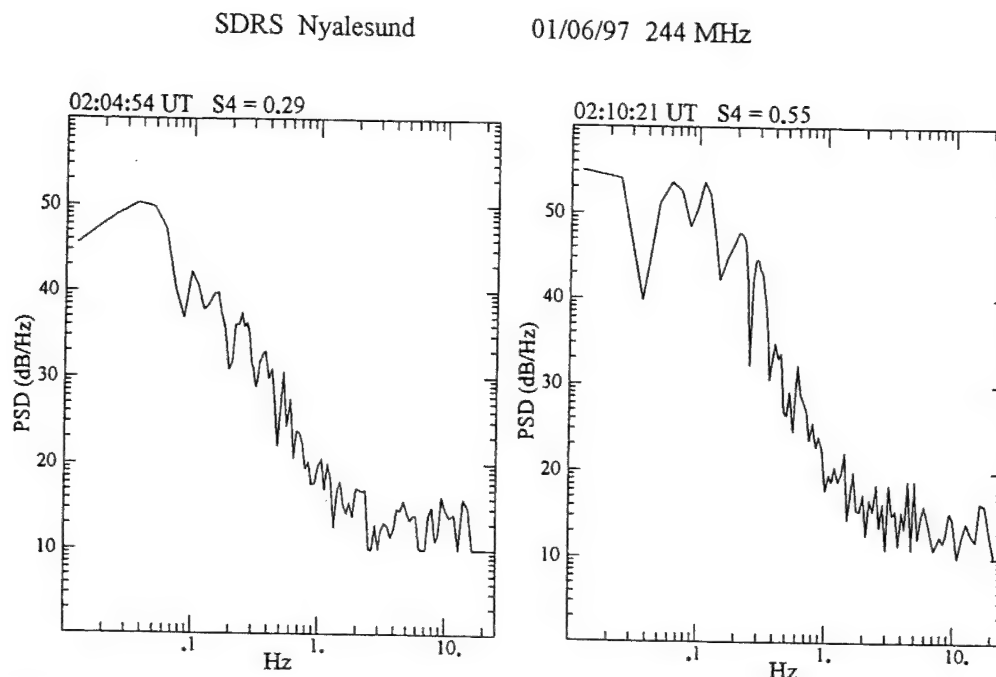


Figure 5. Same as in Figure 4 but obtained during early morning magnetic local time (MLT) hours. Narrowband spectra with Fresnel maximum are illustrated.

tivity around magnetic noon (0850 UT) was observed on January 10 and 12. The pattern changed drastically on January 11, however, when a long enduring prenoon scintillation event during 0000–1000 UT (0400–1400 MLT) was observed, as well as two additional events in the afternoon and early evening period during 1600–2200 MLT. During the prenoon period the Fresnel frequency of scintillation spectra were observed to be as high as 1 Hz. Using the expression given earlier that relates the irregularity drift velocity to the Fresnel frequency, we find that at this time, irregularity drift perpendicular to the propagation path was about 1 km/s. The digisonde at Ny Alesund detected polar cap patches and determined horizontal drifts that increased from 1 km/s at 0000 UT to 1.5 km/s around 0600 UT, which then decreased to about 600 m/s after 1200 UT. These results indicate that the station became a polar cap station due to the expansion of the auroral oval to lower latitudes under these magnetically active conditions, as confirmed by optical images that show no auroral emission within the entire field of view of the imager. This is probably the reason why the diurnal pattern of 250-MHz scintillation on January 11 was distinctly different from other days.

We used the GPS satellite data provided by the

IGS station at Ny Alesund to further investigate the patch characteristics. The IGS stations are equipped with dual-frequency (1.2 and 1.6 GHz) GPS receivers and provide differential carrier phase and differential group delay data at 30-s intervals. The GPS data were analyzed to estimate the total electron content (TEC) of the ionosphere and also the magnitudes of large-scale irregularity structures from the rate of change in differential carrier phase, which is equivalent to the rate of change of TEC. The rate of change of TEC is derived from the differential carrier phase data, which are provided at 30-s intervals. The data are filtered to remove variations with periods longer than 15 min, and then the rate of change of TEC is obtained at 1-min intervals from 30-s TEC values. This algorithm was first developed by J. A. Klobuchar and P. Doherty at Phillips Laboratory (now Air Force Research Laboratory) and has now been adapted by various groups for ionospheric studies at low and high latitudes by the use of the widely dispersed IGS network of stations [Doherty *et al.*, 1994]. In a recent paper, Pi *et al.* [1997] have indicated how measurements of the rate of change of TEC by the global IGS network may be exploited to monitor the instantaneous global distribution of ionospheric irregularities. Figure 9 shows the 350-km subionospheric position of

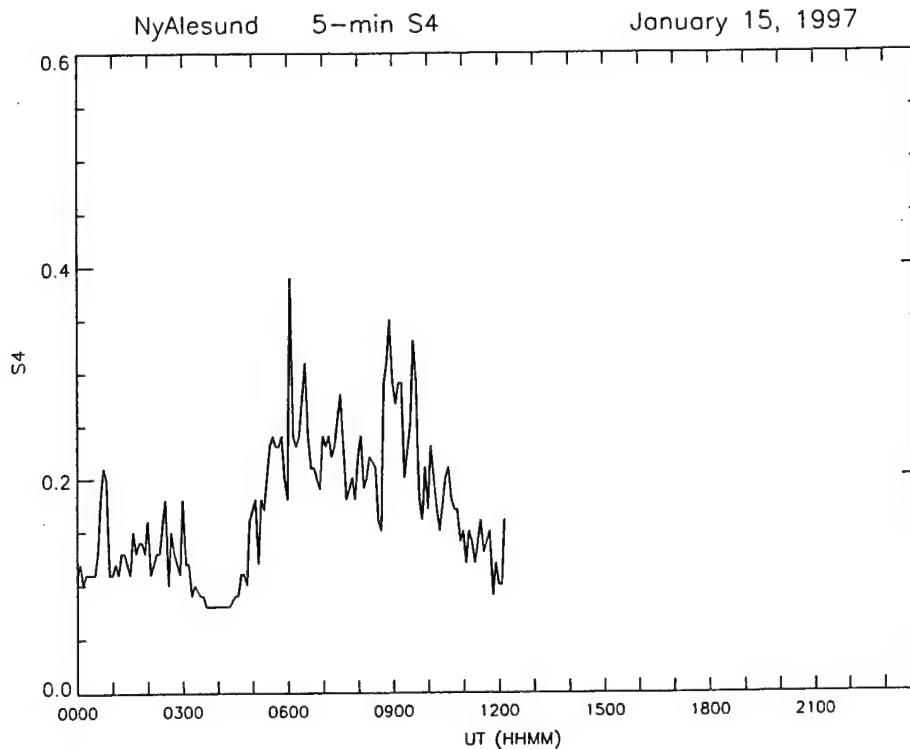


Figure 6. Same as in Figure 3 but performed on January 15, 1997.

GPS satellites, viewed from Ny Alesund, in the day sector between 0600 and 1800 MLT. The diamonds along the tracks signify locations where the rate of change of TEC exceeded $1 \text{ TEC unit min}^{-1}$ (1 TEC unit = $10^{16} \text{ electrons m}^{-2}$).

Figure 9 shows that the subionospheric track of satellite prn 26, viewed from Ny Alesund, crossed magnetic noon. The differential carrier phase and group delay data were combined to determine the total electron content. This result is illustrated in Figure 10, which shows the variation of equivalent vertical TEC as a function of universal time. The alternate increases and decreases of TEC signify the transit of polar cap patches across the GPS propagation path. It may be noted that, on average, the patches are associated with an increase of TEC by about 2 TEC units and the patch durations are about 30 min. The patches are very weak because of the prevailing solar minimum condition. The digisonde measurements at Ny Alesund indicated that at this time the horizontal drift is about 600 m s^{-1} . By combining the duration and the drift of the patches, we obtain the horizontal patch dimensions as 1080 km.

The convecting patches develop intermediate scale irregularities through the gradient drift instability mechanism [Chaturvedi and Huba, 1987; Tsunoda, 1988, and references therein]. With prevailing drift velocities as high as $500\text{--}1000 \text{ m s}^{-1}$, patches with relatively gentle spatial gradients of electron density of the order of 50 km, perpendicular to the magnetic field and in the direction of the drift, are expected to become unstable within about a minute and develop intermediate scale irregularities [Basu *et al.*, 1995]. In addition, since the patches may transit through all or part of the cusp enroute to the polar cap [Sojka *et al.*, 1994; Decker *et al.*, 1994], it is conceivable that the patches will be structured in density due to structured cusp electric fields [Maynard *et al.*, 1991; Basinska *et al.*, 1992] or structured particle precipitation from the magnetosheath. The association of density and electric field structures in velocity shear regions at auroral latitudes has been established from satellite in situ measurements [Basu *et al.*, 1988] and accounted for theoretically by several authors [Keskinen *et al.*, 1988; Basu and Coppi, 1990; Ganguli *et al.*, 1994]. We discussed earlier the presence of 250-MHz scintillation in the cusp region, which establishes the presence

SDRS Nyalesund

01/15/97 244 MHz

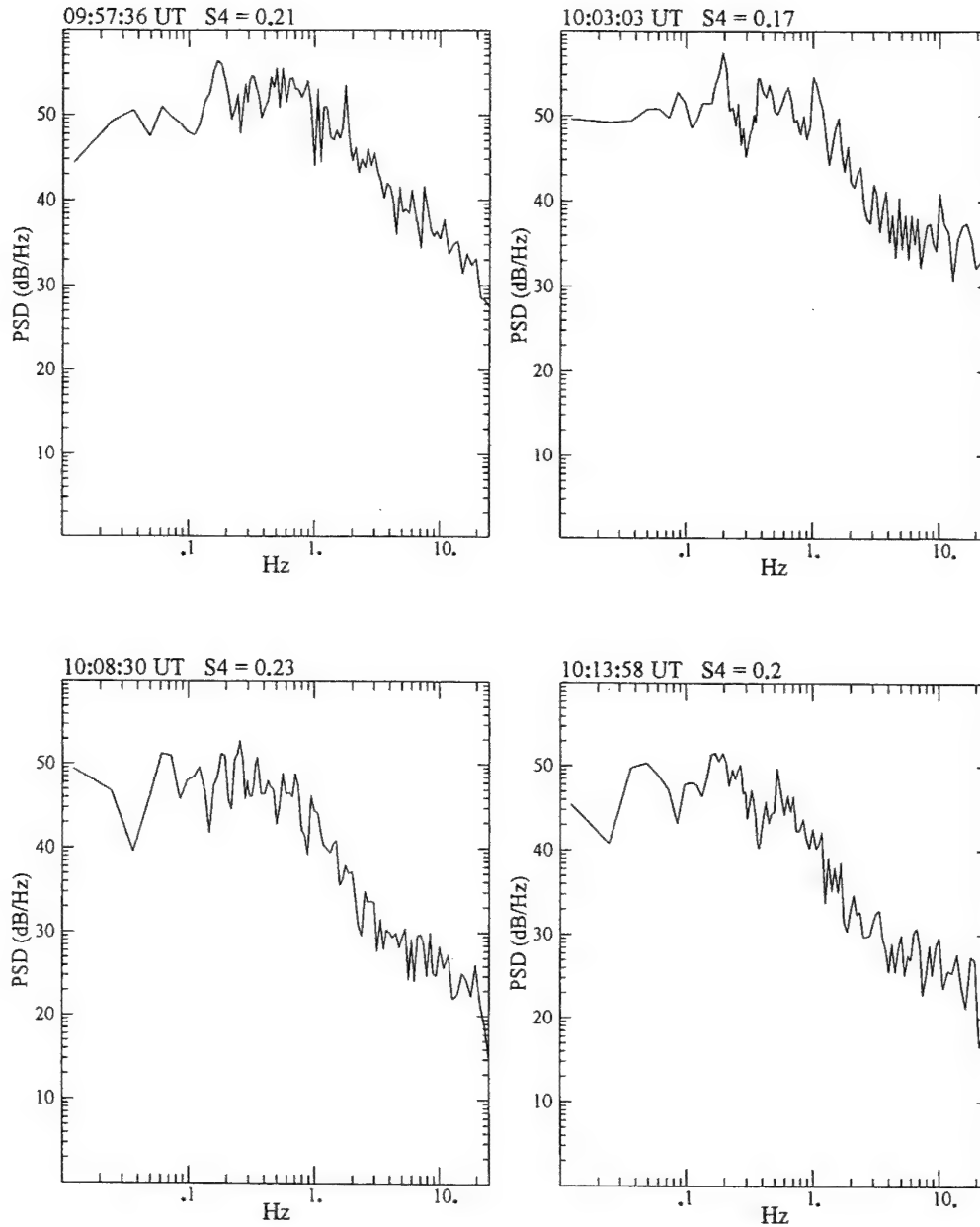


Figure 7. Same as in Figure 4 but on January 15, 1997.

of intermediate scale density irregularities in the range of about 1 km to 100 m. The patches may therefore enter the polar cap after being structured in the cusp at such subkilometer scales. However, since the cusp is localized, these irregularities will decay after the patches exit the source region. The approx-

imate lifetime of the intermediate scale density irregularities in the winter polar cap ionosphere is proportional to the square of irregularity scale size, perpendicular to the geomagnetic field, divided by the electron perpendicular diffusion coefficient. For an altitude of 350 km, 100-m and 1-km scale size density

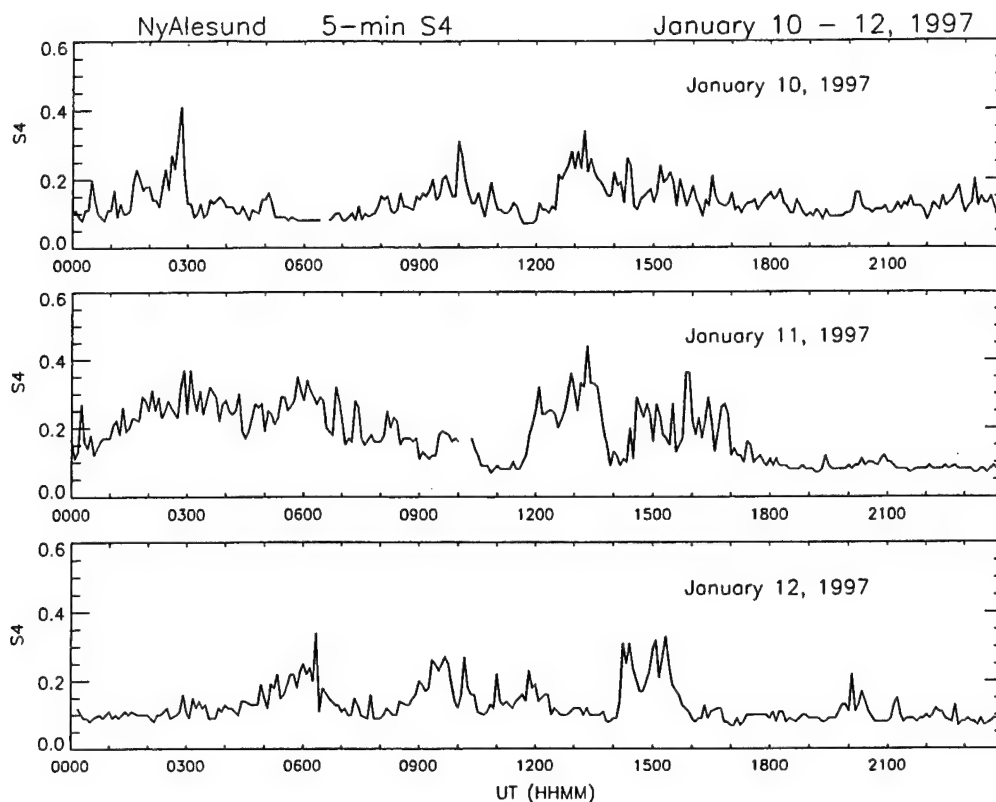


Figure 8. Shown is the variation of S_4 index of scintillation at 250 MHz with universal time observed during the magnetic storm period of January 10–12, 1997. The top and middle panels show the variations during the storm period of January 10 and 11, 1997, respectively, and the bottom panel shows the variation observed on January 12, 1997, immediately after the magnetic storm.

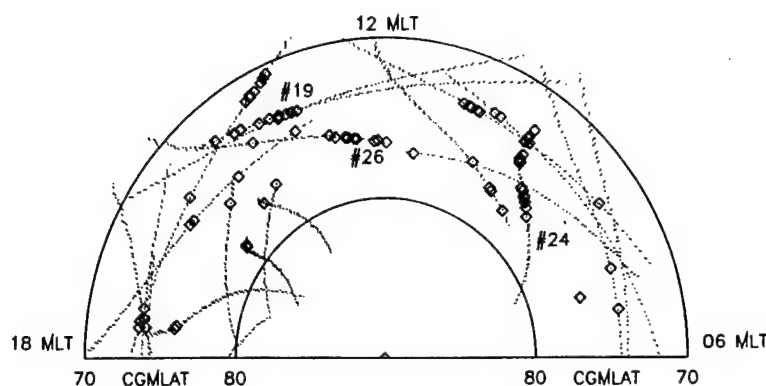


Figure 9. The 350-km subionospheric tracks of Global Positioning System (GPS) satellites as observed from Ny Alesund, Svalbard, on January 11, 1997. The tracks are illustrated in MLT-CGMLAT coordinates. The diamonds indicate that the rate of change of the total electron content (TEC) exceeded 1 TEC unit per minute (1 TEC unit = 10^{16} electrons m^{-2}). Some of these tracks are identified by the corresponding satellite prn's.

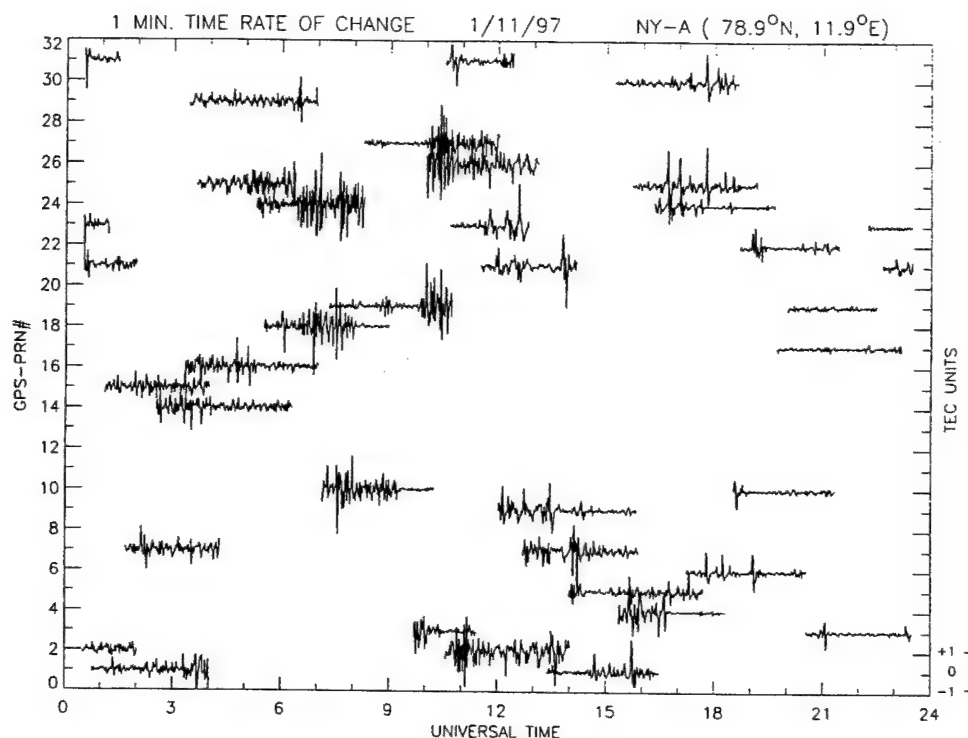


Figure 11. Shown are the rates of change of TEC as recorded by different satellites at Ny Alesund at different universal times during the magnetic storm period of January 11, 1997. The ordinate refers to prn of GPS satellites. The scale for the rate of change of TEC is indicated at the right bottom edge of the diagram.

ties and therefore determine the irregularity wavelengths with 30-s sampling of GPS carrier phase.

Amplitude scintillation measurements of GPS signals at 1.6 GHz were also conducted by using a receiver that recorded the signal amplitude at 50 Hz and processed on-line the S_4 scintillation index every 82 s. The amplitude scintillation data are plotted in Figure 12 in the same format as Figure 11. In this case, however, the separation between the successive horizontal lines corresponds to $S_4 = 0.25$. It may be seen that the receiver failed to detect any amplitude scintillation from a GPS satellite (prn 26). Some of the satellites, such as prn 23, show scintillation-like activity a little before 0900 UT. The events are not scintillation but are caused by multipath effects at low elevation angles encountered during the rise and set of the satellite. Unlike phase scintillations, where the irregularity wavelength sampled in an experiment depends on the velocity of the irregularities, amplitude scintillations are caused by irregularities in the range of the Fresnel dimension to a dimension

smaller by about a decade. Thus, with irregularities at a range of 400 km, amplitude scintillations at the GPS frequency of 1.6 GHz are caused by irregularities in the wavelength range from 390 m, the Fresnel dimension, to about 30 m. These irregularity wavelengths (390–30 m) are 2–3 orders of magnitude smaller than those (36 km) detected by phase fluctuation measurements. Thus, in the presence of high ionospheric convection, the detection of large phase fluctuations may not signify the presence of smaller irregularities or be of sufficient strength to cause detectable levels of amplitude and phase scintillation.

4. Conclusions

Under solar minimum conditions of January 1997, weak ($S_4 < 0.4$) amplitude scintillations at 250 MHz were persistently observed during daytime at about 2° poleward of the nominal cusp region. Such scintillations, indicating the presence of subkilometer scale electron density irregularities, were observed not only

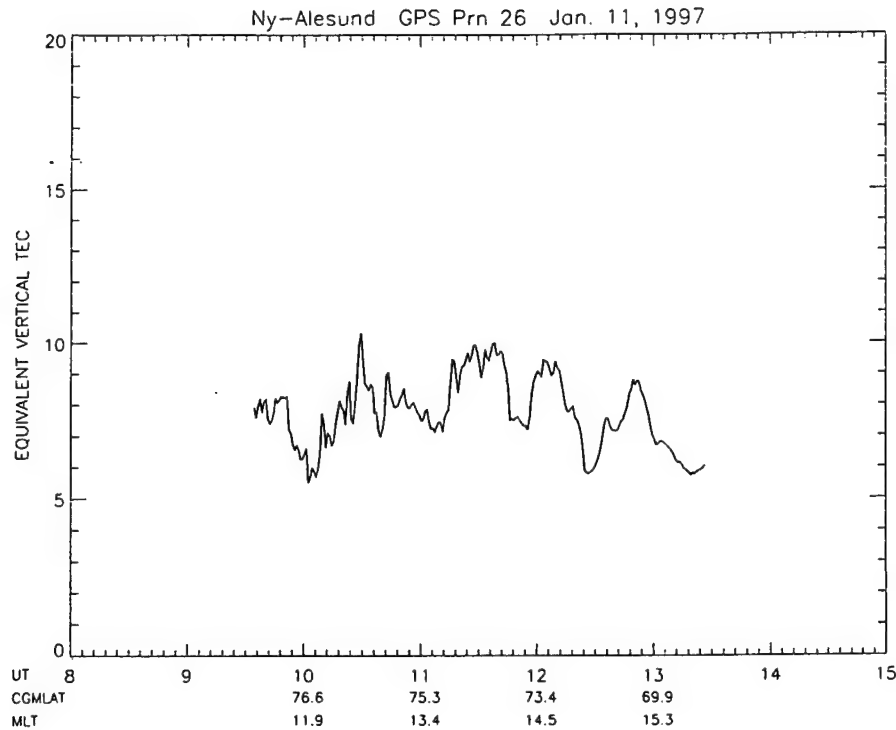


Figure 10. The equivalent vertical total electron content determined during the magnetic storm period of January 11, 1997, using the GPS observations of the International GPS Geodynamic Service (IGS) at Ny Alesund. Patches with about 2 TEC units were detected.

irregularities will decay with typical time constants of the order of minutes and hours, respectively. In view of such long lifetimes of subkilometer scale irregularities, the patches will already be structured when they enter the polar cap. This will contribute to a reduction of the growth time of irregularities in convecting patches by the gradient drift instability mechanism.

We shall now discuss the plasma structuring of patches by determining the rate of change of TEC from two frequencies (1.2 and 1.6 GHz) of GPS satellite observations as well as measuring amplitude scintillations of GPS signals at 1.6 GHz. Figure 11 shows the results of the rate of change of TEC per minute on January 11, 1997, which was determined from the IGS GPS data from Ny Alesund. Each horizontal line represents a GPS satellite with a specific prn and shows phase fluctuations expressed as fluctuations in changes of TEC per minute. The change of 1 TEC unit per minute corresponds to the spacing between the lines in the bottom right corner of the diagram. This representation has been effectively used by *Aarons et al.* [1996] and *Aarons* [1997]

for irregularity studies at both equatorial and high latitudes. Figure 11 shows that the satellite (prn 26) recorded changes mostly around ± 1 TEC min^{-1} around 1200 UT when it detected patches. If we recall that the digisonde recorded drifts of 600 m s^{-1} at this time, then the differential carrier phase data with a Nyquist period of 60 s correspond to irregularity wavelengths of 36 km. *Aarons* [1997] has recently performed a careful study of the rate of change of TEC at high latitudes by using the IGS data from 11 high-latitude stations. From this study he concluded that during solar minimum the rate of change of TEC (phase fluctuations) was lower at corrected geomagnetic latitudes $>80^\circ$ as compared with that in the auroral oval. This observation depends on the fact that the phase fluctuations (or the rate of change of TEC) are a function of both change in TEC and the irregularity velocity. It is not clear if the lower values in the polar cap, compared with the auroral oval stations as reported by *Aarons* [1997], are a result of smaller irregularity amplitudes or smaller velocities. In the present study, with digisonde and spectral studies of scintillation, we could estimate the veloci-

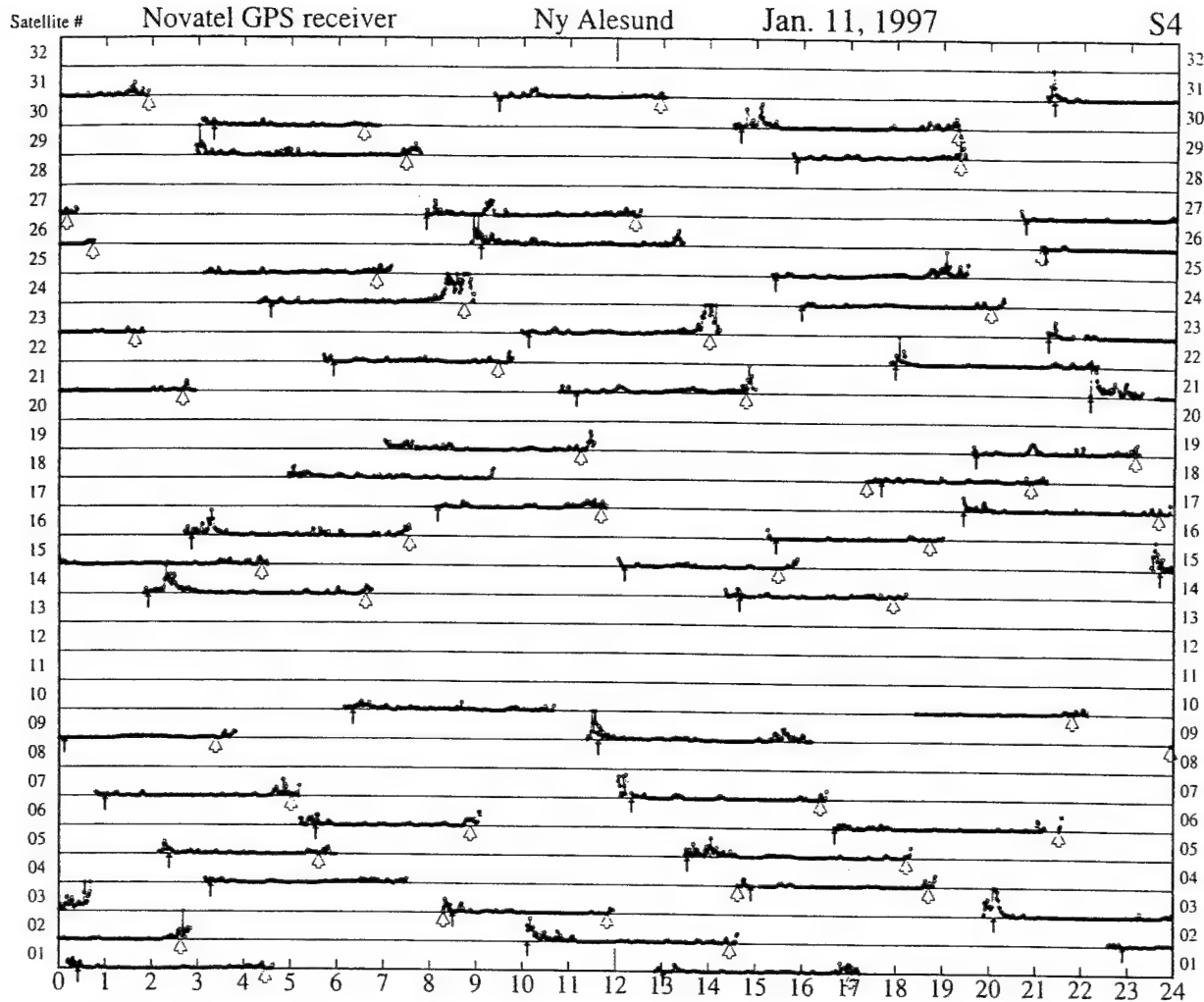


Figure 12. Shown is the amplitude scintillation at 1.6 GHz detected by different GPS satellites at different universal times during the magnetic storm period of January 11, 1997. The spacing between successive horizontal lines corresponds to an amplitude scintillation index of $S_4 = 0.25$. The figure shows that no amplitude scintillation was recorded. The scintillation-like variations are due to multipath effects which are encountered at low elevation angles.

near magnetic noon but also over much of the daytime, typically between 0900 MLT and 1500 MLT. The irregularities immediately poleward of the cusp may be convected from the proper cusp region or may be locally generated in the "cusp plume" region [Newell *et al.*, 1991]. The presence of irregularities in a longitudinally broad region slightly poleward of the cusp is probably related to the plasma mantle at low altitudes, which was first identified by Newell *et al.* [1991]. The discrete auroral features observed by these authors in this region and the associated field-

aligned currents may be the source of the observed irregularities.

The dayside scintillation is characterized by frequency spectra which are generally broad but are occasionally interspersed by narrowband spectra. In our previous study in the cusp region at Sondrestrom, Greenland, we detected velocity shear and also observed broad frequency spectra of scintillations, implying the presence of turbulent plasma flows [Basu *et al.*, 1994]. This result was explained in terms of shear instabilities. Baker *et al.* [1995] have recently used

high-latitude HF radar data and established that the important radar characteristic of the cusp are the wide and complex Doppler power spectra. They recognized that plasma instability processes may impact the Doppler spectra but favored the alternative in which the wide spectra resulted from a structure within the $\mathbf{E} \times \mathbf{B}$ drift velocities. In this paper, we are reporting broad frequency spectra of scintillations poleward of the cusp region not only around magnetic noon but also away from noon. It is quite likely that in the presence of discrete auroral forms in the mantle [Newell et al., 1991; Murphree et al., 1990], shear instabilities may operate in this region and cause velocity turbulence in the nonlinear stage. This may also explain the observed broad frequency spectra of scintillation. Ganguli et al. [1994] have recently developed theories to show that a small amount of velocity shear in the transverse flow is sufficient to excite large-scale Kelvin-Helmholtz modes, which can nonlinearly steepen to excite microinstabilities that may energize ions.

We observed patches with small TEC enhancements only during the major magnetic storm. Modeling studies indicate that in view of the high geographic latitude of the cusp in the Ny Alesund sector, the corresponding polar cap patches and associated irregularities are weak and have low occurrence [Basu et al., 1995]. We showed that at high latitudes in the presence of large convection speed, the IGS data sampled at 30-s intervals provide phase fluctuations at very large scales (40 km) and may not serve as an effective tracer of scintillation. With faster data sampling this IGS network may, however, be a very effective forecaster of scintillation.

Acknowledgments. We thank the staff of the Norsk Polarinstitut Research Station at Ny Alesund for their support during the January 1997 campaign and for continuous monitoring of the satellite receiving system. We gratefully acknowledge the help of JPL for supplying the GPS bias data. The work at Air Force Research Laboratory, Hanscom AFB, was partially supported by the Air Force Office of Scientific Research under task 2310G9.

References

- Aarons, J., Global positioning system phase fluctuations at auroral latitudes, *J. Geophys. Res.*, **102**, 17,219, 1997.
- Aarons, J., J. P. Mullen, H. Whitney, A. Johnson, and E. Weber, UHF scintillation activity over polar latitudes, *Geophys. Res. Lett.*, **8**, 277, 1981.
- Aarons, J., M. Mendillo, R. Yantosca, and E. Kudeki, GPS phase fluctuations in the equatorial region during the MISETA campaign, *J. Geophys. Res.*, **101**, 26,851, 1996.
- Baker, K. B., J. R. Dudeney, R. A. Greenwald, M. Pinnock, P. T. Newell, A. S. Rodger, N. Mattin, and C.-I. Meng, HF radar signatures of the cusp and low-latitude boundary layer, *J. Geophys. Res.*, **100**, 7671, 1995.
- Basinska, E. M., W. J. Burke, N. C. Maynard, W. J. Hughes, J. D. Winningham, and W. B. Hanson, Small-scale electrodynamics of the cusp with northward interplanetary magnetic field, *J. Geophys. Res.*, **97**, 6369, 1992.
- Basu, B., and B. Coppi, Plasma collective modes driven by velocity gradients, *J. Geophys. Res.*, **95**, 21,213, 1990.
- Basu, S., Su. Basu, P. K. Chaturvedi, and C. M. Bryant Jr., Irregularity structures in the cusp/cleft and polar cap regions, *Radio Sci.*, **29**, 195, 1994.
- Basu, S., Su. Basu, J. J. Sojka, R. W. Schunk, and E. MacKenzie, Macroscale modeling and mesoscale observations of plasma density structures in the polar cap, *Geophys. Res. Lett.*, **22**, 881, 1995.
- Basu, Su., S. Basu, E. MacKenzie, and H. E. Whitney, Morphology of phase and intensity scintillations in the auroral oval and polar cap, *Radio Sci.*, **20**, 347, 1985.
- Basu, Su., S. Basu, E. MacKenzie, P. F. Fougere, W. R. Coley, N. C. Maynard, J. D. Winningham, M. Sugiura, W. B. Hanson, and W. R. Hoegy, Simultaneous density and electric field fluctuation spectra associated with velocity shears in the auroral oval, *J. Geophys. Res.*, **93**, 115, 1988.
- Buchau, J., B. W. Reinisch, E. J. Weber, and J. G. Moore, Structure and dynamics of the winter polar cap *F* region, *Radio Sci.*, **18**, 995, 1983.
- Chaturvedi, P. K., and J. D. Huba, The interchange instability in high-latitude plasma blobs, *J. Geophys. Res.*, **92**, 3357, 1987.
- Decker, D. T., C. E. Valladares, R. Sheehan, Su. Basu, D. N. Anderson, and R. A. Heelis, Modeling daytime *F* layer patches over Sondrestrom, *Radio Sci.*, **29**, 249, 1994.
- Doherty, P., E. Raffi, J. Klobuchar, and M. B. El-Arini, Statistics of time rate of change of ionospheric range delay, in *Proceedings ION GPS-94*, p. 1589, Inst. of Navig., Alexandria, Va., 1994.
- Ganguli, G., Y. C. Lee, P. J. Palmadesso, and S. L. Ossakow, Ion waves in a collisional magnetoplasma with a field-aligned current and a transverse velocity shear, in *Proceedings of the 1988 Cambridge Workshop in Theoretical Geoplasma Physics, Polar Cap Dynamics and High Latitude Ionospheric Turbulence*, pp. 231–242, Scientific, Cambridge, Mass., 1989.
- Ganguli, G., M. J. Keskinen, H. Romero, R. Heelis, T. Moore, and C. Pollock, Coupling of microprocesses and macroprocesses due to velocity shear: An application to the low-altitude ionosphere, *J. Geophys. Res.*, **99**, 8873, 1994.
- Kersley, L., C. D. Russell, and D. L. Rice, Phase scintilla-

- tion and irregularities in the northern polar ionosphere, *Radio Sci.*, **30**, 619, 1995.
- Keskinen, M. J., H. G. Mitchell, J. A. Fedder, P. Satyanarayana, S. T. Zalesak, and J. D. Huba, Nonlinear evolution of the Kelvin-Helmholtz instability in the high-latitude ionosphere, *J. Geophys. Res.*, **93**, 137, 1988.
- Lotova, N. A., Temporal scintillation spectra with allowance for the solar-wind velocity distribution: Theory, *Geomagn. Aeron.*, **21**, 447, 1981.
- Maynard, N. C., T. L. Aggson, E. M. Basinska, W. J. Burke, P. Craven, W. K. Peterson, M. Sugiura, and D. R. Weimer, Magnetospheric boundary dynamics: DE 1 and DE 2 observations near the magnetopause and cusp, *J. Geophys. Res.*, **96**, 3505, 1991.
- Maynard, N. C., E. J. Weber, D. R. Weimer, J. Moen, T. Onsager, R. A. Heelis, and A. Egeland, How wide in magnetic local time is the cusp? An event study, *J. Geophys. Res.*, **102**, 4765, 1997.
- Murphree, J. S., R. D. Elphinstone, D. Hearn, and L. L. Cogger, Large-scale high-latitude dayside auroral emissions, *J. Geophys. Res.*, **95**, 2345, 1990.
- Newell, P. T., and C.-I. Meng, Mapping of the dayside ionosphere to the magnetosphere according to particle precipitation characteristics, *Geophys. Res. Lett.*, **19**, 609, 1992.
- Newell, P. T., W. J. Burke, C.-I. Meng, E. R. Sanchez, and M. E. Greenspan, Identification and observations of the plasma mantle at low altitude, *J. Geophys. Res.*, **96**, 35, 1991.
- Pi, X., A. J. Mannucci, U. J. Lindqwister, and C. M. Ho, Monitoring of global ionospheric irregularities using the worldwide GPS network, *Geophys. Res. Lett.*, **24**, 2283, 1997.
- Sandholt, P. E., M. Lockwood, T. Oguti, S. W. H. Cowley, K. S. C. Freeman, B. Lybekk, A. Egeland, and D. M. Willis, Midday auroral breakup events and related energy and momentum transfer from the magnetosheath, *J. Geophys. Res.*, **95**, 1039, 1990.
- Smith, M. F., and M. Lockwood, The pulsating cusp, *Geophys. Res. Lett.*, **17**, 1069, 1990.
- Sojka, J. J., M. D. Bowline, and R. W. Schunk, Patches in the polar ionosphere: UT and seasonal dependence, *J. Geophys. Res.*, **99**, 14,959, 1994.
- Tsunoda, R. T., High-latitude *F* region irregularities: A review and synthesis, *Rev. Geophys.*, **26**, 719, 1988.
- Valladares, C. E., S. Basu, J. Buchau, and E. Friis-Christensen, Experimental evidence for the formation and entry of patches into the polar cap, *Radio Sci.*, **29**, 167, 1994.
- Weber, E. J., J. Buchau, J. G. Moore, J. R. Sharber, R. C. Livingston, J. D. Winningham, and B. W. Reinisch, *F* layer ionization patches in the polar cap, *J. Geophys. Res.*, **89**, 1683, 1984.
- Weber, E. J., J. A. Klobuchar, J. Buchau, H. C. Carlson Jr., R. C. Livingston, O. de la Beaujardiere, M. McCready, J. G. Moore, and G. J. Bishop, Polar cap *F* layer patches: Structure and dynamics, *J. Geophys. Res.*, **91**, 12,121, 1986.
- S. Basu, J. Bongiolatti, T. W. Bullett, H. Kuenzler, and E. J. Weber, Air Force Research Laboratory, AFRL/VSBI, 29 Randolph Road, Hanscom Air Force Base, MA 01731. (e-mail: santimay@aol.com; bullett@plh.af.mil; webere@plh.af.mil)
- P. Doherty, E. MacKenzie, and R. Sheehan, Institute for Scientific Research, Boston College, Newton, MA 02159.
- M. J. Keskinen, Plasma Physics Division, Naval Research Laboratory, 4555 Overlook Avenue, SW, Washington, D. C. 20375. (keskinen@ppd.nrl.navy.mil)
- P. Ning, KEO Consultants, 24 Brookline Avenue, Brookline, MA 02146.

(Received January 19, 1998; revised May 5, 1998; accepted May 8, 1998.)

Observations of plasma density structures in association with the passage of traveling convection vortices and the occurrence of large plasma jets

C. E. Valladares¹, D. Alcaydé², J. V. Rodríguez³, J. M. Ruohoniemi⁴, A. P. Van Eyken⁵

¹Institute for Scientific Research, Boston College, Newton Center, MA, USA

²CESR-CNRS – 9 Av. Cl Roche – F31028 Toulouse Cedex 04 – France

³Ball Aerospace & Technologies Corp., Boulder, CO, USA

⁴The Johns Hopkins University, Applied Physics Lab, Laurel, MD, USA

⁵EISCAT Scientific Association, Ramfjordmoen, N9020 Tromsø, Norway

Received: 16 February 1998 / Revised: 23 November 1998 / Accepted: 26 November 1998

Abstract. We report important results of the first campaign specially designed to observe the formation and the initial convection of polar cap patches. The principal instrumentation used in the experiments comprised the EISCAT, the Sondrestrom, and the Super DARN network of radars. The experiment was conducted on February 18, 1996 and was complemented with additional sensors such as the Greenland chain of magnetometers and the WIND and IMP-8 satellites. Two different types of events were seen on this day, and in both events the Sondrestrom radar registered the formation and evolution of large-scale density structures. The first event consisted of the passage of traveling convection vortices (TCV). The other event occurred in association with the development of large plasma jets (LPJ) embedded in the sunward convection part of the dusk cell. TCVs were measured, principally, with the magnetometers located in Greenland, but were also confirmed by the line-of-sight velocities from the Sondrestrom and SuperDARN radars. We found that when the magnetic perturbations associated with the TCVs were larger than 100 nT, then a section of the high-latitude plasma density was eroded by a factor of 2. We suggest that the number density reduction was caused by an enhancement in the O^+ recombination due to an elevated T_i , which was produced by the much higher frictional heating inside the vortex. The large plasma jets had a considerable (> 1000 km) longitudinal extension and were 200–300 km in width. They were seen principally with the Sondrestrom, and SuperDARN radars. Enhanced ion temperature (T_i) was also observed by the Sondrestrom and EISCAT radars. These channels of high T_i were exactly collocated with the LPJs and some of them with regions of eroded plasma number density. We suggest that the LPJs bring less dense plasma from later local times. However, the recent time history of the plasma flow is important to define the depth of the density depletion. Systematic changes in the latitudinal location and in the intensity of the LPJs were observed in the 2 min time resolution data of the SuperDARN radars. The effect of the abrupt

changes in the LPJs location is to create regions containing dayside plasma almost detached from the rest of the oval density. One of these density features was seen by the Sondrestrom radar at 1542 UT. The data presented here suggest that two plasma structuring mechanisms (TCVs and LPJs) can act tens of minutes apart to produce higher levels of density structures in the near noon F-region ionosphere.

Key words. Ionosphere (ionospheric irregularities) · Magnetospheric physics (electric fields; polar cap phenomena)

1 Introduction

Since the first observations of plasma density were conducted at very high latitudes, it became evident that large-scale (> 100 km) plasma density structures were always present within the polar cap (Hill, 1963; Sato and Rourke, 1964). The first systematic examination of these polar cap structures started years later when several complementary instruments, such as an all-sky intensified photometer (ASIP), a digital ionosonde, and scintillation receivers operated simultaneously at Thule, Greenland (86° geomagnetic latitude) (Buchau *et al.*, 1983). Soon thereafter, it was concluded that two important classes of large-scale density structures prevailed within the polar cap: sun-aligned arcs and polar cap patches (Weber and Buchau, 1981).

The works by Lassen (1972), Berkey *et al.* (1976) and Ismail *et al.* (1977) had previously demonstrated that the sun-aligned F-region arcs existed inside the polar cap preferentially when the magnetic conditions were quiet or equivalently when the B_z component of the IMF was directed northward. In analogy to this discovery, Buchau *et al.* (1983) noted that the polar cap patches

occurred during magnetically active periods or IMF B_z southward conditions. Buchau *et al.* (1983) defined the patches as spatially confined enhancements in the F-region number density above its background level. The density enhancements are usually a factor of 2 during solar minimum conditions, but can reach a factor of 10 during solar maximum years (Buchau and Reinisch, 1991). The patches move in the antisunward direction (Fukui *et al.*, 1994), lack polar cap particle precipitation (excluding polar rain) (Weber *et al.*, 1986), have sizes between 100 and 1000 km, and possess a patchy signature in the 630.0 nm airglow emissions.

The strong UT dependence of the patch occurrence in the Northern Hemisphere, and the fact that the auroral oval, almost fixed in magnetic coordinates, is able to reach lower geographic latitudes at the same UT hours that the patches are observed, provide strong support for the source of the high density plasma of the patches to be sun-produced plasma created at latitudes equatorward or near the auroral oval (Buchau *et al.*, 1985; de la Beaujardiere *et al.*, 1985). Incoherent scatter radar observations by Foster and Doupnik (1984) and by Kelly and Vickrey (1984) in fact confirmed that subauroral/auroral plasma gets routed through the dayside throat region and enters into the polar cap forming a continuous and elongated tongue-of-ionization (TOI). While the observation of the TOI, extending all the way across the polar cap, provided a source of the enhanced plasma, the patchy nature of the density enhancements implied the existence of an additional mechanism capable of breaking off the seemingly continuous TOI.

Several mechanisms have been suggested to explain the formation of polar cap patches and their complete detachment from the auroral oval (see reviews by Tsunoda, 1988 and Crowley, 1996 for a general discussion of formation mechanisms). In a general sense, the formation of polar cap patches could be explained by the particular characteristics of the plasma electrodynamics that occurs in the midday cusp region (Rodger and Graham, 1996). Therefore, it is worthwhile to observe in great detail all the physical processes that occur near the midday ionosphere. Two prominent processes in this region are the large flows and the midday auroral breakup events that have been observed with the EISCAT incoherent scatter radar (ISR) in association with cusp dynamics (Sandholt *et al.*, 1990; Lockwood *et al.*, 1990). The large plasma flows have been explained by Cowley *et al.* (1991) to form channels in the region adjacent and poleward of the open-closed field line boundary. These large flows are a direct result of the tension force on newly opened field lines. The role of the large plasma flows in the formation of patches has, in fact, been introduced by Rodger *et al.* (1994). These authors, based on ionospheric velocities measured by the PACE radar, concluded that short-lived plasma jets (~ 2 km/s) occurred within a few minutes of the formation of polar cap patches and near the dayside cusp. Additional support for the large flow mechanism was provided by Valladares *et al.* (1994). Measurements conducted with the Sondrestrom ISR showed that the large flows were exactly collocated with density deple-

tions and elevated ion temperatures. It was argued then that enhanced O^+ recombination, due to the elevated T_i values, eroded a section of the TOI and created a discrete entity of high density plasma. A modeling effort of this event, using a set of twin vortices to represent the large plasma flow, showed that the detachment of the patch from the auroral oval occurs not when the twin vortices are stationary, but instead when they are allowed to move with the background plasma (Valladares *et al.*, 1996). These authors also demonstrated that even for vortices extending 9° in longitude and with a 25 kV potential drop, 60% of the plasma density decrease can be attributed to transport of less dense plasma from earlier or later local times.

The purposes of this work are: to present the variability of the plasma velocity structures in a much larger spatial context and with higher temporal resolution than has been presented before, to provide the longitudinal extension of the large plasma flows, and to evaluate the uniformity of the plasma density in regions away from the convection throat region. Another motivation consists of discussing how these velocity features act to produce density break-off events and therefore increase the level of plasma density structuring.

With these goals in mind, a major campaign was launched on February 1996 with the participation of the EISCAT and the Sondrestrom incoherent scatter radars (ISR) and the Super-DARN network of coherent radars. This study presents data that was collected on February 18, 1996, during this campaign. The events described here occurred after the IMF B_z reversed to a southward direction. While the general goals of the project were to observe how the patches are formed and how they exit from the polar cap, in this publication we only deal with the formation of polar cap patches and their entrance into the polar cap.

2 General observations

As mentioned in the introduction, the following high-latitude radars provided precise information on the ionospheric parameters: the EISCAT, Tromsø ISR, the Sondrestrom, Greenland ISR, and several HF coherent radars of the SuperDARN network (Greenwald *et al.*, 1995). In addition, the magnetic field values measured by the Greenland chain of magnetometers were also included into this study. Figure 1 shows the location and the area probed by both incoherent scatter radars. As indicated in this figure, the Sondrestrom radar conducted a series of 360° azimuth scans followed by an elevation scan in a plane perpendicular to a constant invariant latitude line (-27° from geographic north). A sequence of an azimuth and an elevation scans was repeated every 8 min. The EISCAT UHF radar operated in an azimuth scanning mode, covering an area of 90° . The scans started at geographic north and reached geographic west in 15 min. This was one of the first opportunities that such a type of scan was exercised with the EISCAT UHF radar. The EISCAT VHF antenna beam was split in two directions to provide a measure of

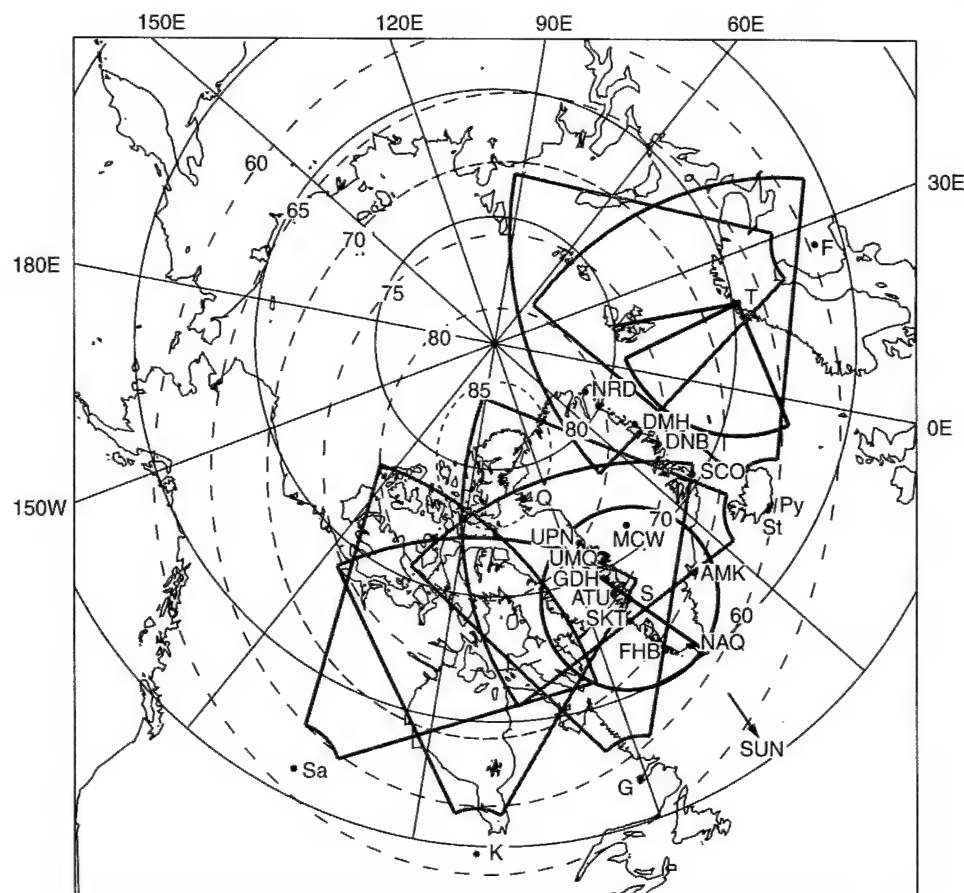


Fig. 1. Illustration of the different radar sites and their approximate fields-of-view (FOV) located at high latitudes. The gray traces delineate the areas probed by the SuperDARN radars that were operational during the experiment. The light gray contour represents the FOV of the Goose Bay radar. The antenna-scanning configuration of the Sondrestrom and EISCAT radars used on February 18, 1996, is displayed in black. The large black dots indicate the locations

where the radars and magnetometers of the Greenland chain are placed. Their geographic locations are as follow: Q = Qaanaaq (77.5° N, 69.2° W); S = Sondrestrom (66.9° N, 50.9° W); T = Tromsø (69.6° N, 19.2° E); Sa = Saskatoon (52.2° N, 106.5° W); K = Kaspuskasing (49.4° N, 82.3° W); G = Goose Bay (53.3° N, 60.5° W); Py = Pykkvibaer (63.8° N, 19.2° W); F = Finland (62.3° N, 26.6° E)

the vector velocity. During the experiment only five of the SuperDARN radars were in operation. Their field-of-views are depicted by the gray contours of Fig. 1. The area covered by the Goose Bay (G) radar is displayed in light gray to indicate that on February 18, 1996 this radar was on maintenance and did not perform measurement of the plasma velocities. Consequently, we could not combine the line-of-sight velocities from Stokkseyri and Goose Bay to estimate the 2-D horizontal velocity vector. Each of the coherent radars completed a $\sim 60^\circ$ scan every 2 min.

2.1 Solar wind observations

On February 18, 1996, both the WIND and IMP-8 satellites were favorably located for measuring the IMF. WIND was positioned at $X = +173.8 R_E$ distance in front of the magnetopause, and IMP-8 was situated ($X = 4.5$, $Y = 29.3$, and $Z = 28.0 R_E$) at the dusk flank of the magnetosphere, and upstream from the bow shock. Figure 2 shows the value of the three compo-

nents of the IMF measured by the WIND satellite. This figure shows that between 1330 and 1400 UT the B_z IMF component slowly changed from north to south. At 1356 UT, B_z becomes negative and remains around -2 nT for the next 3 h. During the time of the B_z reversal, the B_y and B_x components were near zero and $+5$ nT respectively. Thus, at the time of the B_z reversal the IMF was practically directed in the $+B_x$ direction.

We have estimated the propagation delay for the effect of the IMF transitions, detected by the WIND satellite at $+173 R_E$, to be felt at the ionosphere. This calculation is based on the expressions advanced by Lockwood *et al.* (1989) and the solar wind parameters measured by the WIND and IMP-8 satellites. Both WIND and IMP-8 observed that the solar wind velocity was quite steady and equal to 450 km/s. However, the IMP-8 measurements were interrupted between 1347 UT and 1642 UT, which is the time of interest. Based on the steadiness of the solar wind velocity observed by WIND, and before and after the data gap for IMP-8, we inferred that the solar wind was 450 km/s at the time of the B_z reversal.

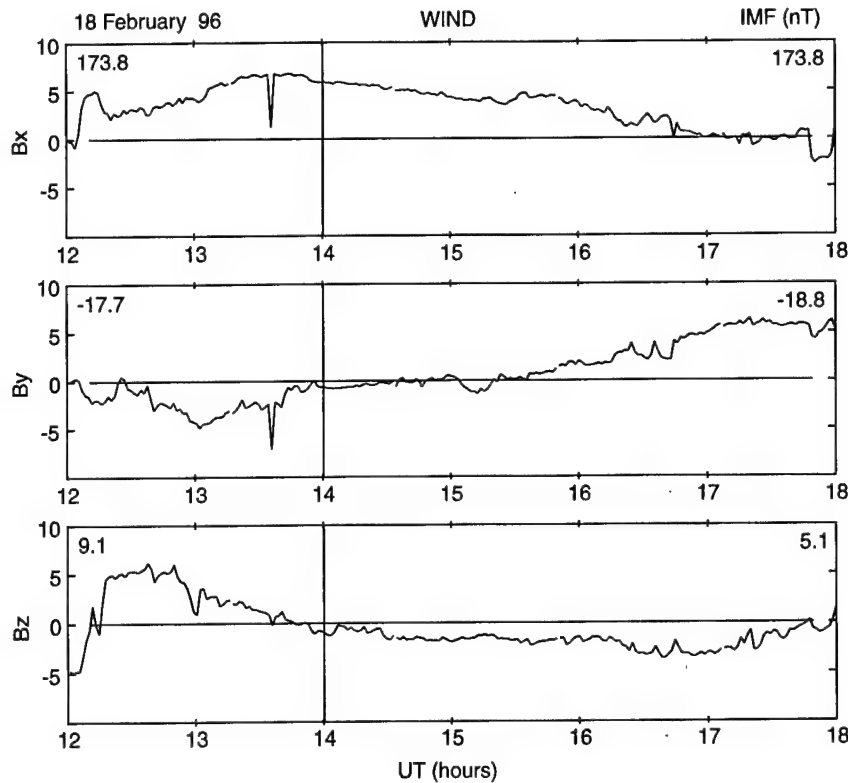


Fig. 2. Interplanetary magnetic field measured by the WIND satellite at 173.8 Earth radii, well in front of the magnetopause. All three IMF components are shown in GSM coordinates. Units for all three quantities are nanoteslas

While the IMF measured by the WIND satellite near the libration point can be in many instances equal to the solar wind magnetic field impinging the magnetopause, it may in some other instances be highly variable in time and space (Kelly *et al.*, 1986). Crooker *et al.* (1982) have also cautioned that the correlation between the IMF measured by two satellites, one located near the libration point and the other closer to the bow shock, can fall sharply if the satellite positioned toward the Sun is more than $90 R_E$ away from the Sun-Earth line. WIND measurements were taken at $Y = +18 R_E$, $Z = +8 R_E$, less than $90 R_E$ from the Sun-Earth line. Thus, we do not expect a drastic variation of the IMF due to the large separation of the spacecraft. To increase the confidence in the IMF values measured by WIND, we performed a correlation analysis between these values and the IMF measured by IMP-8. The agreement was very good for all three IMF components. In fact, a clear delay time of 31 min was obtained for the three components of the magnetic field gathered near 13 UT, and about 40 min for the IMF values corresponding to 17 UT. Having validated the WIND IMF values, we proceeded to use the expression given by Lockwood *et al.* (1989), and computed a propagation delay from the WIND satellite location to the cusp equal to 67.7 min.

2.2 SuperDARN observations

Figure 3 displays the line-of-sight velocity measured in a sequence of four consecutive scans by five of the SuperDARN HF and VHF radars (Greenwald *et al.*,

1995). As mentioned earlier only five of the HF radars operated on February 18, 1996. These were: Saskatoon, Kapuskasing, Stokkseyri, Pykkvibaer and Finland radars. Coherent HF radars are sensitive to scattering produced by small-scale F-region number density irregularities. The doppler shift of the back-scattered signal is equal to the component of the ionospheric plasma drift along the radar line-of-sight (Ruohoniemi *et al.*, 1987). The SuperDARN velocities, and several other parameters displayed in this work, have been represented employing the corrected geomagnetic coordinate system defined by Baker and Wing (1989). The magnitude and the direction of the velocity have been coded using arrows of different lengths and different types. Figure 3a, corresponding to the observation period between 1506 and 1508 UT, shows the line-of-sight velocity before the passage of a set of TCV. At this time the plasma velocity does not exceed 500 m/s in any region where the SuperDARN radars detected coherent echoes. Two minutes later, (Fig. 3b) the velocity in a region near noon suddenly rises to values larger than 1000 m/s and the area with irregularities, in the postnoon sector, becomes much broader. A region of large plasma flow extends between 68° and 80° magnetic latitude and between 12 and 14 local time. Two channels of large flows seem to form near the dayside. One is centered at 70° and the other is at 77° magnetic latitude. Figure 3c, d indicates that the large plasma flows persist, at least for the following 4 min, and that the region in between the two channels is filled up, forming a much broader region containing large flows. The spatial distribution of these velocity structures will be defined in Sect. 3 where we

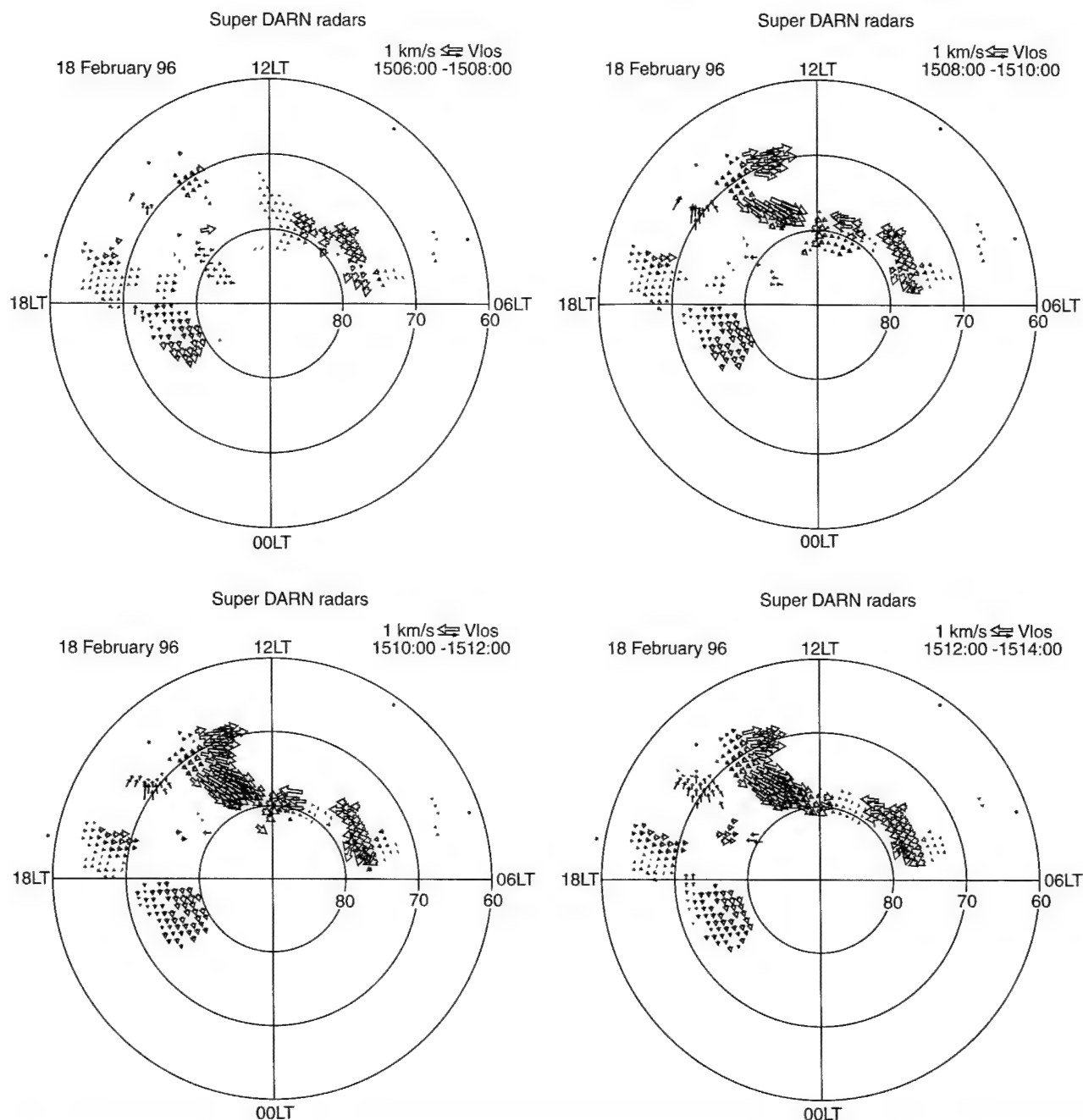


Fig. 3. Line-of-sight velocities measured by five of the SuperDARN radars on February 18, 1996. Note the change in the magnitude of the velocities in the frame that started at 1508 UT

combine convection data from different ground-based sensors.

In Fig. 4, we present the cross polar cap potential (Φ_{PC}) that was obtained after conducting a spherical harmonic fitting to all the velocities measured by the HF radars for each of the 2-min segments. Prior to 1506 UT the potential is below 60 kV, after this time Φ_{PC} presents a series of fluctuations varying between 70 and 90 kV. Four Φ_{PC} maxima are detected between 1500 and 1630 UT. The first occurs at 1508 UT; this is near the time of the initial appearance of the two channels of large plasma flow. We have subtracted 67.7 min of propaga-

tion delay from the time of the first Φ_{PC} maximum. The resulting time, 1400:18 UT, is very close to the time when B_z reverses sign. This is indicated in Fig. 2 as vertical bars in all three IMF components. The other Φ_{PC} maxima occurred at 1530, 1550, and 1606 UT. These four polar cap potential intensifications may be attributed to a general increase of the flow velocities within the whole polar cap ionosphere. However, in some cases they could be produced by the sudden appearance of localized velocity structures. A detailed analysis of two of these events is presented in the following two sections.

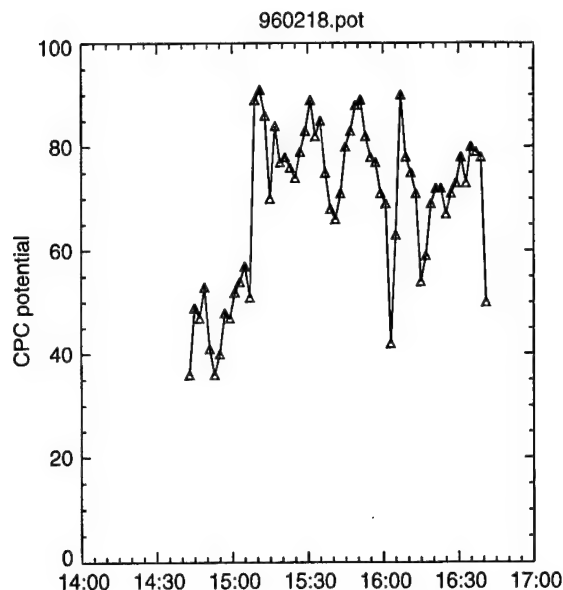


Fig. 4. Time variation of the polar cap potential across the polar cap. The potential was calculated based on the line-of-sight velocity measured by five of the HF SuperDARN radars. Notice the rise of the potential at 1508 UT

3 Patch formation associated with TCV

The first intensification of the cross polar cap potential (1508 UT) occurred a few minutes after the reversal of B_z (including the propagation delay). However, this increase in the polar cap potential seems to be the response of the fitting algorithm to the appearance of two “channels” of large velocities, somewhat localized in their extension and spatially restricted only to the near noon sector.

In this section we combine measurements of magnetic fluctuations gathered by the ground-based magnetometers in Greenland and the line-of-sight velocities from different radars to understand the nature of the velocity structures and the effects that these features produce on the dayside uniform number density. The following subsections deal with an in-depth analysis of the period between 1505 and 1520 UT.

3.1 Magnetometer observations

Figure 5 shows 20-s resolution plots of the magnetic field fluctuations measured by the ground-based magnetometers located on the west coast, ice cap and east coast of Greenland. The seven traces at the top of each panel correspond to stations on the west coast of Greenland. Traces labeled DNB and SCO correspond to stations on the east coast. MCW is one of the MAGIC stations located at the ice cap. The geographic location of these magnetometer stations can be seen in Fig. 1.

The prominent features in Fig. 5 are the large magnetic deviations seen between 1505 and 1530. The D (eastward) and Z (vertical) components show spiky variations with amplitude near 100 nT. These magnetic fluctuations resemble the signatures of TCV observed by Friis-Christensen *et al.* (1988), McHenry *et al.* [1990],

and Clauer and Ridley (1995) also using the Greenland array of magnetometers. Friis-Christensen *et al.* (1988) argued that their observations were consistent with a twin vortex pattern of convection associated with two field-aligned current filaments separated by 600 km in the east-west direction. They suggested that the observed TCV were probably related to a readjustment of the magnetopause boundary. More recently, Clauer and Ridley (1995) observed a continuous train of TCVs moving westward across the magnetic noon sector. These authors combined data from the Greenland magnetometers, the Sondrestrom radar and the DMSP satellite to conclude that the source of the vortices was possibly a Kelvin-Helmholtz mechanism or perhaps magnetic merging during an interval of IMF oriented predominantly in the $+B_y$ direction. In this publication we are not addressing the association of these TCVs to any magnetospheric/magnetopause process, even though we recognize that this would be a very worthy endeavor. Our goal in this section is to understand the type of N_e structuring that a passage of a series of TCVs produces in the midday high latitude ionosphere.

3.2 Sondrestrom ISR observations

Figure 6 presents maps of the electron number density collected during three consecutive AZ scans and corresponding to the period between 1457:28 and 1519:32 UT. The plot format is similar to Fig. 3 of Valladares *et al.* (1994), but here the scans cover 360° of the sky and the antenna elevation angle is 30° . Figure 6a shows a quasi-uniform F-region, where the F-region peak density slowly decreases from south-to-north following a typical daytime dependency with the SZA. Figure 6b, obtained between 1505:42 and 1511:20 UT, displays narrow density depletion located at the northern part of the scan ($-100, 400$ km). The time that this N_e depletion was detected with the Sondrestrom ISR coincides closely with the initiation of the large plasma flows, as measured by the coherent radars, and with the spiky magnetic fluctuations detected by some of the Greenland chain magnetometers. Figure 6c shows the number densities observed in the following AZ scan that started at 1513:55 UT. This figure reveals that a much broader density depletion was formed in the northeastern region of the scan ($350, 350$ km). We can not conclude that a density breakoff, or a complete detachment of a plasma slab from the oval has occurred. However, the density plots indicate that the level of structuring has increased. At the same time the density feature has been displaced poleward from a distance of 425 km from the radar to a location 500 km away from the radar site. Figure 6d displays a color-coded representation in the Corrected Geomagnetic coordinate system of the number density presented in Fig. 6c.

3.3 EISCAT ISR observations

Figure 6d shows also the number density measured by the UHF EISCAT ISR during the 90° azimuth scans

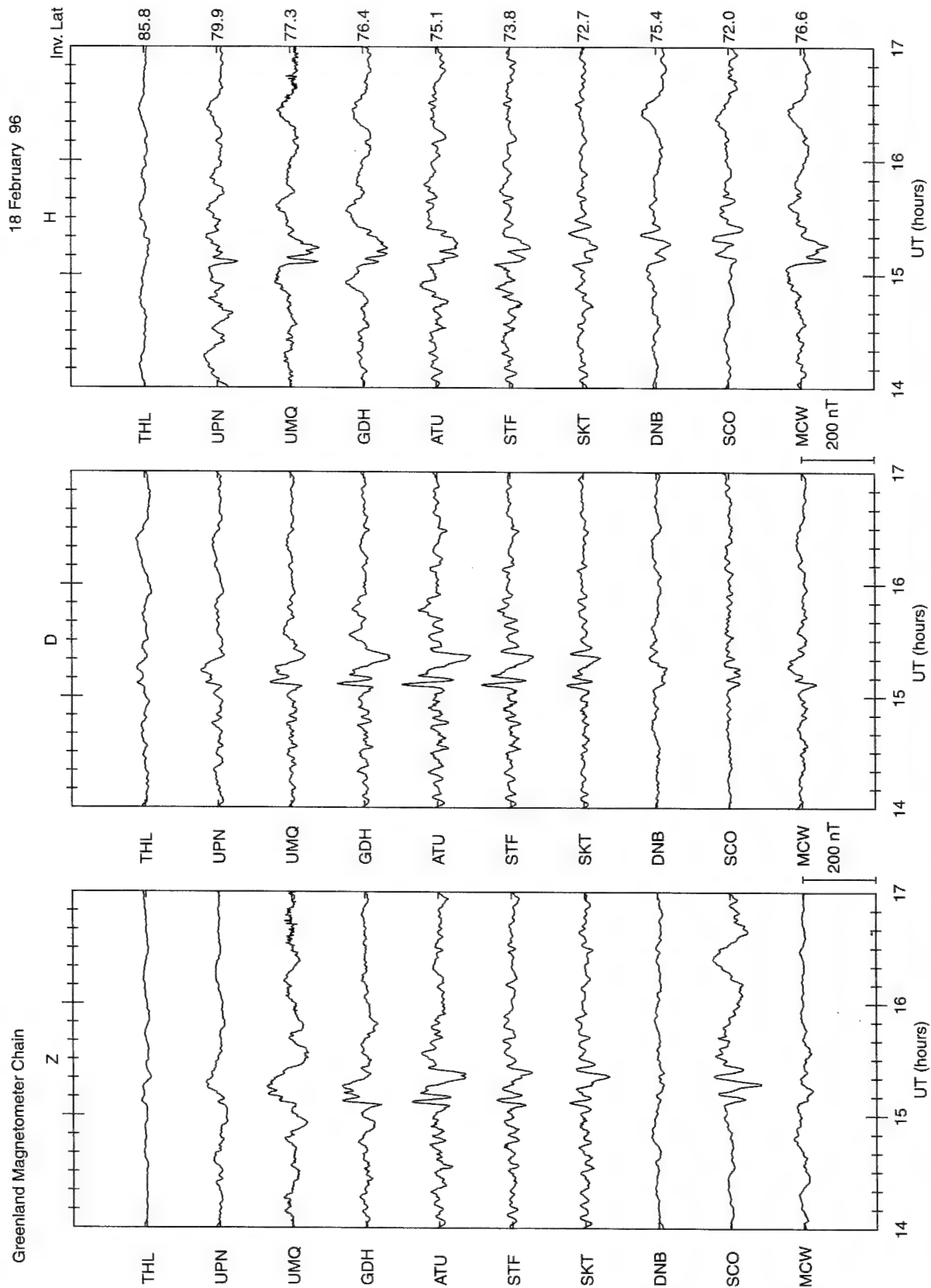
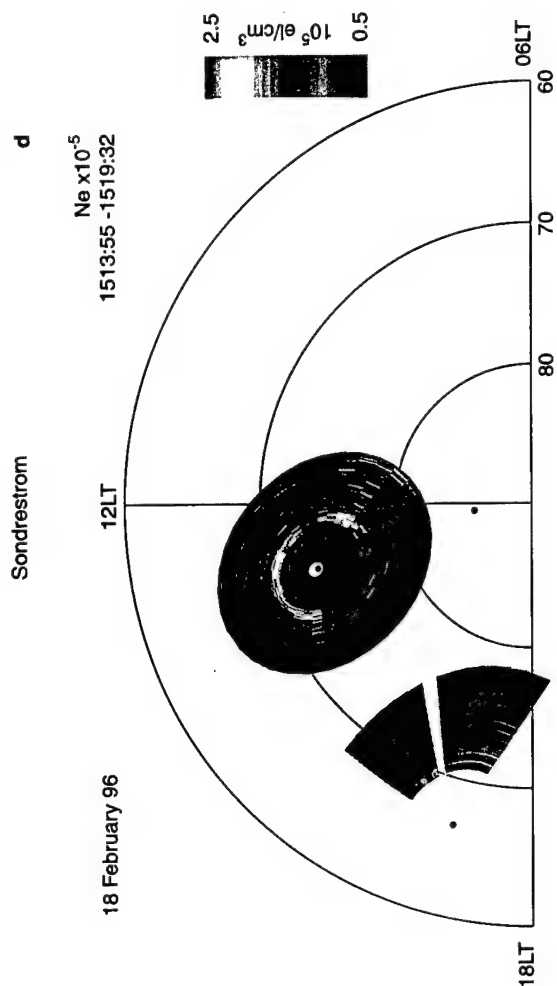
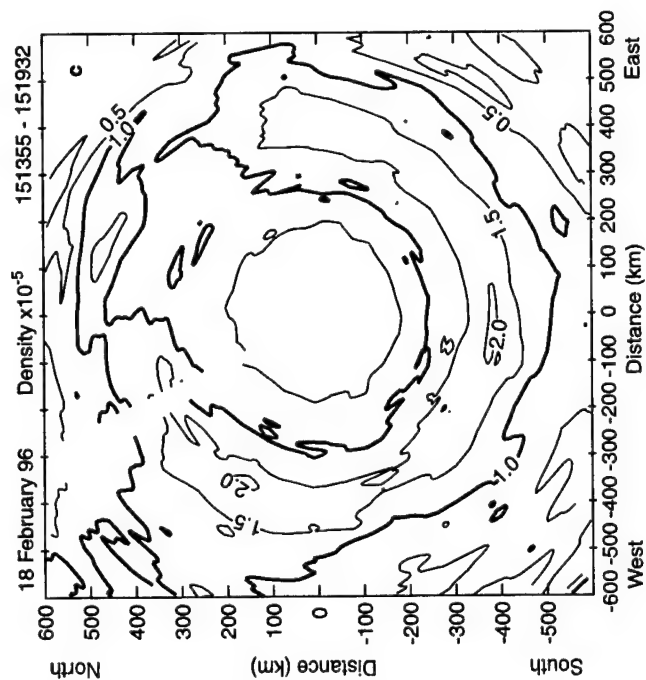
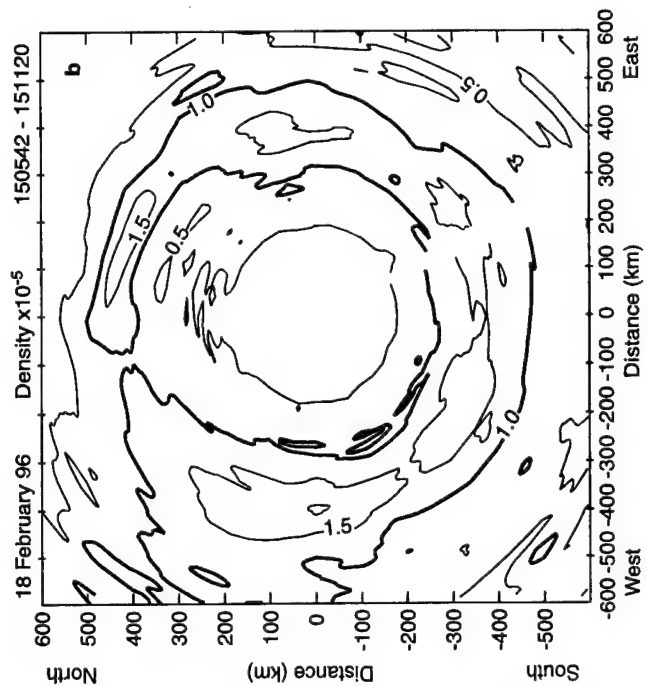
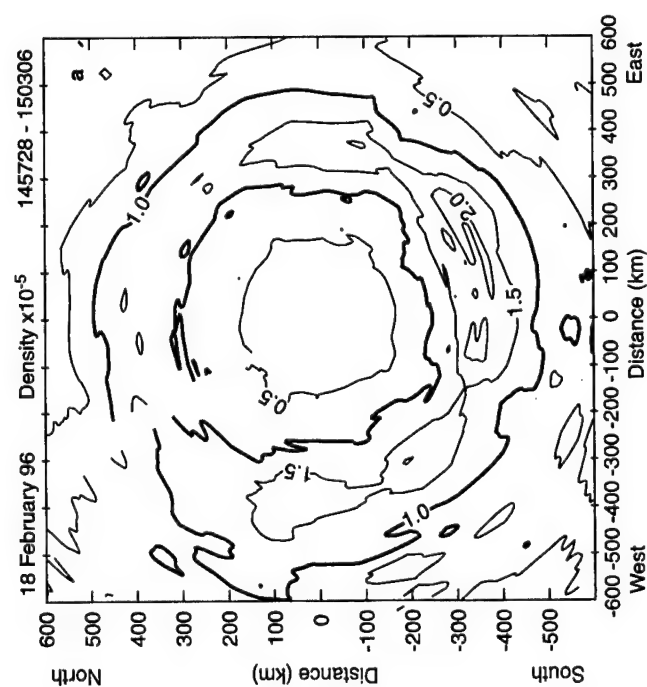


Fig. 5. Stacked plot of the Z , D , and H components of the magnetic deviations from the Greenland chain of magnetometers from 1400 to 1700 UT. Note the spiky features that start at 1506 UT associated with the traveling convection vortices. The locations of the respective stations are shown in Fig. 1



See p. 1028 for figure legend

Fig. 6a–d. Plasma density measured by the Sondrestrom ISR on February 18, 1996, during three consecutive azimuth scans. The values gathered during the azimuth scans at 30° elevation are displayed in the *first 3 panels*, projected on a plane tangent to the Earth at the radar site. **d** shows the density measured between 1513:55 and 1519:32 (c) projected into a corrected geomagnetic coordinate system

that were conducted between 1500 and 1515 UT. This partial scan shows that the peak number density is quite uniform and near $1.5 \times 10^5 \text{ cm}^{-3}$. Neither auroral nor boundary blobs are present in this limited scan. The line-of-sight (LOS) velocities (not shown here) indicated that the area probed by the radar was embedded within a region of sunward convection. The electron temperature was $< 2000 \text{ K}$ and uniform suggesting the absence of localized precipitation. Based on the uniform density at EISCAT, we conclude that the structuring seen at Sondrestrom must be created *in situ* and not transported by the sunward convection.

3.4 Analysis of localized velocity structures

In this section, we combine experimental data from different sensors to define the intensity, location and size of the TCVs. Then, we use this information to associate the formation of a deep density depletion, as seen with the Sondrestrom ISR, to the precise location of the TCV containing large flows. Each of the techniques that were used to obtain the plasma drift suffer some inherent limitations. These limitations are in the form of the spatial and temporal coverage and in the relationship between the measured geophysical quantity and the plasma convection. An incoherent scatter radar (and also a coherent radar) provides a direct measurement of the $\mathbf{E} \times \mathbf{B}$ plasma drift. But, these measurements give only one component of the 2-dimensional horizontal flow. [The third component, the one along the \mathbf{B} field, is usually assumed to be null. Valladares and Carlson (1991) have reported precise measurements of the plasma velocity component along the field line, undertaken also with the Sondrestrom ISR, of a value equal to 25 m/s. This value is well below the 50 m/s statistical uncertainty of the LOS velocity.] The Sondrestrom ISR employed 5.5 min to complete a 360° azimuth scan. The SuperDARN radar used 2 min to scan a sector close to 60°. These scanning rates highly impair the possibility of a radar to fully probe the velocities associated with a rapidly moving TCV, such as the ones observed on February 18, 1996. The magnetic deflections measured by ground-based magnetometers are closely related to the Hall currents, and these currents are proportional to the plasma convection. Therefore, our analysis of the TCV velocities heavily relies on the magnetic field data.

A cross correlation between the H component of the magnetic fluctuations from two stations, GDH (west coast) and MCW (MAGIC), located at approximately the same magnetic latitude but 500 km to the east, gives a phase delay of 87 s. The magnetic pulse first appears at GDH and then travels to MCW. This implies a phase

motion of the vortex in the eastward direction equal to 5.7 km/s.

Figure 7, plotted in a time reversed coordinate, shows the equivalent drifts from the stations located on the west coast of Greenland using the common convection vortex format (Clauer and Ridley, 1995). In this representation we can observe the east-west extension of the vortices. To display the equivalent plasma convection, the magnetic traces were rotated 90° counter-clockwise, and were also filtered subtracting a 40 min running average. Several vortices are clearly identified in Fig. 7; a few others are more difficult to interpret due to the rapid evolution of the vortex electrodynamics. The first vortex appears at 1505 UT and corresponds to a clockwise plasma rotation. A second vortex seems to transit at 1508 and a third at 1510 UT. However, the latter two vortices were not completely defined due to their rapid time evolution when they were crossing Greenland's west coast. Figure 8 presents a quasi-instantaneous view of the first three vortices. After 1515 UT three more vortices passed, all moves eastward.

Figure 8 provides snapshots of the plasma flow in a large area of the high latitude ionosphere, extending 14° in magnetic latitude and 3 hours in local time. We present 8 frames, each 1 min apart, during the passage of the three vortices that occurred between 1505 and 1512 UT. The equivalent drifts, deduced from the magnetic deflections of the Greenland magnetometers, are plotted as red vectors. We use longer vectors to represent larger magnetic fluctuations. The Sondrestrom LOS velocities are displayed using black or white arrows depending upon the sign of the velocity (toward or away the station). The LOS velocity from the Stokkseyri HF radar are depicted using green vectors. The large dot with the initial "St" indicates the location of the Stokkseyri HF radar; and the location of the magnetometer stations are each labeled in the panel corre-

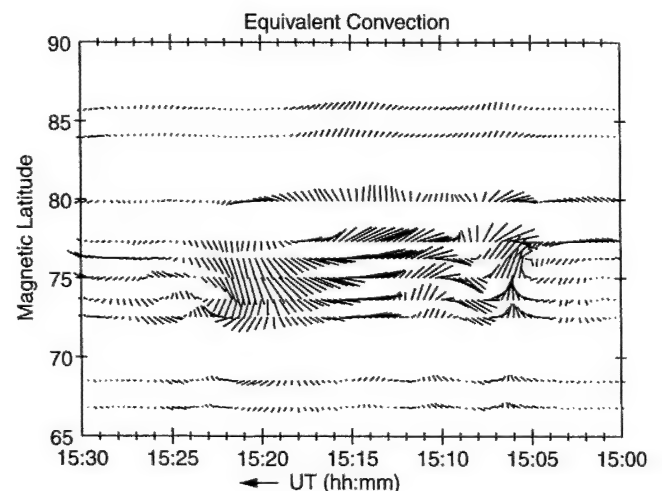


Fig. 7. Plot of the horizontal magnetic perturbation vectors corresponding to the variations of Fig. 5. The vectors have been rotated 90° counterclockwise and plotted every 20 s during the time interval between 1500 and 1530 UT. Note the time scale increases from *right to left* in order to display the east-west extension of the vortices that were traveling eastward

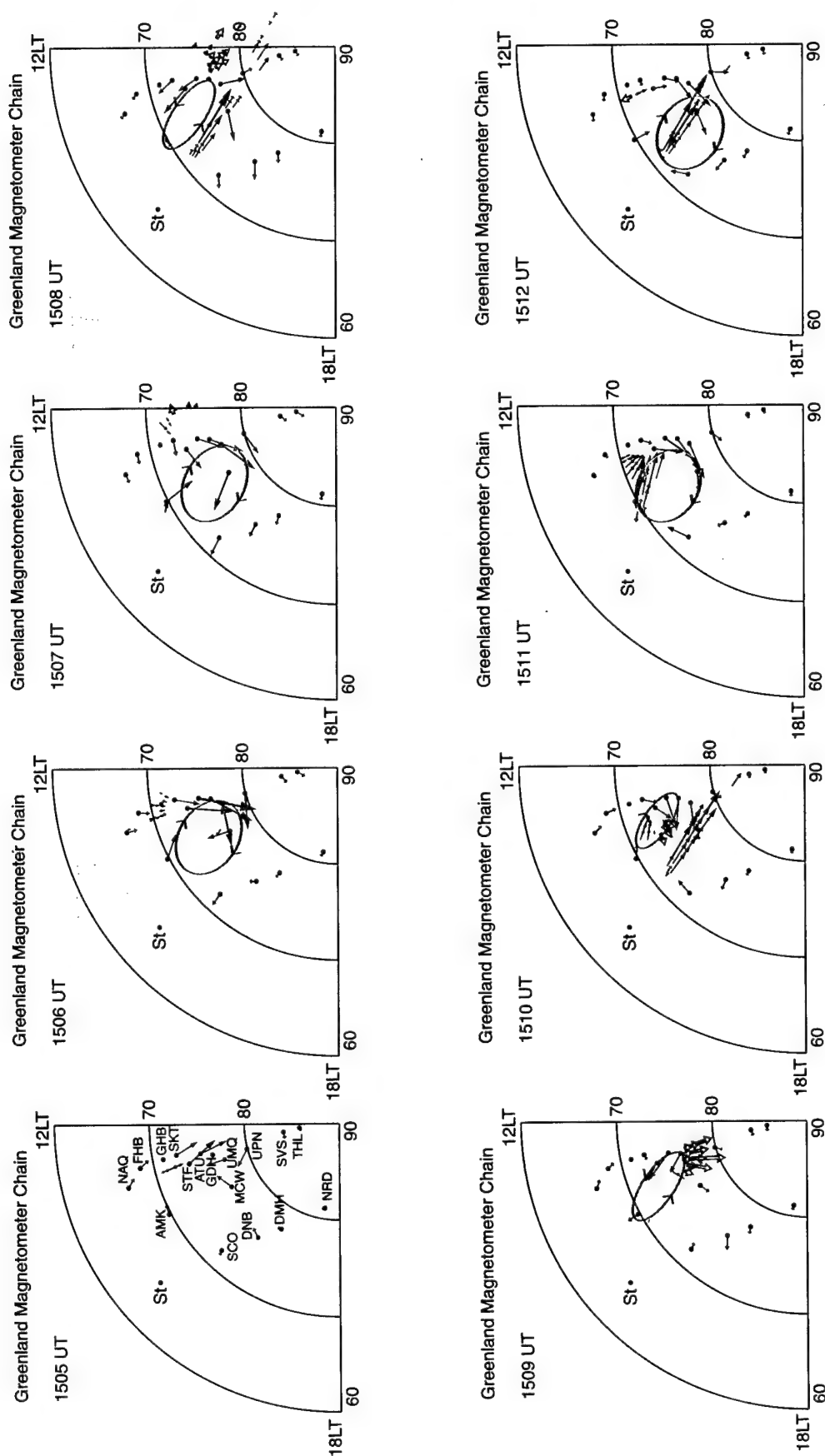


Fig. 8. Series of polar plots of the instantaneous equivalent drifts measured by the Greenland chain of magnetometers and line-of-sight velocities from the Sondrestrom (black and white arrows) and the Stokseyri (green arrows) radars. The ellipses in each frame display our subjective position of the vortices at each time of the measurements. The latitudinal circles are in steps of 10°

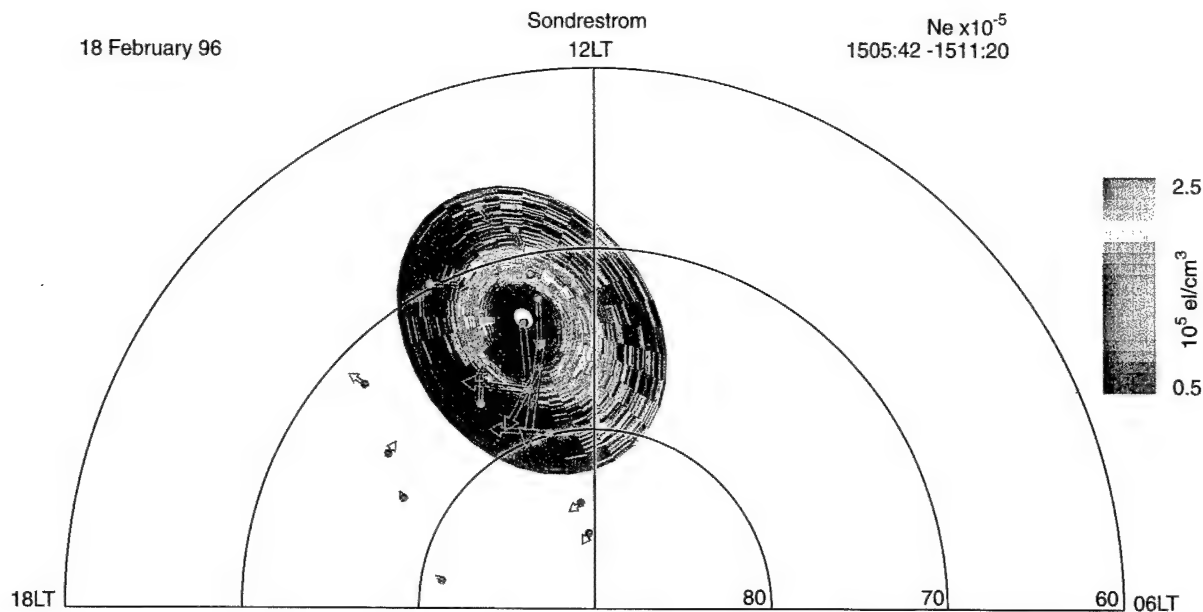


Fig. 9. Plot of the number density measured by the Sondrestrom radar between 1505:42 and 1511:20 UT. Superimposed in *red arrows* are the equivalent drifts measured by the magnetometers at 1506 UT.

Note the precise collocation of the region of large drifts and the F-region density depletion toward the north of the station

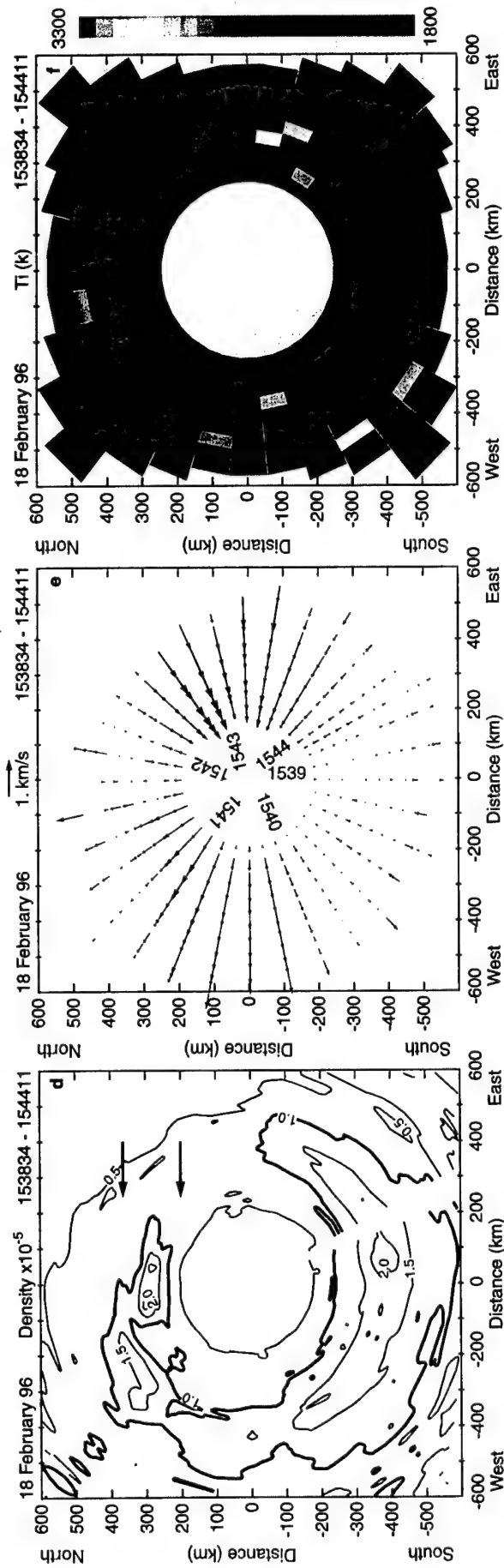
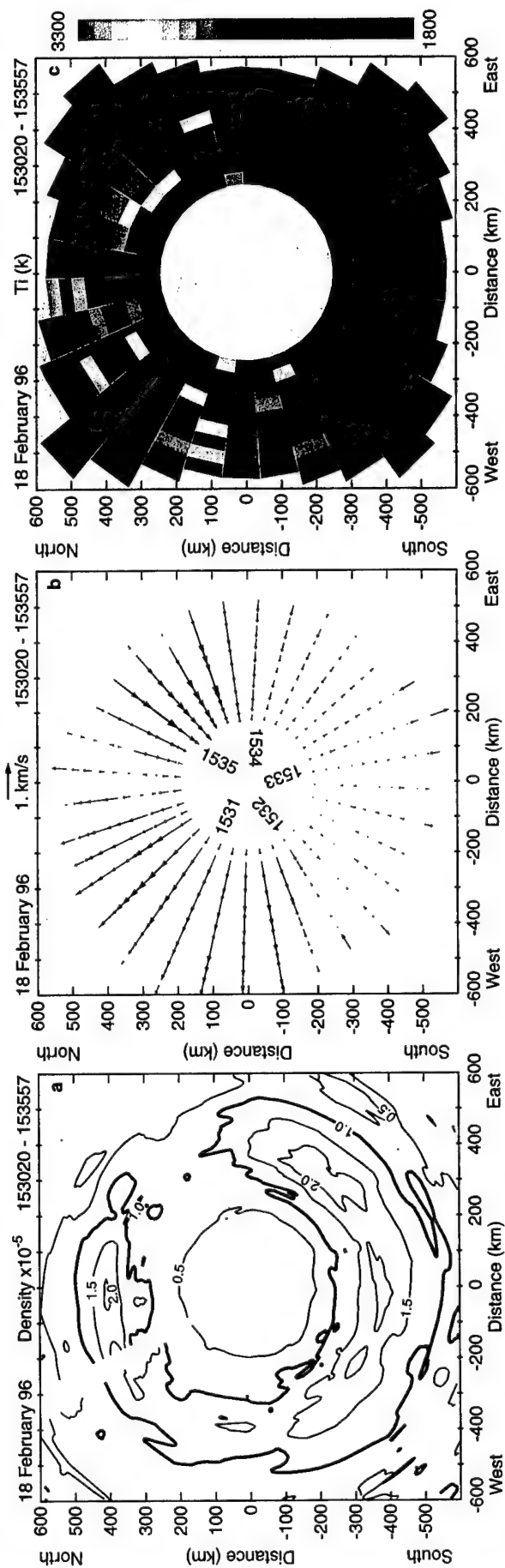
sponding to 1505 UT. We have used only the afternoon quadrant of the CG coordinate system to display the vectors. The gray circles with arrows, as seen in some of the panels, denote our subjective interpretation of the location and size of the TCV associated with the observed plasma velocities. Each panel in Fig. 8 shows the equivalent drifts measured at the minute and the LOS velocities from the Sondrestrom and Stokkseyri radars gathered ± 20 s from the time indicated at the top left corner of each panel.

Figure 8 shows that at 1506 UT a vortex was centered at approximately 74° magnetic latitude. This vortex is seen in later frames to move eastward and then fade as it moves away from the dayside at 1508 UT. The vortex observed at 1506 UT has a clockwise vorticity, which corresponds to a filamentary field aligned current directed away from the Earth. At 1508 UT, a second vortex appears with a counter-clockwise plasma motion and consequently a current polarity opposite to the previous vortex. This vortex is more elliptical and its reconstruction is in agreement the Stokkseyri LOS velocities (green vectors) in the part of the vortex of poleward flows. At 1510 UT, the third vortex appears centered at 72.5° magnetic latitude. In the following two panels, this vortex expands poleward and becomes more circular. During the passage of the third vortex, the Sondrestrom ISR was scanning toward the east and south of the station (1510 UT). In the east sector, the radar detected small amplitude LOS velocities reversing sign. This is indicative that the radar was pointing nearly perpendicular to the vortex flow and in agreement with the vortex flow at both sides from the point of perpendicularity. When the radar is scanning to the south the LOS velocities are again consistent with a clockwise vortical motion. In general, it seems that the vortices have a rapid onset and probably last only few

minutes during their transit across Greenland. In spite of this short lifetime the effect of the vortices on the density, as seen in Fig. 9, is very pronounced.

Figure 9 shows the number density of Fig. 6b translated to a CG coordinate system. We have also superimposed the equivalent drifts measured by the magnetometers at 1506 UT. The radar scan started at 1505:42 UT, when the antenna was pointing toward magnetic south. The antenna scanned clockwise, reaching the N_e depletion at 1508:50 UT. This depletion is collocated with strong poleward equivalent drifts. As shown in Fig. 7, this poleward flow associated with the vortex passage lasted from 1505:40 to 1507:00 UT. This time seems long enough to create a factor of 2 density depletion which remained almost unchanged for several minutes. (It was seen by the Sondrestrom ISR at 1508:50 UT.) The magnetic perturbations were the largest during the period under discussion here, exceeding 100 nT. We do not have a direct radar measurement of the velocities in the first vortex, but based on the LOS velocities measured by the Stokkseyri, we infer that they were probably of the order of 2.5 km/s. These large velocities were able to create a substantial frictional Joule heating and enhance the temperature dependent O^+ recombination coefficient. This enhancement of the loss rate is responsible for eroding the number density at the F peak from a background level of $1.5 \times 10^5 \text{ cm}^{-3}$ down to $0.7 \times 10^5 \text{ cm}^{-3}$, as observed in the northern part of Fig. 6b.

Fig. 10a–f. Number density, line-of-sight velocity and ion temperature measured by the Sondrestrom ISR on February 18, 1996, during the time interval from 1530:20 and 1544:11 UT. The location of the density trough is seen in both density plots extending in the east-west direction. Enhanced V_{los} and T_i are seen somewhat collocated with the N_e depletions. See text for details



4 Patch formation associated with large plasma flows

After 1528 UT, the ground-based magnetometers did not detect the spiky magnetic deflections. In spite of this lower magnetic activity the Sondrestrom radar observed very pronounced density depletions and N_e structures. In this section, we present the line-of-sight velocities from the SuperDARN, the Sondrestrom, and the EISCAT radars to imply that a different process, channels containing large plasma jets (LPJs), developed at high latitudes between 1530 and 1630 UT. Several LPJs were seen near the poleward boundary of the auroral oval during this time interval. The result of the occurrence of the first two LPJs was to form two sharp density depletions and a patch-like feature in between the density depletions.

4.1 Sondrestrom ISR observations of LPJ

Figure 10 presents the number density, line-of-sight velocity (V_{los}), and the ion temperature measured by the Sondrestrom ISR during two consecutive AZ scans. The three panels at the top of Fig. 10 show the N_e , V_{los} and T_i parameters observed during a 360° counter-clockwise scan conducted between 1530:20 and 1535:57 UT. The three panels in the bottom row depict the same geophysical quantities but measured during a clockwise scan that started at 1538:34 and ended at 1544:11 UT. The times at the center of Fig. 10b, e indicate the exact hour and minute when the antenna was pointing at the precise azimuth angle where the numbers are placed.

The variability of the number density near the Sondrestrom station is registered in Fig. 10a. This figure shows that the deepest depletion ($0.5 \times 10^5 \text{ cm}^{-3}$) is located between 40° and 70° clockwise azimuth from geographic north. A second density depletion, however less pronounced (10^5 cm^{-3}), is placed to the west of the station. Eight minutes later, Fig. 10d reveals that the deep depletion has evolved into a much wider extension, spanning from 35° up to 90° azimuth and aligned in the east-west direction. The poleward side of this depletion is indicated by arrow 1. A second depletion in Fig. 10d is indicated by arrow 2. This latter channel is located to the north and 400 km away from the station had initially a density equal to $\sim 2 \times 10^5 \text{ cm}^{-3}$ (Fig. 10a) and has later decreased down to $0.5 \times 10^5 \text{ cm}^{-3}$ (Fig. 10d). The result of the formation of the N_e depletion is to create a density feature bounded equatorward by the reduced densities mentioned, and poleward by another channel of low densities. Therefore, a narrow region, almost 100 km wide (in the north-south direction), and containing peak densities equal to $2.0 \times 10^5 \text{ cm}^{-3}$ was created almost detached from the auroral oval. This density feature is located upstream the sunward convection in the dusk cell, and probably in a region where the flow is sunward.

The location of the T_i enhancements has also varied between the two scans. Figure 10c shows that T_i is above the background value of 2000 K at the northern part of the scan. Peak values of T_i are at $\sim 35^\circ$ and -45°

azimuth. Figure 10f reveals that the T_i enhancements have become more localized. They are restricted to 2 different areas of the scan, one at 55° and the other at -60° azimuth angle. Careful comparison of the N_e and T_i plots for both scans indicates that the deep density depletions are not exactly collocated with the larger values of T_i . This is more evident at the western part of both scans, and especially in the northwestern part of the first scan (see Fig. 10a), where T_i is above 4000 K and there is no apparent N_e depletion. This fact suggests that the erosion of the plasma density is an accumulative effect and the depth of the N_e depletion depends not upon the instantaneous convection (or instantaneous T_i enhancement), but instead upon the recent-time history (5–10 min) of the velocity field and upon the value of the density at the point where the plasma originates. The discrepancy between the location of the T_i enhancement channels and the N_e depletions can be attributed to distribution of the gradients of the background density. The eastern depletion is fed by plasma residing at later local times, which is less dense than the plasma that feeds the western depletion. The following subsection presents maps of V_{los} , gathered with the SuperDARN radars with a much higher resolution, to capture the evolution of the flows during the formation of the N_e depletion.

4.2 SuperDARN radar observations of LPJ

Figure 11 reproduces V_{los} measured with two of the SuperDARN coherent radars. Each frame covers only the postnoon-dusk quadrant and the magnetic latitude range between 60° and 90° . The magnitude and sign of V_{los} have been color-coded to avoid cluttering the figures. Almost every panel of Fig. 11 shows values of V_{los} above 1 km/s in a region near noon and extending between 73° and 77° magnetic latitude. The four panels at the top show V_{los} reaching 1500 m/s in a region where the convective flows are mainly zonal and the direction of the line-of-sight from the Stokkseyri radar is probably almost parallel to this zonal flow. Poleward of the region of large flows ($> 78^\circ$ mag. latitude) the velocity decreases rapidly and becomes near 0 m/s at 80° . Equatorward of the region of large flows, the Stokkseyri radar did not measure plasma flows probably due to the absence of density structures. We have superimposed on the plot that starts at 1532 UT a continuous trace that delineates the region where V_{los} is larger than 1 km/s. This contour line has also been duplicated in the following two panels to indicate how the location of large V_{los} changes in the two scans that followed 1534 UT. The high velocities in the panel that starts at 1536 UT are located a few degrees poleward from their original location at 1532 UT. It has moved very rapidly to this location. The channel of large V_{los} seems to decay in the adjacent panel at 1538 UT, but it reappears 2 min later at 1540 UT near its prior more equatorial location. The LPJ remains stationary at this location until 1554 UT (not shown here) when it briefly moves back to a poleward location. It is worth mentioning that coherent

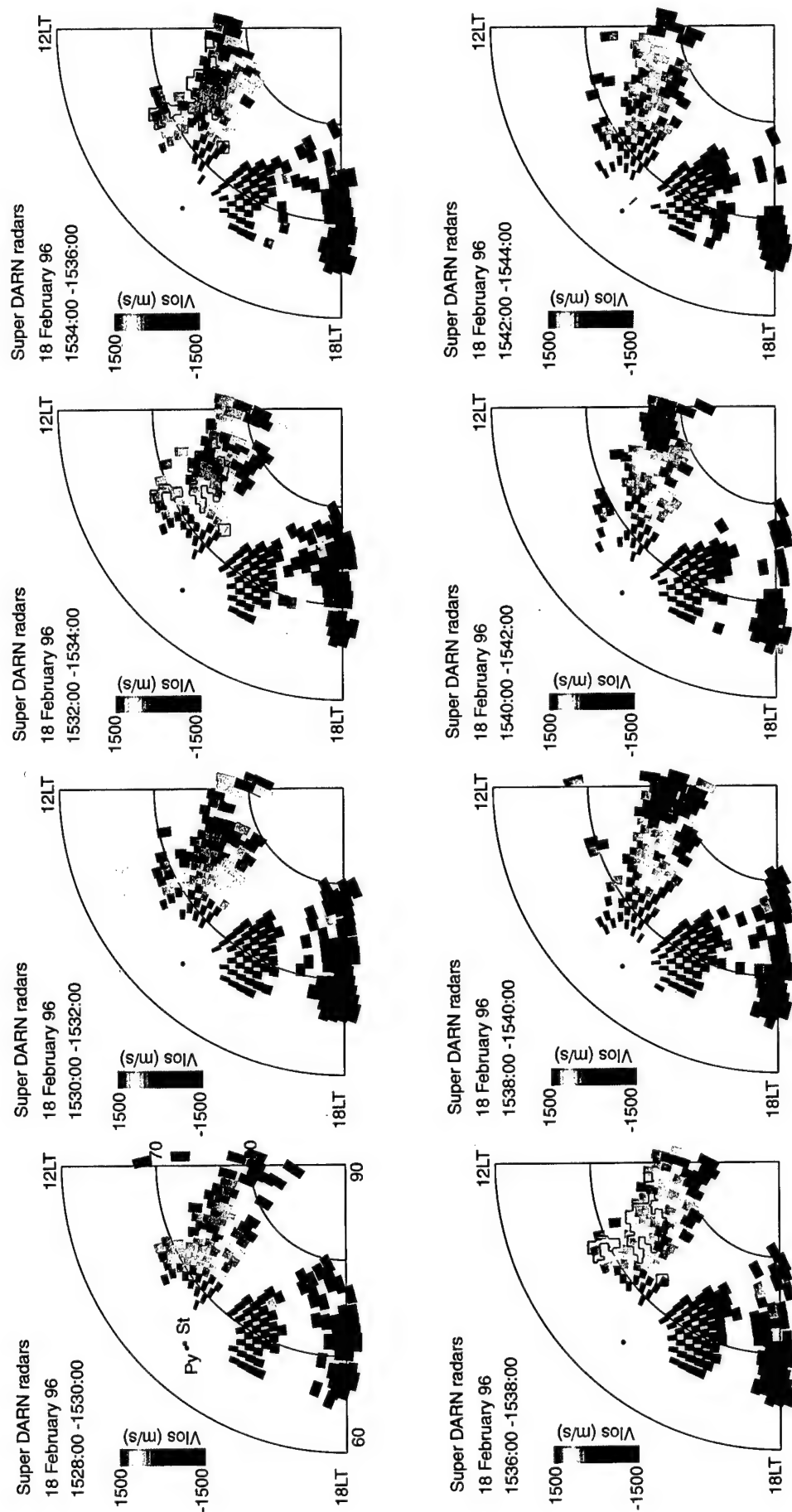


Fig. 11. Series of polar plots of V_{los} obtained from the Stokseyri and Pykkvibaer radars between 1528 and 1544 UT. The contour line in three of the panels represents the region where V_{los} was larger than 1000 m/s during the scan that started at 1532 UT. Note in the panel corresponding to 1536 UT how the location of this region changed and became more poleward

as well as incoherent radars are able to measure only one component of the velocity vector. Thus, it is quite possible that the radar has detected a large V_{los} due solely to a better alignment between the vector velocity and the line-of-sight radar direction. In the following subsection, we present resolved horizontal velocities, and demonstrate that the movement of the channel of large V_{los} toward higher latitudes corresponds to a phase motion of the LPJ and not to a realignment of the plasma velocity with the radar looking direction.

4.3 Analysis of velocities associated with LPJ

To emphasize that the variability of the location of the large plasma jets is a likely mechanism of patch formation, we have conducted a novel calculation of the vector velocities using V_{los} measurements conducted with the EISCAT, Sondrestrom, and SuperDARN radars and some information derived from statistical convection patterns. The algorithm that was used to resolve the velocities consisted of a multi-step process which can be defined in the following manner. First, we computed the horizontal velocity vector pairing V_{los} from the Stokkseyri and Sondrestrom radars only for cases when the probed volumes from these two radars were nearly collocated. We repeated the same procedure for the overlapping line-of-sight velocities measured with the Pykkvibaer and EISCAT radars. In this analysis only two components of the full vector velocity are calculated; the third component, the one along the magnetic field, is assumed to be zero (Valladares and Carlson, 1991). Results of this analysis are presented in Fig. 12a–d, where we show the horizontal velocities for four periods around the time of the poleward phase motion of the LPJ. Large westward flows, very typical of the near noon dusk cell, are seen in the first three panels. Figure 12d shows a clockwise rotation of the flows near noon, also a characteristic of a smaller dusk cell in a typical 2-cell pattern.

Second, we performed a least square fitting analysis of several Heelis-type convection patterns (Heelis *et al.*, 1982) to the horizontal velocities obtained in step 1. Third, after the best fit was obtained, we used the information of the plasma flow direction in the selected convection pattern to determine the component of the velocity perpendicular to the line-of-sight in the SuperDARN observations. The resolved horizontal velocities for each measurement of V_{los} of the Stokkseyri and Pykkvibaer radars are presented in Fig. 12e–h.

Figure 12e shows the presence of a LPJ containing velocities above 2 km/s and located between 72° and 75° magnetic latitude at 14 LT. The LPJ is embedded in a region of sunward convection, close to the location where the plasma convection turns to an antisunward orientation. The LPJ extends longitudinally up to 16 LT, however, with much reduced velocities of order 1 km/s at the tail of the LPJ. These values are much lower than the values observed at 14 LT, but they are still bounded latitudinally by smaller velocities. At 1534 UT, the LPJ has shifted to higher latitudes but the

maximum values are slightly less pronounced. Two minutes later the LPJ intensifies, and moves poleward, extending between 75° and 77° magnetic latitude (note the dotted line is traced at 75°). Simultaneously, there exists a reduction in the size of the polar cap. At 1542 UT (not shown here) the LPJ returns to its previous more equatorward location and stays at this magnetic latitude for 10 min, before moving poleward again.

Figure 12 does not show any of the SuperDARN V_{los} data measured in the dawn cell. At this local time the dawn cell is located westward of the Sondrestrom site. Measurements conducted with the Saskatoon and Kapuskasing radars in the morning sector did not present any signature of LPJs. These radars observed only modest line-of-sight velocities of order 500 m/s.

5 Discussion

Several mechanisms have been previously suggested to explain the formation and transit of the polar cap patches. Tsunoda (1988), in his extended review paper, outlined the most important processes conducive for patch formation. He stressed the importance of continuous changes in the sign of the IMF B_y or B_z components and/or the localized production of plasma density in the cusp region as prime candidates for patch formation. Recent work undertaken by Sojka *et al.* (1993, 1994) have demonstrated that in fact the B_y switching mechanism not only generates isolated density enhancements inside the polar cap, but equally important it reproduces the seasonal and UT morphology of the polar cap patches seen at the center of the polar cap (Buchau *et al.*, 1983). The net effect of a B_y flip can be understood as a redirection of the elongated TOI toward different locations within the polar cap. Repetitive flips of B_y will successively chop the otherwise continuous TOI. A more detailed comparison between the occurrence of scintillations near the center of the polar cap and the morphology of the TOI density, when it transits across the polar cap, has revealed a remarkable similarity between their seasonal and UT dependencies (Basu *et al.*, 1995). This agreement endorses the fact that the TOI is the source of the density enhancements within the patches. However, in spite of the success of the B_y switching mechanism, statistics of the switching rate of B_y do not conform with the rate that patches are seen transiting the polar cap (10–20 min). Moreover, any patch formation mechanism that uses the TOI as the source of the enhanced plasma will have a UT and a seasonal statistics very similar to the ones described by Sojka *et al.* (1994). Therefore, this new mechanism will be in agreement with the statistics of scintillations at the center of the polar cap (Basu *et al.*, 1995).

Another mechanism of patch formation that has been studied recently is the IMF B_z switching mechanism described by Valladares *et al.* (1998). However, this mechanism may only produce a single polar cap patch shortly after B_z turns negative. Unless an additional mechanism is invoked, a single B_z flip will not reproduce the most salient feature of polar cap patches which is the

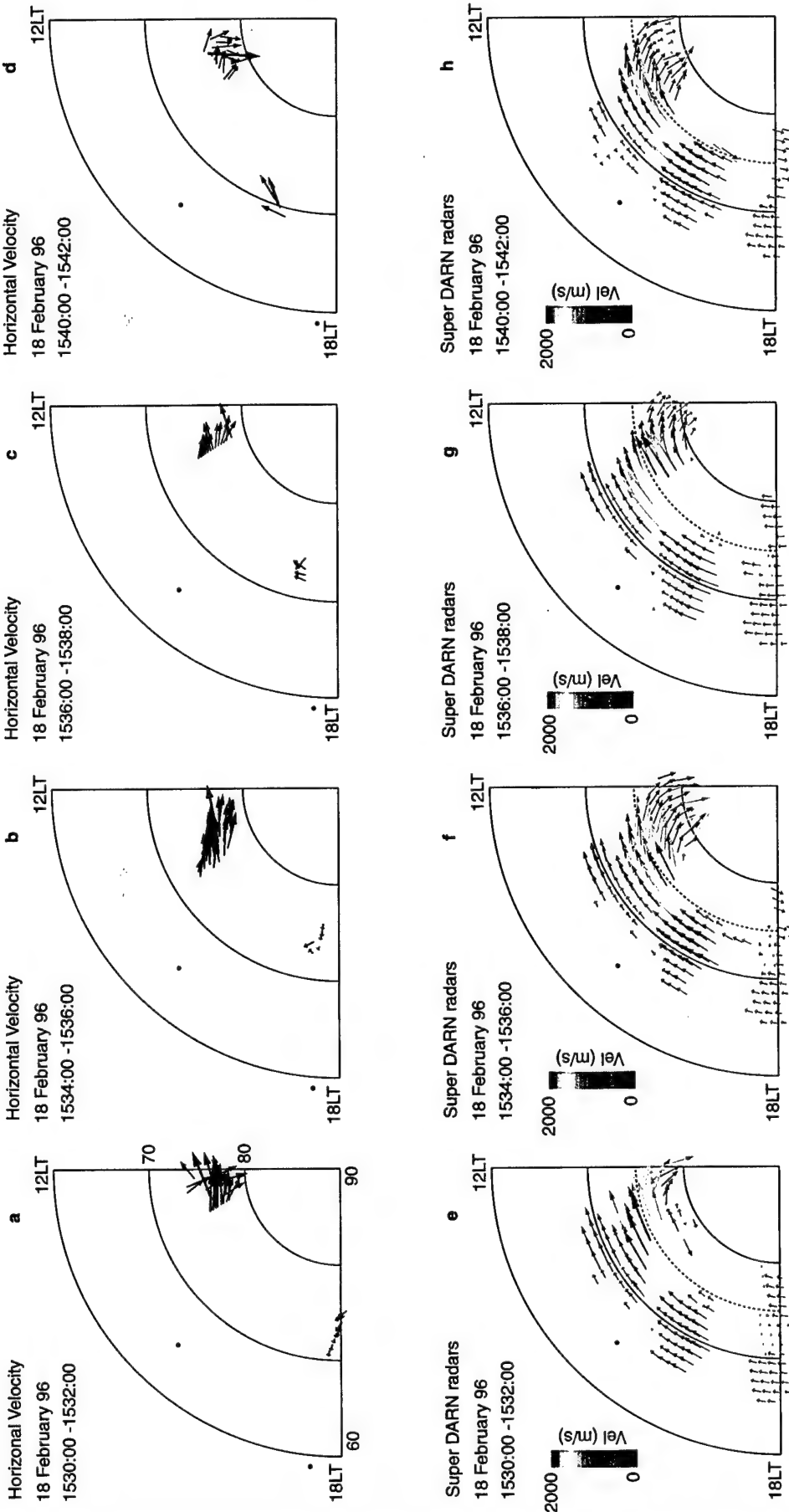


Fig. 12. Selected panels during the evolution of the LPI. The *top row* shows resolved horizontal velocity vectors for four selected periods during the evolution of the LPI. These vectors were obtained by combining V_{res} data from the SuperDARN and incoherent radars. The *bottom row* shows resolved velocities using some information derived from statistical convection patterns. See text for more details about the algorithm being used

repetitiveness of the patches when they transit the polar cap. During IMF B_z southward conditions, we typically observe, inside the polar cap, a train of several patches and rarely a single patch (Weber *et al.*, 1991; Fukui *et al.*, 1994).

In a different approach, Rodger *et al.* (1994), and Valladares *et al.* (1994) suggested that flow channel events or large plasma jets can produce enhanced losses creating a region of reduced number densities across the TOI. Rodger *et al.* (1994) suggested that a patch could be formed by the combined effect imposed by the presence of a channel containing large plasma flow and a reorganization of the convection pattern caused by changes in the IMF B_y component.

In this work, we put forth evidence for two different mechanisms that are able to generate large-scale (> 100 km) density structures acting near the poleward boundary of the oval during B_z south conditions. We also indicate the manner in which the background convection can carry the newly formed density structures toward and into the polar cap.

The first patch formation mechanism described deals with the passage of a train of TCVs through the dayside ionosphere to produce channels embracing lower densities. After the vortices have passed, the density structure will be convected into the polar cap by the dayside flow velocity of a typical B_z -south 2-cell convection pattern. Figure 13 presents our conceptual interpretation of how a patch-like structure can be formed in the dayside region. The large flow velocity residing at the interface between two adjacent vortices will produce an enhanced loss of the plasma density (see dotted area in Fig. 13). This region of reduced number density will rotate, following the vortex outer radius isolating a region of dayside number density. After the vortex has moved outside the region of depleted densities, the region of low density will start to fill up by solar ionization. However, this refilling process could well take up to tens of minutes. During this time, polar antisunward convection will transport the newly formed

patch-like structure into and toward the center of the polar cap. Note that in this scenario the patch will be a close image of the vortex.

On February 18, 1996, a series of six vortices were reconstructed based on the equivalent magnetometer drifts (Fig. 7) and the instantaneous flows of Fig. 8. Thus, it is also likely the flows associated with any of the five successive vortices have distorted the original poleward aligned density depletion by stirring the plasma. In this picture, further breaking, splitting, and tearing of the patch-like structure into smaller patch-like structures may have occurred later. This second-step structuring may explain the appearance of the density feature, seen by the Sondrestrom radar 450 km north of the station, during the scan that started at 1513:55 UT (Fig. 6c, d).

The first intensification of the polar cap potential in Fig. 4 was associated with the transit of the first vortex which contained the largest velocities of order 2.5 km/s (measured by the Stokkseyri radar). The other remaining five vortices, although clearly detected by the magnetometers, were not associated with very large flows and did not seem to carve out detectable density depletions.

As postulated before, we believe that the density depletion was probably carved out by enhanced O⁺ recombination. However, we recognize the possible role of plasma evacuation in forming an auroral ionospheric cavity (Doe *et al.*, 1993) and removing part of the ionospheric electrons as they become charge carriers for a downward field-aligned current (Doe *et al.*, 1995). Note that the second vortex, observed at 1507 UT and adjacent to the region of depleted densities, has a counter-clockwise rotational flow which indeed corresponds to downward directed current. Modeling work is needed to assess the importance of plasma evacuation and/or enhanced loss rate in producing the density depletions observed by the Sondrestrom ISR.

The second intensification of the cross polar cap potential occurred at 1530 UT (Fig. 4). We believe this is associated with the excitation of the LPJ seen in Fig. 12e. The LPJ becomes weaker and narrower at later local times; at the same time the polar cap potential decreases to values near 70 kV. This second mechanism that created large-scale structures on February 18, 1996, involves large plasma jets, but incorporates new, key information provided by the SuperDARN radars. The LPJs are not stationary but instead are affected by a periodic latitudinal phase motion. In general terms, LPJs are very efficient in creating regions of low plasma by bringing less dense plasma from earlier or later local times. They may require only few minutes to attain deep depletions (Valladares *et al.*, 1996). The large plasma velocity of the LPJ enhances the O⁺ recombination loss and due to its large longitudinal extension, much less dense plasma can be carried from later local times. This mechanism is different from the mechanism suggested by Rodger *et al.* (1994) which depended on a timely variation of the B_y component. Although in other cases the poleward motion of the LPJ could be attributed to variations of the IMF B_y component, measurements of

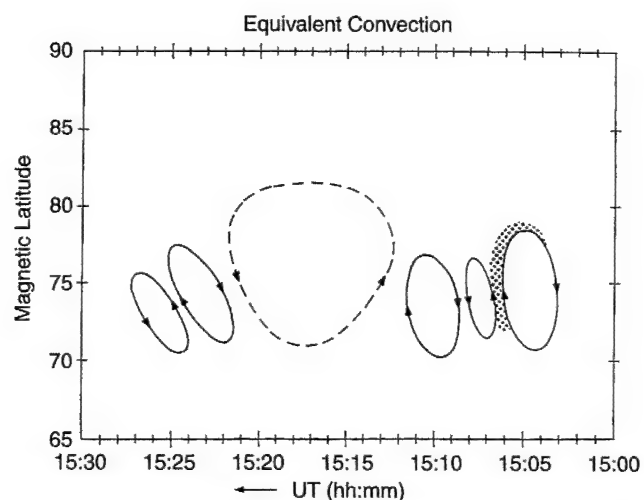


Fig. 13. Schematic drawing showing the transit of the TCVs and the density depletion formed in between the regions of large flow

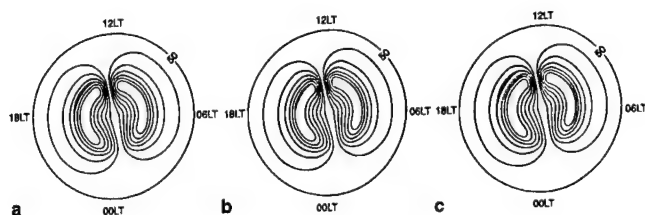


Fig. 14a–c. Schematic representation of the evolution of the LPJ and its possible effect for the formation of an isolated density structure bounded by two regions of recently depleted densities

the IMF carried out by the WIND satellite at the time of interest (14–15 UT) registered only mild variations of B_y (between 0 and -1 nT).

The two azimuth scans of Fig. 10 display the formation of a density structure bounded by two channels of reduced densities (see arrows in Fig. 10d). This density structure was observed by the Sondrestrom radar approximately at 1542 UT. Both low-density channels coincide with the location of the two LPJs that were seen in the SuperDARN data of Fig. 12e and g.

Figure 14 illustrates our concept on how the LPJ phase motion developed. It is initially located at 73.5° magnetic latitude and then changes to 77° magnetic latitude a few minutes later. A region of dayside density, represented by the shaded area of Fig. 14c, is confined by two regions of low density, one poleward and another equatorward. After the region of dayside density is isolated from the rest of the oval densities, it will be carried by the antisunward plasma convection and enter the polar cap, thus initiating its transit toward the nightside of the polar cap.

Whalen (1989) presented number densities measured during the IGY, and characterized the daytime F layer trough under conditions of solar maximum, winter solstice. He postulated that the afternoon trough is generally continuous and stationary for a duration of many hours in a magnetic latitude/magnetic local time coordinate system. We have found a density depletion located between 73° and 77° magnetic latitude that forms and persists after B_z turns south containing some characteristics very similar to the trough described by Whalen (1989). In addition, we have confirmed that it is collocated with channels containing large flows (or LPJs) that extended for thousands of kilometers (Fig. 12e–g). The SuperDARN radars complete a scan every two min and this high resolution data has revealed a new important feature which is instrumental for the formation of the polar cap patches. There exists a phase motion of the LPJ which occurs on a time scale of 10–20 min. This cyclical motion of the LPJ may create the sequence of patches that are commonly detected within the polar cap (Buchau *et al.*, 1983).

6 Conclusions

This study has led to the following conclusions:

1. The Greenland chain of magnetometers in conjunction with the Sondrestrom and Stokkseyri radars

observed the transit of a train of vortices moving eastward across Greenland. Up to six vortices were identified in the magnetometer data. They were moving with a velocity equal to 5.7 km/s.

2. The Sondrestrom ISR confirmed the formation of a density depletion closely collocated with a region where very intense equivalent plasma drifts were seen 2 min earlier. The plasma erosion was caused by an enhancement of the T_i dependent recombination rate of O^+ augmented by Joule frictional heat. We speculate that the circular motion of the plasma inside the vortex may create an elliptical torus of reduced density. This region of low density may convect toward and across the polar cap following the typical B_z south convection pattern which dominated during the observations.
3. The EISCAT, the Sondrestrom, and the SuperDARN radars detected the width, longitudinal extension, and temporal evolution of a large plasma jet that appeared in the dayside sector of the dusk cell a few minutes after the TCVs were extinct. The LPJs were not stationary. They moved poleward, faded, and then reappeared in a matter of minutes.
4. A factor of 4 density depletion and ion temperatures above 4000 K were seen by the Sondrestrom ISR sometimes coinciding with the location of the LPJ.
5. The latitudinal poleward motion of the LPJ created an elongated density structure bounded by two regions of low-density plasma. This almost isolated density structure is seen in Fig. 10d and was scanned by the Sondrestrom radar at 1542 UT. Two regions, indicated by arrows in Fig. 10d, were previously eroded; however, at different times by two LPJs located at different latitudes. Important contributors to the formation of the regions of low density are the time-history of the plasma flow and the gradient in the background daytime ionosphere.
6. Another poleward motion of the LPJ was observed 18 min later, suggesting that this mechanism of patch formation may indeed produce a sequence of density features separated by 10–20 min.

Acknowledgements. We thank Peter Stauning of the Danish Meteorological Institute for making the magnetometer data available for this study, J. Kelly and M. McCready for providing the Sondrestrom radar data in raw format, R.P. Lin for providing us the WIND 3DP plasma observations and K. Fukui for drafting Fig. 13 and 14. We acknowledge the valuable effort provided by P. Knoop of the University of Michigan for installing the UARC system at the EISCAT site, and T. Pedersen of USU for traveling to Sondrestrom. The work at Boston College was partially supported by NSF grants INT-9603362, ATM-9404088, and ATM-9613925, and by Air Force Research Laboratory contracts F19628-97-C-0094, and in Toulouse under CNRS Grant 97N92/0157. JVR was supported during the February 1996 campaign by a National Research Council-AFOSR Research Associateship and by travel funds from the Phillips Laboratory Geophysics Directorate. The analysis of the SuperDARN data was supported by NSF Grant ATM-9502993. Support for the operation of the Super DARN radars used in this study was provided by funding agencies in Canada, France, the UK, and the USA. We thank the Danish Commission for Scientific Research

in Greenland for permission to conduct ground experiments at Sondrestrom under continuing project A16-91. EISCAT is an International Scientific Association supported by the Research Councils of Finland (SA), France (CNRS), Germany (MPG), Japan (NIPR), Norway (NAVF), Sweden (NFR) and the United Kingdom (PPARC).

The Editor in Chief thanks J. Scali for his help in evaluating this paper.

References

- Baker, K. B., and S. Wing, A new magnetic coordinate system for conjugate studies of high latitudes, *J. Geophys. Res.*, **94**, 9139, 1989.
- Basu, S., Su. Basu, J. J. Sojka, R. W. Schunk, and E. MacKenzie, Macroscale modeling and mesoscale observations of plasma density structures in the polar cap, *Geophys. Res. Lett.*, **22**, 881, 1995.
- Berkey, T., L. L. Cogger, S. Ismail, and Y. Kamidi, Evidence for a correlation between sun-aligned arcs and the interplanetary magnetic field direction, *Geophys. Res. Lett.*, **3**, 145, 1976.
- Buchau, J., and B. W. Reinisch, Electron density structures in the polar F region, *Adv. Space Res.*, **11**, (10)29, 1991.
- Buchau, J., B. W. Reinisch, E. J. Weber, and J. G. Moore, Structure and dynamics of the winter polar cap F region, *Radio Sci.*, **18**, 995, 1983.
- Buchau, J., E. J. Weber, D. N. Anderson, H. C. Carlson, Jr., J. G. Moore, B. W. Reinisch, and R. C. Livingston, Ionospheric structures in the polar cap: their origin and relation to 250-MHz scintillation, *Radio Sci.*, **20**, 325, 1985.
- Clauer, C. R., and A. J. Ridley, Ionospheric observations of magnetospheric low-latitude boundary layer waves on August 4, 1991, *J. Geophys. Res.*, **100**, 21873, 1995.
- Cowley, S. W. H., J. P. Morelli, and M. Lockwood, Dependence of convection flows and particle precipitation in the high-latitude dayside ionosphere on the *X* and *Y* components of the interplanetary magnetic field, *J. Geophys. Res.*, **96**, 5557, 1991.
- Crooker, N. U., G. L. Siscoe, C. T. Russell, and E. J. Smith, Factors controlling degree of correlation between ISEE 1 and ISEE 3 interplanetary magnetic field measurements, *J. Geophys. Res.*, **87**, 2224, 1982.
- Crowley, G., Critical review on ionospheric patches and blobs, in *The Review of Radio Science 1992–1996*, Oxford University Press, 1996.
- de la Beaujardiere, O., J. D. Craven, V. B. Wickwar, G. Candal, J. M. Holt, L. A. Frank, L. H. Brace, D. S. Evans, and J. D. Winningham, Universal time dependence of nighttime F region densities at high latitudes, *J. Geophys. Res.*, **90**, 4319, 1985.
- Doe, R. A., M. Mendillo, J. F. Vickrey, L. Zanetti, and R. Eastes, Observations of nightside auroral cavities, *J. Geophys. Res.*, **98**, 293, 1993.
- Doe, R. A., J. F. Vickrey, and M. Mendillo, Electrodynamical model for the formation of auroral ionospheric cavities, *J. Geophys. Res.*, **100**, 9683, 1995.
- Foster, J. C., and J. R. Doupnik, Plasma convection in the vicinity of the dayside cleft, *J. Geophys. Res.*, **89**, 9107, 1984.
- Friis-Christensen, E., M. A. McHenry, C. R. Clauer, and S. Vennerstrom, Ionospheric traveling convection vortices observed near the polar cleft: a triggered response to sudden changes in the solar wind, *Geophys. Res. Lett.*, **15**, 253, 1988.
- Fukui, K., J. Buchau, and C. E. Valladares, Convection of polar cap patches observed at Qaanaaq, Greenland during the winter of 1989–1990, *Radio Sci.*, **29**, 231, 1994.
- Greenwald, R. A., *et al.*, DARN/SuperDARN: a global view of the dynamics of high-latitude convection, *Space Sci. Rev.*, **71**, 761, 1995.
- Heelis, R. A., J. K. Lowell, and R. W. Spiro, A model of the high-latitude ionospheric convection pattern, *J. Geophys. Res.*, **87**, 6339, 1982.
- Hill, J. R., Sudden enhancements of F layer ionization in polar regions, *J. Atmos. Sci.*, **20**, 492, 1963.
- Ismail, S., D. D. Wallis, and L. L. Cogger, Characteristics of polar cap sun-aligned arcs, *J. Geophys. Res.*, **82**, 4741, 1977.
- Kelly, J. D., and J. F. Vickrey, F region ionospheric structure associated with antisunward flow near the dayside cusp, *Geophys. Res. Lett.*, **11**, 907, 1984.
- Kelly, T. J., N. U. Crooker, G. L. Siscoe, C. T. Russell, and E. J. Smith, On the use of a sunward libration-point-orbiting spacecraft as an interplanetary magnetic field monitor for magnetospheric studies, *J. Geophys. Res.*, **91**, 5629, 1986.
- Lassen, K., On the classification of high latitude auroras, *Geophys. Publ.*, **29**, 87, 1972.
- Lockwood, M., P. E. Sandholt, S. W. H. Cowley, and T. Oguti, Interplanetary magnetic field control of dayside auroral activity and the transfer of momentum across the dayside magnetopause, *Planet. Space Sci.*, **11**, 1347, 1989.
- Lockwood, M., P. E. Sandholt, A. D. Farmer, S. W. H. Cowley, B. Lybekk, and V. N. Davda, Auroral and plasma flow transients at magnetic noon, *Planet. Space Sci.*, **38**, 973, 1990.
- McHenry, M. A., C. R. Clauer, and E. Friis-Christensen, Relationship of solar wind parameters to continuous dayside, high latitude, traveling ionospheric vortices, *J. Geophys. Res.*, **95**, 15007, 1990.
- Rodger, A. S., and A. C. Graham, Diurnal and seasonal occurrence of polar cap patches, *Ann. Geophysicae*, **14**, 533, 1996.
- Rodger, A. S., M. Pinnock, J. R. Dudeney, K. B. Baker, and R. A. Greenwald, A new mechanism for polar patch formation, *J. Geophys. Res.*, **99**, 6425, 1994.
- Ruohoniemi, J. M., R. A. Greenwald, K. B. Baker, J.-P. Villain, and M. A. McCready, Drift motions of small-scale irregularities in the high latitude F-region: an experimental comparison with plasma drift motions, *J. Geophys. Res.*, **92**, 4553, 1987.
- Sandholt, P. E., M. Lockwood, T. Oguti, S. W. H. Cowley, K. S. C. Freeman, B. Lybekk, A. Egeland, and D. M. Willis, Midday auroral breakup events and related energy and momentum transfer from the magnetosheath, *J. Geophys. Res.*, **95**, 1039, 1990.
- Sato, T., and G. F. Rourke, F-region enhancements in the Antarctic, *J. Geophys. Res.*, **69**, 4591, 1964.
- Sojka, J. J., M. D. Bowline, R. W. Schunk, D. T. Decker, C. E. Valladares, R. Sheehan, D. N. Anderson, and R. A. Heelis, Modeling polar cap F region patches using time varying convection, *Geophys. Res. Lett.*, **20**, 1783, 1993.
- Sojka, J. J., M. D. Bowline, and R. W. Schunk, Patches in the polar ionosphere: UT and seasonal dependence, *J. Geophys. Res.*, **99**, 14 959, 1994.
- Tsunoda, R. T., High-latitude F region irregularities: a review and synthesis, *Rev. Geophys.*, **26**, 719, 1988.
- Valladares, C. E., and H. C. Carlson Jr., The electrodynamic, thermal, and energetic character of intense sun-aligned arcs in the polar cap, *J. Geophys. Res.*, **96**, 1379, 1991.
- Valladares, C. E., Su. Basu, J. Buchau, and E. Friis-Christensen, Experimental evidence for the formation and entry of patches into the polar cap, *Radio Sci.*, **29**, 167, 1994.
- Valladares, C. E., D. T. Decker, R. Sheehan, and D. N. Anderson, Modeling the formation of polar cap patches using large plasma flows, *Radio Sci.*, **31**, 573, 1996.
- Valladares, C. E., D. T. Decker, R. Sheehan, D. N. Anderson, T. Bullett, and B. W. Reinisch, Formation of polar cap patches associated with north-to-south transitions of the interplanetary magnetic field, *J. Geophys. Res.*, in press, 1998.
- Whalen, J., The daytime F layer trough and its relation to ionospheric-magnetospheric convection, *J. Geophys. Res.*, **94**, 17169, 1989.
- Weber, E. J., and J. Buchau, Polar cap F-layer auroras, *Geophys. Res. Lett.*, **8**, 125, 1981.

Weber, E. J., J. A. Klobuchar, J. Buchau, H. C. Carlson, Jr., R. C. Livingston O. de la Beaujardiere, M. McCready, J. G. Moore, and G. J. Bishop, Polar cap F layer patches: structure and dynamics, *J. Geophys. Res.*, **91**, 121, 1986.

Weber, E. J., J. F. Vickrey, H. Gallagher, L. Weiss, C. J. Heinselman, R. A. Heelis, and M. C. Kelley, Coordinated radar and optical measurements of stable auroral arcs at the polar cap boundary, *J. Geophys. Res.*, **96**, 17 847, 1991.



PERGAMON

Journal of Atmospheric and Solar-Terrestrial Physics 61 (1999) 127–139

Journal of
ATMOSPHERIC AND
SOLAR-TERRESTRIAL
PHYSICS

Global aspects of plasma structures

Sunanda Basu^{a,*}, Cesar Valladares^b

^a Division of Atmospheric Sciences, National Science Foundation, 4201 Wilson Boulevard, Arlington VA 22230, U.S.A.

^b Institute for Scientific Research, Boston College, 140 Commonwealth Avenue, Chestnut Hill MA 02167, U.S.A.

Received 27 March 1998; received in revised form 24 August 1998; accepted 19 October 1998

Abstract

This topical review provides an overview of the progress achieved under Project 3.1, entitled 'Global Aspects of Plasma Structures (GAPS)' during the lifetime of the Solar Terrestrial Energy Program (STEP) from 1990–97. The mandate of the GAPS project covered middle and high latitude plasma structuring. However, given the requirement of limited length for this overview, only high latitude studies will be covered because of the particularly collaborative nature of the effort, made possible by an international program such as STEP. High latitude plasma structuring studies have progressed from joint experimental campaigns involving many locations and diagnostic techniques, and several focused international workshops that united experimenters and modelers. They have provided the groundwork for studying the macroscale (hundreds of km) and mesoscale (km and smaller) plasma structures at high latitudes under two distinct configurations of the interplanetary magnetic field (IMF).

When the IMF is directed southward, we observe macroscale, enhanced density structures known as 'patches.' We have documented much on their origin, modification by the electric field structure in the cusp, airglow signatures in the polar cap, interaction with the neutral medium, mesoscale structuring causing scintillations, convection through the polar cap, and eventual exit into the auroral oval. This has led to several modeling efforts, demonstrating patch formation via temporal changes in the large-scale flow configuration in the cusp. Additionally, we have successfully linked the climatology of the macroscale structure model to the mesoscale structure in the polar regions, an advance that may lead to truly predictive irregularity models for forecasting effects on communication and navigation systems during the upcoming solar maximum.

For northward IMF conditions, we have advanced our ability to simulate Sun-aligned arcs using a magnetosphere-ionosphere (M-I) coupled model, driven by realistic magnitudes of electric fields, conductivities and currents. The simulation has been enabled by utilizing an extensive ground-based optical database supported by satellite measurements of their morphological characteristics, including their dawn-dusk motion, dependence on IMF By, and propensity for multiple structuring. We soon expect significant advances resulting from several newly established powerful instruments in the northern and southern polar regions. © 1999 Elsevier Science Ltd. All rights reserved.

1. Introduction

The primary aim of the STEP project entitled, 'Global Aspects of Plasma Structures (GAPS)' was to study the source, evolution, and ultimate fate of macro- (~hundreds of km) and meso- (~km and smaller) scale structures at high and middle latitudes. This brief topical review confines our attention to high latitude structures only, a subject in which vigorous experimental efforts,

with close interactions between the experimental and modeling communities, has led to fairly substantial progress. The two aforementioned communities, primarily independent through the 1980s, have had much increased interaction through a series of three focused workshops held at Peaceful Valley, Colorado, in 1992, 1994 and 1997, and the subsequent special sections in *Radio Science* (1994, 1996, and the planned publication in 1998).

Experimentally, the two states of the polar ionosphere controlled by the IMF, and their association with high latitude plasma structures known as patches, blobs and F-region Sun-aligned arcs, were discovered in the 1980s (see reviews by Tsunoda, 1988; Carlson, 1994; Crowley,

* Corresponding author. Tel.: +1-703-306-1529.

E-mail address: sbasu@nsf.gov. (S. Basu)

1996; and Zhu et al., 1997, and references therein). Tremendous progress in the past five years or so has been enabled by the activities of GAPS, and its National Science Foundation Coupling Energetics and Dynamics of Atmospheric Regions (CEDAR) Program counterpart, known as the High Latitude Plasma Structure (HLPS) Group. This was accomplished by attracting a critical mass of international scientists with diverse interests and backgrounds. As Crowley (1996) aptly states, such research was previously hampered, "...because it required continuous detailed measurements over the enormous area within and around the polar cap. This period saw the maturing of a comprehensive instrument network, capable of making many of the necessary measurements with high temporal and spatial resolution. Current observations are also well supported by the modeling efforts, which have blossomed during the last few years, and which are able to qualitatively reproduce many of the observed features."

This review covers the most recent advances in our understanding of plasma structuring and electrodynamics under (i) southward IMF conditions, (ii) a transition state from southward to northward IMF and (iii) northward IMF conditions. Most of the results on which this review is based (Sojka, 1998) were presented and discussed at the third Peaceful Valley Workshop held in June, 1997.

2. Plasma structuring under southward IMF

2.1. Patch morphology and modeling

The new element in patch studies, originally started in the early 1980s near Thule, Greenland, by Weber et al. (1984), is the availability of satellite- and ground-based morphological data from the southern hemisphere (SH) in addition to extensive northern hemisphere (NH) data published earlier (Crowley, 1996, and references therein). The SH morphology is expected to be different because of the greater offset of the magnetic pole from the geographic pole: 14.5° in the SH as compared to 11° in the NH.

Coley and Heelis (1998a) have studied the patch morphology, based on the Dynamics Explorer-2 (DE-2) satellite F-region ion-density data, for both the NH and SH. They developed an algorithm to identify enhancements in satellite derived F region ion density measurements, and detected patches based on the horizontal scale size of the enhancement (≥ 100 km but smaller than 2000 km), the increase in ion density over background ($\geq 100\%$), and the density gradients on the edges of the enhancement ($\geq 40\%$ density increase over 140 km) (Coley and Heelis, 1995). The data base of patches from DE-2 covers the relatively high sunspot period of August 1981–February 1983, when 450 patches were observed in

the altitude range of 225–600 km, evenly split between the NH and SH.

They next examined the occurrence frequency of ionization patches as a function of IMF, season and UT. Figure 1 shows a contour plot of the occurrence frequency of polar patches from DE-2 data for the NH during the IMF B_z southward conditions. The units on the contour lines are the number of patches observed per h of spacecraft observations above 75° invariant latitude. Although patches tend to occur in a four-month wide band, the occurrence probability maximizes during the winter solstice in the broad time interval between 12 and 22 h UT, when between 4–5 patches are seen per h. This is consistent with ground-based observations (Buchau et al., 1985; Basu et al., 1995) and with models in which ionospheric dayside plasma is drawn into the polar cap when the cusp region is near or just equatorward of the dayside terminator (Sojka et al., 1994a).

The corresponding plot for the SH is presented in Fig. 2. Again, patches are seen to occur in a broad band seasonally centered on the winter solstice (note change in seasonal axis), as expected. Similarly to the NH, the patches are distributed from about 10–22 UT, with maximum at about 1230 UT, and another broad maximum around 1900–2200 UT. The maximum occurrence frequency around 1230 UT is $\sim 10 \text{ h}^{-1}$, which is twice as large as the secondary maximum in the SH at the later UT, as well as twice the peak occurrence seen in the NH. In contrast to the NH, where patch formation tends to maximize when the cusp is near its most dayward location around 1700 UT, we note from Fig. 2 that, in the SH, when the cusp is at its most sunlit location at about 0300 UT, a region of minimum patch formation is observed. A possible reason for this is given at the end of this section.

Other recent observations of patches using ground-based HF radars have been made from Halley Bay in Antarctica (Rodger and Graham, 1996). Polar patches have a very characteristic pattern on backscatter power display at HF frequencies; they are seen to separate from the poleward edge of a strong scattering region, which often has the characteristic of the cusp (Baker et al., 1995). The diurnal variation in the occurrence of patches shows a broad, rather flat peak between 12 and 18 UT. Considering the different techniques involved, these statistics are not too dissimilar from the in situ SH morphology shown in Fig. 2.

2.2. Patch generation mechanisms

Sojka et al. (1994a) have simulated the seasonal and UT dependencies of patches in the northern polar ionosphere by using the Utah State University time dependent ionospheric model (TDIM). Patch formation is achieved by changing the plasma convection pattern from A to DE, described by Heppner and Maynard (1987), in

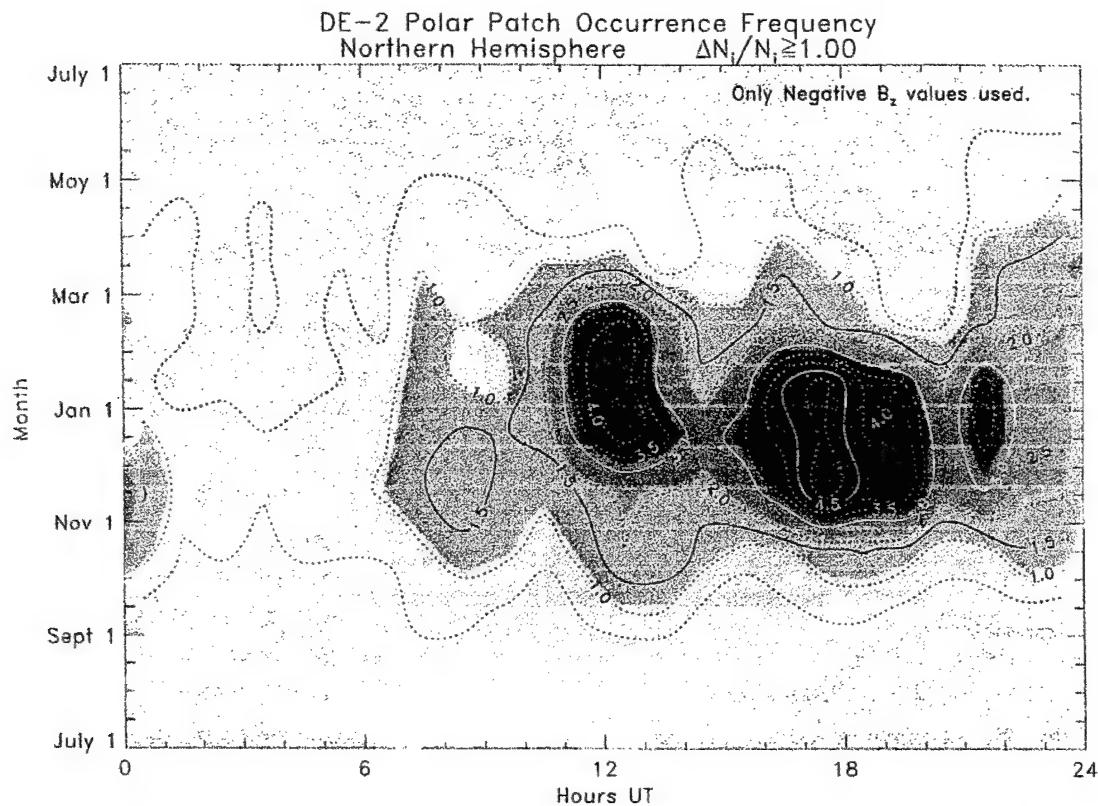


Fig. 1. Contour plot of the occurrence frequency of polar patches as measured by DE 2 in the northern hemisphere vs UT and month of the year when the z component of the IMF is negative. The units on the contour lines are the number of patches observed per h of spacecraft observation above 75 ILAT (from Coley and Heelis, 1998a).

response to temporal changes in the IMF B_z component during periods of southward IMF. This mechanism redirects the plasma flow from the dayside high-density region, which is the source of the tongue of ionization (TOI) density feature, through the throat and leads to patches, rather than a continuous TOI. The model predicts that the patches are absent at winter solstice (NH) between 0800 and 1200 UT, and that they have their largest seasonal intensity also at winter solstice between 2000 and 2400 UT, as shown in their Plate 1. The corresponding situation for the SH is shown in Fig. 3, which presents snapshots of $N_m F_2$ in the SH in mid-winter (day 180), at 2-h UT intervals, starting at the top left with 01, 03, 05 UT, followed on the next row with 07 UT, etc. (J.J. Sojka, private communication, 1998). The color key shows the electron density (on a linear scale) in cm^{-3} . We note that, between 03–05 UT, the cusp is mostly sunlit and high densities are present throughout the polar cap. A few hours later (09–11 UT), the TOI is still dense, while the background density level is reduced. This is the time when the largest TOI to background ratios should be observed. The DE-2 data show the largest patch occur-

rence somewhat later at 1230 UT. However, it is very interesting to note the ramifications of the much larger offset of 14.5° in the SH between the geographic and magnetic axes. This larger offset puts the entire polar cap in sunlight in the 03–05 UT time frame, when the background ion density goes up and it requires a larger absolute density enhancement to provide the contrast to qualify as an ionization patch. In the DE-2 data, this is reflected in a background density that maximizes at $\sim 2.0 \times 10^5 \text{ cm}^{-3}$ at around 0300 UT in the SH polar cap, when it is in its most dayward location. At around 1900 UT the background density minimizes at $\sim 1 \times 10^5 \text{ cm}^{-3}$ (Coley and Heelis, 1998a). It may be noted from Fig. 3, that between 15–19 UT the TOI seems to be replaced by a negative TOI (purple color), when the convection through the cusp is seen to bring in very low densities from the dayside trough region. It is interesting to speculate whether this negative TOI shows up as ‘patches’ in the DE-2 data around 1900–2200 UT, since patch identification is based on relative difference in density between contiguous regions. Obviously, much careful work needs to be done in the SH to bring model and

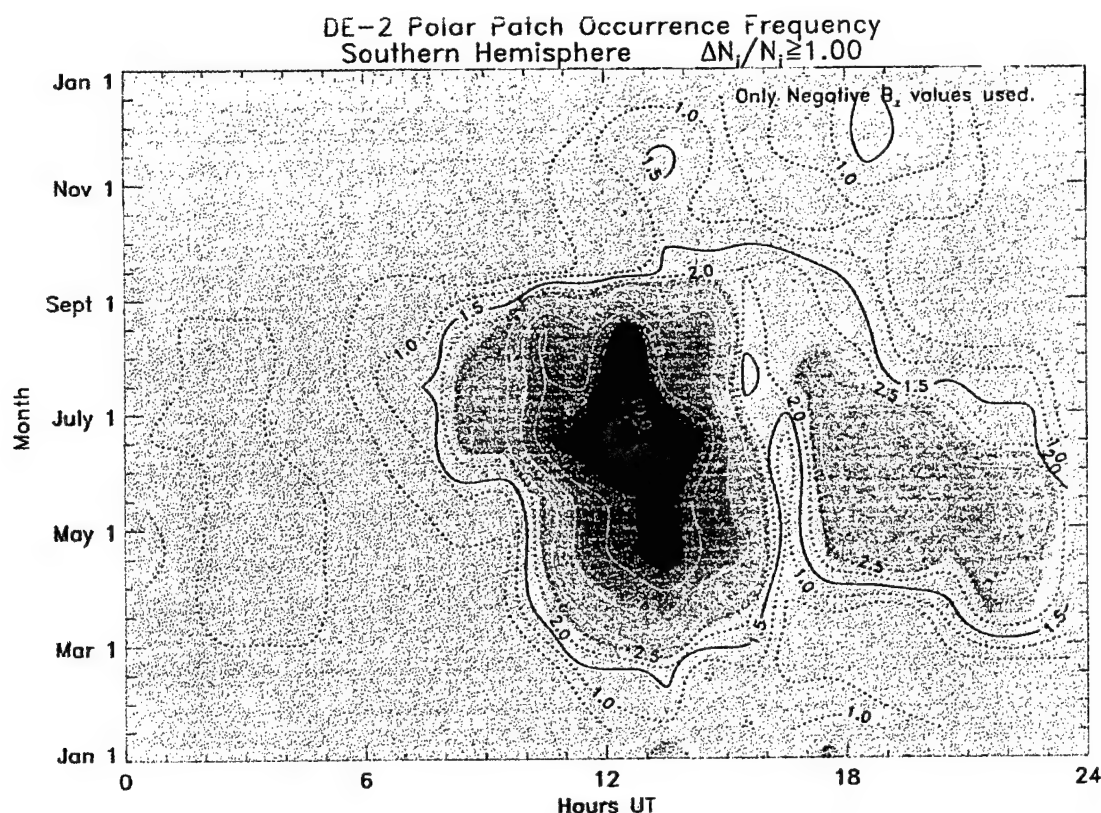


Fig. 2. Contour plot of the occurrence frequency of polar patches as measured by DE 2 in the southern hemisphere vs UT and month of the year when the z component of the IMF is negative. The units on the contour lines are the number of patches observed per h of spacecraft observation above 75 ILAT (from Coley and Heelis, 1998a).

observations into quantitative agreement, including a consideration of different convection pattern vis-à-vis the terminator boundary. This initial attempt at a comparison between model and observations is to make the reader aware that conjugacy arguments using NH morphology will not suffice for a description of SH patch occurrence because of the larger offset between the geographic and magnetic axes.

We presented above one mechanism by which patch formation is achieved, namely, by changing the plasma convection pattern in response to the IMF B_z component during periods of southward B_z (Sojka et al., 1994a). Several other mechanisms have been suggested to explain the formation of polar cap patches and their complicit detachment from the auroral oval (cf reviews by Tsunoda (1988) and Crowley (1996) for a general discussion of formation mechanisms). We briefly further substantiate one mechanism, namely the role of large plasma flows in the formation of patches (Rodger et al., 1994; Valladares et al., 1994a). This is primarily because the recent experiment done by Valladares et al. (1998a) shows the efficacy of a coordinated, international effort, in which the fields

of view of the various HF SuperDARN radars and the EISCAT and Sondrestrom incoherent scatter radars, and several magnetometer arrays, covered half the polar cap, poleward of 60°N , as shown in Fig. 4. With this extensive array of instrumentation, these authors could prove that intense plasma jets containing line-of-sight velocities of $1\text{--}1.5\text{ km s}^{-1}$ had large longitudinal extension ($>1000\text{ km}$), and $200\text{--}300\text{ km}$ latitudinal width, and were found to be co-located with decreased number densities. Such plasma density reductions were due to an enhancement in the O^+ recombination related to an elevated ion temperature, caused by frictional heating. Systematic changes in the latitudinal location and intensity of these large plasma jets create discrete regions of decreased density, detached from the rest of the oval density, which show up as patches in the polar cap.

2.3. Small-scale structuring in patches

A recent study has shown a fairly remarkable similarity between polar cap scintillation observations caused by mesoscale irregularities and the USU TDIM predictions

NmF₂ Southern Hemisphere day 180

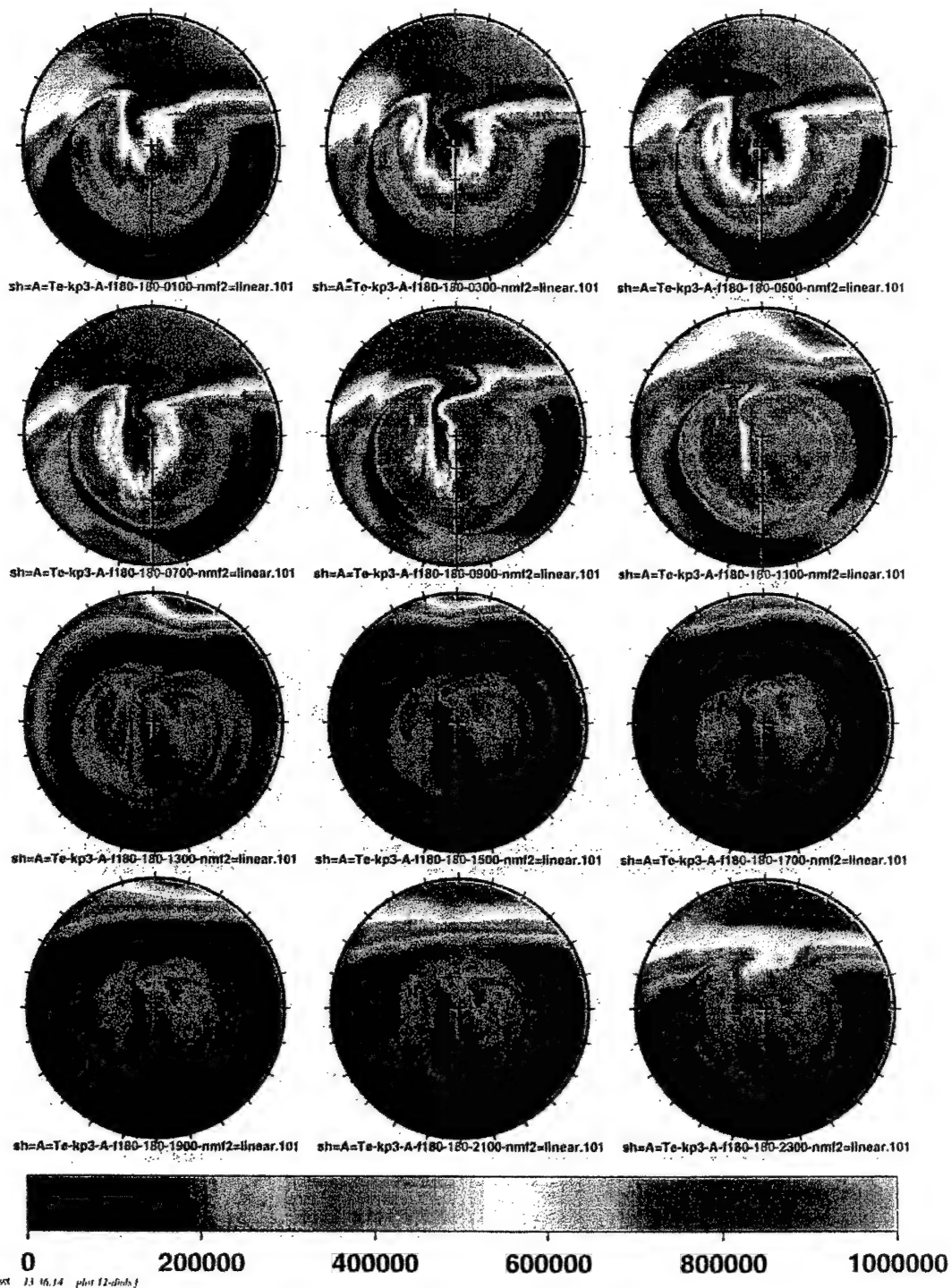


Fig. 3. Snapshots of $N_m F_2$ in the southern hemisphere in mid-winter (day 180). Snapshots are at 2 h UT intervals; top row left to right are 1, 3, 5 UT, then the next row are 7, 9, 11 UT, etc. The patches were generated by using the TDIM and changing the convection between A and DE patterns of Heppner and Maynard (1987). Color key is in (linear) electron density (cm^{-3}). (Simulation made available by J. J. Sojka, 1998).

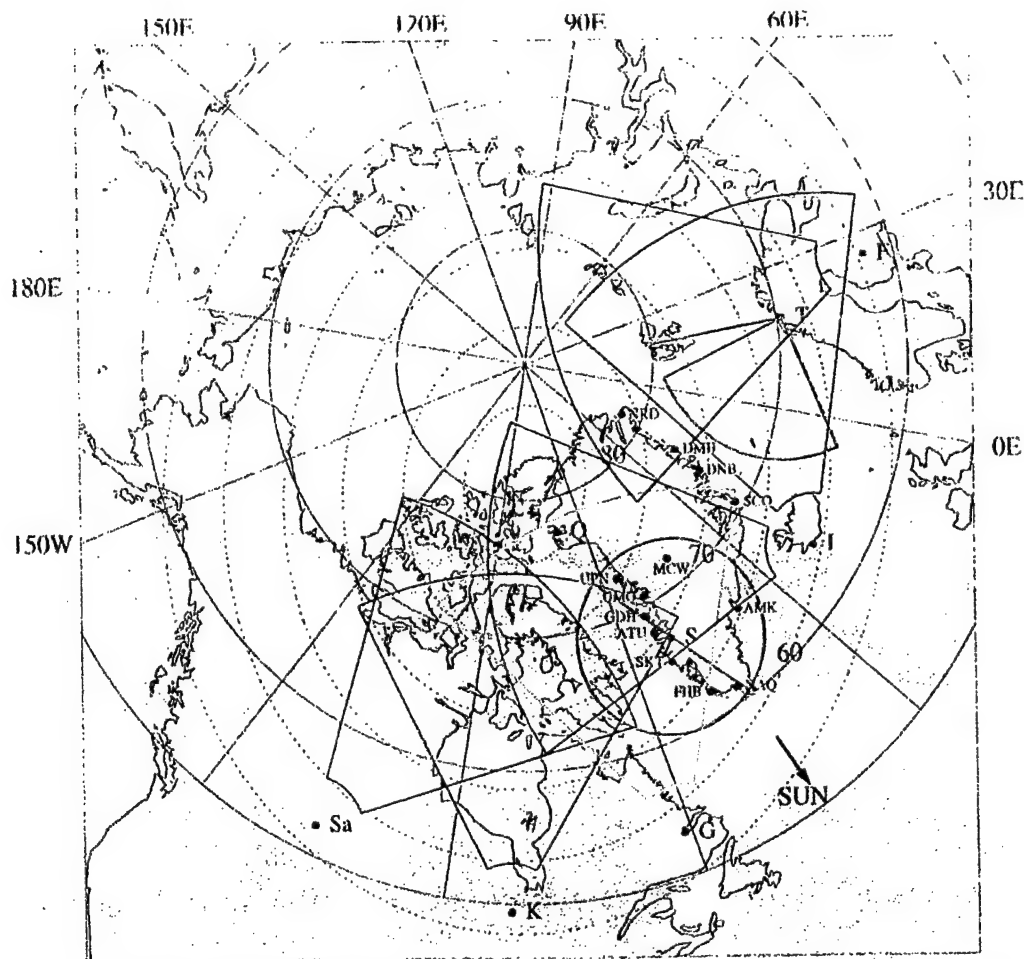


Fig. 4. Illustration of the different radar sites and their approximate fields of view (FOV) located at high latitudes. The red traces delineate the areas probed by the SuperDARN radars that were operational during the experiment. The orange contour represents the FOV of the Goose Bay radar. The antenna scanning configuration of the incoherent scatter radars at Sondrestrom and EISCAT used on 18 February 1996 are displayed in green. The large black dots, distributed across Greenland, indicate the locations where magnetometers of the Greenland chain are placed (from Valladares et al., 1998a).

of mesoscale structures—namely polar cap patches—under southward IMF B_z conditions (Basu et al., 1995). This statistical result, indicating the coexistence of macro- and mesoscale structures, implies that mesoscale structures causing scintillations of satellite signals develop at the edges of polar cap patches through the gradient drift instability process and permeate the entire patch. This result had been demonstrated earlier by Basu et al. (1990a) from a case study of DE-2 satellite in situ measurements. Indeed, the growth time of the gradient drift instability (Ossakow et al., 1978) at the edges of polar cap patches can be shown to be of the order of tens of minutes if we assume modeled values of electron density gradients as being tens of kilometers and consider the observed anti-sunward convection of several hundred

m s^{-1} . The global scale growth rate of the instability has also been modeled from TDIM, which indicates that growth rates can be extremely fast in the case of time varying electric fields (Sojka et al., 1998). However, fast growth times of all irregularity scales predicted by two-dimensional theories imply disintegration of the patches. This is contrary to observations and simulations, which show that patches retain their integrity as they convect from the dayside cusp towards the nightside, and may indeed evolve into boundary blobs, in the auroral oval (Basu et al., 1994; Pedersen et al., 1998; Anderson et al., 1996). This topic has recently been investigated further by Guzdar et al. (1998), who have performed nonlinear three dimensional simulations of gradient drift instability and showed that the effects of dynamics parallel to the

magnetic field stabilize macroscales (i.e., maintains patch integrity) and the non-linear state is dominated by meso-scale structures. These studies provide a promising foundation for the modeling of polar cap patches, their trajectories, and associated irregularities that may impact HF communications and cause scintillation-induced data losses in satellite communication systems, and errors in GPS navigation systems, particularly during the upcoming solar maximum period.

Recently, a few observational results of irregularity characteristics in the polar regions have been presented. Based on scintillation observations, Erukhimov et al. (1996) concluded that the anisotropy of the irregularities within an auroral scintillation patch varies with their scale lengths such that these are sheetlike at large scales (> 1 km) and rodlike at smaller scales. A statistical study of kilometer scale irregularities, based on DE-2 measurements, shows their significant summer/winter variation, and that the strongest irregularity amplitude and velocity turbulence occur in the cusp region (Kivanc and Heelis, 1997). Observations of scintillations of VHF signals from polar beacon satellites show unique k -spectrum characteristics of scintillations in the ionospheric cusp, suggesting that electron density irregularities are associated with velocity turbulence (Basu et al., 1998). These authors also show that Global Positioning System receivers barely detected scintillations during the solar minimum, but were able to record phase variations associated with relatively large scale (tens of km) density structures.

3. Transition state from IMF South to North

Most researchers in the field of high latitude plasma structuring tend to think of the polar atmosphere as alternating between two states depending on the sign of IMF B_z as depicted in Plate 1 of Carlson (1994). However, optical and radio instruments co-located at Qaanaaq, Greenland ($\Lambda = 86^\circ$) deep within the NH polar cap have been utilized to identify simultaneous polar cap patches and Sun-aligned arcs in a single common 1000 km field-of-view. This is an amalgam of the two states shown in Carlson's diagram. In particular, Valladares et al. (1998b) found a polar cap transition state from a patch-dominated to an arc-dominated pattern in 19 cases studied during 1989–92. The temporal evolution of 630 nm images seen within the polar cap provide valuable information for investigating the time delays that are required for the establishment of the new pattern of plasma velocity and associated macroscale plasma density structuring. The digisonde, also located at Qaanaaq, is used to confirm that the optical patches correspond to actual enhancements in the number density and a simultaneous lowering of the $h_m F_2$ values. These two factors increase the capability of the imager to differentiate between patches and the background airglow.

The observed coexistence of patches and arcs is due to a slower response of the patches in exiting the polar cap, as compared to the relatively sudden appearance of polar cap arcs, presumably driven by dayside reconnection between the IMF and open flux tubes drawn initially equatorward toward the cusp. The slow buildup and decay of patches also explains why arcs and patches are seen by the imager to co-exist for rapid B_z reversals only from South to North, not from North to South (even when arcs outlived a southward transition of the IMF for over 60 min). Detection of patches for B_z northward conditions has been reported by McEwen and Harris (1996) using optical techniques and by Coley and Heelis (1998b) using in situ density data.

4. Polar cap arcs

In the last eight years, new modern optical observatories have started operations in the high latitude regions of both hemispheres, providing more global views of the polar cap aurora. At the same time a satellite constellation, equipped with state-of-the-art instrumentation, is now able simultaneously to probe several regions in the solar wind, the magnetosphere, and the ionosphere. Satellites located at various distances from Earth (DMSP, Akebono, Polar, and Fast), transiting across the magnetosphere (Geotail), and embedded within the solar wind (IMP-8 and WIND), have opened up new avenues of research and promise to answer the most important questions related to polar cap arcs. This section reviews the most recent scientific achievements by the GAPS/HLPS community in this field. For a more complete treatise, we encourage the reader to consult the comprehensive review paper on polar cap arcs by Zhu et al. (1997).

4.1. IMF control of arc morphology

The early result about polar cap arcs being inherently a northward IMF phenomena was confirmed and extended using images from Qaanaaq, Greenland by Valladares et al. (1994b). The analysis of 150 polar cap arcs by these authors indicated that the arc occurrence decreased as the B_z component of the IMF became more negative. However, these ' B_z South arcs' were found to be formed during B_z northward periods and decayed in the succeeding 20–30 min after the IMF had turned southward. Examination of polar cap arcs from Vostok, Antarctica ($\Lambda = -83.5^\circ$) showed that the B_z and B_y IMF components produce a strong control on the distribution of the aurora inside of the polar cap (Troshichev and Gusev, 1994). An IMF 'garden hose' configuration (B_z and B_y of opposite sign) implied symmetrical auroral distribution at both morning or evening sectors of both N and S polar

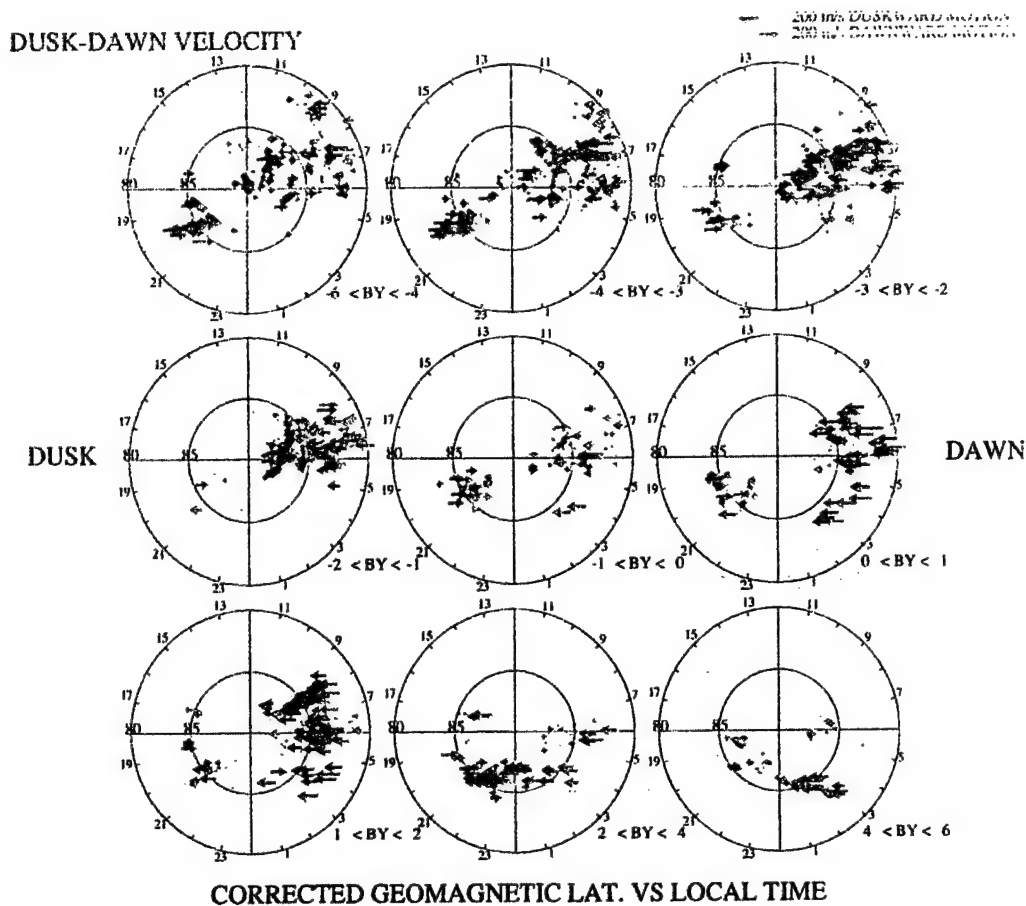


Fig. 5. Series of polar plots showing the location within the polar cap of the arc motion toward dawn (red) or toward dusk (blue). The size of the arrows is proportional to the value of the dawn-dusk arc velocity. Red arrows populate most of the polar cap for large and negative values of B_y . The number of red arrows decreases and becomes more restricted to the dusk side as B_y becomes less negative, and even positive. The blue arrows (duskward moving arcs) present an opposite behavior, as B_y becomes less negative and more positive, they expand and populate most of the polar cap (from Valladares et al., 1994b).

caps. During 'orthogonal garden hose' configuration (B_z and B_y of equal sign), polar cap arcs appeared only at either the evening or morning sector. Using the results previously published by Elphinstone et al. (1990), Troshichev and Gusev (1994) concluded that the B_y component defined the evening or morning sector of the polar cap in which polar cap arcs appeared. Arcs appeared in the evening sector of the N polar cap for B_y positive and in the morning sector for B_y negative. This B_y relationship was found to be opposite in the S polar cap.

Images from Qaanaaq were also used to study the relation of the dawn-dusk motion of polar cap arcs and the IMF B_z component. Figure 5 shows the results of the analysis of 1400 images. Each frame of Fig. 5 presents the arc velocities for different ranges of B_y . The arcs that have dawnward velocities are in red and the duskward moving arcs are shown as blue arrows. In the plot corresponding to $-6 < B_y < -4$ nT (upper left corner), the

arcs moving downward are located in the dusk hemisphere and cover a large part of the dawn hemisphere. They extend up to 82° (of latitude in the dawn hemisphere). The other subframes of Fig. 5 show that as B_y becomes more positive the population of dawnward moving arcs is greatly reduced in the dawn hemisphere; it is replaced by duskward moving arcs. Based on this, Valladares et al. (1994b) suggested that the direction of motion not only depends on the sign of B_y but also on the location of the arc within the polar cap. They suggested that the arcs move toward a boundary whose location depends on the magnitude of B_y . When B_y is equal to zero the boundary is located at the center of the polar cap and shifts towards dawn or dusk following the sign of B_y . A detailed analysis of the plasma velocity across three polar cap arcs demonstrated that the motion of the optical emissions was equal to the ionospheric flow, thus suggesting that the polar cap arcs move with

the ionospheric plasma (Gallagher et al., 1995). Consequently, the motion of the arc appeared to represent the motion of the flux tubes. Valladares et al. (1994b) explained their observations postulating that the arc motion (or flux tube motion) was due to the entrance of open flux tubes into the polar cap, producing a general displacement of the cells and consequently of the arcs which are embedded within the convection cells. The implicit assumption in this model is the role of magnetic merging as the main mechanism that powers the dynamics of the polar cap arcs.

In the last three years, a renewed interest has emerged in the understanding of the manner in which transpolar arcs, theta (Θ) and 'horse collar' auroras are formed and how they evolve inside the polar cap. Newell and Meng (1995) used data from the Polar Bear, DMSP and IMP-8 satellites to imply that transpolar auroras can originate near the auroral oval by the entrance of flux tubes equatorward of the arcs. They argued that a transpolar arc was produced when a timely North to South flip of the B_z component of the IMF occurred after a prolonged period of B_z northward condition. This idea has been disputed by Cumnock et al. (1997), who have used images from the DE-1 satellite to demonstrate that the appearance of theta auroras is correlated with changes of the IMF B_z component and with steady values of B_z . Cumnock et al. (1997) showed that Θ auroras are formed both from an expanded duskside region when B_z changed from positive to negative and from a dawnside region when B_z changed from negative to positive.

In contrast, the more numerous weak F-region polar cap arcs seem to occur under different types of conditions. Some of them occur spontaneously, appearing well inside the polar cap and embedded within regions of sheared plasma flows. Other arcs, situated near the polar cap boundary, develop during poleward contractions of the polar convection pattern. Berg et al. (1994) used data from a rocket launched from Sondrestrom, and ground-based instrumentation, to conclude that two auroral arcs were injected into the polar cap at a velocity on the order of a few km s^{-1} . Both arcs were initially located inside the auroral oval and moved into regions of sunward flow during times of a decaying magnetospheric condition. It was implied that the polar flow had adjusted to a lower energy state and that this readjustment was accompanied by polar cap arcs.

4.2. Magnetospheric configuration associated with polar cap arcs

At the present time there is no unified consensus about the magnetospheric region from which the polar cap arcs map. The prevalent view is that the weak polar cap F-region arcs map from open field lines threading the magnetosheath, and the most energetic arcs (transpolar and theta auroras) are on closed field lines mapping to the

low latitude boundary layer (LLBL) or even the plasma sheet (PS). Rodriguez et al. (1997) addressed this issue from a different point of view, and examined the decay time and direction of arc decay for 10 polar cap arcs. All these arcs decayed in an antisunward manner. Eight of the arcs decayed between 15–30 min after the IMF B_z component had switched from positive to negative. Two of the arcs decayed 60–65 min after the IMF turned southward. The mechanism which accounts for the anti-sunward decay of the eight arcs with a short time delay of 15–30 min after B_z becomes negative is the convection of new open flux tubes from the cusp to the center of the polar cap due to dayside merging. The other 2 arcs (time delays = 60–65 min) were found to be on closed field lines, probably mapping to the distant LLBL. Rodriguez et al. (1997) used the mapping considerations of Birn et al. (1991) and concluded that the topology and dynamics of the two arcs with long delays could be explained if the arcs mapped to a region extending from the plasma sheet to the magnetosheath in the dawnside of the equatorial plane that drifts antisunward, and then decays toward the plasma sheet. This concept is illustrated in Fig. 6. Here, it is evident that the further downstream the arcs map to the distant LLBL, the closer the arcs lie to the center of the polar cap, and the deeper into the LLBL, the more the arcs extend into the nightside.

These types of studies, probably in association with in situ measurements in the magnetotail, are needed to decide between alternatives for mapping the polar cap arcs. Equally important is to find the source of the particles, momentum, and energy that drive the F-region polar cap arcs and the transpolar auroras. Observations of polar cap arcs using satellites placed at different altitudes will be able to elucidate the physical mechanism responsible for the entry of the precipitating charged particle population and then the acceleration mechanism along the field lines within the polar cap for northward IMF conditions.

4.3. Ionospheric measurements of polar cap arcs

Early observations of polar cap arcs demonstrated that the polar cap auroras were the optical signature of upward Birkeland currents and that the arcs were collocated with velocity shears or velocity gradients. These studies were extended and placed in a more quantitative framework when a rocket was launched into a polar cap Sun-aligned arc by Weber et al. (1989). Detailed information of the current system, the thermal, and energetic characteristics of an F-region polar cap arc was obtained by these authors. They found that the plasma flow was sunward along the arc and small and duskward across the arc. The duskward drift was in agreement with the duskward motion of the optical arc. Weber et al. (1989) concluded that the arc was drifting duskward under the influence of a driving electric field.

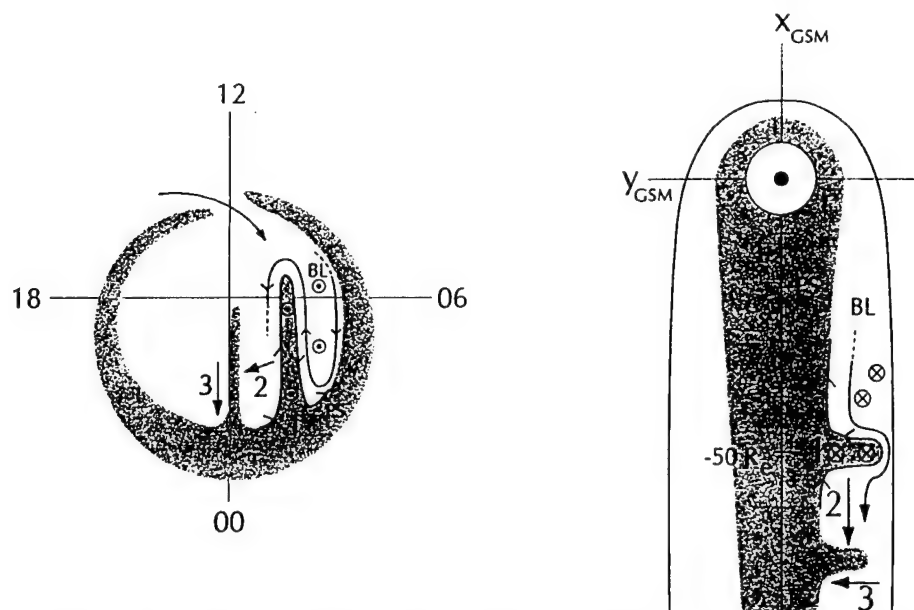


Fig. 6. Northern hemisphere polar cap motions (left) and possible mapping to motions in the equatorial plane of the distant tail flanks (right). Arrows indicate convection, dots (crosses) indicate upward (downward) field aligned currents, and BL and PS refer to (low latitude) boundary layer and plasma sheet. Dawnward flow into the polar cap due to dayside merging for $B_z > 0$ is one possible cause of duskward arc drift. A polar cap arc attached to the early morning oval (1) drifts duskward (2), then decays antisunward (3) after B_z turns negative. The conjugate behavior in the equatorial plane consists of an extension of the plasma sheet towards the magnetosheath that drifts antisunward, then retracts toward the center of the tail (from Rodriguez et al., 1997).

Valladares and Carlson (1991) used the Sondrestrom incoherent scatter radar to perform antenna scans across an energetic Sun-aligned arc. Strong electron temperature enhancements (> 2000 K) within the sheets of ionization due to charged particle precipitation were detected in the radar scans. Dawn-to-dusk decreases in the antisunward plasma flow and upward currents of order $1 \mu\text{Am}^{-2}$ were measured. The high velocity edge of the arc (dawnside) marked the location of strong Joule heating driven by downward Poynting flux. This electromagnetic energy was found to be larger than the kinetic energy deposited by the precipitating electrons.

Obara et al. (1993) used data from the Akebono satellite (1 Re altitude) to show that, for most arcs detected by the satellite, the region of particle precipitation coincided with regions of convergent electric fields. However, they found that sometimes a steep electric field convergence was located just at one side of the arc precipitation; in a few other cases no precipitation occurred in regions of convergent electric fields. It is possible that in these few cases the level of precipitating electrons was substantially lower and fell below the sensitivity threshold. This fact points out the need for using multiple diagnostics to understand the evolution of polar cap arcs fully.

Basu et al. (1990b) compared total electron content (TEC) and scintillation measurements associated with

polar cap arcs taken during two different phases of the solar cycle. The TEC increase was approximately three times larger in the high sunspot case as compared to the low sunspot event. This is an intriguing observation, which also implies that the particle precipitation during high sunspot conditions creates a much higher ionization level. The high level of scintillation was found to be accompanied by gradients in the plasma flow. This endorses the view that medium-scale irregularities are probably caused by the non-linear Kelvin–Helmholtz instability driven by sheared flows (Keskinen et al., 1988). Much work remains to be done on plasma structuring associated with Sun-aligned arcs. The planned Polar Cap Observatory (PCO) should help enormously in this respect. However, concurrent optical, frequency-agile-radar (FAR) and digisonde measurements have been started at the Early Polar Cap Observatory (EPCO) at Resolute Bay, Canada (Doe et al., 1997). This will allow polar cap arcs to be probed over a range of spatial scales bounded at large scales by the all-sky field of view (hundreds of km) and at small scales by the FAR transmitter wavelengths (tens of m).

4.4. Time dependent model of polar cap arcs

A time dependent model of the magnetosphere–ionosphere (M–I) coupling along a field line connected to a

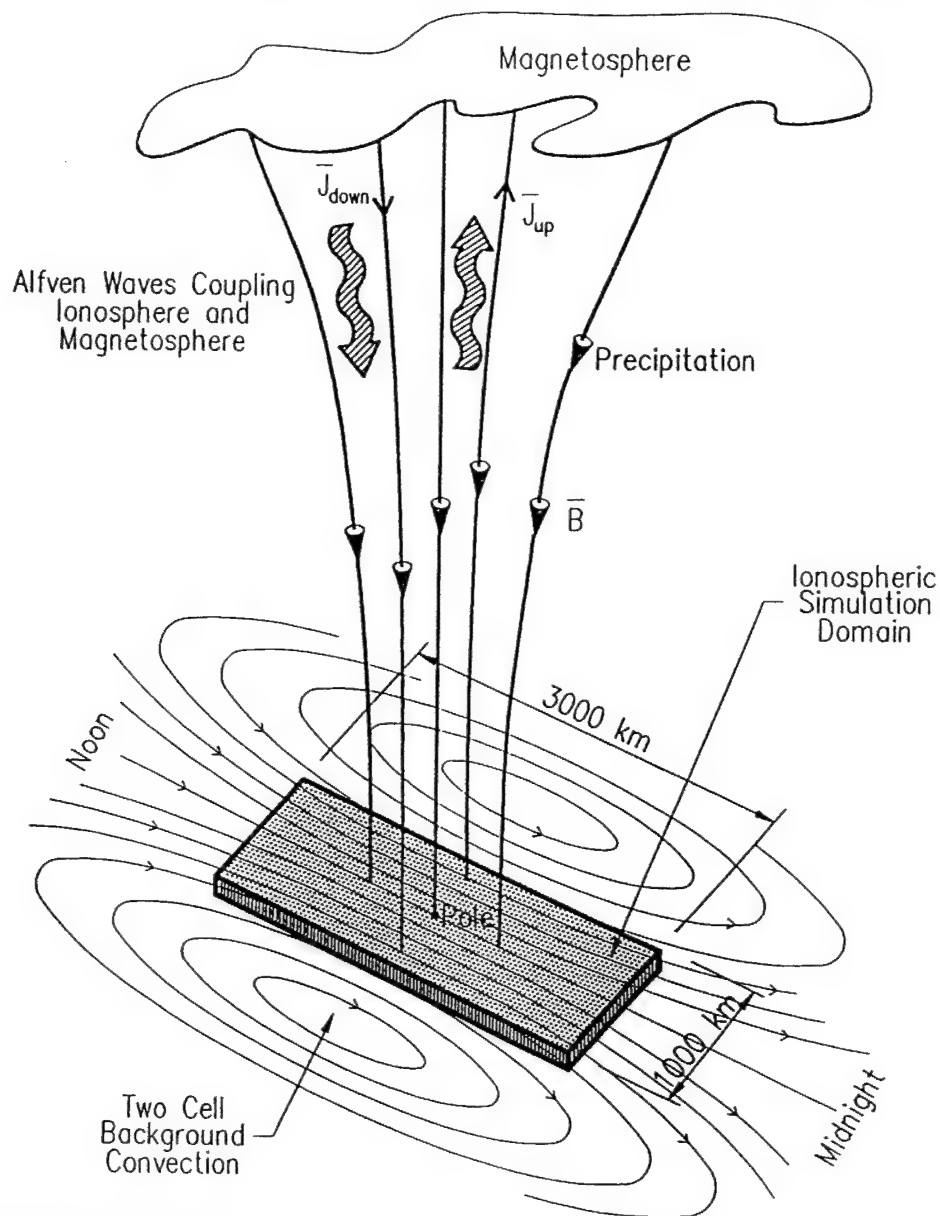


Fig. 7. A schematic diagram showing the geophysical framework of the polar cap arc model proposed by Zhu et al. (1993).

polar cap arc was developed by Zhu et al. (1993). Figure 7 shows a schematic diagram of the M-I framework of the polar cap model. A novel feature of this model is that the arc dynamics is not treated as a phenomenon merely controlled by the magnetosphere; instead the M-I coupled model considers the role of the ionosphere in reflecting Alfvén waves and the importance of changes in the ionospheric conductivity to launch secondary Alfvén waves toward the magnetosphere. The Zhu et al. (1993) model has made it possible to conduct, for the first time, a quantitative comparison between morphological par-

ameters of polar cap arcs defined by numerous GAP-S/HLPS campaigns and numerical results from a polar cap model. The time dependent model of polar cap arcs showed that multiple polar cap arcs were not formed by multiple structures in the magnetosphere. Instead, they were internally generated in the M-I system as a result of the self-consistent coupling. Sojka et al. (1994b) found that the number of multiple arcs depended on the magnitude of the large scale background convection electric field. The spacing between arcs was found to be a function of the hardness of the primary magnetospheric pre-

cipitation (Zhu et al., 1994). An independent corroboration of the validity of the time dependent M-I coupling model of polar cap arcs was carried out by Obara et al. (1996). These authors examined the energy spectra of electrons impinging on multiple polar cap arcs measured by the Akebono satellite and compared them with model predictions. Evidence was found that the harder precipitation led to a wider spacing of the multiple polar cap arcs.

In the next few years we should be able to use imagers, radars, and scintillation receivers, already located within the polar cap, to study how the electrodynamics evolves in time and how this varies as a function of the arc intensity, alignment, and their dawn-dusk motion. We should be able to determine how the arc electrodynamics adjusts itself to temporal changes of the 'global' polar cap convection. The deployment and completion of the network of Automatic Geophysical Observatory (AGO) stations in Antarctica (Doolittle, 1997) offers another great opportunity. This will allow a thorough investigation of the dynamics of transpolar arcs and, together with the UV images from the Polar satellite, the possibility to test different theories of the mapping properties of theta auroras and transpolar arcs. We should be able to discriminate between different models of polar cap arcs. Conjugate measurements of transpolar arcs with the AGO imagers in the SH and with Polar above the NH should be able to observe whether or not transpolar arcs expand from opposite sides (i.e. morning or evening sides) and move toward the other side of the polar caps in the two hemispheres. Models of polar cap convection for northward IMF, such as that of Reiff and Burch (1985), have predicted the formation of conjugate auroras in both polar caps but probably on different sides. After we are able to respond to this question and others about northward IMF magnetospheric topology, we will be one step closer to achieving a forecasting capability for the occurrence and development of polar cap arcs.

Acknowledgements

We thank our colleagues for making their results available to us in advance of publications. Sunanda Basu acknowledges the Independent Research and Development Program at NSF, that made her participation in the GAPS Project possible. The work at Boston College was partially supported by NSF grants INT-9603362, OPP-9708101, and by Air Force Research Laboratory contract F19628-97-C-0094. We thank Santimay Basu and Robert Robinson for their careful reading of the manuscript.

References

- Anderson, D.N., Decker, D.T., Valladares, C.E., 1996. Modeling boundary blobs using time varying convection. *Geophys. Res. Lett.* 23, 579.
- Baker, K.B., Dudeney, J.R., Greenwald, R.A., Pincock, M., Newell, P.T., Rodger, A.S., Mattin, N., Meng C.-I., 1995. HF radar signatures of the cusp and low-latitude boundary layer. *J. Geophys. Res.* 100, 7671.
- Basu, Su., Basu, S., MacKenzie, E., Coley, W.R., Sharber J.R., 1990a. Plasma structuring by the gradient drift instability at high latitudes and comparison with velocity shear driven processes. *J. Geophys. Res.* 95, 7799.
- Basu, Su., Basu, S., Weber, E.J., Bishop, G.J., 1990b. Plasma structuring in the polar cap. *J. Geomag. Geoelectr.* 42, 763.
- Basu, S., Basu, Su., Chaturvedi, P.K., Bryant, C.M., 1994. Irregularity structures in the cusp/cleft and polar cap regions. *Radio Sci.* 29, 195.
- Basu, S., Basu, Su., Sojka, J.J., Schunk, R.W., MacKenzie, E., 1995. Macroscale modeling and mesoscale observations of plasma density structures in the polar cap. *Geophys. Res. Lett.* 22, 881.
- Basu, S., Weber, E.J., Bullett, T.W., MacKenzie, E., Doherty, P., Kuenzler, H., Sheehan, R., Ning, P., Bongiolatti, J., 1998. Characteristics of plasma structuring in the cusp/cleft region at Svalbard. *Radio Sci.* (in press).
- Berg, G.A., Kelley, M.C., Mendillo, M., Doe, R., Vickrey, J., Kletzing, C., Primdahl, F., Baker, K.D., 1994. Formation and eruption of sun-aligned arcs at the polar cap-auroral oval boundary. *J. Geophys. Res.* 99, 17,577.
- Birn, J., Hones, E.W., Craven, J.D., Frank, L.A., Elphinstone, R.D., Stern, D.P., 1991. On open and closed field lines regions in Tsyganenko's field model and their possible associations with horse collar auroras. *J. Geophys. Res.* 96, 3811.
- Buchau, J., Weber, E.J., Anderson, D.N., Carlson, H.C., Moore, J.G., 1985. Ionospheric structures in the polar cap: Their origin and relation to 250-MHz scintillation. *Radio Sci.* 20, 325.
- Carlson, H.C., 1994. The dark polar ionosphere: Progress and future challenges. *Radio Sci.* 29, 157.
- Coley, W.R., Heelis, R.A., 1995. Adaptive identification and characterization of polar ionization patches. *J. Geophys. Res.* 100, 23,819.
- Coley, W.R., Heelis, R.A., 1998a. Seasonal and universal time distribution of patches in the northern and southern polar caps. *J. Geophys. Res.* (submitted).
- Coley, W.R., Heelis, R.A., 1998b. Structure and occurrence of polar ionization patches. *J. Geophys. Res.* 103, 2201.
- Crowley, G., 1996. Critical review of ionospheric patches and blobs. In: *Review of Radio Science 1993–96*, Oxford University Press, pp. 619–648.
- Cumnock, J.A., Sharber, J.R., Heelis, R.A., Hairston, M.R., Craven, J.D., 1997. Evolution of the global aurora during positive IMF B_z and varying IMF B_y conditions. *J. Geophys. Res.* 102, 17,489.
- Doe, R.A., Tsunoda, R.T., MacDougall, J.W., 1997. Evolution of decameter and kilometer scale irregularities associated with a polar cap arc. In: *Proceedings of Third Joint Workshop for CEDAR HLPS/STEP GAPS*.
- Doolittle, J.H., 1997. Collaborative study of substorm events at high latitudes from the AGO PENGUIN network. In: *Proceedings of Third Joint Workshop for CEDAR HLPS/STEP GAPS*.
- Elphinstone, R.D., Jankowska, K., Murphree, J.S., Cogger, L.L., 1990. The configuration of the auroral distribution for interplanetary magnetic field B_z northward, 1. IMF B_z and B_y .

- dependence as observed by the Viking satellite. *J. Geophys. Res.* 95, 5791.
- Erukhimov, L.M., Muravjeva, N.V., Myasnikov, E.N., Evstafjev, O.V., Kosolapenko, V.I., 1996. Spectral structure of auroral F layer patches. *Radio Sci.* 31, 629.
- Gallagher, H.A., Carovillano, R.L., Weber, E.J., Fukui, K., Valladares, C.E., 1995. Determination of plasma convection about sun-aligned polar cap auroral arcs from incoherent scatter radar and all sky imaging photometer observations. *EOS Trans. AGU* 76(17), S249.
- Guzdar, P.N., Gondarenko, N.A., Chaturvedi, P.K., Basu, S., 1998. Three dimensional nonlinear simulations of the gradient-drift instability in the high-latitude ionosphere. *Radio Sci.* (in press).
- Heppner, J.P., Maynard, N.C., 1987. Empirical high-latitude electric field models. *J. Geophys. Res.* 92, 4467.
- Keskinen, M.J., Mitchell, H.G., Fedder, J.A., Satyanarayana, P., Zalesak, S.T., Huba, J.D., 1988. Nonlinear evolution of the Kelvin–Helmholtz instability in the high latitude ionosphere. *J. Geophys. Res.* 93, 137.
- Kivanc, O., Heelis, R.A., 1997. Structures in ionospheric number density and velocity associated with polar cap ionization patches. *J. Geophys. Res.* 102, 307.
- McEwen, D.J., Harris, D.P., 1996. Occurrence patterns of F layer patches over the north magnetic pole. *Radio Sci.* 31, 619.
- Newell, P.T., Meng, C.-I., 1995. Creation of the theta auroras: The isolation of plasma sheet fragments in the polar cap. *Science* 270, 1338.
- Obara, T., Mukai, T., Hayakawa, H., Nishida, A., Tsuruda, K., Machida, S., Fukunishi, H., 1993. Akebono (EXOS D) observations of small-scale electromagnetic signatures relating to polar cap precipitation. *J. Geophys. Res.* 98, 11,153.
- Obara, T., Mukai, T., Hayakawa, H., Tsuruda, K., Matsuo, A., Nishida, A., Fukunishi, H., Zhu, L., Sojka, J.J., Crain, D.J., 1996. Multiple polar cap arcs: Akebono (EXOS D) observations. *Radio Sci.* 31, 645.
- Ossakow, S.L., Chaturvedi, P.K., Workman, J.B., 1978. High altitude limit of the gradient drift instability. *J. Geophys. Res.* 83, 2691.
- Pedersen, T.R., Fejer, B.G., Doe, R.A., Weber, E.J., 1998. Incoherent scatter radar observations of horizontal F-region plasma structure over Sondrestrom, Greenland during polar cap patch events. *Radio Sci.* (in press).
- Radio Science, 1994. Special section on CEDAR HLPS/STEP GAPS. 29, pp. 155–406.
- Radio Science, 1996. Special section on CEDAR HLPS/STEP GAPS. 31, pp. 573–678.
- Reiff, P.H., Burch, J.L., 1985. IMF B_z -dependent dayside plasma flow and Birkeland currents in the dayside magnetosphere, 2, A global model from northward and southward IMF. *J. Geophys. Res.* 90, 1595.
- Rodger, A.S., Graham, A.C., 1996. Diurnal and seasonal occurrence of polar cap patches. *Ann. Geophys.* 14, 533.
- Rodger, A.S., Pinnock, M., Dudeney, J.R., Baker, K.B., Greenwald, R.A., 1994. A new mechanism for polar patch formation. *J. Geophys. Res.* 99, 6425.
- Rodriguez, J.V., Valladares, C.E., Fukui, K., Gallagher, H.A., 1997. Antisunward decay of polar cap arcs. *J. Geophys. Res.* 102, 27,227.
- Sojka, J.J., 1998. Interdisciplinary scientists gather for plasma structure workshop. *EOS Trans. AGU* 79, 105.
- Sojka, J.J., Bowline, M.D., Schunk, R.W., 1994a. Patches in the polar ionosphere: UT and seasonal dependence. *J. Geophys. Res.* 99, 14, 959.
- Sojka, J.J., Zhu, L., Crain, D.J., Schunk, R.W., 1994b. Effect of high latitude ionospheric convection on Sun-aligned polar cap arcs. *J. Geophys. Res.* 99, 8851.
- Sojka, J.J., Subramaniam, M.V., Zhu, L., Schunk, R.W., 1998. Gradient drift instability growth rates from global scale modeling of the polar ionosphere. *Radio Sci.* (in press).
- Troshichev, O.A., Gusev, M.G., 1994. IMF B_z and B_y dependencies of polar cap auroral distribution for northward IMF orientation inferred from observations at Vostok station. *J. Atmos. Terr. Phys.* 56, 237.
- Tsunoda, R.T., 1988. High-latitude F region irregularities: a review and synthesis. *Rev. Geophys.* 26, 719.
- Valladares, C.E., Carlson, H.C., 1991. The electrodynamics, thermal, and energetic character of intense sun-aligned arcs in the polar cap. *J. Geophys. Res.* 96, 1379.
- Valladares, C.E., Basu, S., Buchau, J., Friis-Christensen, E., 1994a. Experimental evidence for the formation and entry of patches into the polar cap. *Radio Sci.* 29, 167.
- Valladares, C.E., Carlson, H.C., Fukui, K., 1994b. Interplanetary magnetic field dependency of stable sun-aligned polar cap arcs. *J. Geophys. Res.* 99, 6247.
- Valladares, C.E., Alcayde, D., Rodriguez, J.V., Ruohoniemi, J.M., Van Eyken, A.P., 1998a. Observations of plasma density structuring in association with the passage of traveling convection vortices and the occurrence of large plasma jets. *Ann. Geophys.* (submitted).
- Valladares, C.E., Fukui, K., Sheehan, R., Carlson, H.C., Bullett, T., 1998b. Simultaneous observations of polar cap patches and Sun-aligned arcs during transitions of the IMF. *Radio Sci.* (in press).
- Weber, E.J., Buchau, J., Moore, J.G., Sharber, J.R., Livingston, R.C., Winningham, J.D., Reinisch, B.W., 1984. F layer ionization patches in the polar cap. *J. Geophys. Res.* 89, 1683.
- Weber, E.J., Kelley, M.C., Ballenthin, J.O., Basu, S., Carlson, H.C., Fleischman, J.R., Hardy, D.A., Maynard, N.C., Pfaff, R.F., Rodriguez, P., Sheehan, R.E., Smiddy, M., 1989. Rocket measurements within a polar cap arc: Plasma, particle, and electric circuit parameters. *J. Geophys. Res.* 94, 6692.
- Zhu, L., Sojka, J.J., Schunk, R.W., Crain, D.J., 1993. A time-dependent model of polar cap arcs. *J. Geophys. Res.* 98, 6139.
- Zhu, L., Sojka, J.J., Schunk, R.W., Crain, D.J., 1994. Model study of multiple polar cap arcs: Occurrence and spacing. *Geophys. Res. Lett.* 21, 649.
- Zhu, L., Schunk, R.W., Sojka, J.J., 1997. Polar cap arcs: A review. *J. Atmos. Solar-Terr. Phys.* 59, 1087.

Measurement of the latitudinal distributions of total electron content during equatorial spread *F* events

C. E. Valladares,¹ S. Basu,² K. Groves,² M. P. Hagan,¹ D. Hysell,³ A. J. Mazzella Jr.,⁴ and R. E. Sheehan¹

Abstract. We have constructed latitudinal profiles of the total electron content (TEC) using measurements from six GPS receivers conducted during 1998. The TEC profiles have been divided into two groups: One corresponds to days when plumes or equatorial spread *F* (ESF) develops, and the second group portrays days of no-ESF condition. The presence/absence of ESF is based on the signature of the coherent echoes measured by the Jicamarca Unattended Long-Term Investigation (JULIA) radar and records of scintillations from two sites spaced in latitude. One scintillation station is located near the magnetic equator (Ancon) and the other 12° southward (Antofagasta). The TEC profiles display the typical day-to-day and seasonal variability seen at low latitudes. During the equinoxes, we observed quite often the crests of the anomaly located between 12° and 20° away from the magnetic equator and a trough in-between. The monthly distribution of the appearance of the anomaly and the local time of their appearance are in very good agreement with the reported variability of the upward vertical drifts and the current theory of the equatorial fountain effect. During the equinoxes and the December solstice, the TEC anomaly is observed almost every day, sometimes when there is no ESF activity. Nevertheless, fine inspection of the TEC latitudinal profiles suggests the existence of a close relationship between the temporal evolution of the TEC profiles near sunset and the onset of ESF. We have examined the TEC latitudinal distributions in two different ways. First, we calculated time difference profiles using the distributions corresponding to 1800 and 2000 LT. Second, we used a parameterization of the TEC distributions obtained at 2000 LT. The first method indicates quite drastic increases of the crest values and sharp decreases near the trough during ESF days. In contrast, during days of no ESF there exist almost uniform TEC decreases at all latitudes. The second method displays a preferred high crest/trough ratio (>2), small TEC values at the trough, and large latitudinal integrated values during ESF events.

1. Introduction

The term equatorial spread *F* (ESF) encompasses several turbulent processes and different types of plasma instabilities that grow and propagate in the nighttime equatorial ionosphere. Since the first observation of range-dispersed ionograms in the late thirties [Booker and Wells, 1938], until the more refined measurements of ESF using ground-based radars and satellite-borne sensors, all have indicated the turbulent and the seemingly unpredictable nature of this phenomenon. In particular, the Jicamarca radar has been instrumental in describing the altitude distribution, time

evolution, scale size, vertical and zonal drift, and the magnetic aspect angle dependence of 3-m irregularities associated with ESF [Farley *et al.*, 1970; Woodman and LaHoz 1976; Kudeki *et al.*, 1981; Kelley *et al.*, 1986; Farley and Hysell, 1996]. A milestone in the investigation of ESF was the observation of 3-m irregularities forming altitude-elongated “plumes,” which were tracers of plasma depletions or “bubbles” advecting from the lower altitudes of the *F* layer and quite often intruding into the topside [Woodman and LaHoz, 1976]. These authors suggested that the time evolution of the radar plumes followed the evolution of the Rayleigh-Taylor instability (RTI). The studies undertaken by Kelley *et al.* [1976] and McClure *et al.* [1977] confirmed that the deep plasma depletions, seen at *F* region altitudes, were actually formed at the bottomside and had propagated toward higher altitudes.

In the last 25 years, further measurements of ESF using incoherent scatter radar [Tsunoda, 1980], probes on board satellites [McClure *et al.*, 1977; Valladares *et al.*, 1983], airglow photometers [Mendillo *et al.*, 1992], scintillation receivers [Basu and Basu, 1985], HF transmissions [Jayachandran *et al.*, 1993], and numerical modeling [Ossakow *et al.*, 1979; Zalesak and Ossakow, 1980] have indicated the general morphology of the ESF phenomenon. It

¹Institute for Scientific Research, Boston College, Chestnut Hill, Massachusetts.

²Air Force Research Laboratory, Hanscom Air Force Base, Massachusetts.

³Department of Physics and Astronomy, Clemson University, Clemson, South Carolina.

⁴Northwest Research Associates, Bellevue, Washington.

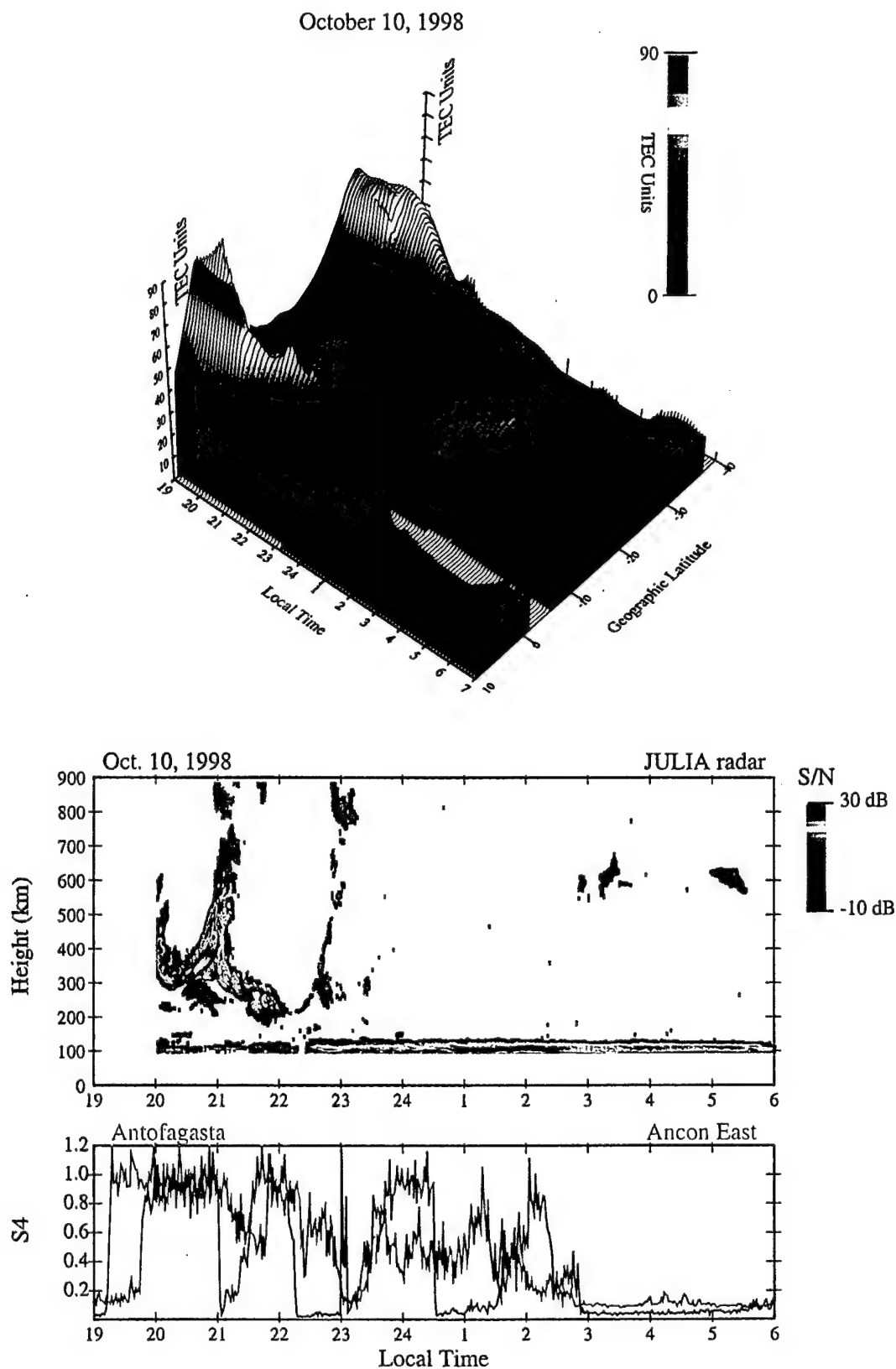


Plate 1. Data collected by the chain of GPS receivers, the JULIA radar, and two scintillation receivers on October 10, 1998. The top plot shows a three-dimensional view of the TEC values displayed as a function of geographic latitude and local time. The middle panel displays a color-coded plot of the magnitude of the coherent echoes gathered by the JULIA radar. The bottom panel shows S4 indices measured by the Ancon east and the Antofagasta west receivers. Note the presence of strong scintillations, plasma plumes extending up to 900-km altitude, and very pronounced anomaly crests.

is now known that several ionospheric conditions can help the RTI to develop. These are (1) the lifting of the *F* layer [Farley *et al.*, 1970; Jayachandran *et al.*, 1993; Sastri *et al.*, 1997], (2) a small or null transequatorial meridional wind [Maruyama and Matuura, 1984; Maruyama, 1996], (3) a simultaneous decay of the *E* region conductivity at both ends of the field lines [Tsunoda, 1985], (4) a sharp gradient at the bottomside of the *F* layer, and (5) penetration of magnetospheric fields. Furthermore, satellite in situ measurements have shown that some bubbles are able to attain supersonic velocities in the early stages of their development [Agsson *et al.*, 1992; Hanson *et al.*, 1997]. In general, bubbles grow much faster than the time predicted by the RTI theory. These latter two facts suggest that the bubble initiation may involve the presence of a seed to make its development occur in a more explosive manner. Kelley *et al.* [1981], and Hysell *et al.* [1990] have indicated that gravity waves may be the seed that is required to initiate the growth of the plasma bubbles.

The development of ESF is closely linked to other processes that occur at local times near sunset, the time when most of the plasma bubbles are triggered. An important feature of the vertical drift is the sudden enhancement that occurs around 1900 LT and before the vertical drift turns downward. This feature was called the pre reversal enhancement (PRE) by Woodman [1970]. The occurrence of the PRE is important because this additional upward velocity displaces the *F* layer further upward, favoring the initiation of ESF. The full development of the PRE has been associated with the sunset decay of the highly conductive *E* layer [Farley *et al.*, 1986] and the time of reversal of the zonal thermospheric wind from a westward to an eastward orientation [Crain *et al.*, 1993]. Basu *et al.* [1996] presented the day-to-day variability of the PRE, observed during a prolonged campaign in South America, and suggested that the appearance of a well-developed PRE was associated with the onset of ESF. More recently, Fejer *et al.* [1999] have indicated that the vertical plasma drift may constitute the only observable that is required to predict the onset of ESF. A fully developed PRE can favor the growth of the RTI in three different ways: (1) It lifts the *F* region to more unstable altitudes, where the damping collisional term is smaller; (2) it implies the presence of an eastward electric field, which is also a destabilizing term in the generalized RTI; and (3) it speeds up the recombination at the lower altitudes of the *F* layer [Hanson *et al.*, 1983, 1986]. Therefore the presence of PRE is an important indicator of a posteriori development of ESF, but other characteristics of the equatorial plasma electrodynamics may also be equally important (e.g., transequatorial wind).

Another important feature of the low-latitude *F* region is an enhancement of the *F* region density that is observed at both sides of the magnetic equator. These have been called the Appleton (also named equatorial) ionization anomalies. They are the result of the upward motion of the plasma at the magnetic equator and its consequent diffusion obliquely along the magnetic field lines [Hanson and Moffett, 1966]. The total electron content (TEC) anomaly starts to develop as early as 1100 LT. It moves away from the equator with increasing local time, as the *F* region at the equator moves to higher altitudes, and it reaches a maximum development around 2000 LT. After 2100 LT the crests of the anomaly sometimes move rapidly toward the equator as the equatorial

ionosphere moves downward. This latter process has been called "the reverse fountain effect" [Sridharan *et al.*, 1993; Balan and Bailey, 1995]. Several researchers have studied the morphology of the equatorial anomaly. Walker *et al.* [1994] used median hourly TEC latitude profiles obtained in Southeast Asia to account for the seasonal and solar cycle variability of the anomaly. These authors indicated that any asymmetry in the amplitude of the crests was due to the transequatorial wind blowing outward from the summer hemisphere and to the proximity of the subsolar point to the location of the largest crest. The asymmetry was more prominent during solstices but was sometimes observable at the equinoxes. On some evenings a strong resurgence of the anomaly takes place; this is probably related to a full development of the PRE. Consequently, precise measurements of the amplitude of both crests have decisive bearing on two of the processes that are intrinsically associated with the initiation of ESF: the vertical drift velocity and the transequatorial thermospheric wind. In addition, it has been suggested that the amplitude of the equatorial anomaly can be used as a precursor of the occurrence of ESF irregularities [Raghavarao *et al.*, 1988; Sridharan *et al.*, 1994]. Sultan and Rich [2000] and Huang *et al.* [2001] used in situ values of the density measured by the Defense Meteorological Satellite Program (DMSP) satellite to formulate a relation between the occurrence pattern of spread *F* and the amplitude and location of the crests.

In this paper we report measurements of the total electron content (TEC) performed with six GPS receivers. Five of them are strategically located south of the magnetic equator on the west side of South America. The geographic location of the six GPS receivers are Bogota (4.64°N, 74.08°W), Ancon (11.78°S, 77.15°W), Arequipa (16.47°S, 71.49°W), Iquique (20.27°S, 70.13°W), Copiapo (27.38°S, 70.34°W), and Santiago (33.15°S, 70.67°W). In this paper we first correlate important features of the latitudinal distribution of TEC to power maps collected by the JULIA radar (11.96°S, 70.4°W, and magnetic latitude (MLAT): 0.5°N). In section 3 we present a statistical analysis of the TEC latitudinal distributions and the S4 indices measured by two UHF spaced-receiver scintillation systems (SRSS). One of the SRSS is located at Ancon (subionospheric point at 10.66°S, 70.4°W, and MLAT: 2.17°N), and the other is placed at Antofagasta (subionospheric point at 25.4° S, 69.95° W, and MLAT: 11.3° S).

In the last few years, GPS receivers have been used to study several processes in the low- and high-latitude ionospheres. Pi *et al.* [1997] used a worldwide network of GPS receivers to monitor the instantaneous global distribution of large-scale ionospheric irregularities. Coker *et al.* [1995] used measurements of the rate-of-TEC index (ROTI) to resolve the spatial boundary of the auroral zone. Kelley *et al.* [1996] studied the performance of GPS systems during the passage of spread *F* depletions across the receiver's line of sight. In other instances, scintillations measured by GPS receivers have backed up and complemented other types of measurements [Weber *et al.*, 1996]. More recently, Lunt *et al.* [1999a,b] have used TEC values calculated from the GPS and Near-Infrared Mapping Spectrometer (NIMS) constellation of satellites to deduce the contribution of the plasmasphere to the total electron content. In all these cases the low cost of the GPS receivers, their portability, and easy deployment have

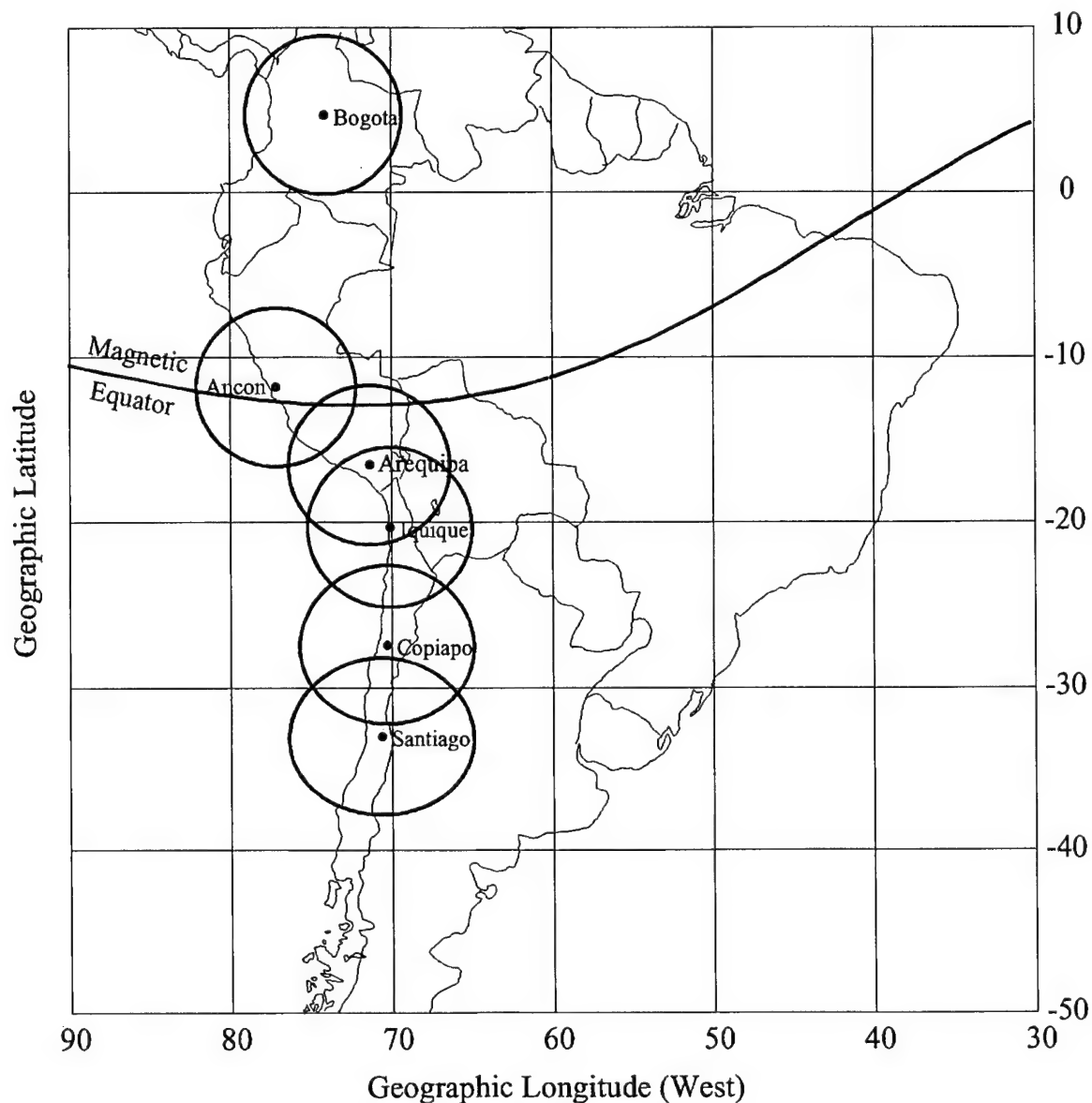


Figure 1. Site locations and field of view (30° elevation) of the six GPS receivers that were used in this study. Note the location of the magnetic equator and the existence of a region between -7° and 0° geographic latitude where TEC is not measured. The GPS receivers located at Arequipa, Iquique, Copiapo, and Santiago evaluate the TEC at latitudes south of the magnetic equator. The receivers situated at Bogotá and Ancon diagnose northward of the magnetic equator.

prompted researchers to increase their usage during dedicated campaigns.

The scope of the paper is not to look for precursors of ESF plumes or scintillation activity but to examine the characteristics of the TEC latitudinal distributions when plumes are seen with the JULIA radar [Hysell and Burcham, 1998] and when UHF scintillations are observed simultaneously at Ancon and Antofagasta.

2. Data Sets

Figure 1 shows the location of all six GPS receivers. Four of the sites (Arequipa, Iquique, Copiapo, and Santiago) are situated south of the magnetic equator. Another one (Ancon) is placed close to the magnetic equator. The sixth receiver (Bogotá) is located well north under the northern crest. Three different data sets were used in this study. The first data set

consisted of the radar maps measured by the JULIA radar in 1998 (34 nights), the second set included S4 indices from the Ancon and Antofagasta scintillation systems for the same year, and the third set included TEC latitudinal distributions derived from the six GPS receivers, also for year 1998.

Plate 1 shows a particular sample from these three data sets corresponding to October 10, 1998, a day in which elongated plumes and strong scintillations were clearly evident. The bottom panel displays strong scintillations measured by the Ancon east (red line) and the Antofagasta (blue trace) receivers. The ray paths from these two sites intersect the *F* region ionosphere at virtually the same magnetic meridian plane but at latitudes separated by almost 12° . This particular geometry permits us to study irregularities that map to different apex altitudes. However, there are two differences. Ancon's observations are carried out using a 25° elevation angle compared to 65° for the Antofagasta measurements.

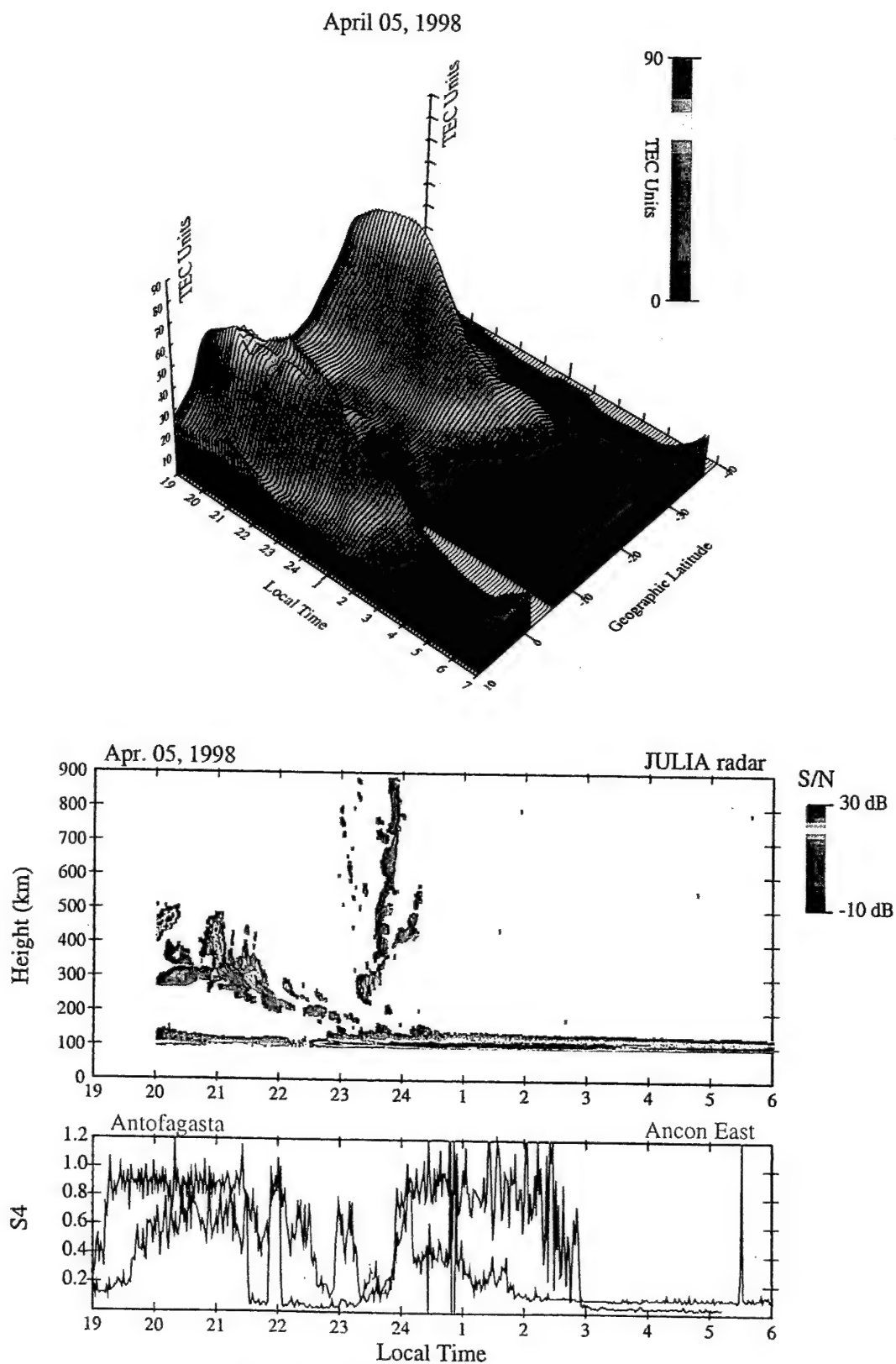
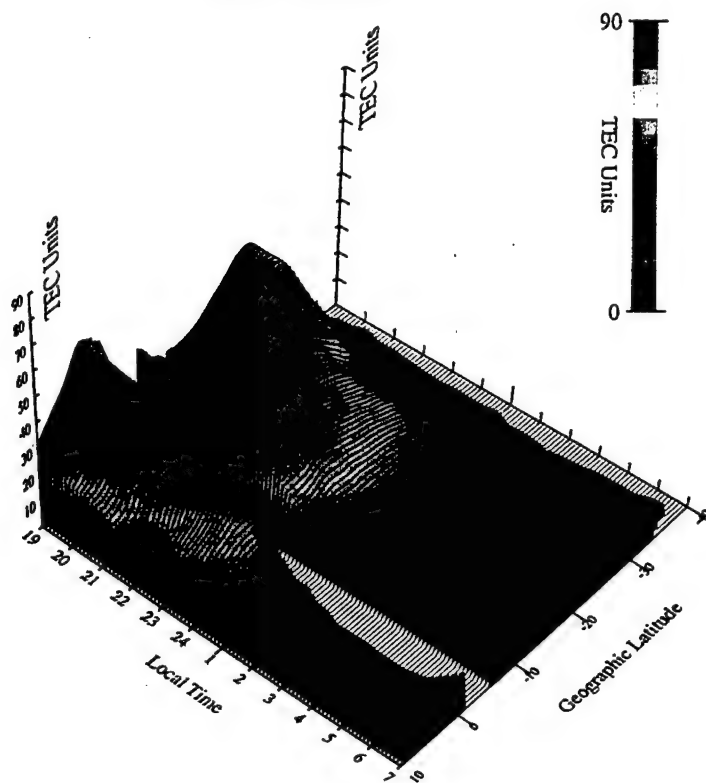


Plate 2. Same as Plate 1, but corresponding to April 05, 1998.

March 29, 1998



October 22, 1998

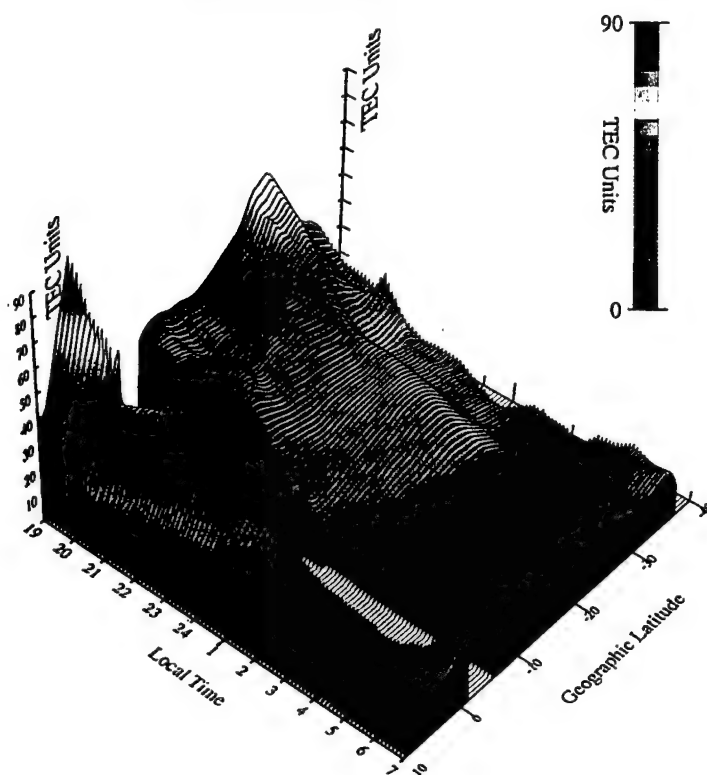


Plate 3. TEC values collected by the chain of GPS receivers on two nights when no scintillation and no coherent echoes were detected. Less pronounced and rapidly decaying crests are seen on these two days.

This makes the scintillations seen at Ancon originate over a longer ray path compared to the scintillations seen at Antofagasta. In addition, it is also possible that the ray path from the Ancon antennas intercepts more than one plasma bubble. It is also known that Antofagasta, being further closer to the southern anomaly crest, has a local plasma density larger than that of Ancon. All these reasons may account for the difference seen sometimes between the scintillation traces at each station. The middle panel of Plate 1 displays a series of plumes measured at Jicamarca using the JULIA radar on October 10, 1998. The first plume, seen at 2000 LT, reaches 600 km, and the other two (2100 and 2300 LT) extend up to at least 900-km altitude. All three plumes are seen connected to a bottomside layer. This layer shows a quasi-sinusoidal modulation in altitude; it is initially at 320 km, then it ascends to ~ 370 km, later lowers to 200 km at 2200 LT, and finally increases up to 280-km altitude at 2250 LT. The top panel is a three-dimensional view of the variability of the TEC as a function of geographic latitude and local time. The TEC curves were obtained by doing a two-dimensional (latitude and local time) regression analysis of the TEC values measured by all six GPS receivers. Prominent features in this panel are the two peaks at both sides of the magnetic equator ($\sim 12^\circ$ geographic latitude), indicative of a pronounced development of the Appleton anomaly. At 1900 LT both crests are larger than 75 TEC units, and the valley or trough is near 40 TEC units. Between 1900 and 2000 LT the amplitude of the peaks increases, and the trough decreases. At 2000 LT the northern crest exceeds 100, the southern anomaly peak reaches 80, and the trough decreases to 28 TEC units. At this local time the latitudinal TEC distribution presents the characteristics of the postsunset resurgence of the anomaly previously discussed by Walker *et al.* [1994]. These authors discussed a postsunset revival of the anomaly in terms of the occurrence of an intense PRE. The asymmetry in the amplitude of the anomaly peaks and the rapid decay of the northern peak may indicate the effect of a pronounced transequatorial meridional wind. Notice the absence of TEC measurements between 2° S and 6° S due to the lack of coverage by our limited network of GPS receivers.

Plate 2 has a layout similar to that of Plate 1. It displays the TEC distributions, the power map from the JULIA radar, and the time series of the scintillations measured on April 5, 1998. The bottom panel shows that the scintillations at Ancon were much weaker than the scintillations at Antofagasta. S_4 values at Antofagasta reached saturated values, and at Ancon the scintillations varied between 0.8 and 0.4. In addition, the onset of scintillations at Antofagasta preceded that at Ancon by 40 min. As mentioned above, these discrepancies may be attributed partially to differences of the geometries being intersected and the variability of the local density at the subionospheric intersections. The JULIA data present a series of small plumes extending up to 500 km between 2000 and 2200 LT; these miniplumes are followed at 2350 LT by a tall and narrow plume extending from 230-km altitude up to >900 -km altitude. There is also a bottomside layer connecting the lower boundary of the plumes, which is observed to be continuously lowering in altitude and seems to end at the equatorial electrojet. The TEC plot shows a pattern of two well-defined peaks, which are increasing in amplitude until 2200 LT. After this time they start decreasing and finally fade at 0100 LT. Both peaks have almost similar amplitudes with maximum values close to 65 TEC units.

Similar to Plate 1, the peak/trough ratio at the time that the plasma plumes are observed is larger than 3.

Plate 3 illustrates two cases when neither scintillations nor radar echoes were detected. During these two days both anomaly peaks are evident; nevertheless, they do not possess a large amplitude like the cases shown in Plates 1 and 2. Important features of the TEC latitudinal distributions are the relatively larger values at the trough and the absence of an early evening reinitiation of the fountain effect as seen in Plates 1 and 2. The TEC distribution for March 29, 1998 (top panel), is approximately symmetric with respect to the magnetic equator. On this day both anomaly peaks decay before local midnight. The trough increases from 28 TEC units at 2000 LT up to 35 units at 2200 LT. This postsunset increase of the trough density is indicative of a reverse fountain effect in which plasma density from the anomaly peaks is transported back to the magnetic equator through a diffusion process in which plasma flows along and up the field lines. The bottom panel of Plate 3 shows the anomaly corresponding to October 22, 1998, a day when both peaks developed asymmetrically. The TEC value at the trough varies between 37 units at 2000 LT and 40 units at 2200 LT. Both anomaly crests decay very rapidly after sunset, and at 2100 LT they are almost nonexistent. At sunset time (1900 LT) both TEC distributions of Plate 3 present a crest/trough ratio less than 2.

3. Data Analysis

We have binned the TEC latitudinal profiles for two opposite states of the equatorial ionosphere. The first state consists of an ionosphere populated by deep and altitude-extended plasma depletions, and the other state is associated with a uniform and undisturbed ionosphere. To determine the altitude extension of the plasma depletions (ESF) we used data from two experimental techniques. First we have employed power maps of coherent echoes collected by the JULIA radar to indicate the maximum altitude of the plasma plumes for all the nights the radar operated in 1998. When the radar echoes surpass 550-km altitude, as the examples shown in Plates 1 and 2, they were counted as nights of deep bubbles. Secondly we have used concurrent observations of strong scintillations by the Ancon east and Antofagasta receivers as a proxy for the occurrence of plumes extending, at least, up to 550-km altitude. It has been demonstrated that an F region located at, say, 350-km altitude at Antofagasta maps above 550-km altitude at the magnetic equator [Basu *et al.*, 1996]. By considering two completely opposite states of the equatorial ionosphere, a very turbulent one (altitude-extended plumes) and a second state of an undisturbed ionosphere, we expect to find significant differences in the characteristics of the TEC latitudinal distributions. A third state consisting of bottomside layers and/or miniplumes (< 500 -km altitude) is not considered in this study.

3.1. Statistics of TEC Distributions Binned According to JULIA Observations

The top panels of Figure 2 show TEC latitudinal distributions measured at 2000 LT for all the nights in 1998 that the JULIA radar observed plumes reaching at least 550 km-altitude. The bottom panels show the TEC distributions for nights when JULIA recorded bottomtype layers or a total

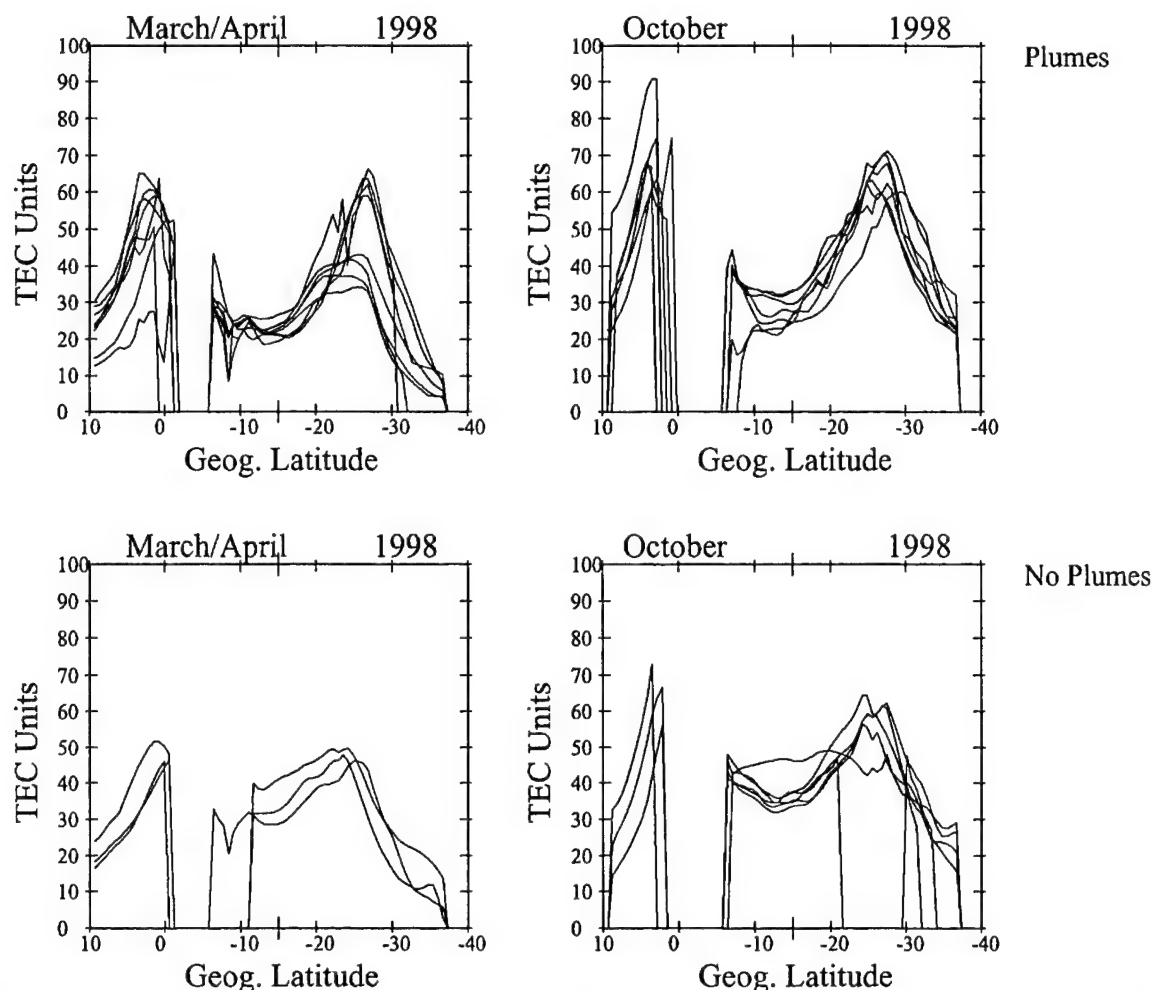


Figure 2. Latitudinal TEC distributions for the equinoxes binned according to the occurrence or not of plumes. Note the difference between the TEC distributions shown in the top panels, corresponding to days of plasma plumes, and the bottom panels for no-plume days. The TEC curves in the top panels show pronounced and narrow crests. The bottom panels exhibit smaller and wider crests.

absence of spread *F* echoes. All four panels (plumes and no plumes) clearly show the double-humped distribution of the low-latitude density and TEC, that are quite typical in the afternoon and early evening [Doherty *et al.*, 1997]. Another distinguishable feature of the TEC distributions is the existence of a trough, which almost always resides at latitudes close to the magnetic equator. Both crests are located at magnetic latitudes varying between 12° and 18° but are not always placed symmetrically with respect to the magnetic equator. Careful comparison of all four panels reveals that the TEC distributions present some significant differences depending upon the presence/absence of elongated plumes. The TEC value at the trough varies between 20 and 30 TEC units during plume days compared with 40 units for no-plume cases. The crests are usually higher and narrower and show steep latitudinal gradients during plume days; they are smaller and shallower during no-plume days. Therefore the ratio of peak/trough is larger during plume cases than it is during events that contain no plumes. Finally, we also noticed that the crests of the TEC anomaly are displaced to higher magnetic latitudes during plume events. The amplitude of the anomaly crests during the month of October peaks 10–15 TEC units higher than that during March/April. This may be partially because of the higher solar flux intensity in October

1998 or an intrinsic difference between both equinoxes. The intensity of the solar flux was 116 (in units of $10^{-22} \text{ W m}^{-2} \text{ Hz}^{-1}$) during October and 108 units during April.

3.2. Statistics of TEC Distributions Binned According to Scintillation Observations

Figure 3 shows the latitudinal distribution of TEC taken at 2000 LT for all plume and no-plume nights when at least four GPS receivers were operating. It is evident that the season exerts a strong control on the formation of the anomalies and on the maximum amplitude of the latitudinal distributions. During the equinoctial months (March, April, September, and October), typical distributions showing well-defined crest-trough-crest features are seen almost everyday. During these months the TEC amplitudes are also the largest, reaching values in excess of 80 TEC units. During the months of February, May, August, and November (transition months) the TEC distributions show, on some days, the presence of the anomalies, but on many other days the TEC profiles are flat, or only a weak anomaly seems to have developed. During these months the peak TEC values are also smaller than the maximum equinoctial values. Excluding December, the solstitial months (January, June, July, and

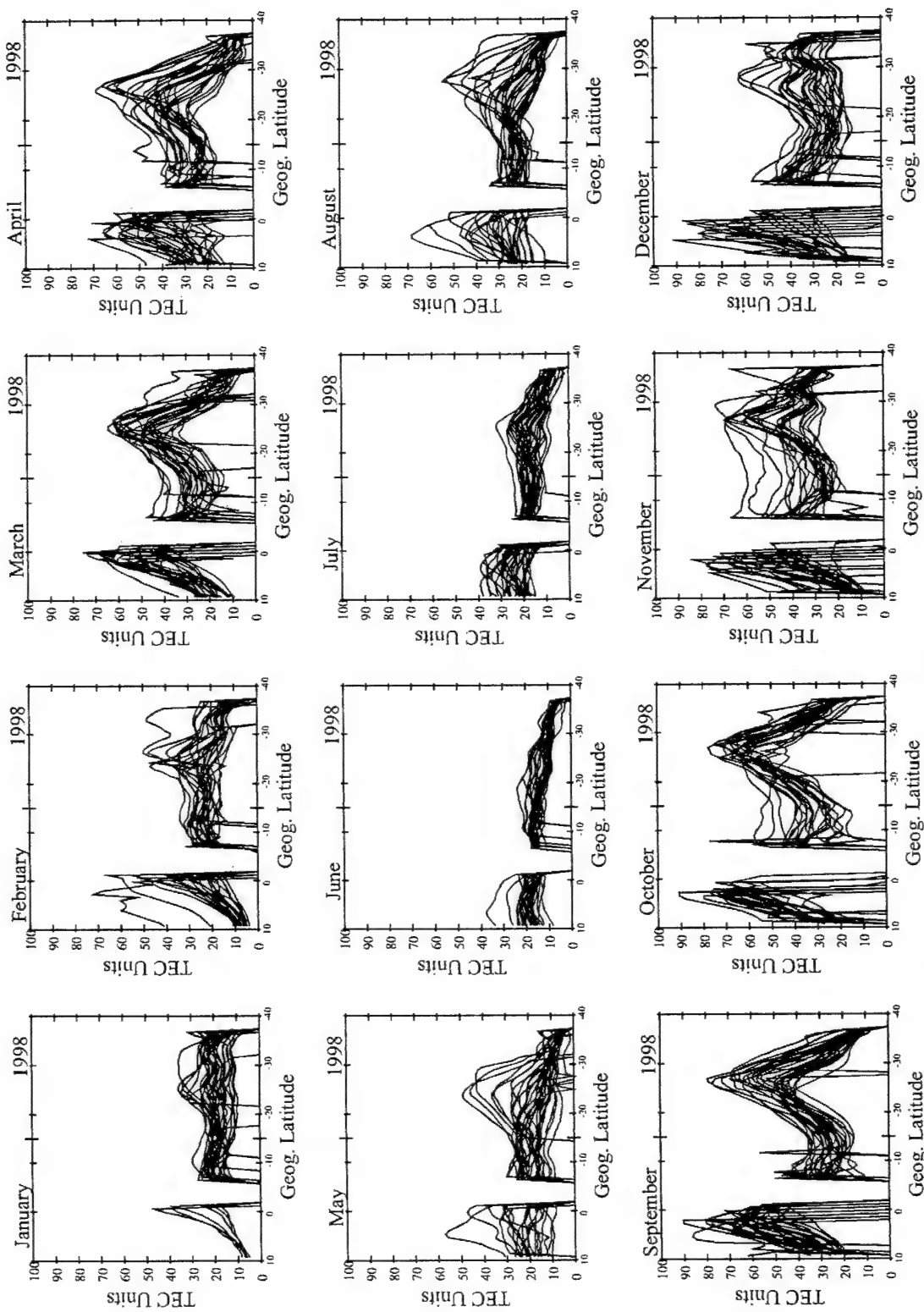


Figure 3. Latitudinal TEC distributions measured at 2000 LT for all days when at least four GPS receivers were operating. Each panel corresponds to one month of observations during 1998. Note the seasonal variability in the occurrence and amplitude of the crests.

December) show TEC distributions without an anomaly crest. During these months the TEC distributions are less than 30 units at all latitudes. They show a peculiar trend of TEC values decreasing from the north toward the south. In general, there exists a day-to-day variability of the TEC distributions, with the smallest values occurring during the solstitial months. As explained in section 5, we believe that this difference in the TEC distribution, observed at 2000 LT, is a consequence of the monthly variability of the equatorial vertical drifts, the meridional neutral wind, and the subsolar location. The seasonal variability of the presence/absence of the anomaly agrees well with the seasonal occurrence of the evening prereversal enhancement seen at Jicamarca during solar minimum conditions [Fejer *et al.*, 1991].

Figure 4 displays the TEC latitudinal distributions only for days when scintillations were seen at both scintillation stations (Ancon and Antofagasta). The anomaly peaks are fully developed every day that scintillations were observed in March, April, September, October, and during most of the cases in November (equinoctial events). Most of the TEC distributions during the months of January, February, and December do not show the presence of the anomaly crests. On a few days only a very weak anomaly or an asymmetric trace is observed (we have called these events the December solstice cases). However, it is conceivable that a weak density anomaly, a sharp gradient in the bottomside density, or a high altitude of the *F* region has occurred although no TEC peaks are evident in our data. The absence of a TEC crest suggests that during these months the fountain effect and the implied lifting of the *F* layer may not play a prominent role in the onset and in the corresponding development of plasma "plumes" during this season. During the months of May, June, July, and August (June solstice), scintillations (and ESF) are seen only rarely in the American sector [Basu and Basu, 1985]. During the month of August, ESF events are accompanied with TEC distributions, presenting characteristics almost similar to the equinoctial cases. During the months of June and July there is only one case per month of ESF, which contains weak anomalies.

Figure 5 shows the TEC latitudinal distributions when no ESF was seen at both stations. Not surprisingly, the anomaly crests are still present for most of the months. In fact, they are observed in all the seasons, in which we observed anomaly peaks in Figure 4 (scintillation cases). However, close inspection of the TEC latitudinal distributions shows prominent differences between the plume and no-plume cases, similar to Figure 2. The no-ESF events seen during the equinoxes show a much higher value in the valley and weaker anomaly peaks than the ESF events (Figure 4). The December solstice cases show again a flat distribution or, in very few cases, a modest anomaly. The numerous events of no ESF that occurred during the June solstice show mainly a flat distribution or very weak anomalies as seen during the months of May and August. In section 4 we parameterize the TEC distribution in order to estimate quantitatively the differences that are related to the ESF activity.

3.3. Statistics of the Time Differences of TEC Distributions

To explore the possibility that the TEC distributions for 1800 LT and earlier times may present different characteristics as a function of the presence/absence of scintillations, we inspected all the TEC distributions between

1500 and 1800 LT. We found no evident distinguishable features; in fact, even during the equinoxes there was no clear difference depending upon scintillation activity. This seems to imply that the ESF onset was probably mostly related to the evolution of the low-latitude density between 1800 and 2000 LT. On the basis of this hypothesis, we carefully looked at the variability of the TEC distributions in this 2-hour period. We subtracted the TEC distribution measured at 1800 LT and the values at 2000 LT, or expressed in mathematical form,

$$\Delta\text{TEC} = \text{TEC}(1800) - \text{TEC}(2000),$$

In this format, positive values indicate a temporal reduction or attenuation of the TEC distributions; negative ΔTEC values indicate a growth or enhancement in TEC. There are some striking distinctions between Figures 6 and 7. Figure 6 shows ΔTEC values for all nights in 1998 when scintillations are seen at both Ancon and Antofagasta. The prominent feature is the strong latitudinal variability in all these curves. During the months of March, April, and from August to December there exists a large ΔTEC value (>20 TEC units) at latitudes near the magnetic equator ($\sim 12^\circ$ geographic latitude) and much smaller values (in many cases negative) at latitudes near the anomaly peaks. This variable pattern indicates that the value of the TEC crests increase and that the TEC trough diminishes during days when ESF occurs. For the solstitial months (January, February, June, and July) there is an indication of a TEC increase near the anomaly peaks, although it is not so pronounced as that observed during the equinoxes. Figure 7 displays ΔTEC values corresponding to days when no scintillations were present. Almost all the ΔTEC curves are quite uniform or present high positive values near the anomaly crests as seen in October and November. The amplitude at the magnetic equator rarely exceeds 20 ΔTEC units, and there are almost no negative ΔTEC values at the crests. These almost flat ΔTEC distributions imply that during 1800 and 2000 LT there exists an almost constant decrease of the TEC at the latitudes covered by the GPS receivers.

4. Parametric Characterization of the TEC Latitudinal Distributions

Figure 8 shows a schematic representation of the low-latitude TEC distribution along a magnetic meridian. In this idealized example the TEC trough is located at $\sim 12^\circ$ geographic latitude. Both crests are displaced 14° away from the magnetic equator, and the peak of the northern crest is larger than the southern. We have observed that this TEC configuration is not uncommon; it occurs quite often during the Southern Hemisphere summer season (December solstice), when a transequatorial wind blows northward. Figure 8 also displays all the parameters that can be used to fully characterize the TEC latitudinal distributions. These quantities are the amplitude and locations of the trough and crests and the integrated excess value of the TEC within the anomaly crests (the southern crest integrated value is depicted here as a shaded area). One of the goals of the present study was to investigate the possibility of parameterizing the TEC latitudinal distributions and to examine if these parameters could be related to the presence/absence of ESF. The main difficulty that we encounter in the present array of GPS receivers is that only one receiver is placed at latitudes north of Ancon to cover an 18° latitudinal span. Thus we restricted

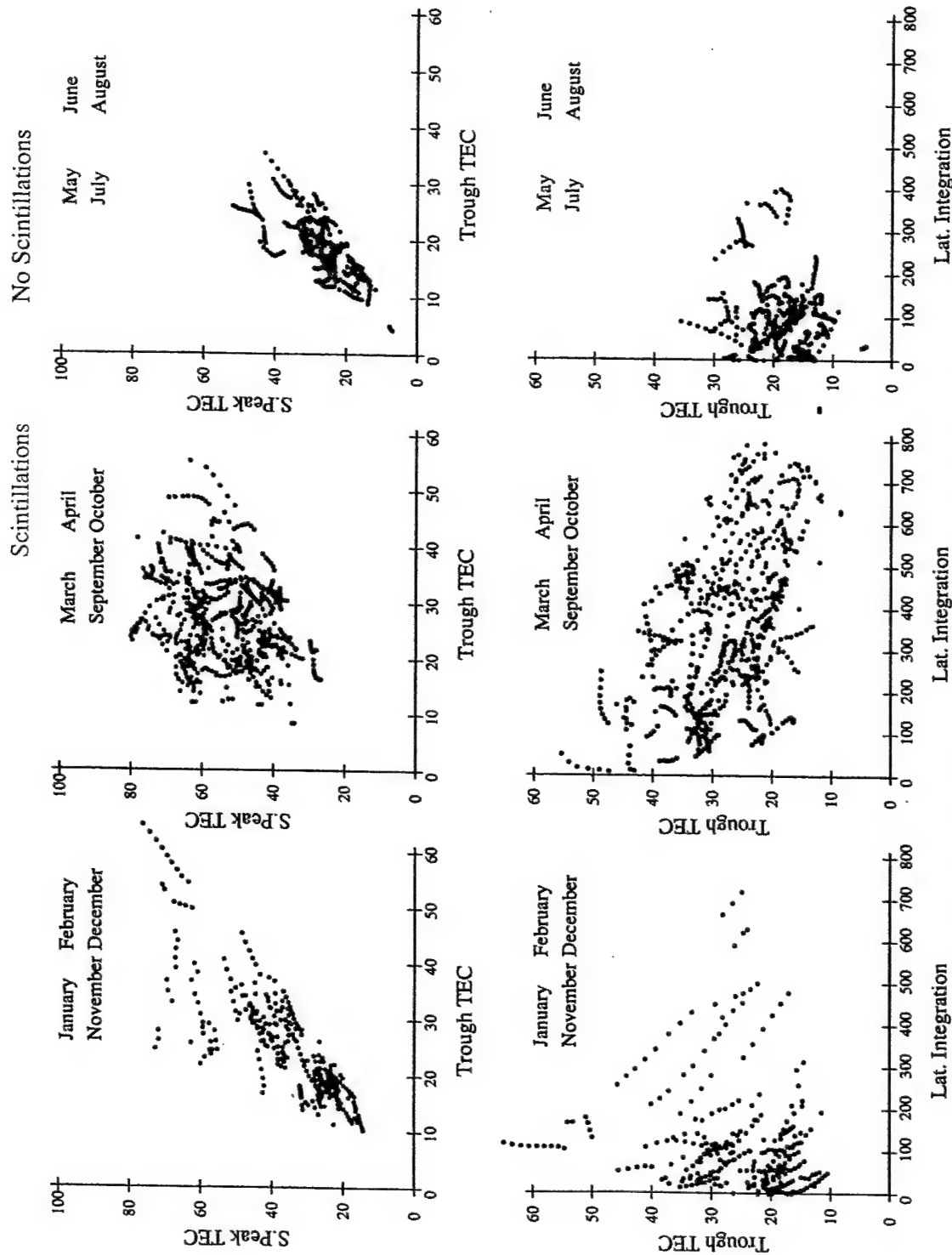


Plate 4. Mass plots of selected parameters extracted from the TEC latitudinal distributions. The dots have been color-coded to represent cases of scintillations (red dots) and no scintillation (blue dots). The top panels show the variability of the TEC peak value of the southern crest versus the value of the trough. The bottom panels display TEC trough values as a function of the integrated TEC value under the southern crest.

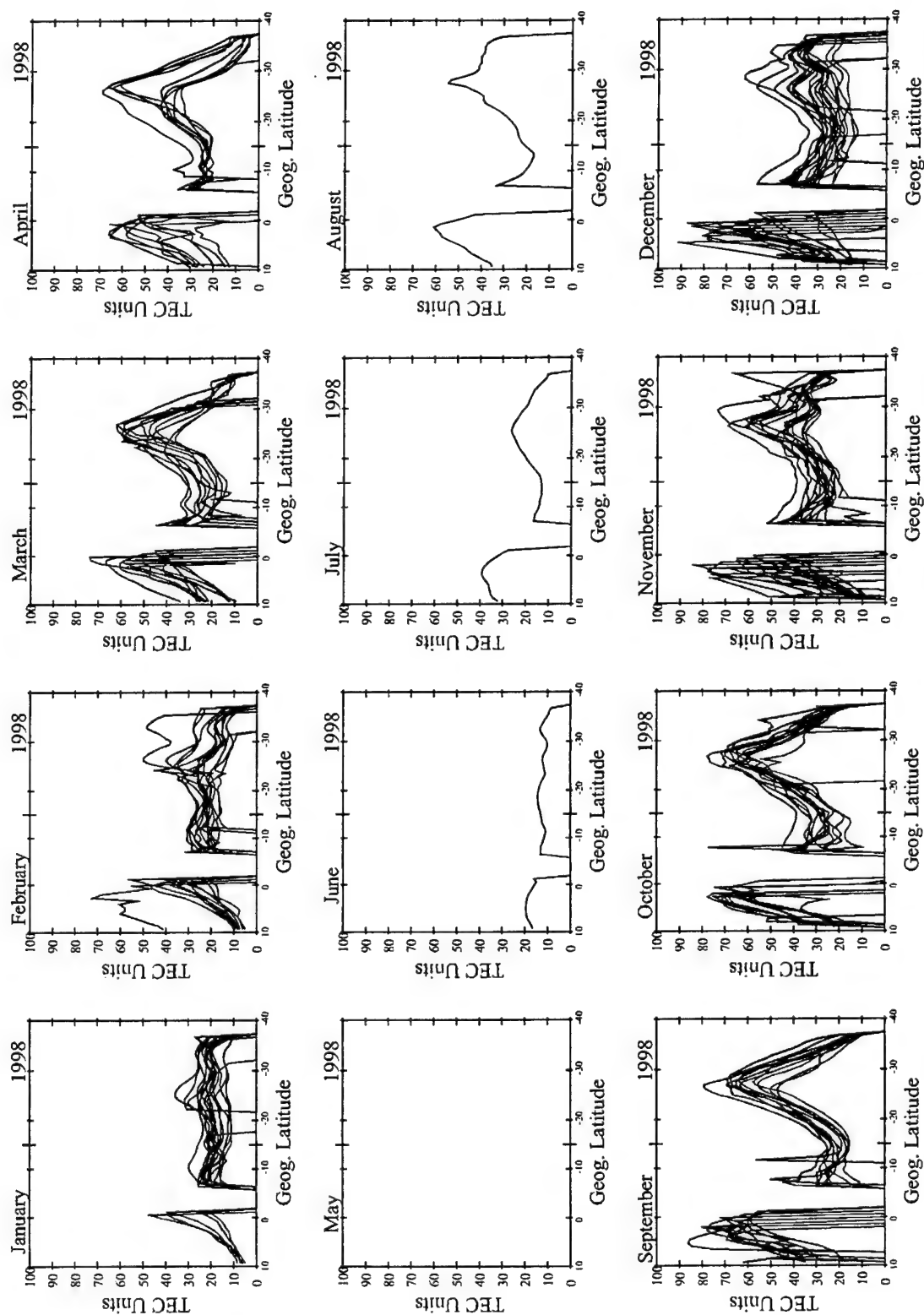


Figure 4. Same as Figure 3 but for nights when scintillations were observed at the Ancon and Antofagasta stations. During the equinoxes the distributions present pronounced crests and a low trough.

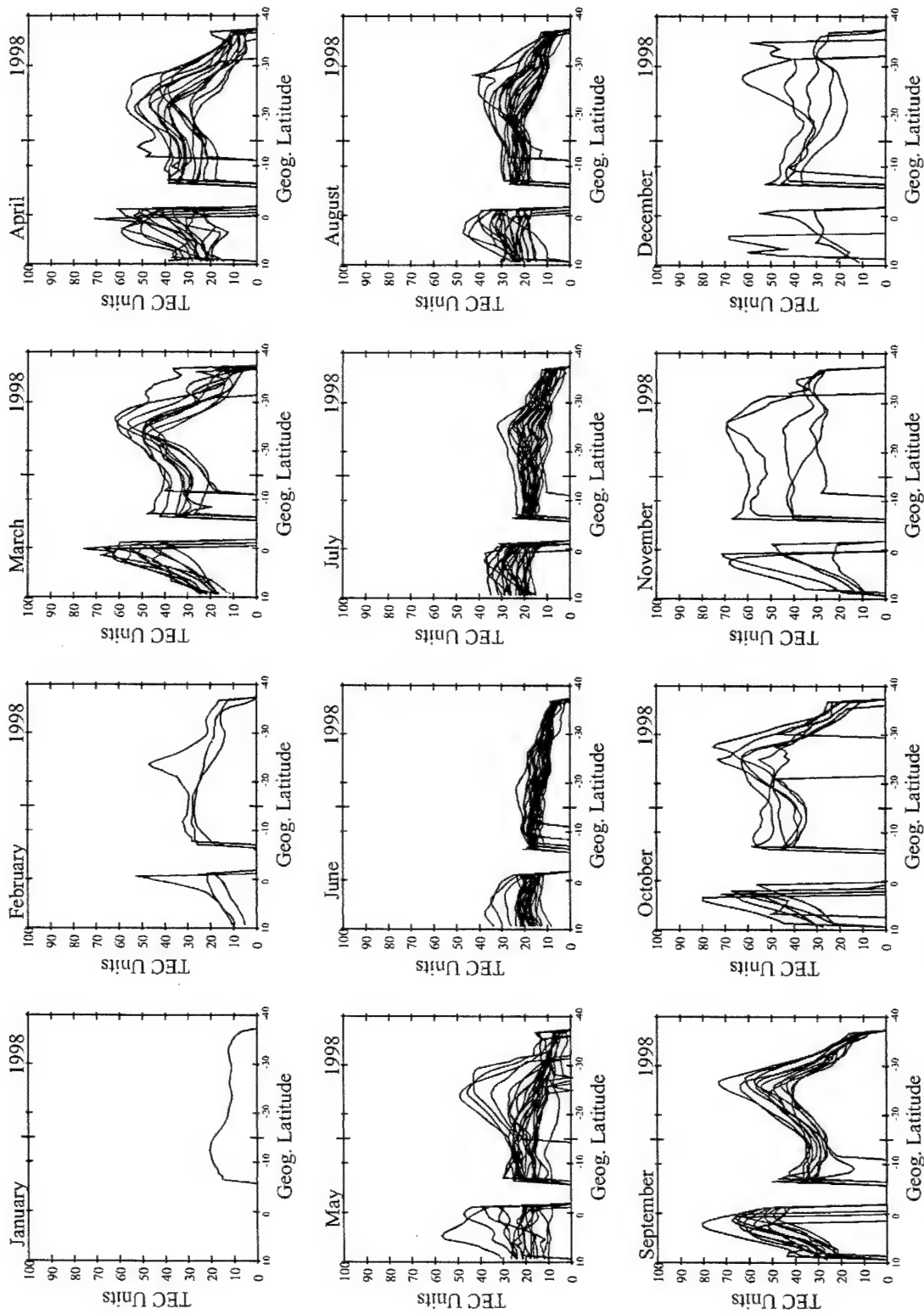


Figure 5. Same as Figure 3, but for nights when scintillations were observed neither at Ancon nor Antofagasta. The equinoctial TEC distributions usually show mild crests and a higher trough.

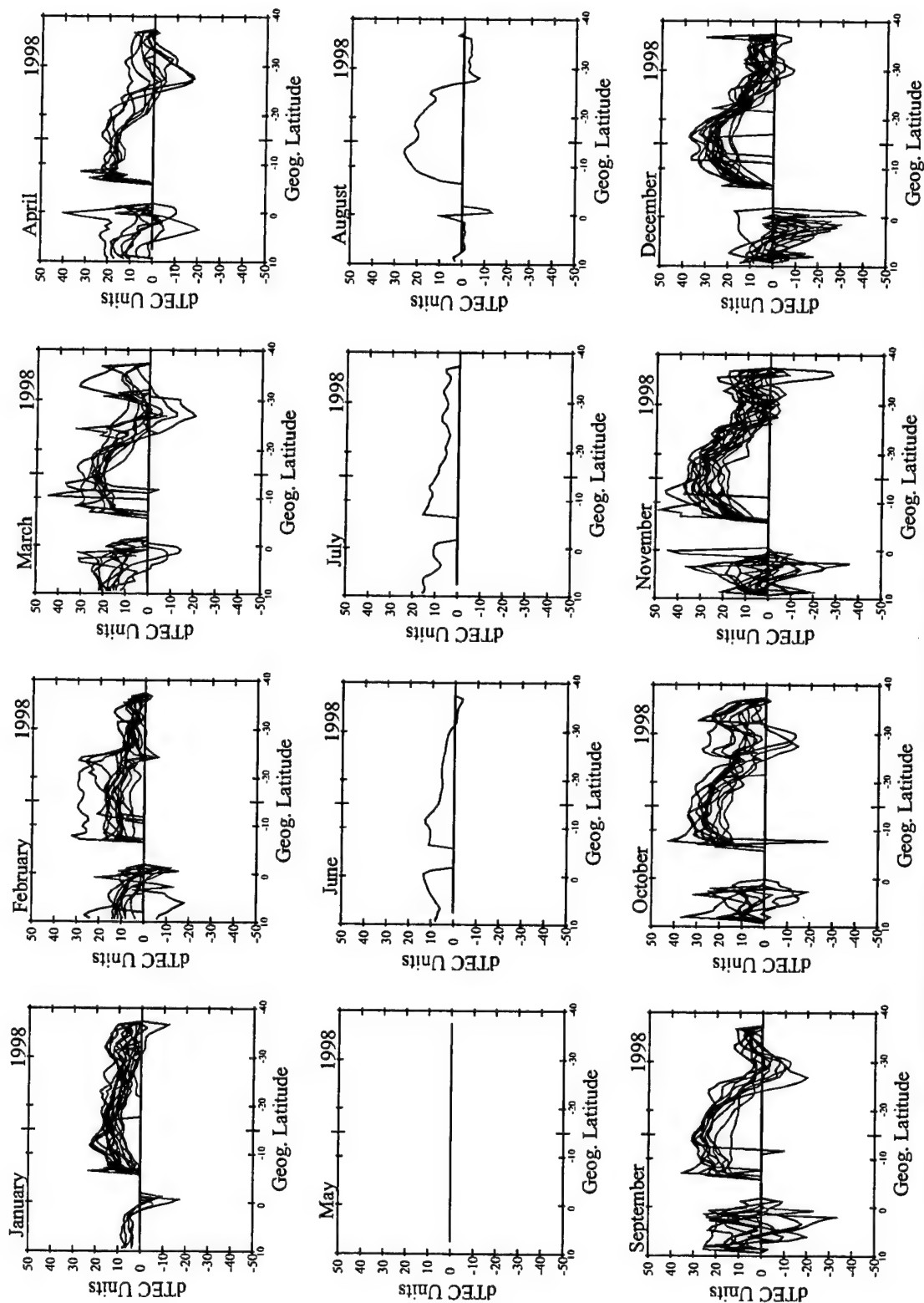


Figure 6. Time difference distributions obtained by subtracting the value of the TEC distributions corresponding to 1800 LT and the curves for 2000 LT. Only days in which scintillations occurred at both stations are plotted.

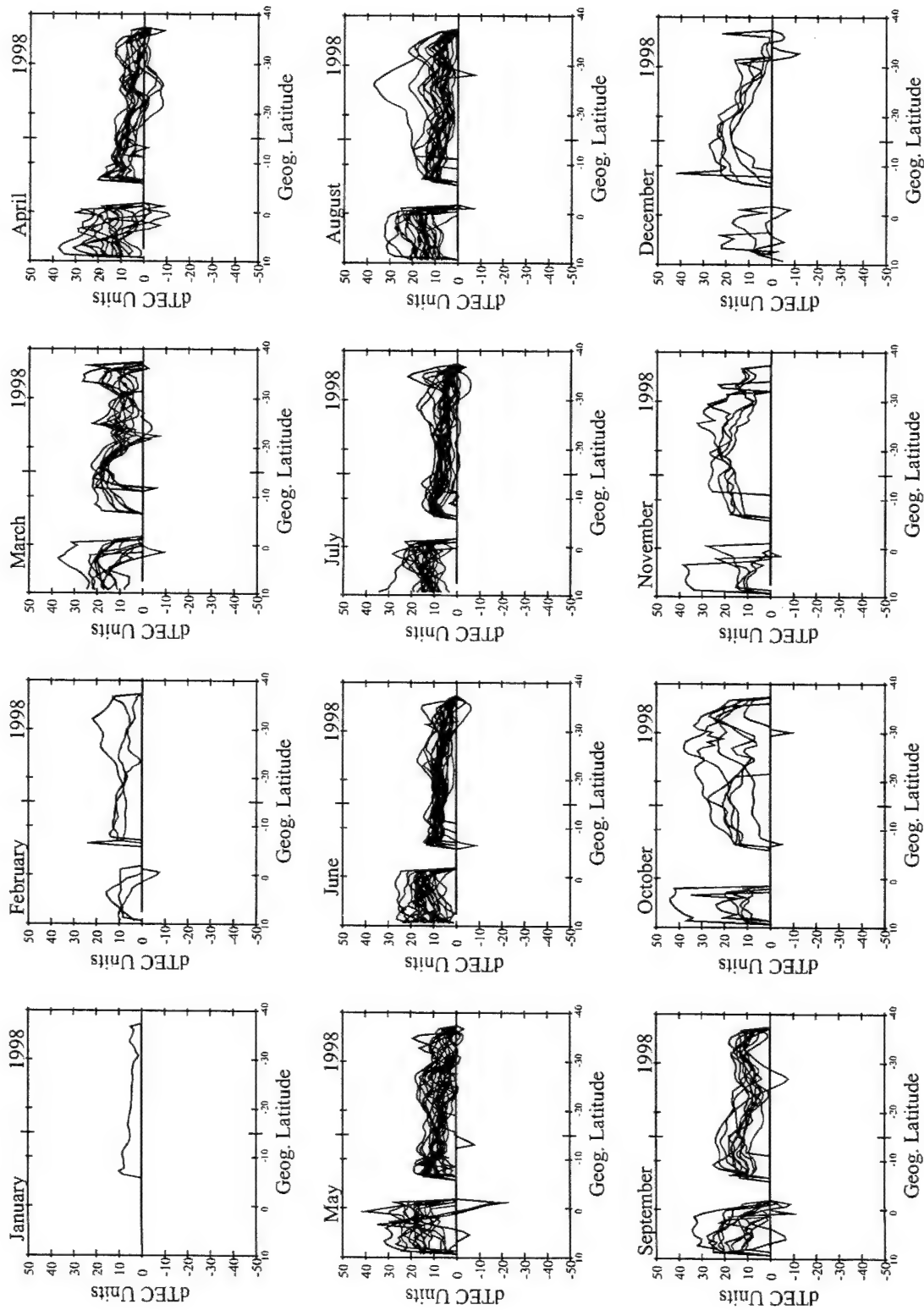


Figure 7. Same as Figure 6, but for days of no scintillations at both stations.

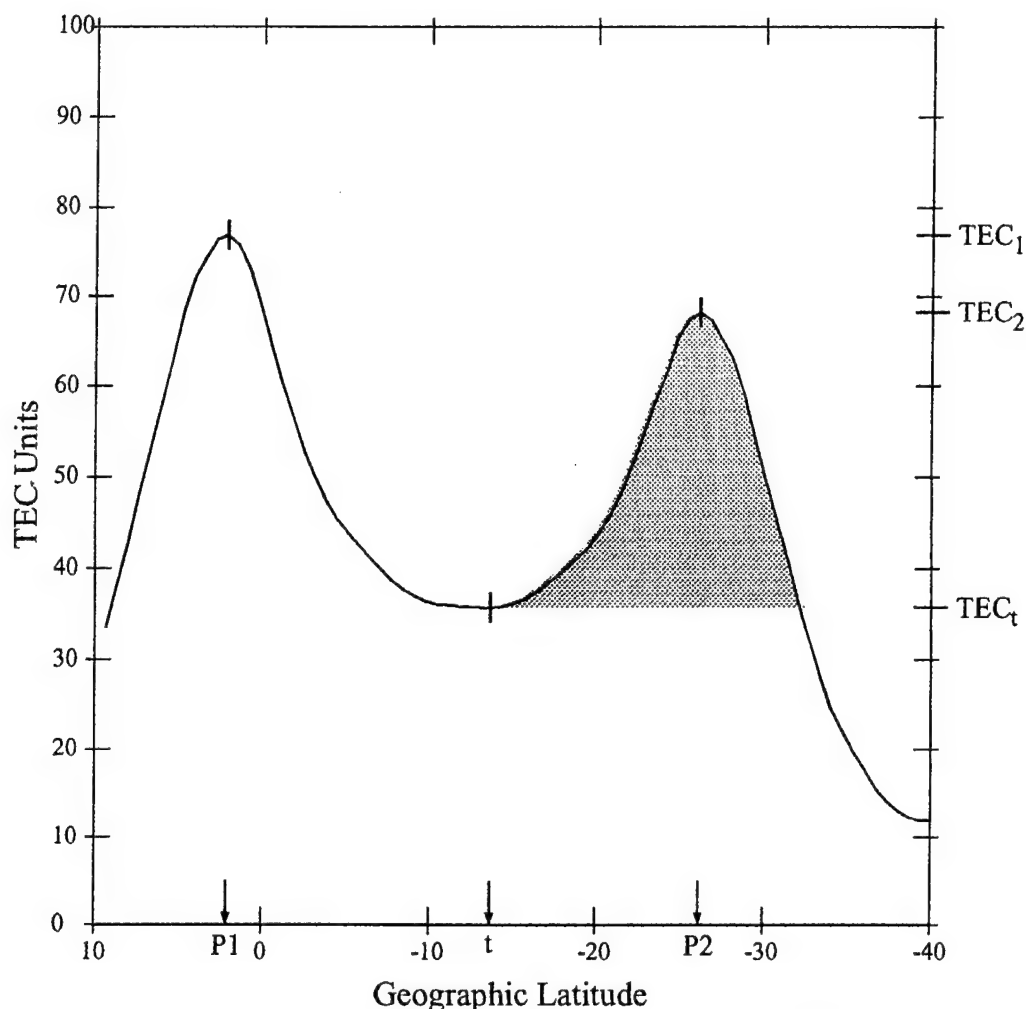


Figure 8. Sketch of a typical latitudinal distribution of TEC values. The arrows in the bottom part of the figure indicate the geographic locations of the crests (P1 and P2) and the trough (t). The shaded area in the southern crest serves to show our interpretation of the integral value of the crest. See text for details.

the TEC parameterization only for values measured at latitudes south of -5° geographic latitude. The amplitude of the trough, the peak value of the southern crest, and the latitudinal integration of excess TEC near the southern anomaly were the only parameters selected to characterize the TEC distributions. The latitudinal integration of excess TEC is related to the total amount of ionization that diffuses along the field lines as the result of the equatorial fountain effect and the transequatorial plasma transport produced by the meridional wind.

The top panels of Plate 4 show mass plots of the amplitude of the southern crest versus the TEC value at the trough at 2000 LT. The bottom panels display the trough amplitude as a function of the TEC latitudinal integration, again at 2000 local time. The three panels in each row correspond to December solstice, equinoxes, and June solstice seasons, respectively. Data from four months are included in each panel; the months included are printed in the upper right corner of each frame. The red dots indicate cases when scintillations were observed at Ancon and Antofagasta. They should equally correspond to cases when plumes extended from the bottomside of the *F* layer up to 550-km altitude. The blue dots imply events when no scintillation is observed at

either site or cases of no ESF. The well-known seasonal occurrence of scintillations is evident in these panels. More red dots are seen during the equinoxes and the December solstice, and the majority of blue dots occur during the June solstitial months. It is important to mention that during some seasons, like the December solstice when the occurrence of scintillations nears 50%, there are not many blue dots, because the TEC distributions are constant in latitude and the processing software fails to compute the location of the crests and the trough.

The frames corresponding to the equinoxes (middle panels) contain the best statistical significance in each of the rows. Close examination of these panels reveals the existence of a weak separation between the red and blue dots in the top row. However, there is a preference for the scintillation (red) dots to have smaller TEC values at the trough than the no-ESF (blue) dots, but there exists a significant overlap. Better separation is observed in the equinoctial data plotted in the bottom row. No-ESF dots are grouped for low values of the latitudinal integration and high trough TEC values. Opposite to this, the ESF dots correspond to high latitudinal integration values and low trough TEC numbers. In summary, the latitudinal integrated value and the amplitude of the trough

are good parameters that can be closely associated with the occurrence of ESF.

5. Discussion

The TEC values presented in this paper were calculated following a series of processing stages, which are potentially affected by errors. Here we briefly review the main characteristics of this analysis. The TEC calculation is based upon the well-known property of the ionospheric and plasmaspheric densities to produce a delay in the pseudorange and an advance in the phase of the GPS signals. These two basic quantities (pseudorange and phase), which are commonly provided by dual-frequency GPS receivers, are combined to obtain the absolute value of the TEC. However, the pseudorange is affected by multipaths, and the phase is affected by cycle slips. In addition, it is necessary to know the satellite transmit bias and the receiver system bias. The first stage of the GPS signal processing consists of finding the value of these biases and eliminating the negative effect of multipaths. This was accomplished using the self-calibration of pseudo-range errors (SCORE) program developed by Bishop *et al.* [1996, 1997]. This algorithm uses the same measurements of the ionospheric delay to derive the sum of the receiver and the satellite biases. The self-consistent calibration is achieved by considering conjunctions of two satellites crossing the same ionospheric volume, in a common latitude and local time sector, and assuming that the TEC value is equal in the common volume. This operation is repeated for all the satellite crossings that are observed in a 24-hour period. We use the SCORE program to conduct independent calculations of the biases for all six stations for each day of the year, when at least 4 hours of data had been collected. Day-to-day variations in the biases were no more than a few TEC units. Nevertheless, the receiver bias is subject to seasonal changes, which can account for several TEC units. To obtain this monthly trend, we fitted a quadratic function to the diurnal values of the biases for each satellite and for each station. The new fitted biases were then used to recalculate the values of the TEC. The line-of-sight (oblique) TEC values were also merged with ephemeris values of the sub-ionospheric locations to compute the equivalent vertical TEC. Finally, values from all six stations were put together using a two-dimensional regression analysis, eliminating cases when cycle slips had not been corrected or when unreasonably large values of the TEC were obtained. Another likely source of error is the latitudinal variability of the plasmasphere contribution to the TEC. We minimized this effect by restricting the data that are employed in the regression analysis to satellite elevations larger than 35° . The proof that the plasmasphere density does not alter our results is the fact that a very good agreement was obtained between the TEC values measured at different stations and during latitudinal conjunctions.

The TEC latitudinal profiles of Plates 1 and 2 (corresponding to ESF nights) have indicated that during the early evening the value of the TEC at the trough rapidly decreases; simultaneously, the amplitude of the crests increases or remains unchanged until 2200 LT. We believe that this behavior can be explained in terms of a postsunset revival of the fountain effect driven by the prereversal enhancement of the F region vertical drift velocity. Both plots of Plate 3 (corresponding to no-ESF nights) have shown

that during these nights the anomaly crests were present, but their amplitude and temporal behavior were different as compared to the evolution seen in Plates 1 and 2. The amplitude of the crests of Plate 3 starts decreasing near or before 1900 LT, and the TEC value at the trough increases between 1900 and 2300 LT. This latter behavior has been explained by Balan and Bailey [1995] as the action of the reverse fountain effect driven in this case by a downward vertical drift and a plasma flow from the anomalies toward the trough. The lowering of the equatorial F region produces a pressure imbalance along the field lines, which makes the plasma located at the anomalies diffuse toward the equator by moving up the field lines.

Figure 6 indicates that during the equinoctial and December solstitial months when scintillations are simultaneously observed at both stations, the revival or resurgence of the fountain effect occurs. Figure 7 suggests that when scintillations do not occur at both stations, either a latitudinal uniform decay of TEC or a reverse fountain effect was the typical pattern. This evidence supports a previous study reported by Fejer *et al.* [1999], in which they indicated that the vertical drift velocity was the controlling parameter in the generation of spread F irregularities. These authors associated the occurrence of large prereversal enhancements of the vertical drift with the initiation of strong coherent echoes, and early downward drifts with the absence of unstable layers. We suggest that the same upward drift, which drives the F region to higher and more unstable altitudes, is also responsible for the postsunset revival of the fountain effect and that the occurrence of the early downward drift becomes the driver of the reverse fountain effect. Thus Figures 6 and 7 are indirect proof of the control that the equatorial electrodynamics, and specifically the vertical drift velocity, exert upon establishing the right conditions for the development of ESF. Balan and Bailey [1995] suggested that the reverse plasma fountain could also cause the formation of plasma bubbles and irregularities at high altitudes. We found no indication of this effect in the data for 1998 that we analyzed. However, it is possible that this effect is quite rare or solar cycle dependent.

During the June solstice we found that the TEC distributions for scintillation cases were similar to the distributions corresponding to days without scintillations. However, in this season, scintillations were observed on only two days. This fact clearly limits the statistical significance of any conclusion that could be drawn from the characteristics of the TEC distributions.

Several studies have indicated the importance of the altitude of the F region in the formation of the ESF irregularities. Farley *et al.* [1970] suggested the existence of an altitude threshold that was required for ESF irregularities to evolve. Jayachandran *et al.* [1993] concluded that the altitude of the F layer, as determined by the time history of the prereversal enhancement of the vertical drift, was the deciding factor for the onset of spread F . These authors proposed that the altitude threshold for ESF to occur varied from 450 km for a solar flux equal to 120 units to 350 km for a flux value of 70 units. In this study we have been able to compare the onset of scintillation with another integrated effect of the vertical drift, namely, the amplitude of the anomaly crest.

One of the highlights of this study has been our ability to calculate the geographic locations of the trough and the peak

of both anomaly crests. We found that the peaks were not always situated symmetrically with respect to the magnetic equator; neither was the trough always centered just at the equator. Similar distributions have been shown by *Walker et al.* [1994], based on measurements conducted in southeast Asia, and *Vladimer et al.* [1997] using measurements conducted with the TOPEX/Poseidon satellite. *Balan and Bailey* [1995] found a weak TEC anomaly in their simulations of the equatorial ionosphere and plasmasphere. These authors obtained crest/trough ratios less than 2, much less than the ratios equal to 5 found in this study. Thus our TEC distributions are consistent with previous experimental measurements but not with previous modeling efforts. This fact points out the need to refine the characteristics of the input parameters that are commonly used to drive the numerical models. We suggest that changing the altitude or latitudinal distribution of the vertical $\mathbf{E} \times \mathbf{B}$ drifts may produce wider or narrower and more or less pronounced anomaly crests. New modeling efforts are needed in order to prove this point.

The presence of asymmetric anomaly peaks and the occurrence of a rapid decay of a larger crest have been interpreted as an indication of the effect of a persistent transequatorial neutral wind blowing the F region density from one hemisphere toward the opposite, creating a larger TEC crest in the downwind hemisphere. If the transequatorial wind persists for several hours after sunset, a significant lowering of the F layer may occur, which initiates a rapid recombination of the F layer. This argument was used by *Maruyama and Matuura* [1984] to suggest that the transequatorial wind could be a stabilizing mechanism due to the lowering of the F region in the upwind hemisphere. We have not seen such an effect, but at the same time we acknowledge the lack of completeness in the Northern Hemisphere portion of our TEC distributions.

We have been able to parameterize the TEC distributions using the location and amplitude of the anomaly peaks as controlling parameters. However, we found that these parameters could not be used unequivocally to define the onset of ESF. In contrast to this, time difference profiles of the distributions at 1800 and 2000 LT had a far superior correlation with the occurrence of ESF. We suggest that carrying out a real-time tracking of the variability of the time difference profiles may help us to get closer to a forecasting capability of the occurrence of ESF. However, several other steps have to be carried out concurrently with making the pseudorange and phase data available on real time. One consists of assessing how much earlier before sunset is it possible to obtain a reliable estimate of the trend that the TEC profiles have at the crests and the trough. Another important one is determining whether all the scintillation events correspond to cases of well-elongated plasma plumes extending to the topside and to see if scintillation events with different characteristics (S4 and spectral slope) are accompanied by different types of TEC distributions. Finally, it is necessary to prove that only a partial pass of a GPS satellite can be used to obtain absolute values of TEC.

6. Conclusions

This investigation has led to the following insights:

1. The SCORE program was used to process daily RINEX files corresponding to all the days in 1998 when data were

acquired by any of the six stations. The excellent agreement that we found in the TEC values measured at common boundaries during consecutive days and at adjacent stations reaffirms the merits of the processing technique that we used to obtain TEC values.

2. The TEC latitudinal distributions show the presence of two crests varying in location between 12° and 20° and a trough situated near the magnetic equator. The crests develop at local times when the vertical velocity is upward. This fact is in agreement with the role of the fountain effect as the generator of the equatorial anomaly. On a few days we observed, in the early evening, an increase of the TEC values at the trough. This fact suggests the appearance of a reverse fountain effect occurring right after sunset.

3. We determined the presence/absence of ESF (plumes) based on the RTI maps collected by the JULIA radar and records of scintillation from two stations spaced in latitude. One of the scintillation stations is located near the magnetic equator (Ancon), and the other one is located at -11° magnetic latitude (Antofagasta).

4. Close comparison between the appearance of ESF and the difference of TEC profiles obtained at 1800 and 2000 LT indicates that during the equinoxes and the December solstice, ESF develops on nights when there is a decrease of the TEC values at the trough and an augmentation of TEC at the crests.

5. The location and amplitude of the crests and trough and the integrated TEC value inside the southern anomaly have been used to parameterize the TEC distributions. We found that during the equinoxes the TEC value at the trough can be related to the ESF activity. When the trough TEC value is below 30 units, plumes were present most of the time, but for higher values the plumes were absent.

6. The presence of only one GPS receiver at latitudes north of Ancon limited the possibilities of resolving the northern crest in 1998. Nevertheless, a new GPS receiver has already been deployed at 3.8°S latitude (7.8° magnetic latitude) in February 2000, and four more will be placed in late 2000 and 2001. This will allow us to fully characterize the northern crest of the anomaly and to examine the effect of the meridional winds by looking at the asymmetry of the peaks.

Acknowledgments. The authors would like to thank G. Bishop of the Air Force Research Laboratory for allowing us to use the SCORE program, which was instrumental in the success of this study. M. Bevis and E. Kendrick of the University of Hawaii provided data from their Iquique and Copiapo stations; both stations are part of the South Andes Project (SAP). We are grateful to Su. Basu for her helpful comments and suggestions on the paper. We thank Jorge Espinoza and Ruben Villafani for their dedication to the smooth operation of the spaced receiver scintillation instrument at Ancon, Peru. One of the authors (C.E.V.) thanks R. F. Woodman and the personnel of the Jicamarca Radio Observatory for their hospitality during a six-month sabbatical visit in which part of this work was conducted. The work at Boston College was partially supported by NSF grants ATM-9714804 and ATM-9819912, and by Air Force Research Laboratory contract F19628-97-C-0094. The work at the Air Force Research Laboratory was partially supported by AFOSR task 231069 and 2311SDA4. The observatory of Ancon is operated by the Geophysical Institute of Peru, Ministry of Education. The Jicamarca Radio Observatory is operated by the Geophysical Institute of Peru, Ministry of Education, with support from the National Science Foundation Cooperative Agreements ATM-9022717 and ATM-9408441 to Cornell University. Janet G. Luhmann thanks Graham J. Bailey and another referee for their assistance in evaluating this paper.

References

- Aggson, T. L., N. C. Maynard, W. B. Hanson, and J. L. Saba, Electric field observations of equatorial bubbles, *J. Geophys. Res.*, **97**, 2997, 1992.
- Balan, N., and G. J. Bailey, Equatorial plasma fountain and its effects: Possibility of an additional layer, *J. Geophys. Res.*, **100**, 21,421, 1995.
- Basu, S., and S. Basu, Equatorial scintillations: Advances since ISEA-6, *J. Atmos. Terr. Phys.*, **47**, 753, 1985.
- Basu, S., et al., Scintillations, plasma drifts, and neutral winds in the equatorial ionosphere after sunset, *J. Geophys. Res.*, **101**, 26795, 1996.
- Bishop, G. J., A. Mazzella, E. Holland, and S. Rao, Algorithms that use the ionosphere to control GPS errors, paper presented at *Position Location and Navigation Symposium (PLANS)*, Inst. of Electr. and Electr. Eng. Piscataway, N. J., 1996.
- Bishop, G. J., A. J. Mazzella, S. Rao, A. Batchelor, P. Fleming, N. Lunt, and L. Kersley, Validations of the SCORE process, paper presented at *ION National Technology Meeting*, Inst. of Navig., Alexandria, Va., 1997.
- Booker, H. G., and H. W. Wells, Scattering of radio waves by the *F* region of the ionosphere, *J. Geophys. Res.*, **43**, 249, 1938.
- Crain, D. J., R. A. Heelis, G. J. Bailey, and A. D. Richmond, low-latitude plasma drifts from a simulation of the global atmospheric dynamo, *J. Geophys. Res.*, **98**, 6039, 1993.
- Doherty, P. H., P. J. Gendron, R. Loh, and D. N. Anderson, "The spatial and temporal variations in ionospheric range delay", paper presented at the *Institute of Navigation GPS-97*, Sept. 1997.
- Farley, D. T., and D. L. Hysell, Radar measurements of very small aspect angles in the equatorial ionosphere, *J. Geophys. Res.*, **101**, 5177, 1996.
- Farley, D. T., B. B. Balsley, R. F. Woodman, and J. P. McClure, Equatorial spread *F*: Implications of VHF radar observations, *J. Geophys. Res.*, **75**, 7199, 1970.
- Farley, D. T., E. Bonelli, B. G. Fejer, and M. F. Larsen, The prereversal enhancement of the zonal electric field in the equatorial ionosphere, *J. Geophys. Res.*, **91**, 13,723, 1986.
- Fejer, B. G., E. R. de Paula, S. A. Gonzalez, and R. F. Woodman, Average vertical and zonal *F* region plasma drifts over Jicamarca, *J. Geophys. Res.*, **96**, 13,901, 1991.
- Fejer, B. G., L. Scherliess, and E. R. de Paula, Effects of the vertical plasma drift velocity on the generation and evolution of equatorial spread *F*, *J. Geophys. Res.*, **104**, 19,859, 1999.
- Groves, K. M., et al., Equatorial scintillation and systems support, *Radio Sci.*, **32**, 2947, 1997.
- Hanson, W. B., and R. J. Moffett, Ionization transport effects in the equatorial *F* region, *J. Geophys. Res.*, **71**, 5559, 1966.
- Hanson, W. B., S. Sanatani, and T. N. L. Patterson, Influence of the *E* region dynamo on equatorial spread *F*, *J. Geophys. Res.*, **88**, 3169, 1983.
- Hanson, W. B., B. L. Cragin, and A. Dennis, The effect of vertical drift on the equatorial *F*-region stability, *J. Atmos. Terr. Phys.*, **48**, 205, 1986.
- Hanson, W. B., W. R. Coley, R. A. Heelis, and A. Urquhart, Fast equatorial bubbles, *J. Geophys. Res.*, **102**, 2039, 1997.
- Huang, C. Y., W. J. Burke, J. S. Machuzak, L. C. Gentile, and P. J. Sultan, DMSP observations of equatorial plasma bubbles in the topside ionosphere near solar maximum, *J. Geophys. Res.*, **106**, 8131, 2001.
- Hysell, D. L., and J. D. Burcham, JULIA radar studies of equatorial spread *F*, *J. Geophys. Res.*, **103**, 29155, 1998.
- Hysell, D. L., M. C. Kelley, W. E. Swartz, and R. F. Woodman, Seeding and layering of equatorial spread *F* by gravity waves, *J. Geophys. Res.*, **95**, 17,253, 1990.
- Jayachandran, B., N. Balan, P. B. Rao, J. H. Sastri, and G. J. Bailey, HF Doppler and ionosonde observations on the onset conditions of equatorial spread *F*, *J. Geophys. Res.*, **98**, 13,741, 1993.
- Kelley, M. C., G. Haerendel, H. Kappler, A. Valenzuela, B. B. Balsley, D. A. Carter, W. L. Ecklund, C. W. Carlson, B. Hausler, and R. Torbert, Evidence for a Rayleigh-Taylor type instability and upwelling of depleted density regions during equatorial spread *F*, *Geophys. Res. Lett.*, **3**, 448, 1976.
- Kelley, M. C., M. F. Larsen, and C. LaHoz, Gravity wave interaction of equatorial spread *F*: A case study, *J. Geophys. Res.*, **86**, 9087, 1981.
- Kelley, M. C., et al., The Condor equatorial spread *F* campaign: Overview and results of the large scale measurements, *J. Geophys. Res.*, **91**, 5487, 1986.
- Kelley, M. C., D. Kotsikopoulos, T. Beach, and D. L. Hysell, Simultaneous global positioning system and radar observations of equatorial spread *F* at Kwajalein, *J. Geophys. Res.*, **101**, 2333, 1996.
- Kudeki, E., B. G. Fejer, D. T. Farley, and H. M. Ierikic, Interferometer studies of equatorial *F* region irregularities and drifts, *Geophys. Res. Lett.*, **8**, 377, 1981.
- Lunt, N., L. Kersley, G. J. Bishop, and A. J. Mazzella Jr., The contribution of the protonosphere to GPS total electron content: Experimental measurements, *Radio Sci.*, **34**, 1273, 1999a.
- Lunt, N., L. Kersley, G. J. Bishop, A. J. Mazzella Jr., and G. J. Bailey, The protonospheric contribution to GPS total electron content: Two-station measurements, *Radio Sci.*, **34**, 1281, 1999b.
- Maruyama, T., Modeling study of equatorial ionospheric height and spread *F* occurrence, *J. Geophys. Res.*, **101**, 5157, 1996.
- Maruyama, T., and N. Matuura, Longitudinal variability of annual changes in activity of equatorial spread *F* and plasma bubbles, *J. Geophys. Res.*, **89**, 10,903, 1984.
- McClure, J. P., W. B. Hanson, and J. H. Hoffman, Plasma bubbles and irregularities in the equatorial ionosphere, *J. Geophys. Res.*, **82**, 2650, 1977.
- Mendillo, M., J. Baumgardner, X. Pi, P. J. Sultan, and R. Tsunoda, Onset conditions for equatorial spread *F*, *J. Geophys. Res.*, **97**, 13,865, 1992.
- Ossakow, S. L., S. T. Zalesak, B. E. McDonald, and P. K. Chaturvedi, Nonlinear equatorial spread-*F*: Dependence on altitude of the *F* peak and bottomside background electron density gradient scale length, *J. Geophys. Res.*, **84**, 17, 1979.
- Pi, X., A. J. Mannucci, U. J. Lindqwister, and C. M. Ho, Monitoring of global ionospheric irregularities using a worldwide GPS network, *Geophys. Res. Lett.*, **24**, 2283, 1997.
- Raghavarao, R., M. Nageshwararao, J. Hanumath Sastri, G. D. Vyas, and M. Sriramara, Role of equatorial ionization anomaly in the initiation of equatorial spread-*F*, *J. Geophys. Res.*, **93**, 5959, 1988.
- Sastri, J. H., M. A. Abdu, I. S. Batista, and J. H. A. Sobral, Onset conditions of equatorial (range) spread *F* at Fortaleza, Brazil, during the June solstice, *J. Geophys. Res.*, **102**, 24,013, 1997.
- Sridharan, R., R. Sekar, and S. Gurubaran, Two-dimensional high-resolution imaging of the equatorial plasma fountain, *J. Atmos. Terr. Phys.*, **55**, 1661, 1993.
- Sridharan, R., D. PallamRaju, R. Raghavarao, and P. V. S. Ramarao, Precursor to equatorial spread-*F* in OI 630.0 nm dayglow, *Geophys. Res. Lett.*, **21**, 2797, 1994.
- Sultan, P. J., and F. I. Rich, Observations and modeling of the seasonal and longitudinal occurrence pattern of equatorial spread-*F*, paper presented at Chapman Conference on Space Weather: Progress and Challenges in Research and Applications, AGU, Clearwater, Fla., March 2000.
- Tsunoda, R. T., On the spatial relationship of 1-m equatorial spread *F* irregularities and plasma bubbles, *J. Geophys. Res.*, **85**, 185, 1980.
- Tsunoda, R. T., Control of the seasonal and longitudinal occurrence of equatorial scintillations by the longitudinal gradient in the integrated *E* region Pedersen conductivity, *J. Geophys. Res.*, **90**, 447, 1985.
- Valladares, C. E., W. B. Hanson, J. P. McClure, and B. L. Cragin, Bottomside sinusoidal irregularities in the equatorial *F*-region, *J. Geophys. Res.*, **88**, 8025, 1983.
- Vladimer, J. A., P. Jastrzebski, M. C. Lee, P. H. Doherty, D. T. Decker, and D. N. Anderson, Longitude structure of ionospheric total electron content at low latitudes measured by the TOPEX/Poseidon satellite, *Radio Sci.*, **34**, 1239, 1999.
- Walker, G. O., J. H. K. Ma, and E. Golton, The equatorial ionospheric anomaly in electron content from solar minimum for South East Asia, *Ann. Geophys.*, **12**, 195, 1994.
- Weber, E. J., et al., Equatorial plasma depletion precursor signatures and onset observed at 11° south of the magnetic equator, *J. Geophys. Res.*, **101**, 26,829, 1996.
- Woodman, R. F., Vertical drift velocities and east-west electric fields at the magnetic equator, *J. Geophys. Res.*, **75**, 6249, 1970.
- Woodman, R. F., and C. LaHoz, Radar observations of *F* region equatorial irregularities, *J. Geophys. Res.*, **81**, 5447, 1976.

Zalesak, S. T., and S. L. Ossakow, Nonlinear equatorial spread F : Spatially large bubbles resulting from large horizontal scale initial perturbations, *J. Geophys. Res.*, **85**, 2131, 1980.

S. Basu and K. Groves, Air Force Research Laboratory, Hanscom AFB, MA 01731.

M. P. Hagan, R. E. Sheehan, and C. E. Valladares, Institute for Scientific Research, Boston College, 140 Commonwealth Ave., Chestnut Hill, MA 02467. (valladar@bc.edu).

D. Hysell, Department of Physics and Astronomy, Clemson University, Clemson, SC 29634.

A. J. Mazzella Jr., Northwest Research Associates, Bellevue, WA 98809.

(Received November 15, 2000; revised March 21, 2001; accepted March 23, 2001.)

Ionospheric effects of major magnetic storms during the International Space Weather Period of September and October 1999: GPS observations, VHF/UHF scintillations, and in situ density structures at middle and equatorial latitudes

Sunanda Basu,¹ Santimay Basu,² C. E. Valladares,³ H.-C. Yeh,⁴ S.-Y. Su,⁴
E. MacKenzie,³ P. J. Sultan,² J. Aarons,⁵ F. J. Rich,² P. Doherty,³
K. M. Groves,² and T. W. Bullett²

Abstract. In this paper we present a study of the ionospheric effects of a halo coronal mass ejection (CME) initiated on the Sun on September 20, 1999, and causing the largest magnetic storm during this month on September 22–23, 1999, with the hourly *Dst* index being -167 nT at ~ 2400 UT on September 22. The recurrent CME on October 18 caused an even larger magnetic storm on October 22, 1999, with *Dst* of -231 nT at ~ 0700 UT. The ionospheric effects of these two major magnetic storms are studied through their effects on a prototype of a Global Positioning System (GPS)-based navigation system called Wide Area Augmentation System (WAAS) being developed by the Federal Aviation Administration for use in the continental United States and their impact on global VHF/UHF communication systems. It is shown that the penetration of transient magnetospheric electric fields equatorward of the shielding region at midlatitudes, which have been well-correlated in the past with rapid changes in the well-known *Dst* index (or through its recently available high resolution 1-min counterpart the SYM-H index), can cause large increases of total electron content (TEC), TEC fluctuations, and saturated 250-MHz scintillation, and these, in turn, may have significant impacts on WAAS. The local time of *Dst* changes (and not just *Dst* magnitude) was found to be very important for WAAS, since the largest effects on TEC are seen near dusk. The prompt penetration of these magnetospheric electric fields all the way to the magnetic equator causes augmentation or inhibition of equatorial spread *F*. The global ionospheric response to these storms has been obtained from ground-based TEC observations with a GPS network and space-based in situ density and electric field measurements using the Republic of China Satellite-1 (ROCSAT-1) and several Defense Meteorological Satellite Program satellites. These prompt penetration electric fields cause VHF/UHF scintillations and GPS TEC variations at low latitudes in the specific longitude sector for which the early evening period corresponds to the time of rapid *Dst* variations and maximum *Dst* phase. The effects of the delayed ionospheric disturbance dynamo and those of decreased magnetospheric convection on postmidnight irregularity generation are shown to be confined to a part of the same longitude range that actively responded to the prompt penetration of electric fields in the early evening sector.

1. Introduction

The Solar Terrestrial Energy Program–Research, Applications and Modeling Phase (S-RAMP) Group of the Scientific Committee for Solar Terrestrial Physics (SCSTEP) con-

ceived and coordinated a month-long campaign interval during September 1999 as an International Space Weather Period (ISWP) to follow the progress of space weather events from their initiation on the Sun to their impacts at the Earth, including their effects on space-based and ground-based technological systems and for assessment of the accuracy of specification and forecasting techniques. A great deal of material on the geoeffective solar wind events during this month has been compiled in a special Web page for which the URL is http://aoss.engin.umich.edu/intl_space_weather/sramp/ to which the reader is referred for additional information (J. U. Kozyra, private communication, 1999). Here we provide some basic information on the interplanetary shocks and southward interplanetary magnetic fields (IMF) that triggered the largest magnetic storm during the core campaign period.

This large magnetic storm was triggered by an interplanetary magnetic cloud (IMC) event extending from 2000 UT on September 22 to 0700 UT on September 23 with maximum IMF >

¹Atmospheric Sciences Division, National Science Foundation, Arlington, Virginia, USA.

²Space Vehicles Directorate, Air Force Research Laboratory, Hanscom Air Force Base, Massachusetts, USA.

³Institute for Scientific Research, Boston College, Chestnut Hill, Massachusetts, USA.

⁴Institute of Space Science, National Central University, Chung-Li, Taiwan.

⁵Center for Space Physics, Boston University, Boston, Massachusetts, USA.

25 nT. This IMC was able to drive a major magnetic storm with minimum *Dst* of -167 nT at ~ 2400 UT on September 22. The most likely solar source was a faint but complete halo coronal mass ejection (CME) event seen at 0606 UT on September 20 which had a travel time of 63 hours (or a speed of 660 km s^{-1}) to reach Earth. The following month a CME recurrent with the September 20 event was observed at 0006 UT on October 18. This resulted in another major magnetic storm with minimum *Dst* of -231 nT, which occurred at 0700 UT on October 22, 1999. This latter CME was a partial 210° wide halo type which took 77 hours (or a speed of 540 km s^{-1}) to reach Earth. This storm has also been made part of the ISWP study. We will utilize both storms in this paper, to emphasize that ionospheric effects on specific communication or navigation systems are greatly dependent on the local time of maximum magnetic perturbations and not just on the magnitude of the perturbations. Thus we shall show that the September 1999 storm had a more severe effect on such systems in the United States than the October 1999 storm even though the latter was classified as a much bigger magnetic storm.

Since one of the major objectives of this enterprise was to provide as complete as possible space-based and ground-based observations of these space weather events, we tried to use several global databases to follow the effects of these storms on the total electron content (TEC) and plasma density irregularity structure of the middle- and low-latitude ionosphere. In particular, we chose to cover the middle-latitude ionosphere as an important Global Positioning System (GPS)-based navigation system is being developed for this region in the continental United States. Earlier morphological studies by *Aarons et al.* [1972] and *Aarons and Allen* [1971] have shown that the middle-latitude ionosphere is quite benign, its characteristics being generally determined by the diurnal, seasonal, and solar cycle variations in solar production. It is only during major magnetic storms that this predictable variability can be dramatically overturned as the high-latitude convection pattern expands equatorward. Numerous studies made over the last three decades using the Millstone Hill incoherent scatter radar and the TEC and scintillation network of the Air Force Research Laboratory have delineated the major features of ionospheric storms which result from large energy inputs to the upper atmosphere associated with major magnetic storms. *Foster* [1993] presents a good review of the results obtained starting from 1970. For instance, the enhancement of TEC during local dusk at 1800 LT is well known [*Mendillo et al.*, 1970]. *Rishbeth and Hanson* [1974] suggested that this increase was caused by advection of relatively dense plasma into the observing volume, a fact that was confirmed by observations made at Millstone Hill [*Evans*, 1973; *Buonsanto et al.*, 1979]. *Buonsanto* [1999] in his comprehensive review on ionospheric storms points out that this dusk effect of TEC increase should be distinguished from a more long-lived positive storm effect which is due to large-scale changes in the thermospheric circulation caused by heating in the auroral zone. After the TEC increase at dusk, particularly at high midlatitudes, there is a sharp transition to a negative phase, which can generally be attributed to the equatorward motion of the midlatitude trough [*Mendillo and Klobuchar*, 1975; *Buonsanto et al.*, 1979]. Geostationary satellite observations at 137 MHz made from Hanscom Field, Massachusetts, for which the subionospheric (350 km) location is $L = 2.8$ showed abrupt onset of scintillations during such major magnetic storms which were coincident with sharp TEC decreases and the appearance of stable auroral red (SAR) arcs

[*Basu*, 1974]. At that time, Basu hypothesized that perhaps the same processes that give rise to SAR arcs at the equatorward edge of the plasmopause are also responsible for generating field-aligned plasma density irregularities of approximately kilometers to hundreds of meters scales that give rise to VHF scintillations.

In the intervening two decades many studies have provided evidence for the presence of intense convection electric fields in the expanded auroral oval [*Foster and Aarons*, 1988; *Yeh et al.*, 1991, and references therein] while transient fields penetrate equatorward of the shielding region at midlatitudes [*Gonzales et al.*, 1983; *Burke et al.*, 1998]. *Foster and Rich* [1998] provide a good summary of such results. Unfortunately, the Millstone Hill incoherent scatter radar (ISR) was not operating during these particular September and October storms, the ISR World Days being scheduled near the middle of the month in both cases. Thus, for these two storms we utilize the scintillation data from Hanscom Air Force Base (AFB), Massachusetts, the Digisonde data from Millstone Hill, and the TEC fluctuation data from the nearby station in Westford, Massachusetts, to monitor the small (approximately kilometers to hundreds of meters) and large (approximately tens of kilometers) scale irregularity behavior in conjunction with Defense Meteorological Satellite Program (DMSP) F12, F13, and F14 overflights to monitor the particles and fields and thermal density structure in the topside ionosphere. In addition, we utilize GPS TEC data from a latitudinal chain of International GPS Service for Geodynamics (IGS) stations to monitor TEC across the continental United States.

Since a major objective of the ISWP is to monitor the effects on technological systems, we chose to study the possible impact of these storms on the Wide Area Augmentation System (WAAS) of the Federal Aviation Administration (FAA). The WAAS is a system which provides corrections to enable aviation users of the Standard Positioning Service (SPS) GPS capabilities to achieve accuracy, integrity, and availability in all phases of flight from enroute through precision approach to airports [*Dehel et al.*, 1999]. One of the corrections provided by the WAAS to enable accuracy improvements is the correction for the signal delay due to the ionosphere. Users of the SPS GPS system are currently limited to the L_1 frequency (1.575 GHz) and are not directly able to measure the delay of the signal due to the ionosphere. The WAAS provides this delay information in the form of a grid of data, which is transmitted to the user as part of the corrections. One of the questions confronting the users of the WAAS system is the effect of ionospheric storms, with its associated steep TEC gradients particularly during the current sunspot maximum phase. It is thus important to establish their effects on system operation and to explore the possibility of impact mitigation through predictions.

While studying the midlatitude impacts, it became apparent that penetration electric fields during magnetic storms would also affect WAAS-like systems currently under development in countries such as Japan, India, and the Latin American region. We thus utilized a latitudinal chain of TEC stations operating from Bogota, Colombia, to Santiago, Chile [*Valladares et al.*, 2001], in conjunction with TEC fluctuation data at numerous low-latitude stations from the IGS network to provide a global description of such perturbations. The effect of amplitude scintillation on the GPS and VHF/UHF communication systems was studied by utilizing the Air Force Research Laboratory (AFRL) scintillation network in the South American and

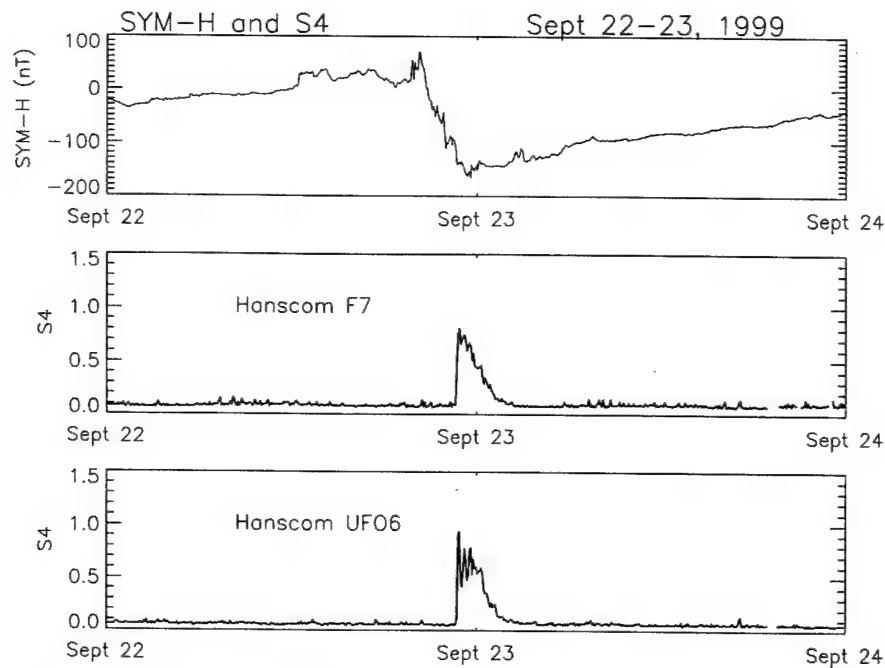


Figure 1. Scintillation index S4 at 250 MHz from two geostationary satellites Fleetsat 7 (F7) and UFO6 (U6) received at Hanscom Air Force Base (AFB), Massachusetts, plotted against SYM-H index for September 22–24, 1999.

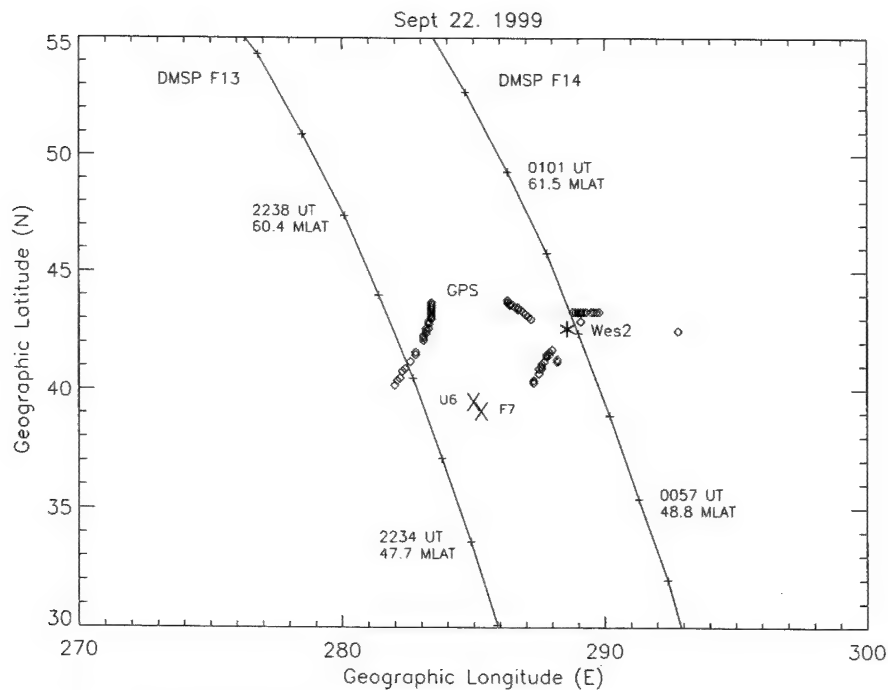


Figure 2. The 350-km intersection points for F7 and U6 for scintillation data from Hanscom AFB, Massachusetts, shown in Figure 1. Several subionospheric (350 km) tracks of GPS satellites from Westford (Wes2 indicated by a star) obtained between 2200 and 2400 UT on September 22 are also shown. The diamonds on the tracks indicate total electron content (TEC) fluctuations $>1 \text{ TEC U min}^{-1}$. Two Defense Meteorological Satellite Program (DMSP) subsatellite tracks (indicated by solid lines) close to Hanscom are also shown; the F13 track is for 2233–2240 UT on September 22, and the F14 track is for 0056–0102 UT on September 23. The corrected magnetic latitudes (MLATs) of the 110-km field line mapped positions of the DMSP satellites are indicated along the tracks at two specific UTs.

F13

22 Sept 1999

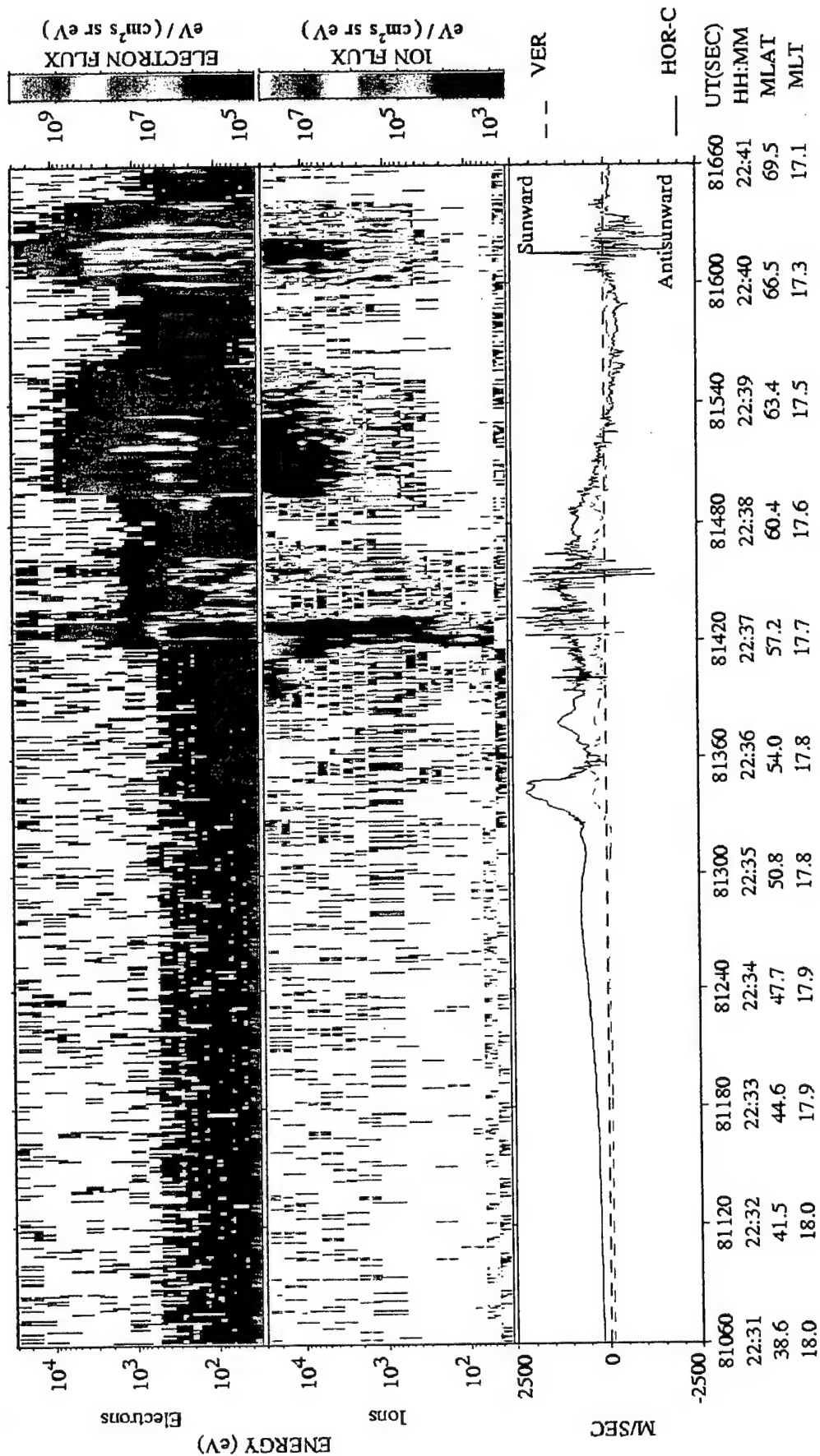


Plate 1. DMSP F13 measurements for the satellite track shown in Figure 2. The top and middle plots contain energy versus time spectrograms for downcoming electron and ion fluxes. Color codes for directional differential fluxes, particles ($\text{cm}^2 \text{ s sr eV}^{-1}$) are given to the right of the spectrograms. All parameters are plotted as functions of UT, MLAT, and the magnetic local time. The bottom plot gives the horizontal (solid line) and vertical (dashed line) components of plasma drift. A large horizontal and sunward drift structure of 2000 m s^{-1} is seen between 2235:20 and 2236:00 UT.

South Atlantic sectors. A novel feature is the extensive LT coverage provided by the high-resolution (1024 Hz) in situ measurements at 600 km from the Republic of China Satellite-1 (ROCSAT-1) with an inclination of 35° in addition to the coverage at 840 km provided by the Sun-synchronous DMSP satellites at specific LT.

2. September 22–24, 1999, Magnetic Storm

We will first present the perturbations in the middle-latitude ionosphere as a result of this magnetic storm and eventually follow the perturbations all the way to the equatorial ionosphere. Along the way, we will point out the possible impacts on WAAS and similar systems that may be operating under similar storm conditions.

2.1. Midlatitude Effects

The top panel of Figure 1 shows the high-resolution (1-min) values of the SYM-H index [Iyemori *et al.*, 2000], which closely follows the hourly *Dst* index developed by Sugiura and Poros [1971]. During this storm a fairly strong ring current developed with the SYM-H index reaching below -160 nT just prior to 2400 UT on September 22. The middle and bottom panels show the scintillation index S4 (defined by Briggs and Parkin [1963]) at 250 MHz from two geostationary satellites F7 and UFO6 plotted as a function of UT from Hanscom AFB, Massachusetts. The sudden onset of scintillations at 2240 UT on both ray paths as SYM-H (*Dst*) index drops precipitously is very evident. The geographic coordinates of the subionosphere (350 km) intersection are shown in Figure 2. The intersection points in the ionosphere are extremely close for the two geostationary satellites giving rise to simultaneous onsets of the scintillations. The orbits of two DMSP satellites and the subionospheric intersections of several GPS satellites obtained between 2200 and 2400 UT from the nearby station of Westford, Massachusetts, are also shown for subsequent use.

Earlier measurements by Wygant *et al.* [1998] on the CRRES spacecraft during the March 24, 1991, geomagnetic storm had shown that the large-scale magnetospheric electric field repeatedly penetrated into the inner magnetosphere between $L = 2$ and $L = 4$ when the rate of change of *Dst* was of the order of -50 nT h⁻¹. In this instance that rate of change was -75 nT h⁻¹ between 2200 and 2300 UT on September 22, 1999. Thus the impulsive onset of scintillations at $L = 2.8$ (53° magnetic latitude (MLAT) in this longitude sector) for the Hanscom intersection points is in all likelihood linked to the appearance of electric fields and plasma density gradients in that vicinity. (For a discussion of the relationship between different magnetic coordinate systems in this longitude sector and the representation of DMSP positions in geographic and magnetic coordinates to be discussed below, see Basu *et al.* [1983a].) The scintillation event lasts for ~ 2 hours. The Millstone Hill radar has documented many instances of such fields and gradients at ionospheric heights [Yeh *et al.*, 1991; Foster, 1993; Foster and Rich, 1998]. Unfortunately, as mentioned earlier, the radar was not operating on that day, but the two DMSP orbits shown in Figure 2, particularly the F13, provides unmistakable evidence for a large penetration electric field in the vicinity of Hanscom at 1748 MLT, i.e., at dusk. Plate 1 shows DMSP F13 measurements taken at northern high latitudes on September 22, 1999, just west of the ionospheric intersection points for the F7 and UFO6 satellites in the early evening magnetic local time (MLT) sector between 2231 and

2241 UT. The top and middle plots contain directional differential fluxes of downcoming electrons and ions with energies between 30 eV and 30 keV in energy versus time color spectrogram format [Hardy *et al.*, 1984]. The bottom panel shows the horizontal and vertical components of the plasma drift obtained from the ion drift meter (IDM) on board the satellite [Rich and Hairston, 1994]. The most important point for our purpose is the large horizontal sunward drift of ~ 2000 m s⁻¹ and a small generally upward drift seen between 52°–54° MLAT (2235:20–2236 UT) and straddling the two satellite intersection points equatorward of the energetic electron and ion precipitation boundaries. The sunward or westward drift is caused by a northward electric field of magnitude ~ 100 mV m⁻¹ consistent with measurements at the Millstone Hill radar under similar conditions quoted above. Such westward and small upward drifts were also evident in the DMSP F14 data, the orbital track for which was shown in Figure 2.

Two other measurements, namely, those using the GPS receivers [Doherty *et al.*, 1994] and the Digisonde [Reinisch and Xueqin, 1983] provide evidence for an abrupt *F* region height rise and increase in the TEC. The TEC data from Westford, Massachusetts (42.6°N, 288.5°E), are shown in Figure 3 for September 22, 1999. These data are obtained by using the carrier phase and group delay measurements of GPS signals at L_1 (1.575 GHz) and L_2 (1.227 GHz) reported at 30-s intervals along the slant path from the receiver to the satellites. Using the ionospheric zenith angles, we convert the slant TEC to equivalent vertical TEC shown. The plot is obtained by combining TEC observations from the entire constellation of GPS satellites above 30° elevation over the 24-hour UT period and taking care of satellite and receiver biases in an appropriate manner [Doherty *et al.*, 1994]. Although the TEC variation is not as smooth as that seen on quiet days (quiet day behavior is shown in Figure 5), the most significant aspects of the data are the increase in TEC of ~ 10 TEC units (10^{16} el m⁻²) around 2130 UT followed after 2200 UT by the precipitous drop of 35 TEC units at the very fast rate of ~ 1 TEC unit min⁻¹. Similarly, the Digisonde data (not shown) operating at this station also exhibit a sudden increase in the height of the ionosphere starting after 2135 UT followed by a large decrease in the critical frequency f_oF_2 (consistent with the approach of a trough) from 9.5 MHz at 2135 UT to 4.5 MHz at 2250 UT, and the ionograms show evidence of spread *F* throughout this time period. This afternoon height rise and TEC increase in the storm initial phase have been widely reported in the literature. They are considered to be a combined effect of an eastward electric field in the presence of sunlight and advection of plasma from lower latitudes [Foster, 1993, and references therein].

The precipitous drop in f_oF_2 and TEC is accompanied by large fluctuations in TEC starting at 2210 UT as shown in Figure 4. This diagram was obtained by considering the differential carrier phase data alone along the line of sight over each 30-s interval [Pi *et al.*, 1997; Basu *et al.*, 1999; Bhattacharyya *et al.*, 2000]. Figure 4 shows that TEC fluctuations were very small throughout the day until 2200 UT. Shortly thereafter, very large fluctuations, some as large ± 5 TEC units min⁻¹, are seen for several tens of minutes on almost all the satellite ray paths visible from Westford at that time. The subionospheric tracks for these satellites were shown in Figure 2. The small diamonds along the GPS satellite tracks show the locations for which the TEC fluctuations were greater than 1 TEC unit min⁻¹. Large-magnitude fluctuations on the order of ± 5 TEC

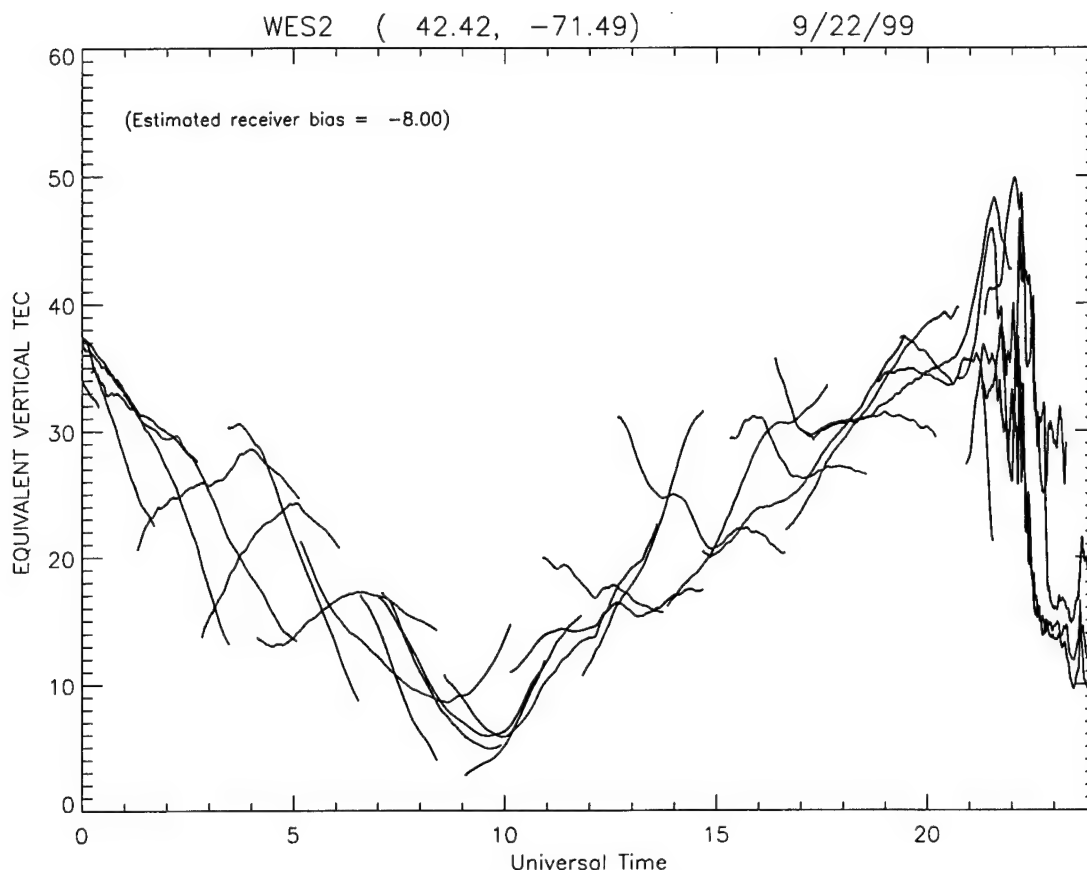


Figure 3. The equivalent vertical TEC measured using GPS satellites at Westford, Massachusetts (WES2), on September 22, 1999.

units min^{-1} are expected to be a problem for the WAAS system (A. J. Mannucci, private communication, 2000). If we consider the TEC fluctuations at Westford and the scintillations at Hanscom AFB to be two different manifestations of the irregular structure of the ionosphere, then it is possible to estimate the rate of equatorward motion of this irregularity front by considering the subionospheric separation between the TEC and scintillation ray paths and the delay in onset times. Using this separation to be 425 km and the delay to be 30 min, we obtain an average equatorward motion of $\sim 230 \text{ m s}^{-1}$ for the disturbance. Thus the 30-s sampling interval of the TEC fluctuations corresponds to a spatial scale of $\sim 7 \text{ km}$ or minimum resolvable north-south irregularity wavelengths of 14 km. In other words, the TEC fluctuations are caused by tens of kilometers scales as compared to the intensity scintillations at 250 MHz, which are caused by irregularities on the order of a kilometer or smaller (determined by the Fresnel dimension). Possible causes of these large- and small-scale irregularities will be discussed in section 4.

To determine the behavior of this large-scale gradient across the continental United States, where the WAAS system is to operate, we investigated the TEC behavior at the NE-SW chain of stations of the IGS network. The GPS TEC data from Westford, Massachusetts (WES2), North Liberty, Iowa (NLIB), Colorado Springs, Colorado (AMC2), and Pietown, New Mexico (PIE1), over a 4-day period covering the storm are shown in Figure 5. Their locations together with those of other IGS sites including stations in the equatorial region are shown in Figure 6. This diagram was kindly provided by X. Pi

and shows a small subset of the total number of IGS stations [Pi *et al.*, 1997]. The TEC scale in Figure 5 is shown in terms of range delay to make this diagram more useful to the WAAS users. To compare Figures 3 and 5 one should recall that 6.15 TEC units is equivalent to 1 m of range delay at the GPS L_1 (1.575 GHz) frequency. The storm time TEC increase causes a range delay of 8 m at Westford rising to 12 m at lower latitudes. This is followed by a much more dramatic TEC decrease from 12 to 2 TEC units in the course of an hour at some stations, owing to the equatorward motion of the midlatitude trough. The motion of these large-scale features from N-S across the United States is very evident. An unexpected and sharp range delay change of this magnitude is expected to be of concern to WAAS users. The TEC behavior on September 21 is introduced as the normal quiet day behavior for comparison to the storm time behavior on September 22. While at Westford the storm time TEC curve shows mostly a change of shape (an abrupt increase followed by a fast decrease) with both the quiet day and storm TEC causing 6–8 m range delay, the TEC behavior at lower latitudes shows an increase from 8 to 12 m in the delay introduced by the ionosphere.

The TEC increase is followed by a severe decrease on September 23, first in the existence of very low nighttime TEC values in the trough followed by a significant decrease in TEC during the daytime. This is the well-known storm negative phase caused by a composition change of the ambient ionosphere [cf. Buonsanto, 1999, and references therein]. From the point of view of the WAAS users, a decrease of 4 m in the range delay is expected at most stations during the daytime due to the storm negative phase.

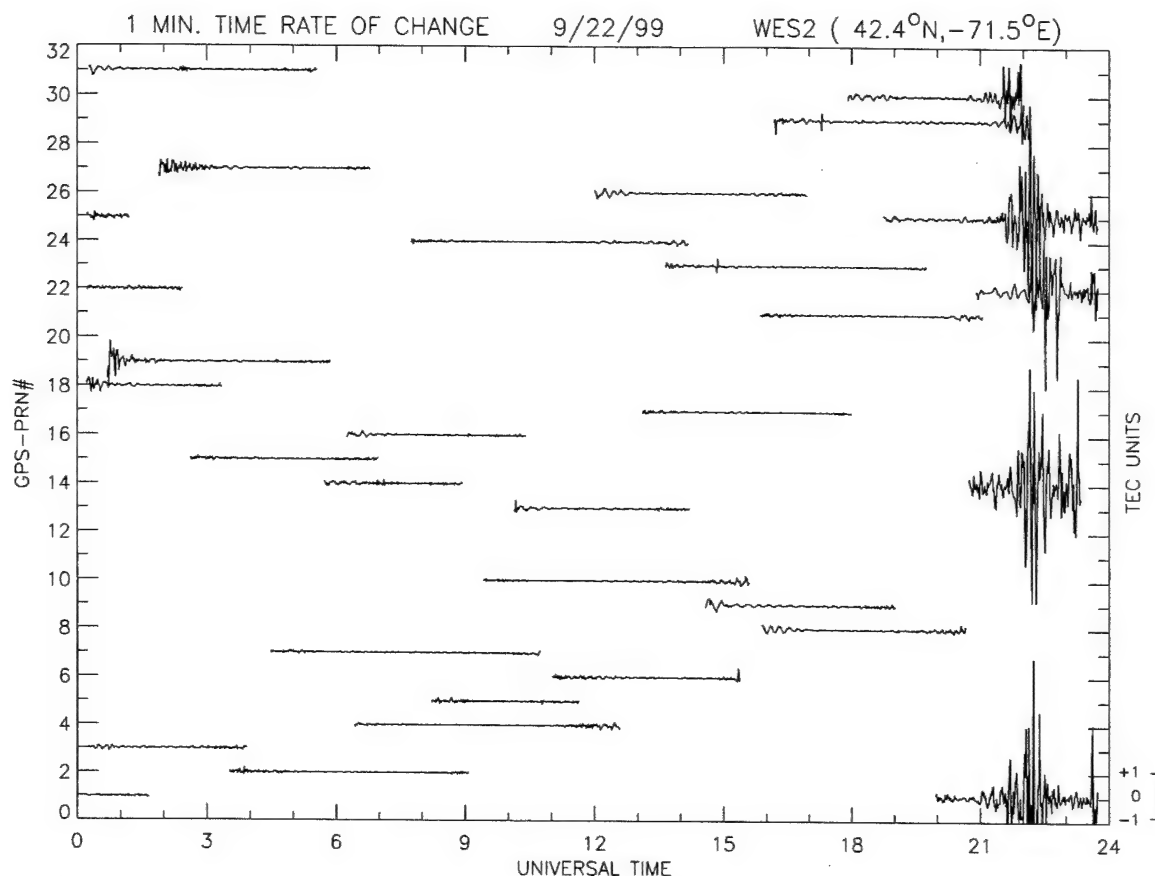


Figure 4. The time rate of change of TEC in TEC units ($10^{16} \text{ el m}^{-2}$) min^{-1} measured using data shown in Figure 3 at Westford, Massachusetts (WES2), on September 22, 1999.

However, since this is a gradual change, it is much easier to accommodate than the TEC increase and decrease at the storm onset. Normal TEC values giving rise to expected range delays are finally approached on September 24. Thus the ionospheric storm caused as a result of the magnetic storm has a large measurable impact on a navigation system operating in what was expected to be a relatively benign midlatitude ionosphere.

2.2. Equatorial Effects

The effect of the magnetic storm seemed to create enhanced effects at lower mid-latitudes as evidenced by the TEC behavior shown in Figure 5. This was interpreted as a combined effect of the prompt penetration of the eastward electric field into the ionosphere and the storm-enhanced plasma density and consequent TEC increase seen in the dusk sector by Foster [1993]. A natural extension of this midlatitude study seemed to be the investigation of the effect of this prompt penetration on equatorial scintillations and TEC gradients and their consequent impacts on WAAS-like systems being developed for low latitudes.

An important feature of the low-latitude F region is the presence of the equatorial anomaly, with peaks in the plasma density at $\pm 15^\circ$ dip latitude and minima at the magnetic equator. They are the result of the upward motion of the plasma at the magnetic equator and its consequent diffusion along the magnetic field lines [Hanson and Moffett, 1966]. The TEC anomaly starts to develop as early as 1100 LT. The crests move away from the equator with increasing local time, as the F

region at the equator moves to higher altitudes and reaches a maximum development around the afternoon hours [Basu and Das Gupta, 1968]. On some evenings a strong resurgence of the anomaly takes place; this is probably due to the well-known prereversal enhancement (PRE) of the vertical drift, which generally occurs around 1900 LT [Woodman, 1970; Tanaka, 1981]. A well-developed PRE has been found to be one of the most important indicators associated with the onset of equatorial spread F (ESF) by Basu *et al.* [1996] and Fejer *et al.* [1999]. In a very recent paper, Valladares *et al.* [2001] have shown the existence of a close relationship between the temporal evolution of the TEC profiles as a function of latitude near sunset and the onset of ESF. Their data came from the year 1998. We utilize that array of TEC stations in South America extending from Bogota, Colombia, to Santiago, Chile, in conjunction with ground scintillation observations from Ancon, Peru, and Antofagasta, Chile, shown in Figure 7, to study the effect of this magnetic storm on the equatorial ionosphere.

The scintillation data from Ancon, Peru, using the F8 satellite are shown in Figure 8. It starts rather abruptly at 2308 UT (1808 LT), as is generally the case at equatorial stations [Basu *et al.*, 1978]. However, there are two surprising aspects to these measurements. One is the start of the scintillations at 1808 LT, which is actually 15 min before E region (100 km) sunset at the satellite intersection point, and the other is the total absence of scintillations throughout the night at the F7 intersection point to the west of Ancon, which is separated from the F8 intersection point by 630 km. Thus it seems that the scintillation onset

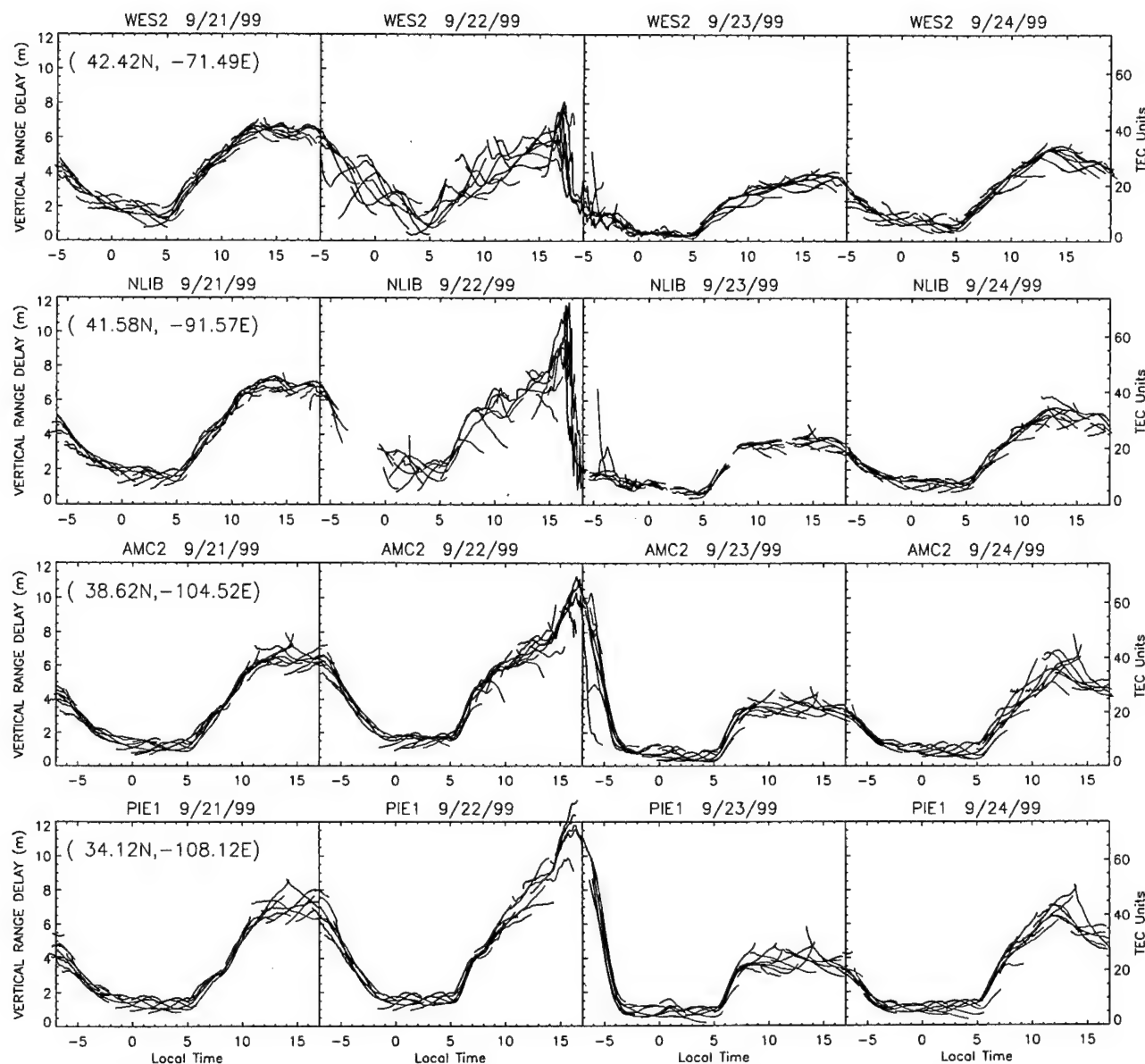


Figure 5. Range delays recorded at four stations in the International GPS Service for Geodynamics (IGS) network, namely, Westford, Massachusetts (WES2), North Liberty, Iowa (NLIB), Colorado Springs, Colorado (AMC2), and Pietown, New Mexico (PIE1), during September 21–24, 1999. Range delay can be related to TEC at 1.575 GHz by noting that a 6.15 TEC units change causes a 1-m range delay.

is related to the prompt penetration of eastward electric field made possible by the conductivity gradients near sunset. Further, the equatorial prompt penetration at dusk was very localized in longitude. There was no scintillation at 1.7 GHz for the Antofagasta G8 ray path which was within the irregularity zone, thereby indicating that the integrated strength of turbulence caused by the disturbance was not large enough to create perturbations at such a high frequency. The scintillations on both F7 and F8 ray paths during the evening of September 21–22 from Ancon are most likely due to the expected occurrence of ESF on normal quiet days at equinox during solar maximum in the Peruvian sector [Aarons, 1993].

In the absence of Jicamarca radar data we utilized the array of GPS TEC stations shown in Figure 7 to study the latitudinal behavior of TEC in the hope of getting some clues to the vertical plasma drift behavior which may have some bearing on

the scintillation asymmetry to the west and east of Ancon. The latitude variation of TEC was computed by utilizing GPS data as was done by Valladares *et al.* [2001] the only difference being that the latitude variation was computed separately for data obtained to the west and east of 72°W longitude. Further, only the data from the southern half were utilized, because of the gaps in the chain to the north. Our scintillation ray paths also intersect close to the magnetic equator and to the south of it. The data in Figure 9 show a fairly remarkable difference between the east and west cuts with the former showing evening anomaly peak development at 1800 UT (2300 LT) and 1900 LT (0000 UT) whereas the latter shows TEC peaks at the equator, thereby indicating that the evening anomaly had not formed in the west. While this does not provide a cause for the difference, this asymmetric behavior provides evidence for the enormous importance of the PRE of the vertical drift in the generation of ESF.

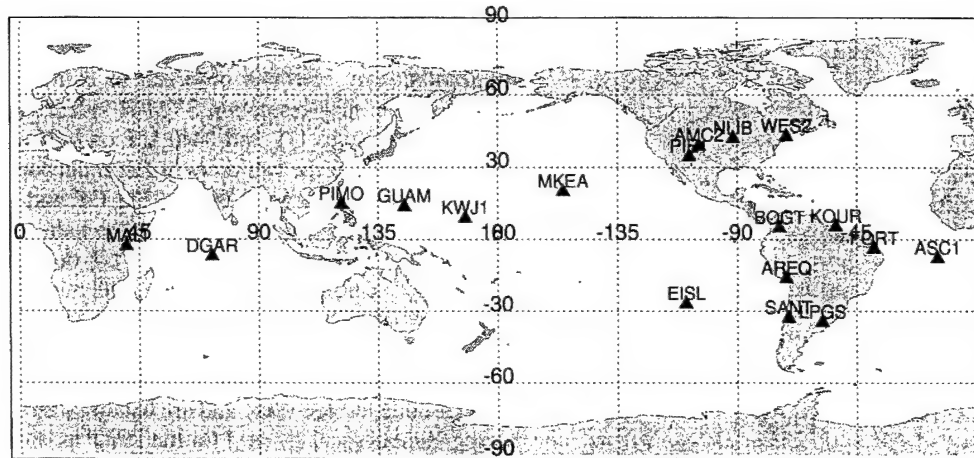


Figure 6. Global map showing IGS stations that provided data for this study. MALI, Malindi; DGAR, Diego Garcia; PIMO, Manila; KWJ1, Kwajalein; MKEA, Hawaii; EISL, Easter Island; BOGT, Bogota; KOUR, Kourou; AREQ, Arequipa; SANT, Santiago; LPGS, LaPlata; FORT, Fortaleza; ASC1, Ascension Island.

The TEC and scintillation data taken together provide indirect proof that the westward boundary of the penetration electric field in the equatorial region is probably close to 73°W (287°E). To provide an eastward boundary, we checked several global databases, both space- and ground-based. The DMSP F12 and F14 data of topside densities at 840 km, which crossed the magnetic equator at 321°E at 2318 UT and 324°E at 2306 UT, respectively (near the eastern edge of Brazil), were the only ones to show perturbations in the form of density depletions in the equatorial region. These passes are at 2100 LT, and one expects irregularities to show up in the topside by this time. No other passes in the vicinity showed any signatures of topside disturbances. Unfortunately, the ROCSAT-1 data were not available during the night of September 22–23. This is because the severe Taiwan earthquake of September 21 knocked out power to the mission operation centers for a couple of days.

In terms of ground-based data sources from the IGS network, the TEC fluctuation data of the type shown in Figure 4 for Westford were checked for many equatorial stations at different longitudes shown on the global map in Figure 6. There was an absence of fluctuations at Hawaii (MKEA), Easter Island (EISL), Bogota (BOGT), Arequipa (AREQ), and Santiago (SANT), i.e., stations on islands in the Pacific Ocean and along the west coast of South America. However, TEC fluctuations were observed at Kourou (KOUR), Fortaleza (FORT), and LaPlata (LPGS) on the east coast of South America. The TEC fluctuations started at 2110 UT in Fortaleza, Brazil (*E* region sunset is 2107 UT), and continued intermittently up to 0800 UT on September 23; the magnitude, however, never exceeded ± 2 TEC units min^{-1} . The Fortaleza ground-based data are thus consistent with the DMSP F12 and F14 orbits presented earlier. Both scintillations and IGS data are available from Ascension Island (ASC1). The Ascension Island 250-MHz scintillation data had an abrupt onset at 2127 UT (2027 LT), i.e., a fairly late start for a station where *E* region sunset is at 1930 UT with no gigahertz scintillation observed that night. This probably indicates that the scintillation was caused by structures that drifted in from the west. The Ascension Island IGS data showed significant TEC fluctuations after 2100 UT and continued intermittently up to 0400 UT.

Unfortunately, no IGS stations are available on the west coast of Africa, the closest one being on the east coast at Malindi (MALI), which showed no storm-related TEC perturbations. For completeness, we checked the station at Diego Garcia (DGAR) and those in the Far East such as Manila (PIMO) and Kwajalein (KWJ1). However, since the time of storm onset corresponds to the postmidnight to morning hours at these stations, no perturbations in TEC were detected. No late time disturbances, such as that attributed to the prompt penetration due to a northward turning of the IMF (see the overshielding concept discussed by Kelley [1989]) or that due to the ionospheric disturbance dynamo [Blanc and Richmond, 1980; Fejer *et al.*, 1999], were detected on the western side of South America for this particular storm. However, the TEC fluctuation data for Fortaleza and the 250-MHz scintillation data from Ascension provide evidence for a postmidnight event in the 0300–0500 LT time frame. Using ACE data, we found that the northward turning of the IMF for this storm had taken place at 0048 UT, if the expected propagation delay is included (J. Fedder, private communication, 2001). This is pre-midnight LT for both Ascension Island and Fortaleza, such that the prompt penetration due to overshielding is not expected to lead to fresh irregularity generation. Thus it seems that the postmidnight event is probably due to the effect of the disturbance dynamo alone. Unfortunately, no postmidnight zonal drift data were available that could have put this hypothesis on a firmer footing.

Given the various caveats we have mentioned, this storm in its development phase seemed to have had a positive effect on irregularity formation rather than an inhibition on the generation of equatorial irregularities in a very limited range of longitudes between 73°W and 15°W. In other words, the prompt penetration of the electric field in the eastward direction due to increased magnetospheric convection seemed to be confined to the longitude region which was close to the *E* region sunset for the UT range over which SYM-H (*Dst*) showed maximum variation including the time period when it remained at its most minimum level. Any positive late time effect also seemed to be confined to a part of this longitude range. We will return to a discussion of this point vis-à-vis the findings of storm time electric field models [Spiro *et al.*, 1988;

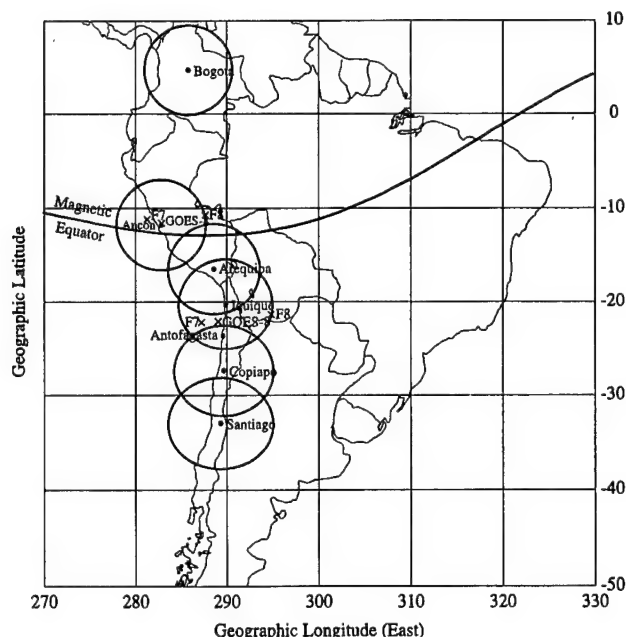


Figure 7. Equatorial array of GPS stations on the west coast of South America providing latitude variation of TEC data. The circles around the stations indicate 30° elevation coverage. Also shown are 350-km ionosphere intersection points to Fleetsat 7 (F7), Fleetsat 8 (F8), and GOES 8 from Ancon, Peru, and Antofagasta, Chile.

Fejer and Scherliess, 1997; Scherliess and Fejer, 1997] in section 4.

3. October 21–23, 1999, Magnetic Storm

We will follow the scenario used for the September 22–24 storm to describe this major October storm.

3.1. Midlatitude Effects

In Figure 10 we show the VHF scintillation data from two geostationary satellites observed at Hanscom AFB plotted against the high-resolution SYM-H index. The onset of scintillation at 0120 UT and 0440 UT on both ray paths is well correlated with the two times of fast reductions in the SYM-H (or *Dst* index) between 0000–0200 UT and 0400–0600 UT, each of ~ 45 nT h^{-1} . The minimum value of -230 nT for SYM-H was reached around 0700 UT on October 22. While the first scintillation region is ~ 100 min wide, the second interval of high scintillation is 4 hours long, which includes 2 hours of moderate scintillation.

In the absence of the Millstone ISR data, we utilize the Digisonde located there and are benefited by the 5-min sounding interval specially used for the ISWP as shown in Figure 11. The fall in f_oF_2 , from a flat peak of 12 MHz starts from 2100 UT on October 21 (not shown) and is part of a gradual sunset decay. It is greatly accelerated beyond 0050 UT on October 22 when f_oF_2 falls from 7.5 to 3.1 MHz (a factor of almost 6 decrease in $N_m F_2$) at 0235 UT with high values of hmF_2 , the height of the peak of the F_2 layer (both characteristics of the trough). It is interesting to note that even though it is close to local midnight, f_oF_2 starts increasing to a value of ~ 6.0 MHz at 0545 UT (0045 LT), and an *E* region makes its appearance between 0400 and 0650 UT. Between 0650 and 0745 UT there is a gap in the data. These effects are generally thought to be due to a varying spectrum of particle-induced ionization. Soft particles can cause *F* region ionization, with some *E* region contribution, and then with a hardening of the precipitating particles affecting the *D* region, we eventually reach a point at which the *F* region cannot be seen at all because of increased radio-wave absorption (J. W. Wright, private communication, 2001). During the entire time period between 0100 and 1100 UT (except the gap region mentioned above), the ionograms

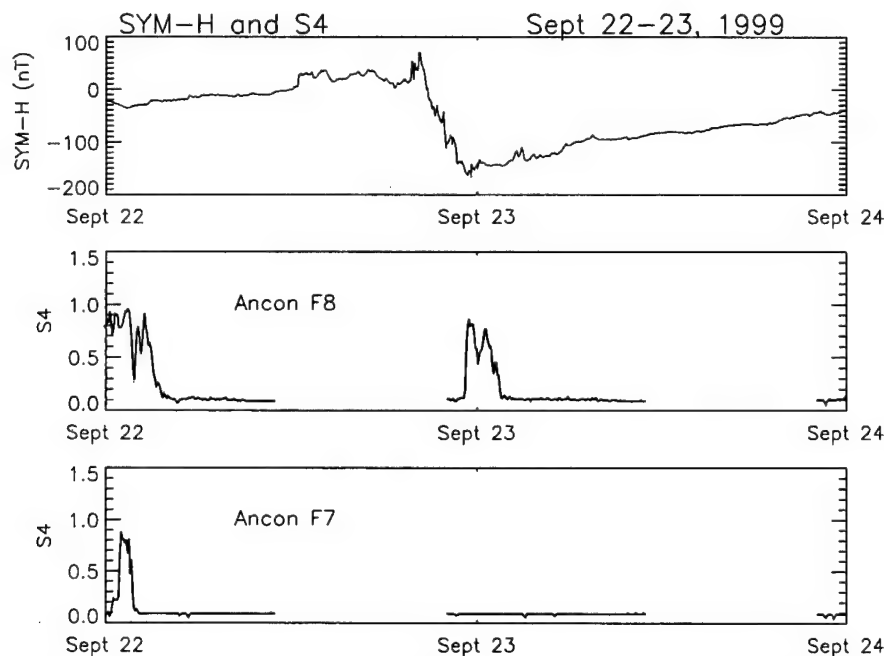


Figure 8. Scintillation at 250 MHz from two geostationary satellites Fleetsat 7 (F7) and Fleetsat 8 (F8) recorded at Ancon, Peru, plotted against the SYM-H index for September 22–24, 1999. Note the complete absence of scintillations on F7 during the evening of September 22–24, 1999. Note the complete absence of scintillations on F7 during the evening of September 22–23, 1999.

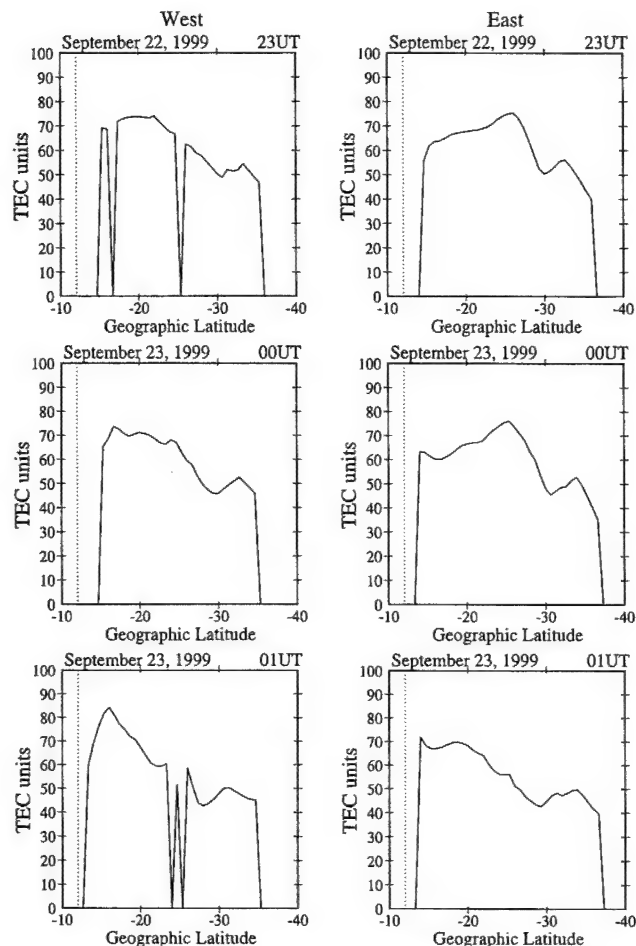


Figure 9. The latitude variation of TEC using the southern half (in magnetic latitudes) of the array computed to the west and east of longitude 72°W. While the data from the eastern half show a clear formation of the equatorial anomaly at 2300 UT (1800 LT) on September 22 and 0000 UT (1900 LT) on September 23 at 25°S (15° magnetic latitude), the western half does not show any evidence for anomaly development with the TEC peak being close to the magnetic equator. The abrupt discontinuities in the plots are the result of data dropouts.

show evidence of spread F with the magnitude of df/f , where df is the frequency spread around the critical frequency, being on the order of 10%.

The equivalent vertical TEC data for October 22, 1999, from Westford, Massachusetts, are shown in Figure 12 and are obtained exactly as detailed in the description for Figure 3. The quick fall in TEC beyond 0000 UT (1900 LT) to below 10 TEC units is very evident. Also very prominent is an increase in TEC to ~20 TEC units between 0400 and 0800 UT. This is followed by another decrease until sunrise the next morning at 1100 UT (0600 LT) when TEC gradually increases in value but reaches a maximum which is only half that seen on the previous day (compare Plate 2). This is quite consistent with the extended negative phase following major magnetic storms due to composition changes in the ionosphere [cf. Buonsanto, 1999].

The TEC fluctuations for October 22 on each GPS satellite are shown in Figure 13. Again, this is obtained in a manner similar to Figure 4. It is rather interesting to note that the TEC fluctuations in the vicinity of 0100 UT associated with the quick TEC fall brought about by the equatorward motion of the

trough are rather moderate (± 1 –2 TEC units) compared to the September 22 case. The large TEC fluctuations in this case (some as large as ± 4 TEC units) are primarily confined to the period between 0630 and 0800 UT, which covers the time when the Digisonde was unable to record the background ionospheric parameters due to increased absorption. It is rather important to note from Figure 12 that these large TEC fluctuations are confined to the trailing edge of the TEC enhancement near local midnight. Since AE (>1000 nT) and $SYM-H$ or Dst (>-200 nT) were both at extreme levels at this time, and the ionograms showed evidence of auroral particle precipitation, it is a very reasonable assumption that this TEC increase is due to an auroral blob generated locally and/or convected into this region whose trailing edge has been structured by the gradient drift instability [Basu et al., 1990]. We will return to a discussion of this point in section 4.

This October 1999 storm was very important from the point of view of the WAAS prototype testing. This was the first major magnetic storm, which could be used to observe the robustness and accuracy of early WAAS algorithms in operation. Plate 2 displays TEC from four stations in the IGS network going from NE to SW (clockwise starting from lower right), as was done in Figure 5 for the September 22 storm. In the October case, however, each station TEC (expressed in terms of vertical range delay) has a vertical range delay overplotted in red. These vertical range delays were obtained from the estimated ionospheric vertical delays provided by the WAAS Ionospheric Grid Points (IGPs). In the panels directly below the TEC data we show the WAAS parameter called Grid Ionospheric Vertical Error (GIVE). The GIVE values are the estimated errors in the IGP values. Plate 2 illustrates that GIVE values increased to 6 m or more when short-term fluctuations were seen in TEC between 0000 and 1000 UT on October 22 (1900 LT on October 21 to 0500 LT on October 22 for Westford). At other times, GIVE values rarely exceeded 1.5 m. As in the case of Figure 5, Plate 2 also shows larger storm effects at the lower-latitude stations in Colorado and New Mexico. In an operational WAAS an aircraft user will interpolate the grid of IGPs for a local vertical range delay, apply that vertical delay to all satellites in view, and then use the GIVE values as an input to a function which estimates overall position error [Dehel et al., 1999]. The impact of ionospheric storm activity on WAAS is currently under intense investigation by a WAAS Ionospheric Working Group (WIWG) (P. Doherty, private communication, 2000). The results shown in Plate 2 are representative of early attempts to observe WAAS behavior during magnetic activity. In general, the September 1999 storm had a much larger effect on the midlatitude ionosphere in the continental United States as compared to the October storm, because the storm's main phase came at an earlier local time even though the October storm had a large negative $SYM-H$ (Dst) per se.

3.2. Equatorial Effects

Following the same logic of studying the effect of the penetrating electric fields on the equatorial ionosphere as in section 2.2, we turn our attention to the equatorial region. The plasma density irregularities associated with this storm produced a widespread effect, in terms of longitude coverage, and long-lived effects, in terms of time coverage. The ROCSAT-1 measurements allowed us to track both these variabilities in a meaningful way. This satellite with the Ionospheric Plasma and Electrodynamics Instrument (IPEI) on board was launched on

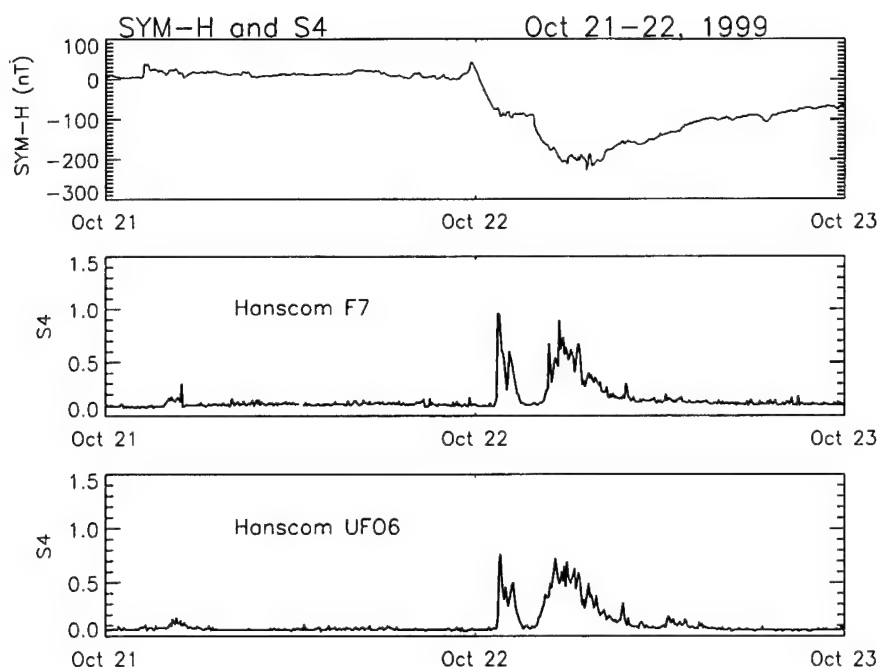


Figure 10. Same as in Figure 1 but for October 22–23, 1999.

January 27, 1999, into an almost circular orbit near 600 km with inclination of 35° [Yeh *et al.*, 1999]. Supporting information was obtained from DMSP F12, F13, and F14, the ground scintillation data, and the TEC data from the IGS network.

One of the more interesting aspects of the scintillation data for this storm is the nearly simultaneous onset at all three Ancon and Antofagasta (F7, F8, and G8) ray paths whose positions were shown in Figure 7. One set of such measurements for the Ancon F7 (at 250 MHz) and G8 (at L band) satellites is shown in Plate 3 for October 22 (Plates 3a and 3d) together with the spaced receiver drift measurements [Basu *et al.*, 1986; Valladares *et al.*, 1996] and power spectral densities (psds) at three specific irregularity scale lengths in Plates 3b and 3c (the drifts and psds are discussed later in the section). The scintillation, particularly at 250 MHz, continued for a long period of time. The simultaneous scintillation onset at these different ray paths and the persistence of scintillations for a long period through the night can be better understood by considering the coordinated density and velocity data from ROCSAT-1.

In Figure 14 we present the data from ROCSAT-1 which were taken at 1024 Hz (but plotted at 1 Hz) for the first two successive orbits on October 22. The data in the top panel shows a snapshot of a series of depletions in density, also known as plasma bubbles [McClure *et al.*, 1977], seen between 0011:30 and 0021:20 UT covering a longitude range within which most of the ray paths from Ancon and Antofagasta intersect except the western fringe (when presumably the satellite moved out of the equatorial irregularity belt). This orbit obtained immediately after storm onset (IMF B_z south) shows the presence of enhanced eastward electric field of $1\text{--}2\text{ mV m}^{-1}$ in the evening period compared to the quiet day pattern on October 20, 1999 (H.-C. Yeh, private communication, 2001). This indicates that the effect of the prompt penetration of the electric field has reached equatorial latitudes. The presence of plasma bubbles and scintillations associated with an eastward electric field indicates that the Rayleigh-Taylor insta-

bility mechanism is operative over a wide swath of longitudes [Ossakow, 1981].

The next ROCSAT orbit at 0145 UT (bottom panel of Figure 14) shows a further development of bubbles with a series of depletions extending from 267° to 300°E longitude straddling the magnetic equator with the deepest depletion containing only 10^2 cm^{-3} located close by. The velocity measurement for this orbit shows a continued presence of an enhanced eastward electric field in the evening period. What is more interesting is the gradual development from westward in orbit 1 to an eastward electric field in orbit 2 over the postmidnight time frame (H.-C. Yeh, private communication, 2001). The latter probably indicates a development of the disturbance dynamo after the storm has continued for a couple of hours. The highest density exceeding 10^6 cm^{-3} is seen at the northern crest of the equatorial anomaly in both the top and bottom panels that constitute orbits 1 and 2 for October 22. Presumably, ROCSAT was sampling the irregularities in the immediate topside, as the F peak tends to be high during sunspot maximum at equinox. It is the irregularities on the high-density walls of such depletions or bubbles that give rise to intense VHF and gigahertz scintillations [Basu *et al.*, 1983b]. It should be noted from the scintillation data on the top and bottom panels of Plate 3 that while the amplitude scintillation at VHF is intense ($S4 \sim 1$) for several hours, the L band G8 scintillation is weak with $S4 < 0.2$. On this night the simultaneous G8 data from Antofagasta (not shown) showed $S4 > 0.5$ up to 0530 UT. It is the greater background density near anomaly peak stations that gives rise to the larger magnitude of scintillations even when bubble structures are seen throughout the equatorial belt. On this night, severe scintillations were observed particularly in a southerly direction, i.e., toward the southern anomaly crest on the GPS $L1$ frequency at Antofagasta with the scintillation maximizing at $S4$ of 1.2 between 0100 and 0200 UT as shown in Figure 15. Such high levels of $S4$ on so many different ray paths may pose a problem for WAAS-like systems in the equatorial region.

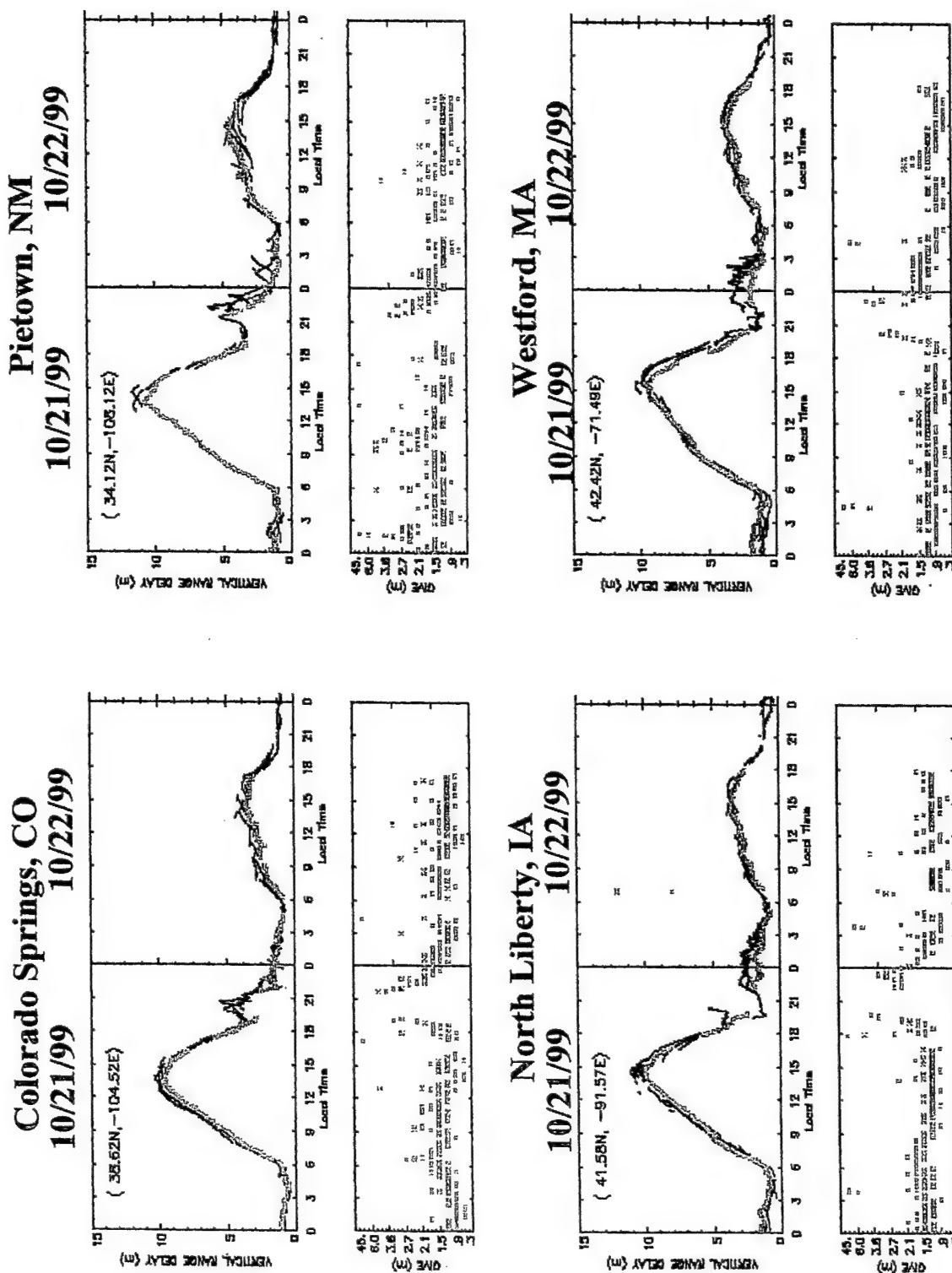


Plate 2. Similar to Figure 5 but for October 21–22, 1999, which has an estimated Wide Area Augmentation System (WAAS) range delay overplotted in red. The output of the WAAS error-bound algorithm called Grid Ionospheric Vertical Error (GIVE) is plotted in meters (m) on the lower panel, and also in red, for each station.

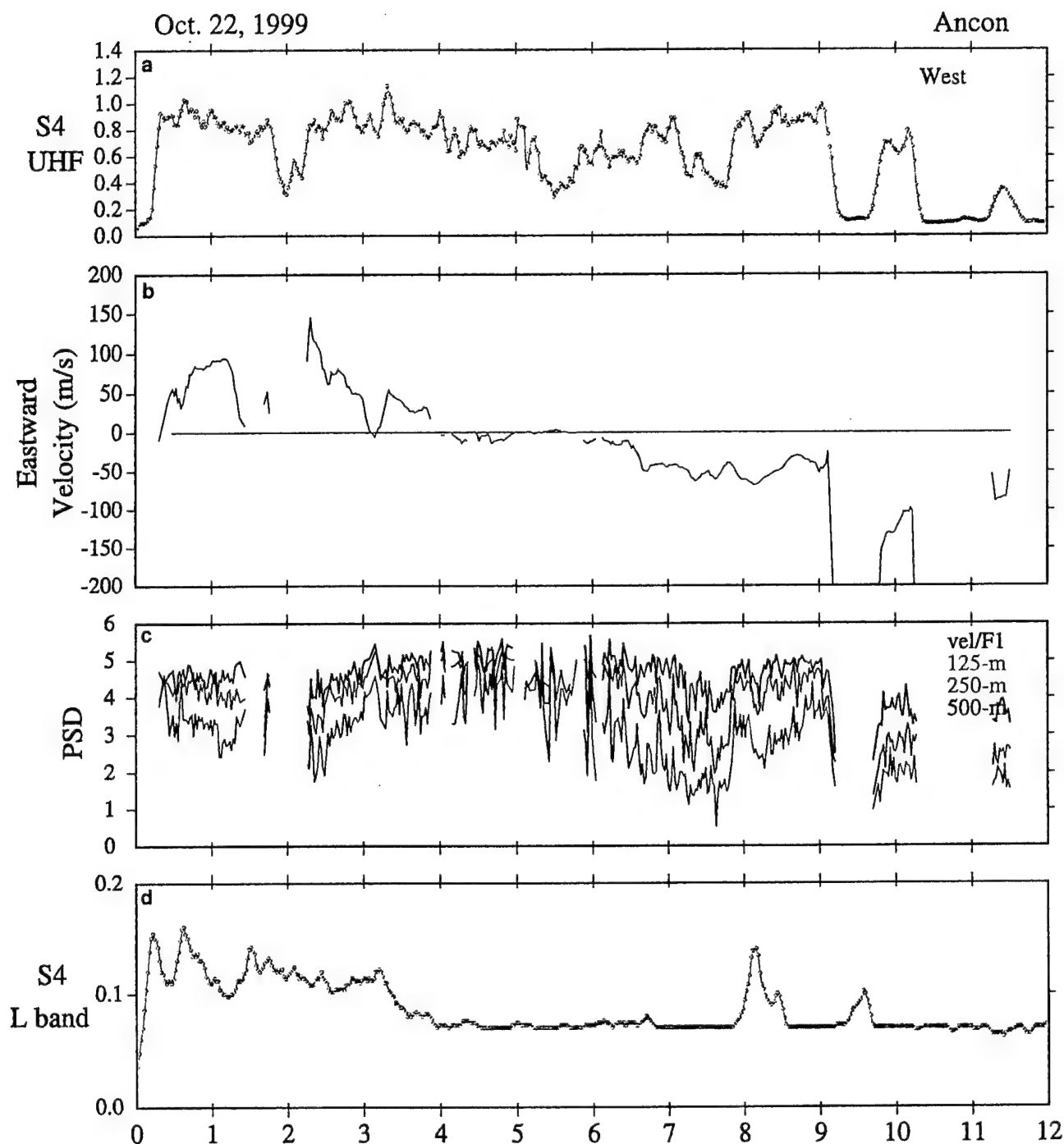


Plate 3. Scintillation data obtained at Ancon, Peru, on October 22, 1999. (a) The 250-MHz (UHF) data from F7 (to the west). (b) The E-W irregularity drift from spaced receiver measurements using the F7 satellite. (c) Power spectral densities in dB Hz^{-1} at 500, 250, and 125 m on a logarithmic scale obtained by combining the fast Fourier transform spectra and the E-W irregularity drift shown in Plate 3b. (d) The 1694-MHz (L band) data from G8.

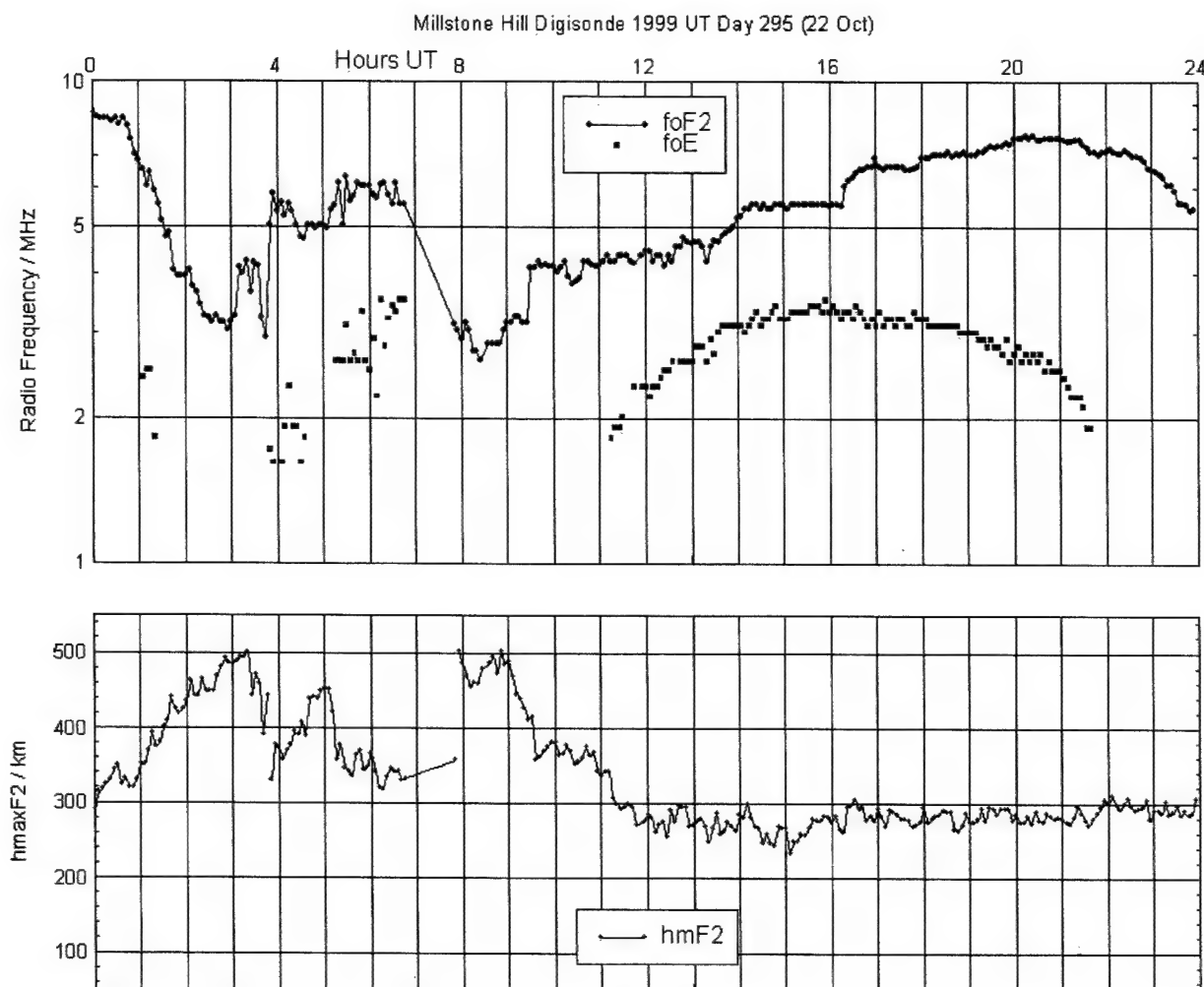


Figure 11. Digisonde data showing the F layer critical frequency f_oF_2 , the E layer critical frequency f_oE , and the maximum height of the F layer hmF_2 observed at Westford, Massachusetts, on October 22, 1999. Note that the appearance of f_oE between 0400 and 0700 UT (2300–0200 LT) implies the presence of auroral particle precipitation. The break in the data from 0700 to 0800 UT is caused by increased absorption.

While the ROCSAT-1 gives a good idea of the E-W extent of the irregularities in the early evening hours, the DMSP F12 and F14 satellites provide a N-S cut through the equatorial irregularities that percolate to the topside and moreover provide a good coverage through the middle latitudes as well. Figure 16 shows the density at 840 km observed by F14 with an equatorial crossing near 0120 UT and one from F12 at 0140 UT both providing an approximate N-S cut through ROCSAT orbit 2 between 0155 and 0200 UT. Both the F14 and F12 orbits provide evidence for a wide belt of equatorial irregularities covering $\pm 20^\circ$ of magnetic latitude. They also provide evidence for deep depletions (10^3 cm^{-3}) reaching the topside. Within the depletions the drifts (not shown) are upward and westward with the background vertical and horizontal drifts being quite small.

In addition to the equatorial density (there is a break in the data for F14) the midlatitude density behavior seen in both DMSP orbits is very consistent with the Digisonde and TEC data from Westford presented in section 3.1. Both types of data show a deep trough at 52° magnetic latitude followed by a density increase or blob poleward of the trough. The DMSP orbits pass just to the west of the Westford (W) station as

shown in the top panel of Figure 16. It is quite conceivable that the auroral blob may be convected equatorward to $\sim 50^\circ\text{N}$ magnetic latitude at later UT as a result of the continued intensification of the magnetic storm up to 0700 UT. As a matter of fact, the DMSP orbits show that there is very little of the entire nighttime global topside ionosphere that is not disturbed.

To return to the equatorial ionosphere, we consider the zonal irregularity drifts shown in Plate 3b. The drifts are mostly eastward in the range of $50\text{--}100 \text{ m s}^{-1}$ between 0100 and 0300 UT and then decrease gradually to very small values between 0400 and 0600 UT, turn actually westward at 0630 UT, and continue in that direction with a magnitude of 50 m s^{-1} (with some larger values) until ~ 1200 UT (0700 LT) when the data ends. (There was a small-magnitude scintillation event between 1300 and 1400 UT that is not shown.) Drifts usually turn westward at sunrise [Woodman, 1972]. Thus the reversal past local midnight during this magnetically disturbed period is, in general, considered to be the effects of an ionospheric disturbance dynamo setting up a neutral wind system driven by joule heating at high latitudes [Blanc and Richmond, 1980]. There was some indication from orbit 2 of the ROCSAT data that a

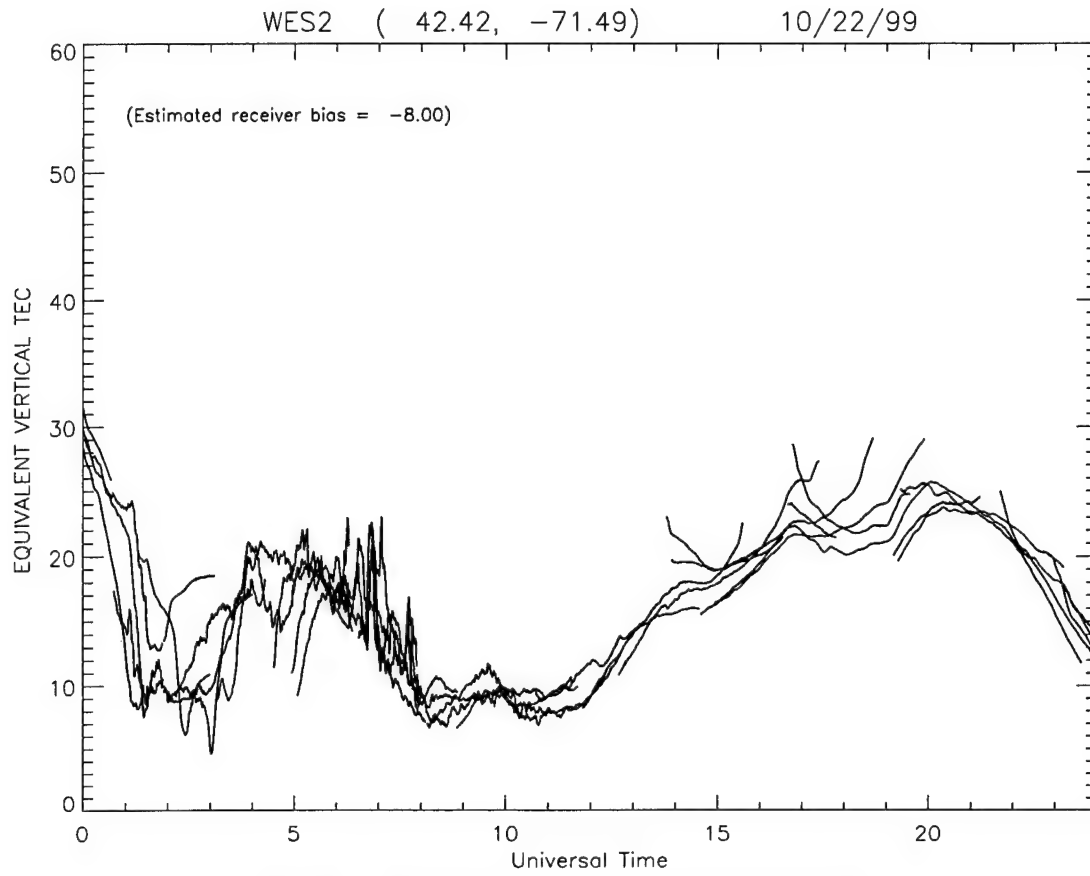


Figure 12. Same as in Figure 3 but for October 22, 1999.

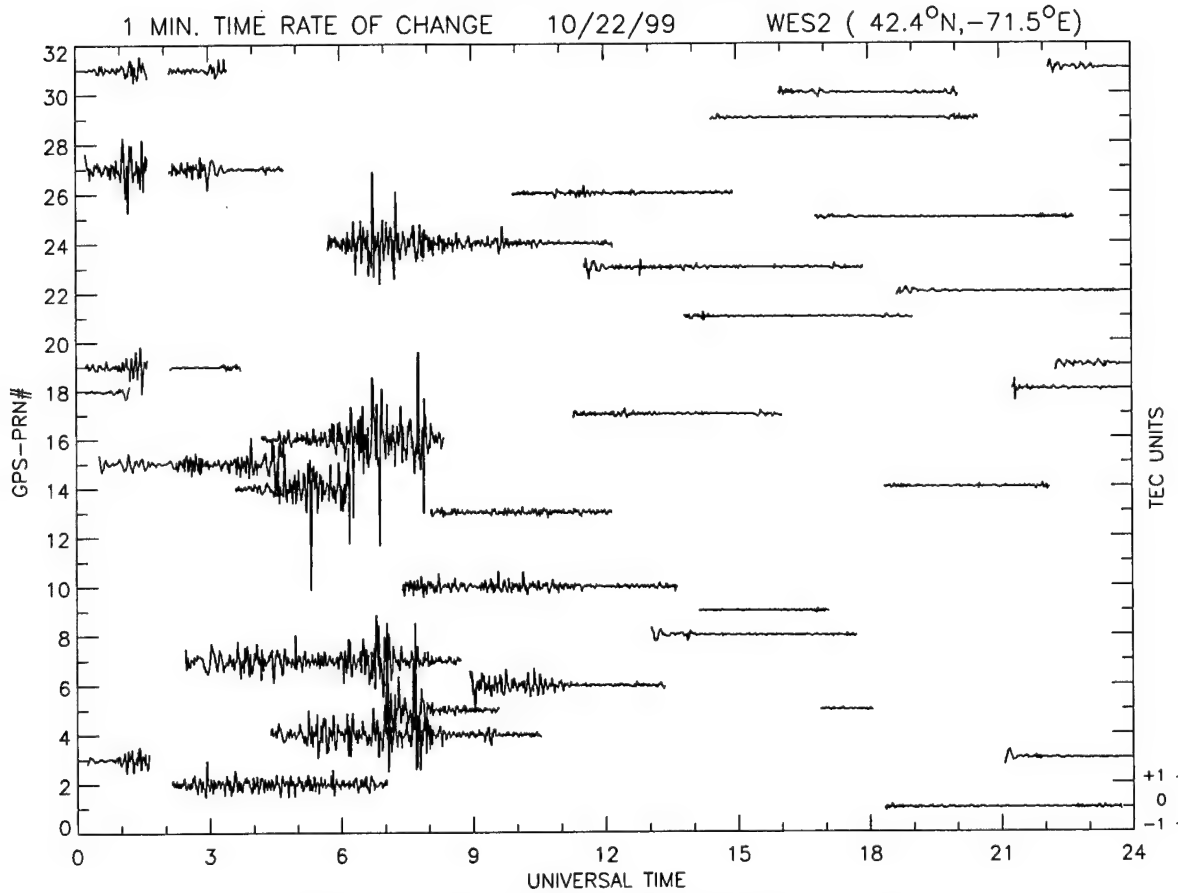


Figure 13. Same as in Figure 4 but for October 22, 1999.

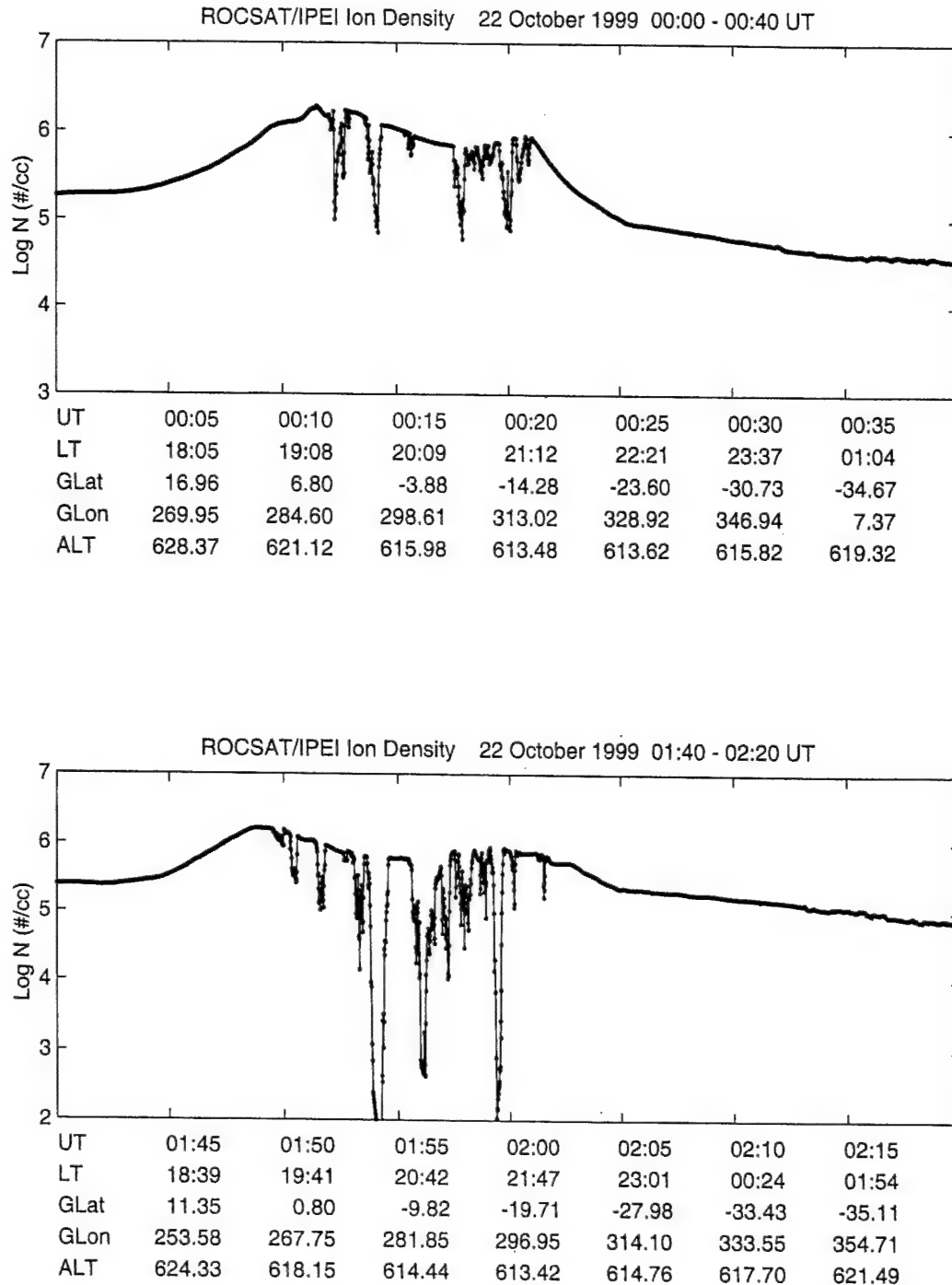


Figure 14. The total ion density measured by the ROCSAT-1 satellite between 0000–0040 and 0140–0220 UT on October 22, 1999. Wide regions of equatorial irregularity structures extending over 30° of longitude range are seen on both orbits at 600-km altitude.

disturbance dynamo process was gradually getting set up. The disturbance dynamo usually requires a few hours [Scherliess and Fejer, 1997] to be established as opposed to the prompt penetration effects both for increasing and decreasing high-latitude convection which occur within tens of minutes of storm intensification [Spiro *et al.*, 1988; Fejer and Scherliess, 1995, 1997]. The scintillation structure starting just prior to 0800 UT (0300 LT) in Plate 3a seems to be due to the fresh generation of equatorial irregularities in the postmidnight hours. We base our hypothesis on several aspects of the scin-

tillation data analysis and the simultaneous ROCSAT data shown in Figure 17. The scintillation data provide two reasons for considering the 0800–0900 UT structure to be freshly generated: (1) Scintillations at gigahertz, though small, are definitely observable after many hours of no gigahertz scintillation, and (2) the psds at specific scale lengths, obtained from a combination of the frequency scale of the fast Fourier transform (FFT) spectra and the irregularity drift shown in Plate 3b and depicted in Plate 3c (plotted on log scale), show large amplitudes. In particular, the psds at 500, 250, and 125 m

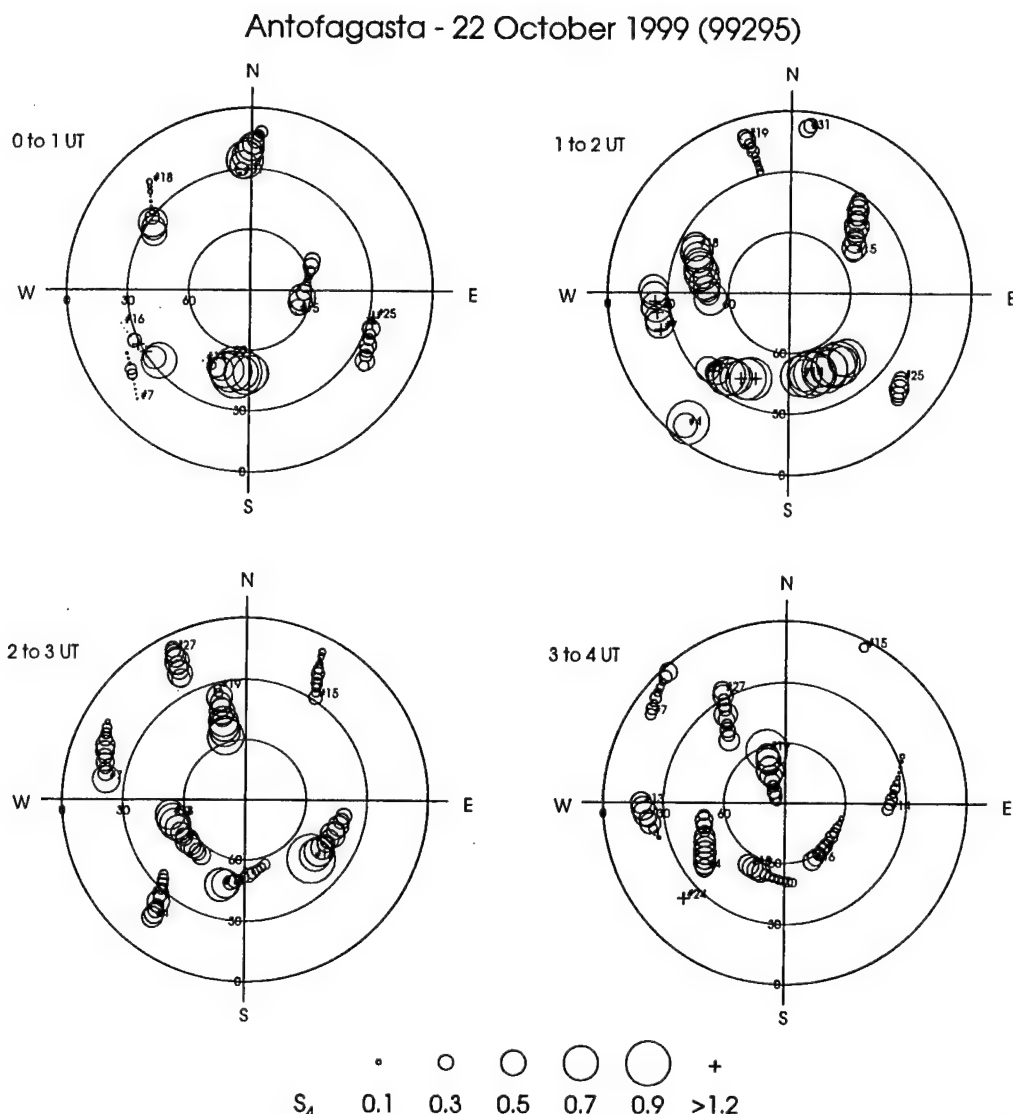


Figure 15. Hourly polar plots of the position and scintillation levels, plotted at 5-min intervals, of all GPS links tracked by the station at Antofagasta, Chile, on October 22, 1999, between 0000 and 0400 UT. Circle size corresponds to S_4 level as shown in the legend. Pseudorandom noise (PRN) numbers are plotted at the initial satellite position. The large concentric circles denote elevation angles of 60° , 30° , and 0° . Between 0100 and 0200 UT, intense levels of scintillation are seen on four satellites simultaneously to the south and west of the station.

become suddenly enhanced. This psd behavior is similar to the scintillation characteristics early in the evening when only freshly generated irregularities are observed.

The corresponding ROCSAT data are shown in Figure 17. The irregularity structures between 0820 and 0830 UT are in the Hawaiian sector, and we will discuss that aspect later when trying to determine a westward boundary for the equatorial irregularities. The other structure near 0850 UT (corresponding to 0335 LT) embraces the field line connected to the scintillation ray path from South America and actually passes to the south of Antofagasta. Yeh *et al.* [2001], on the basis of positive correlation of density depletion and enhanced eastward electric field of $1\text{--}2\text{ mV m}^{-1}$ resulting from the in-phase contributions of the prompt penetration magnetospheric (due to a sudden northward turning of the IMF) and the long-lasting ionospheric disturbance dynamo electric fields, argue for fresh generation for this large irregularity structure, and we

concur on the basis of scintillation characteristics. We shall also discuss these findings in section 4 in more global terms.

As we did for the September 22–23, 1999, magnetic storm, we would like to provide some eastern and western boundaries for equatorial irregularities observed during the October 22 storm. In this case the ROCSAT-1 data are extremely helpful in establishing both eastward and westward boundaries. Plate 4 depicts eight successive orbits on ROCSAT-1, at least five of which showed equatorial irregularities in the early evening generation phase. The portion of the orbits, which are in bold, both yellow and blue show the regions of irregularities. The actual density data showing the presence of irregularities for orbits 1, 2, and 6 have been shown in Figures 14 and 17. It is interesting to note from the LT attached to the first six orbits at irregularity onset that the ROCSAT-1 satellite detected irregularities between 1852 and 1936 LT except for orbit 3. This indicates that, by and large, the satellite must have inter-

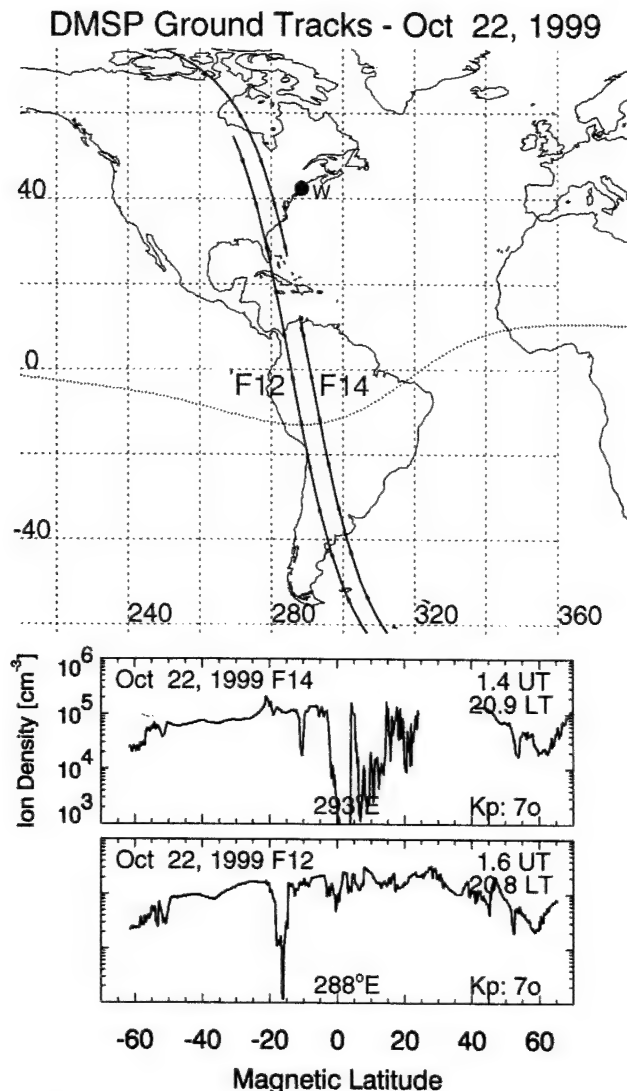


Figure 16. The ion density data at 840 km for the DMSP F12 and F14 orbits (middle and bottom panels) on October 22, 1999, and their orbital tracks (top panel). Wide regions of equatorial irregularities and the existence of the midlatitude trough at $\sim 50^\circ$ with density enhancement poleward of the trough are clearly visible on both satellites particularly in the Northern Hemisphere.

cepted freshly generated irregularities. While orbits 1 and 2 occurred during the 0000–0200 UT period of intensifying SYM-H (or Dst), orbits 4–6 occurred during the second intensification between 0400 and 0600 UT and continued into the time when SYM-H < -200 nT up to ~ 0900 UT. Thus, on the basis of Plate 4, we find that the equatorial irregularities for this magnetic storm were generated over longitudes ranging between $\sim 170^\circ\text{E}$ and 315°E . It is extremely tempting, as in the case of the September 22–23, 1999, storm, to associate the belt of longitudes where E region sunset occurred during times of rapidly increasing negative Dst and Dst minimum phase as the ones affected by a prompt penetration of magnetospheric electric field into equatorial latitudes. In addition, we found at least one region of probable fresh generation of irregularities at 0300 LT in the South American sector (between 235° and 300°E) that was a good candidate for being caused by the

effects of the ionospheric disturbance dynamo perhaps in conjunction with prompt penetration effects due to the northward turning of the IMF as shown in Figure 1 of Yeh *et al.* [2001].

It is very encouraging to note that other ground- and space-based data sets are all consistent with the findings based on ROCSAT-1. For instance, the IGS data for Ascension Island, Malindi, Diego Garcia, Manila, Guam, and Kwajalein showed no activity; that is, no TEC fluctuations were seen, while significant activity was observed at Arequipa, Santiago, and Easter Island. The DMSP F12, F13, and F14 satellite overflights were also consistent with the ROCSAT-1 data presented in Plate 4. Later orbits of ROCSAT-1, namely, orbits 7–12 between 1030 and 1725 UT (orbits 7 and 8 were plotted in Plate 4), all showed smaller-amplitude density irregularities at later local times (0400–0900 LT) but all within the range of longitudes between $\sim 170^\circ$ and 315°E . Many of these orbits passed through the South American sector and are consistent with the scintillation observations which showed continued activity between 0010 and 0910 UT and thereafter with breaks up to 1400 UT.

4. Summary and Discussion

We have studied the ionospheric effects of two major equinoctial magnetic storms ($Dst < -150$ nT) near solar maximum (smoothed sunspot number ~ 150) by considering the scintillation and TEC data from some middle-latitude stations which form part of the IGS network within the United States. We found that the prompt penetration of magnetospheric electric fields caused TEC increases, followed by rapid TEC decreases related to the equatorward motion of the midlatitude trough. These effects were enhanced if the rapid Dst intensifications took place in the afternoon sector near dusk. The equatorward motion of the trough was accompanied by TEC fluctuations, some as large as ± 5 TEC units min^{-1} , and saturated 250-MHz scintillations which may impact the GPS-based navigation system called WAAS and UHF communication links. In its simplest form, the effects of the prompt penetration of electric fields could be traced all the way to the magnetic equator and seemed to be confined to the range of longitudes for which the sunset times (probably at E region heights) coincided with the times of storm intensifications and its maximum phase. Thus, with the study of these two storms, one (in September 1999) for which the storm development and recovery was short and in the 2200–0100 UT time frame, a narrow swath of $\sim 60^\circ$ in the South American and South Atlantic longitudes was affected. The other one (in October 1999) had a much longer development and recovery in the 0000–0900 UT hours and affected a much wider region extending over almost 145° of longitude in the South American and Pacific sectors. Thus extreme variability in irregularity occurrence at particular sites is often encountered during magnetic storms as has been reported by many authors [Aarons *et al.*, 1997; Abdu *et al.*, 1995, and references therein]. Because of the great variety of data types and sites used and different types of effects observed on communication and navigation systems, we provide a summary of our findings and references to the relevant diagrams in Tables 1a and 1b to help the reader.

It should be emphasized that equinox solar maximum conditions are conducive to equatorial irregularity generation at all longitudes during magnetically quiet times (see the review by Basu and Basu [1985, and references therein]). Further, general morphological studies based on Kp also indicate that

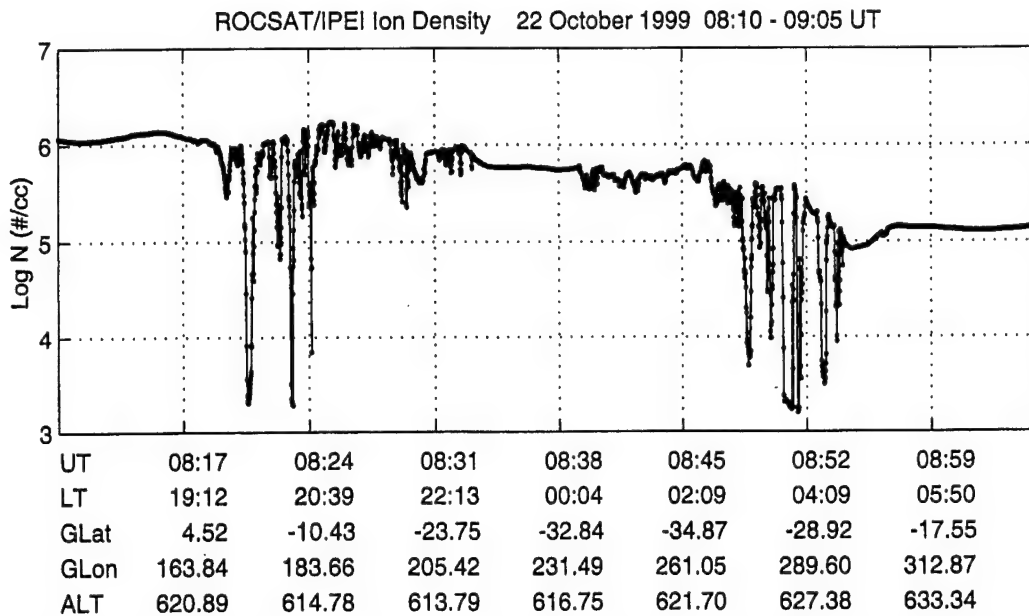


Figure 17. ROCSAT-1 total ion density data at 600 km between 0810 and 0905 UT on October 22, 1999. The irregularity structure near 0820 UT is in the Hawaiian sector whereas that near 0850 UT intersects the magnetic field lines going through the Ancon and Antofagasta stations.

scintillations tend to decrease with high K_p in the early evening hours [Groves *et al.*, 1997]. There is evidence from Jicamarca radar measurements for postmidnight irregularity generation during enhanced geomagnetic activity [Fejer *et al.*, 1999]. However, these times have much lower F region density so that irregularities, even if they are present, cannot cause intense scintillations in the gigahertz range. Our results, albeit limited to only two equinox storms, show that the equatorial irregularities may be enhanced or inhibited depending on the UT of storm intensification and length of the main phase. A recent paper by Huang *et al.* [2000] has pointed out the presence of equatorial bubbles during the initial and main phase of magnetic storms. In our discussion, in the interest of clarity, we have mainly considered the effect of the prompt penetration of electric fields of magnetospheric origin into low latitudes primarily during the increasing phase of the cross polar cap potential associated with the southward turning of the IMF and the intensification of the ring current. We have briefly mentioned the later time effects, due to the northward turning of the IMF and the more gradual onset of the ionospheric disturbance dynamo. In these two particular cases even the post-midnight events occurred within the region affected by the prompt penetration in the early evening hours. In a study of the May 23–24, 1998, great storm event, Aarons *et al.* [1999] had found a very longitude limited equatorial disturbance in the postmidnight phase that the authors attributed to the disturbance dynamo.

Our experimental findings at equatorial latitudes are generally consistent with the model predictions of the short-lived prompt penetration of electric fields both for increased and decreased magnetospheric convection [Fejer and Scherliess, 1997] and the more long-lived disturbance dynamo fields [Scherliess and Fejer, 1997] developed on the basis of Jicamarca radar measurements. These authors have used a linear relationship between the cross polar cap potential and AE , the auroral electrojet index [Ahn *et al.*, 1992], for the development of their empirical models. We have used the variation in the

1-min SYM-H index (which closely approximates the hourly Dst index) as the indicator for the prompt penetration of electric fields. Our results show that for the case of well-identified major magnetic storms during the initial phase, the time variation of the SYM-H index can effectively track the effects due to this type of prompt penetration of electric fields on communication and navigation systems operating at middle and equatorial latitudes. For the disturbance dynamo effects, however, the AE index during such large magnetic storms is probably a more appropriate measure of the energy input into high latitudes. For the September and October storms discussed in this paper the AE index increase and SYM-H decrease occurred in concert, making it difficult to distinguish between the efficacy of the two indices as a proxy for the cross polar cap potential. However, for the case of the July 15, 2000, super-storm, the AE increase occurred several hours prior to the SYM-H decrease due to ring current development. In that case the midlatitude and equatorial impacts due to prompt penetration of the magnetospheric electric field in the initial phase were still better ordered by variations in the SYM-H index which seemed to be taking place in an environment affected by the disturbance dynamo [Foster *et al.*, 2000; Basu *et al.*, 2001]. The effects on systems of these prompt penetration fields in the dusk sector, particularly during solar maximum, are large enough to merit a serious modeling effort for this magnetosphere-ionosphere coupled phenomenon. Indeed, such modeling efforts are underway to calculate the prompt penetration electric field from model results of the stormtime ring current [Ridley and Liemohn, 2001]. It is encouraging to note that in this modeling effort the magnitude of the penetration electric field is related to Dst^* , a solar wind pressure corrected Dst index [Kozyra *et al.*, 1998].

The prompt penetration of magnetospheric electric fields into the midlatitude ionosphere induces variations in TEC that may adversely affect the performance of navigation systems. Garcia *et al.* [2000] have documented a similar case at Arecibo, Puerto Rico, where GPS TEC perturbations were observed in



Plate 4. Equatorial portions of the first eight orbits of ROCSAT-1 between 0000 and 1200 UT on October 22, 1999. The thick yellow and blue lines on the orbits indicate the presence of density irregularities at 600 km. The LT at the onset of irregularities for the first six orbits is indicated on the diagram. These six orbits covered the range of longitudes where a fresh generation of equatorial irregularities was seen during the early and main phase of the October 22, 1999, magnetic storm. The thick blue lines show irregularities in the postmidnight phase.

Table 1a. September 22, 1999, $Dst_{min} \sim -167$ nT at 2400 UT, $(dDst/dt)_{max} \sim 75$ nT h⁻¹ Between 2200 and 2300 UT^a

Ionospheric Effects	Observation	Remarks
Prompt effect at midlatitudes		
Large (\sim km s ⁻¹) westward (sunward) convection velocity and increase of hmF_2 and TEC between 2100 and 2200 UT (1600–1700 LT)	DMSP F13 and F14; Millstone Digisonde; IGS GPS RX	magnetospheric E field penetration before sunset with northward and eastward components (Figure 2, Plate 1, and Figures 3 and 5)
Increase of hmF_2 ; and precipitous decrease of NmF_2 and TEC between 2210 and 2245 UT (1710–1745 LT)	Digisonde; IGS GPS RX	trough moves equatorward (Figures 3 and 5)
Impulsive 250-MHz scintillation and GPS phase fluctuation onset between 2210 and 2240 UT (1710–1740 LT)	Hanscom scintillation RX; IGS GPS RX	plasma instabilities associated with trough gradient cause electron density irregularities with scale lengths of tens of kilometers to tens of meters (Figures 1 and 4)
Prompt effect at equatorial latitudes		
Scintillation at 250 MHz, plasma bubbles, and GPS phase fluctuation; all between 15°W and 73°W	Ancon scintillation RX; South American GPS network; DMSP F12 and F14; global IGS GPS RX	prompt penetration of eastward E field over longitude sector for which early evening period corresponds to the time of rapid Dst (SYM-H) variations; equatorial anomaly development and plasma instability induced topside irregularities (Figures 6–9)
Postmidnight effects at equatorial latitudes		
Postmidnight scintillation in South Atlantic	Ancon and Ascension scintillation RX	possible disturbance dynamo-induced irregularity formation over longitude sector affected by prompt penetration E field

^aTEC, total electron content; IGS, International GPS Service for Geodynamics; GPS, Global Positioning System; RX, Receiver.

conjunction with airglow enhancements during a high geomagnetic activity period. Our study has shown that the LT of penetration of the electric field dictates the magnitude of the system impacts. A specific occurrence at local dusk is the equatorward motion of the midlatitude trough that, in turn, creates plasma instabilities driven by the gradient. If one assumes that in addition to the large sunward (or westward) flow seen in Plate 1, the plasma is moving equatorward in the neutral frame of reference, then this geometry is consistent with the requirements of the gradient drift instability (see the review by Tsunoda [1988]). Sometimes these equatorward and westward motions bring auroral blobs into the erstwhile midlatitude ionosphere, the trailing edges of which are also seen to cause intense 250-MHz amplitude scintillations and TEC fluctuations at GPS frequencies. This unexpected TEC increase and its fluctuations in the midnight time frame caused the largest errors in the WAAS algorithms in the continental United States. Needless to say, the morphology of such trough-wall gradients and auroral blob structures has to be studied using a large data-base such as the one existing at Millstone Hill [Vo and Foster, 2001] so that predictive schemes may be developed for use during magnetic storms.

Finally, we come to a consideration of the effects of penetrating electric fields on the equatorial ionosphere. At the recent Equatorial Aeronomy Symposium in Antalya, Turkey, in May 2000, there was consensus among the participants that the topic is still one of the major unknowns in the field. Most of our information to date has come from the modeling efforts undertaken by B. G. Fejer and L. Scherliess (see references quoted earlier) based on vertical drift measurements by the Jicamarca radar. These single-point measurements have been skillfully interpreted by these authors to provide LT and storm time coverage at all longitudes for both the prompt penetration (for convection increase and decrease) fields and the disturbance dynamo. We took a more global approach in an

attempt to link a UT-driven phenomenon (namely, ring current development) with one dependent on LT, namely, E region sunset, creating conductivity gradients at specific locations. For the two storms discussed here and the July 15, 2000, storm [Basu et al., 2001], we find that equatorial irregularities are generated in the prompt penetration of the development phase at longitudes for which E region sunset is observed during a fast change in the SYM-H index on the order of 50 nT h⁻¹, and SYM-H achieves values in the range of about -150 nT or smaller. Obviously, many more magnetic storms have to be studied under different seasonal and sunspot cycle conditions to test this hypothesis. If it holds, then it could be introduced as a nowcasting tool in equatorial scintillation prediction.

Both these storms provided evidence for the fresh generation of irregularities in the post-midnight time frame. This can be attributed to the disturbance dynamo generated eastward electric field. Both storms also showed a prompt northward turning of the IMF indicating storm recovery, which could have provided a short-lived in-phase contribution to the disturbance dynamo effects. However, for the September 1999 storm the northward turning was not at the appropriate time whereas for the October storm the two effects seemed to have provided an in-phase contribution in the postmidnight irregularity generation. What is quite interesting is that the postmidnight event for both storms occurred within a part of the longitude range affected by prompt penetration in the early evening (generation) period. The same was found to be true for the July 15, 2000, storm [Basu et al., 2001]. If this holds up for more storm studies, it may indicate that the background ionosphere which turned unstable earlier in the evening had a greater likelihood of becoming unstable again in the postmidnight hours. However, since the most favorable time for this joint effect is near 0300 LT [Scherliess and Fejer, 1997], the impacts on commu-

Table 1b. October 22, 1999, $Dst_{min} \sim -231$ nT at 0700 UT, $(dDst/dt)_{max} \sim 45$ nT h⁻¹ During 0000–0200 and 0400–0600 UT

Ionospheric Effects	Observation	Remarks
Prompt effect at midlatitudes		
250-MHz scintillation onset at 0120 and 0440 UT	Hanscom scintillation RX	scintillation structures due to two periods of penetration E fields; monitored by two periods of fast Dst (SYM-H) decreases (Figure 10)
NmF_2 and TEC fast decrease at 0000–0300 UT (1900–2200 LT)	Millstone Digisonde; IGS GPS RX	trough moves equatorward causes first scintillation structure (Figures 10–12)
NmF_2 and TEC increase during 0400–0700 UT (2300–0200 LT)	Digisonde; IGS GPS RX; DMSP F-12 and F-14	auroral blob causes TEC increase; second scintillation event observed (Figures 10–12 and 16)
GPS phase fluctuation between 0500 and 0800 UT	IGS GPS RX	trailing edge of blob structured; WAAS parameter GIVE exceeds 6 m during TEC fluctuation (Figures 12 and 13 and Plate 2)
Prompt effect at equatorial latitudes		
250-MHz and L band scintillation onset at 0010 UT (1910 LT)	Ancon scintillation RX; ROCSAT-1	near-simultaneous plasma bubble generation over 30° longitude interval (Figure 7, Plate 3, and Figure 14)
Strong GPS amplitude scintillation near crest of equatorial anomaly	Antofagasta GPS RX; ROCSAT-1	plasma bubbles extend to equatorial anomaly crest (Figures 14 and 15)
Irregularities in the topside detected over a longitude interval of 170°E–315°E in the local evening hours	ROCSAT-1 satellite	prompt penetration of eastward E field over longitude sector for which early evening period corresponds to the time of rapid Dst (SYM-H) variations (Plate 4)
Topside plasma bubbles cover $\pm 20^\circ$ MLAT	DMSP F12 and F14	plasma bubbles attain high altitudes (>840 km) over the magnetic equator (Figure 16)
Postmidnight effects at equatorial latitudes		
Fresh generation of irregularities and scintillation at 0800 UT (0300 LT) with westward drift	Ancon scintillation RX; ROCSAT-1	IMF B_z northward turning and ionospheric disturbance dynamo induced irregularity generation and westward drift (Plate 3 and Figure 17)

nication and navigation systems may be rather limited as the background densities are much lower at that local time.

Acknowledgments. Sunanda Basu gratefully acknowledges a six-month professional development leave from the National Science Foundation that made this study possible. She thanks the Air Force Research Laboratory at Hanscom AFB, MA, and the National Central University (NCU) at Chung-Li, Taiwan, for hosting her during this period. Santimay Basu also thanks the NCU for its hospitality. The efforts of J. U. Kozyra and D. Webb in providing space weather information through the International Space Weather Clearinghouse Web page are much appreciated. We thank J. W. Wright for his assistance with the Digisonde data analysis. The work at AFRL was supported by AFOSR task 2311AS. The work at Boston College was supported by NSF grant ATM-9819912 and AFRL contract F19628-97-C-0094. The work at NCU was supported by NSC (ROC) grant NSC 89-NSPO (A)-PDD-008-STP01.

Janet G. Luhmann thanks the referees for their assistance in evaluating this paper.

References

- Aarons, J., The longitudinal morphology of equatorial F -layer irregularities relevant to their occurrence, *Space Sci. Rev.*, **63**, 209, 1993.
- Aarons, J., and R. S. Allen, Scintillation boundary during quiet and disturbed magnetic conditions, *J. Geophys. Res.*, **76**, 170, 1971.
- Aarons, J., R. S. Allen, and H. E. Whitney, Observations of scintillations of two satellite beacons near the boundary of the irregularity region, *Planet. Space Sci.*, **20**, 965, 1972.
- Aarons, J., M. Mendillo, and R. Yantosca, GPS phase fluctuations in the equatorial region during sunspot minimum, *Radio Sci.*, **32**, 1535, 1997.
- Aarons, J., M. Mendillo, and B. Lin, The great magnetic storm of May 1998 and its effect on phase fluctuations in the auroral and equatorial regions, paper presented at Ionospheric Effects Symposium, Off. of Nav. Res., Arlington, Va., 1999.
- Abdu, M. A., I. S. Batista, G. O. Walker, J. H. A. Sobral, N. B. Trivedi, and E. R. de Paula, Equatorial ionospheric electric fields during magnetospheric disturbances: Local time/longitudinal dependencies from recent EITS campaign, *J. Atmos. Terr. Phys.*, **57**, 1065, 1995.
- Ahn, B.-H., Y. Kamide, H. W. Kroehl, and D. J. Gorney, Cross polar potential difference, auroral electrojet indices, and solar wind parameters, *J. Geophys. Res.*, **97**, 1345, 1992.
- Basu, S., and A. Das Gupta, Latitude variation of electron content in the equatorial region under magnetically quiet and active conditions, *J. Geophys. Res.*, **73**, 5599, 1968.
- Basu, S., Su. Basu, J. Aarons, J. P. McClure, and M. C. Cousins, On the co-existence of km- and m-scale irregularities in the nighttime equatorial F -region, *J. Geophys. Res.*, **83**, 4219, 1978.
- Basu, S., Su. Basu, J. LaBelle, E. Kudeki, B. J. Fejer, M. C. Kelley, H. E. Whitney, and A. Bushby, Gigahertz scintillations and spaced receiver drift measurements during Project Condor equatorial F -region rocket campaign in Peru, *J. Geophys. Res.*, **91**, 5526, 1986.
- Basu, S., et al., Scintillations, plasma drifts, and neutral winds in the equatorial ionosphere after sunset, *J. Geophys. Res.*, **101**, 26,795, 1996.
- Basu, S., K. M. Groves, J. M. Quinn, and P. Doherty, A comparison of TEC fluctuations and scintillations at Ascension Island, *J. Atmos. Terr. Phys.*, **61**, 1219, 1999.
- Basu, S., Su. Basu, K. M. Groves, H.-C. Yeh, S.-Y. Su, F. J. Rich, and P. J. Sultan, Response of the equatorial ionosphere in the South Atlantic region to the great magnetic storm of July 15, 2000, *Geophys. Res. Lett.*, **28**, 3577, 2001.
- Basu, S., VHF ionospheric scintillations at $L = 2.8$ and formation of stable auroral red arcs by magnetospheric heat conduction, *J. Geophys. Res.*, **79**, 3155, 1974.
- Basu, S., and S. Basu, Equatorial scintillations: Advances since ISEA-6, *J. Atmos. Terr. Phys.*, **47**, 753, 1985.
- Basu, S., E. MacKenzie, S. Basu, H. C. Carlson, D. A. Hardy, F. J. Rich, and R. C. Livingston, Coordinated measurements of low-energy electron precipitation and scintillations/TEC in the auroral oval, *Radio Sci.*, **18**, 1151, 1983a.

- Basu, Su., S. Basu, J. P. McClure, W. B. Hanson, and H. E. Whitney, High resolution in situ data of electron densities and VHF/GHz scintillations in the equatorial region, *J. Geophys. Res.*, **88**, 403, 1983b.
- Basu, Su., S. Basu, E. MacKenzie, W. R. Coley, J. R. Sharber, and W. R. Hoegy, Plasma structuring by the gradient-drift instability at high latitudes and comparison with velocity-shear driven processes, *J. Geophys. Res.*, **95**, 7799, 1990.
- Bhattacharyya, A., T. L. Beach, S. Basu, and P. M. Kintner, Nighttime equatorial ionosphere: GPS scintillations and differential carrier phase fluctuations, *Radio Sci.*, **35**, 209, 2000.
- Blanc, M., and A. D. Richmond, The ionospheric disturbance dynamo, *J. Geophys. Res.*, **85**, 1669, 1980.
- Briggs, B. H., and I. A. Parkin, On the variation of radio star and satellite scintillation with zenith angle, *J. Atmos. Terr. Phys.*, **25**, 339, 1963.
- Buonsanto, M., Ionospheric storms: A review, *Space Sci. Rev.*, **61**, 193, 1999.
- Buonsanto, M. J., M. Mendillo, and J. A. Klobuchar, The ionosphere at $L = 4$: Average behavior and response to geomagnetic storms, *Ann. Geophys.*, **35**, 15, 1979.
- Burke, W. J., et al., Electrodynamics of the inner magnetosphere observed in the dusk sector by CRRES and DMSP during the magnetic storm of June 4–6, 1991, *J. Geophys. Res.*, **103**, 29,399, 1998.
- Dehel, T., K. Pham, and J. Sheftic., National Satellite Test Bed (NSTB) observations of the effects of ionospheric storms on a prototype wide area augmentation system, paper presented at National Technical Meeting, Inst. of Navig., San Diego, Calif., 1999.
- Doherty, P., E. Raffi, J. A. Klobuchar, and M. B. El-Arini, Statistics of time rate of change of ionospheric range delay, paper presented at 7th International Technical Meeting, Inst. of Navig., Salt Lake City, Utah, 1994.
- Evans, J. V., The causes of storm-time increases of the F -layer at midlatitudes, *J. Atmos. Terr. Phys.*, **35**, 593, 1973.
- Fejer, B. G., and L. Scherliess, Time dependent response of equatorial ionospheric electric fields to magnetospheric disturbances, *Geophys. Res. Lett.*, **22**, 851, 1995.
- Fejer, B. G., and L. Scherliess, Empirical models of storm time equatorial zonal electric fields, *J. Geophys. Res.*, **102**, 24,047, 1997.
- Fejer, B. G., L. Scherliess, and E. R. dePaula, Effects of the vertical plasma drift velocity on the generation and evolution of equatorial spread F , *J. Geophys. Res.*, **104**, 19,859, 1999.
- Foster, J. C., Storm time plasma transport at middle and high latitudes, *J. Geophys. Res.*, **98**, 1675, 1993.
- Foster, J. C., and J. Aarons, Enhanced antisunward convection and F region scintillations at mid-latitudes during storm onset, *J. Geophys. Res.*, **93**, 11,537, 1988.
- Foster, J. C., and F. J. Rich, Prompt midlatitude electric field effects during severe geomagnetic storms, *J. Geophys. Res.*, **103**, 26,367, 1998.
- Foster, J. C., S. Basu, Su. Basu, A. J. Coster, and F. J. Rich, Subauroral ionospheric disturbance and space weather effects during the July 15–16, 2000 geomagnetic storm, *Eos Trans. AGU*, **81**(48), Fall Meet. Suppl., SH62A-10, 2000.
- Garcia, F. J., M. C. Kelley, J. J. Makela, P. J. Sultan, X. Pi, and S. Musman, Mesoscale structure of the midlatitude ionosphere during high geomagnetic activity: Airglow and GPS observations, *J. Geophys. Res.*, **105**, 18,417, 2000.
- Gonzales, C. A., M. C. Kelley, R. A. Behnke, J. F. Vickrey, R. Wand, and J. Holt, On the latitudinal variations of the ionospheric electric field during magnetospheric disturbances, *J. Geophys. Res.*, **88**, 9135, 1983.
- Groves, K. M., et al., Equatorial scintillation and systems support, *Radio Sci.*, **32**, 2047, 1997.
- Hanson, W. B., and R. J. Moffett, Ionization transport effects in the equatorial F region, *J. Geophys. Res.*, **71**, 5559, 1966.
- Hardy, D. A., L. K. Schmidt, M. S. Gussenhoven, F. J. Marshall, H. C. Yeh, T. L. Shumaker, A. Huber, and J. Pantazis, Precipitating electron and ion detectors (SSJ/4) for the Block 5D/Flights 4-10 DMSP satellites: Calibration and data presentation, *Tech. Rep. AFGL-TR-84-0317*, Air Force Geophys. Lab., Hanscom Air Force Base, Mass., 1984.
- Huang, C. Y., W. J. Burke, J. S. Machuzak, L. C. Gentile, and P. J. Sultan, DMSP observations of equatorial plasma bubbles in the topside ionosphere near solar maximum, *Eos Trans. AGU*, **81**(48), Fall Meet. Suppl., SA21A-10, 2000.
- Iyemori, T., T. Araki, T. Kamei, and M. Takeda, Mid-latitude geomagnetic indices "ASY" and "SYM" for 1999 (provisional), <http://swdcd.kugi.kyoto-u.ac.jp/aeasy/asy.pdf>, World Data Cent. C2 for Geomagn., Kyoto, Japan, 2000.
- Kelley, M. C., *The Earth's Ionosphere*, pp. 95–104, Academic, San Diego, Calif., 1989.
- Kozyra, J. U., et al., The role of precipitation losses in producing the rapid early recovery phase of the great magnetic storm of February 1986, *J. Geophys. Res.*, **103**, 6801, 1998.
- McClure, J. P., W. B. Hanson, and J. F. Hoffman, Plasma bubbles and irregularities in the equatorial ionosphere, *J. Geophys. Res.*, **82**, 2650, 1977.
- Mendillo, M., and J. A. Klobuchar, Investigations of the ionospheric F -region using multistation total electron content observations, *J. Geophys. Res.*, **80**, 643, 1975.
- Mendillo, M., M. D. Papagiannis, and J. A. Klobuchar, Ionospheric storms at midlatitudes, *Radio Sci.*, **5**, 895, 1970.
- Ossakow, S. L., Spread- F theories: A review, *J. Atmos. Terr. Phys.*, **43**, 437, 1981.
- Pi, X., A. J. Mannucci, U. J. Lindqwister, and C. M. Ho, Monitoring of global ionospheric irregularities using worldwide GPS network, *Geophys. Res. Lett.*, **24**, 2283, 1997.
- Reinisch, B. W., and H. Xueqin, Automatic calculation of electron density profiles from digital ionograms, 3, Processing of bottomside ionograms, *Radio Sci.*, **18**, 477, 1983.
- Rich, F. J., and M. Hairston, Large-scale convection patterns observed by DMSP, *J. Geophys. Res.*, **99**, 3827, 1994.
- Ridley, A. J., and M. W. Liemohn, A model-derived storm time asymmetric ring current driven electric field description, *J. Geophys. Res.*, in press, 2001.
- Rishbeth, H., and W. B. Hanson, A comment on plasma "pile up" in the F region, *J. Atmos. Terr. Phys.*, **36**, 703, 1974.
- Scherliess, L., and B. G. Fejer, Storm time dependence of equatorial disturbance dynamo zonal electric fields, *J. Geophys. Res.*, **102**, 24,037, 1997.
- Spiro, R. W., R. A. Wolf, and B. G. Fejer, Penetration of high-latitude electric field effects to low latitudes during SUNDIAL 1984, *Ann. Geophys.*, **6**, 39, 1988.
- Sugiura, M., and D. J. Poros, Hourly values of equatorial Dst for years 1957–1970, *NASA-GSFC Doc. X-645-71-278*, Goddard Space Flight Cent., Greenbelt, Md., 1971.
- Tanaka, T., Severe ionospheric disturbances caused by the sudden response of evening subequatorial ionospheres to geomagnetic storms, *J. Geophys. Res.*, **86**, 11,335, 1981.
- Tsunoda, R., High-latitude F -region irregularities: A review and synthesis, *Rev. Geophys.*, **26**, 719, 1988.
- Valladares, C. E., R. Sheehan, S. Basu, H. Kuenzler, and J. Espinoza, The multi-instrumented studies of equatorial thermosphere aeronomy scintillation system: Climatology of zonal drifts, *J. Geophys. Res.*, **101**, 26,839, 1996.
- Valladares, C., S. Basu, K. Groves, M. P. Hagan, D. Hysell, A. J. Mazzella Jr., and R. E. Sheehan, Measurement of the latitudinal distributions of total electron content during equatorial spread F events, *J. Geophys. Res.*, in press, 2001.
- Vo, H. B., and J. C. Foster, A quantitative study of ionospheric density gradients at mid-latitudes, *J. Geophys. Res.*, in press, 2001.
- Woodman, R. F., Vertical drift velocities and east-west electric fields at the magnetic equator, *J. Geophys. Res.*, **75**, 6249, 1970.
- Woodman, R. F., East-west ionospheric drifts at the magnetic equator, *Space Res.*, **12**, 968, 1972.
- Wygant, J., D. Rowland, H. J. Singer, M. Temerin, F. Mozer, and M. K. Hudson, Experimental evidence on the role of the large spatial scale electric field in creating the ring current, *J. Geophys. Res.*, **103**, 29,527, 1998.
- Yeh, H.-C., J. C. Foster, F. J. Rich, and W. Swider, Storm-time electric field penetration observed at mid-latitude, *J. Geophys. Res.*, **96**, 5707, 1991.
- Yeh, H. C., S. Y. Su, Y. C. Yeh, J. M. Wu, R. A. Heelis, and B. T. Holt, Scientific mission of the IPEI payload on board ROCSAT-1, *Terr. Atmos. Ocean Sci.*, suppl., p. 19, March 1999.
- Yeh, H. C., S. Y. Su, and R. A. Heelis, Storm time plasma irregularities in the pre-dawn hours observed by the low-latitude ROCSAT-1 satellite at 600 km altitude, *Geophys. Res. Lett.*, **28**, 685, 2001.

J. Aarons, Center for Space Physics, Boston University, Boston, MA 02215, USA.

S. Basu, T. W. Bullett, K. M. Groves, F. J. Rich, and P. J. Sultan, Space Vehicles Directorate, Air Force Research Laboratory, Hanscom AFB, MA 01731-3010, USA.

Su. Basu, Atmospheric Sciences Division, National Science Foundation, 4201 Wilson Boulevard, Rm. 775, Arlington, VA 22230, USA. (sbasu@nsf.gov)

P. Doherty, E. MacKenzie, and C. E. Valladares, Institute for Scientific Research, Boston College, Chestnut Hill, MA 02467, USA.

S.-Y. Su and H.-C. Yeh, Institute of Space Science, National Central University, Chung-Li, 32054 Taiwan.

(Received February 28, 2001; revised June 15, 2001; accepted June 18, 2001.)

Statistics of Scintillations, TEC depletions and radar plumes observed at equatorial latitudes

C. E. Valladares and R. Sheehan

Abstract

A spaced-antenna scintillation system has operated at Ancon (11.8° S, 77.2° W, dip latitude 0.9° N) since May 1994. This system provides a complete characterization of the scintillation signal and the zonal drift of the irregularities at two observing directions. The seasonal occurrence of scintillations shows the well-known maximum during the equinoxes and the December solstice. While the equinoctial maximum is almost constant as a function of solar cycle, the December solstice occurrence increases from 50% at solar minimum to almost 100% during solar maximum. For the June solstice, the occurrence of scintillations varies in the opposite direction, decreasing from 20% during solar minimum to almost 0% at solar max conditions. Daily TEC files from 6 GPS receivers, located also on the west coast of South America, have been used to determine the development of plasma bubbles and the production of TEC depletions in the GPS data. We have designed a computer algorithm to automatically identify and locate the boundaries of TEC depletions. The statistics of these TEC depletions are compared to similar statistics of scintillations and radar plumes recorded by the JULIA radar. The earliest appearance of scintillations agrees well with earliest appearance of TEC depletions. However, the decay time of scintillations is at least one hour after TEC depletions disappear. In very few cases (less than 10 per year), we observe a pattern of scintillations containing a high power law spectra (> 3) with no TEC depletions and no radar plumes.

Introduction

One of the distinguishing features of the equatorial ionosphere is the occurrence of plasma depletions during the nighttime hours. This phenomenon, known as equatorial spread-F (ESF), consists of the sudden advection of a region 100 – 500 km wide containing low density plasma [Woodman and LaHoz, 1976]. This unstable plasma originates at the bottomside of the F-region and rises, in most cases, up to the topside of the F layer. It is known that the bottomside of the nighttime F-region is inherently unstable to the initiation of the Rayleigh-Taylor instability due to the existence of sharp density gradients and the decay of the underlying E-region. During the day the conductivity of the E-layer is able to short out any electric field with a scale size larger than 1 km. Right after sunset, the E-layer recombines rapidly and becomes unable to diminish any electric field associated with the onset of F-region irregularities. While ESF was initially used to describe plasma bubbles and the irregularities that grow within them, it is used now to denote other types of structures seen at low latitudes such as bottomside sinusoids (BSS) [Valladares *et al.*, 1983], bottomside and bottomtype traces [Hysell and Burcham, 1998]. The study of ESF is important because of the disturbance that a turbulent layer produces on satellite and navigation signals. When an UHF or L-band radio signal crosses a turbulent region containing irregularities with scale sizes of order 1 km, the amplitude decreases, the phase varies and the angle of arrival changes substantially. These factors produce a fading of the signal in ground-based receivers, an effect known as scintillations. Since 1994 Boston College has conducted measurements of scintillations using a system of several receivers at Ancon, Peru [Valladares *et al.*, 1996]. Since 1996 the Air Force Research Laboratory has conducted similar measurements at Antofagasta, Chile [Basu *et al.*, 1996; Groves *et al.*, 1997]. In the last two years, Boston College has installed 5 GPS receivers at different locations in Colombia and Peru. These new receivers provide values of the S4 scintillation index and, together with the IGS GPS receivers, the latitudinal distribution of TEC. This paper presents statistics of the S4 scintillation indices, and a comparison to the distribution of TEC depletions measured by several GPS receivers. We also use measurements of coherent echoes recorded by the JULIA system that operates at Jicamarca.

Scintillation and TEC Data

A longitudinal chain of GPS receiver sites now complements the UHF and L-Band scintillation sites at Ancon, Peru and Antofagasta, Chile (Figure 1). The Ancon site is also near the Jicamarca and Julia radars, which provides vertical profiles of returns from 3-m irregularities. Figure 2 shows an extended period of active scintillations observed at Ancon from 0100 to 1400 UT (2100 - 0900 LT). The top two panels are the S4 index and drift velocity measured at the 350 km altitude intersection point along the ray path from the F7 geo-synchronous satellite (Figure 1) located to the west of Ancon. Raw signal levels are collected at 50 Hz by the spaced antenna system and processed at 82 second intervals; generally, S4 values must exceed .15 for the cross-correlation method to yield valid velocities, where the 1 km irregularities that generate scintillation are assumed to move with the zonal ionospheric drift. In the velocity panel the calculated zonal drift velocity V_o (red) fluctuates at the scintillation onset, but quickly settles to a steady 150 m/s eastward drift that slows and reverses to the westward direction 8 hours later. The random velocity V_c (blue), referenced from the bottom of the panel, is, by definition, always positive and is a measure of time and spatial variations in the velocity. The next two panels show the same type of data seen to the east of Ancon at the F8 intersection point. Since this satellite is at a low elevation angle the ray path through the densest part of the ionosphere is longer and is expected to show greater variability, and the idealized plane geometry results in a somewhat larger calculated horizontal velocity. Also, because sunset is earlier to the east, the onset of scintillations associated with bubble formation near the terminator can occur before activity is observed to the west, as happens in this case. In the bottom panel the L-Band S4 has an onset and behavior like the west satellite, although at lower levels. Its ionospheric intersection point is close to the F7 point to the west.

The TEC data from the chain of GPS stations provide valuable information about the time and extent of large scale ionospheric density depletions that lead to scintillations. To compile meaningful statistics and identify interesting case studies, we have developed a quick way to automatically analyze the large amount of data recorded from several satellites simultaneously. Figure 3 is an example of a likely bubble detected by two GPS satellites. Blue and green traces in the figures are the raw TEC and a polynomial fit, respectively. The derivative of the raw TEC (red curve) is used to identify a bubble, delimited by filled and open arrow pairs at the top.

Statistics

Operating since 1994, the Ancon scintillation station has provided S4 and drift velocity data that has been sorted by season, magnetic condition, and solar activity. Figure 4 is a monthly compilation of scintillation occurrence vs local time during 1995. A local time is considered to have scintillations if S4 exceeds 0.15 continuously 10 or more minutes in the interval, from which the percentage occurrence for an entire month is computed. Figure 4 also shows occurrences for quiet ($K_p \leq 3o$) and active ($K_p > 3o$) magnetic activity. The expected seasonal variations are evident, with more frequent occurrence during the equinoxes and the December solstice, while increased magnetic activity tends to extend scintillations to later local times. Figure 5 is the same as Figure 4, except for the year 2000 near the solar maximum peak. It is apparent that the already weak occurrence during the June solstice decreases to less than 20%, while scintillations from the September equinox to the beginning of the March equinox approach 100%. Another way of looking at the distribution of scintillations throughout the year is shown in Figure 6, which plots scintillation and TEC depletion activity vs. local time and day of year during quiet magnetic conditions ($K_p < 3o$). All available data since 1994 is tabulated, and the maximum value at each local time and day of year is plotted. The Ancon west and east intersection points (top panels) display the characteristic seasonal maxima and local time dependence seen in Figures 4 and 5. In the third panel, comparable distributions can be seen in data from Antofagasta, Chile at the F7 intersection point to the west (Figure 1), which lies nearly at the same magnetic longitude as the F8 intersection point to the east of Ancon. Seasonal and local time distributions are similar to those at Ancon, but because of higher ionospheric densities in the ionospheric anomaly located to

the south of Antofagasta, scintillation intensity is generally higher, especially during the September equinox. The last panel shows the depth of TEC depletions identified automatically from data recorded by GPS sites in the South America chain (Figure 1). Although the seasonal distribution and local time onset of TEC depletions and scintillation activity are similar, there is some indication that scintillations persist after the underlying large-scale depletions have decayed.

Finally, although there is usually a close association between ionospheric depletions and scintillation activity, occasionally scintillations are seen without obvious evidence of depletions. Figure 7 shows a case from Ancon of a short scintillation event observed at UHF and L-Band with a somewhat steeper spectral index (< -3) at the onset than usual (Figure 2). At the same time, neither the TEC data, nor the Julia incoherent radar at Jicamarca show any sign of depletions or radar plumes that indicate the presence of an ionospheric bubble (Figure 8). The top panel, constructed from fits to TEC data from the GPS chain, clearly display the northern and southern crests of the anomaly decaying after sunset and a steep latitudinal gradient at the equator. The onset scintillations at Ancon (bottom panel) coincides with the lowering and disappearance of the bottom-side echoes from the Julia data (middle panel), but the absence of altitude extended plumes and the lack of sustained scintillation activity at Antofagasta suggest there was no rising ionospheric bubble that affected latitudes away from the equator.

Conclusions

In this paper, we have shown the monthly and local time variability of scintillations and TEC depletions. Important features of these statistical distributions are: (1) The local time of scintillations (or depletions) onset varies through the year as the local sunset time. (2) scintillations decay at least one hour after the decay of the depletions. (3) The phase of the solar cycle affects the amount of scintillations; it increases in the December solstice as the solar flux augments, but it decreases to low values during the June solstice. We presented one event consisting of strong scintillations near the equator, but neither scintillations at Antofagasta, nor TEC depletions, nor radar echoes with the Julia radar were registered. The general characteristics of this type of event suggests that plasma bubbles are not the only mechanism that is able to generate UHF scintillations.

Acknowledgments

This work was partially supported by NSF grants ATM-9714804 and ATM-9819912, and by Air Force Research Laboratory contract F19628-97-C-0094.

References

- Basu, S., et al., Scintillations, plasma drifts, and neutral winds in the equatorial ionosphere after sunset, *J. Geophys. Res.*, 101, 26795, 1996.
- Groves, K. M., et al., Equatorial scintillation and systems support, *Radio Sci.*, 32, 2947, 1997.
- Hysell, D. L., and J. D. Burcham, JULIA radar studies of equatorial spread F, *J. Geophys. Res.*, 103, 29155, 1998.
- Valladares, C.E., W.B. Hanson, J.P. McClure, and B.L. Cragin, Bottomside sinusoidal irregularities in the equatorial F-region, *J. Geophys. Res.*, 88, 8025, 1983.
- Valladares, C.E., R. Sheehan, S. Basu, H. Kuenzler, and J. Espinoza, The multi-instrumented studies of equatorial thermosphere aeronomy scintillation system: Climatology of zonal drifts, *J. Geophys. Res.*, 101, 26839-26850, 1996.
- Woodman, R.F., and C. LaHoz, Radar observations of F region equatorial irregularities, *J. Geophys. Res.*, 81, 5447, 1976.

Figure Captions

Figure 1. Map of the West Coast of South America showing locations of field sites. Circles indicate the effective field of view at sites with GPS receivers. Crosses indicate ionospheric intersections at 300 km altitude for ray paths to the geo-synchronous F7 and F8 satellites seen by the UHF sites at Ancon and Antofagasta.

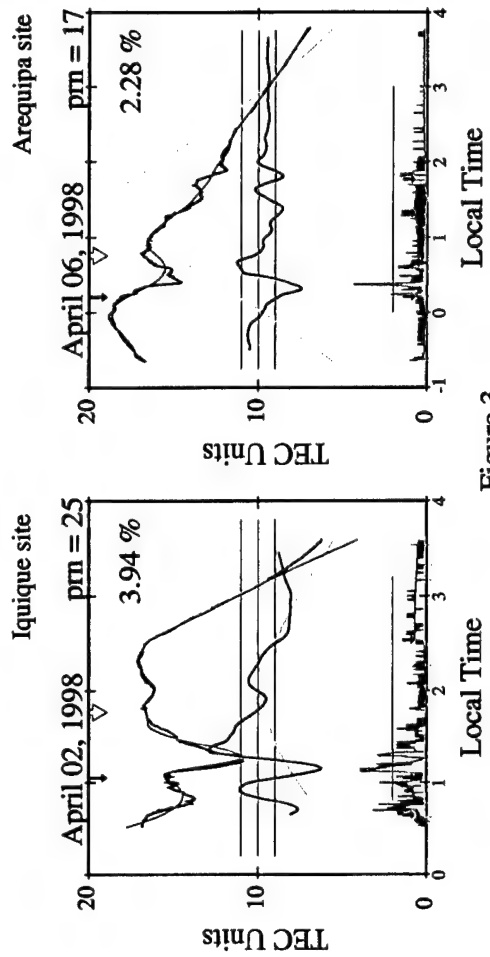
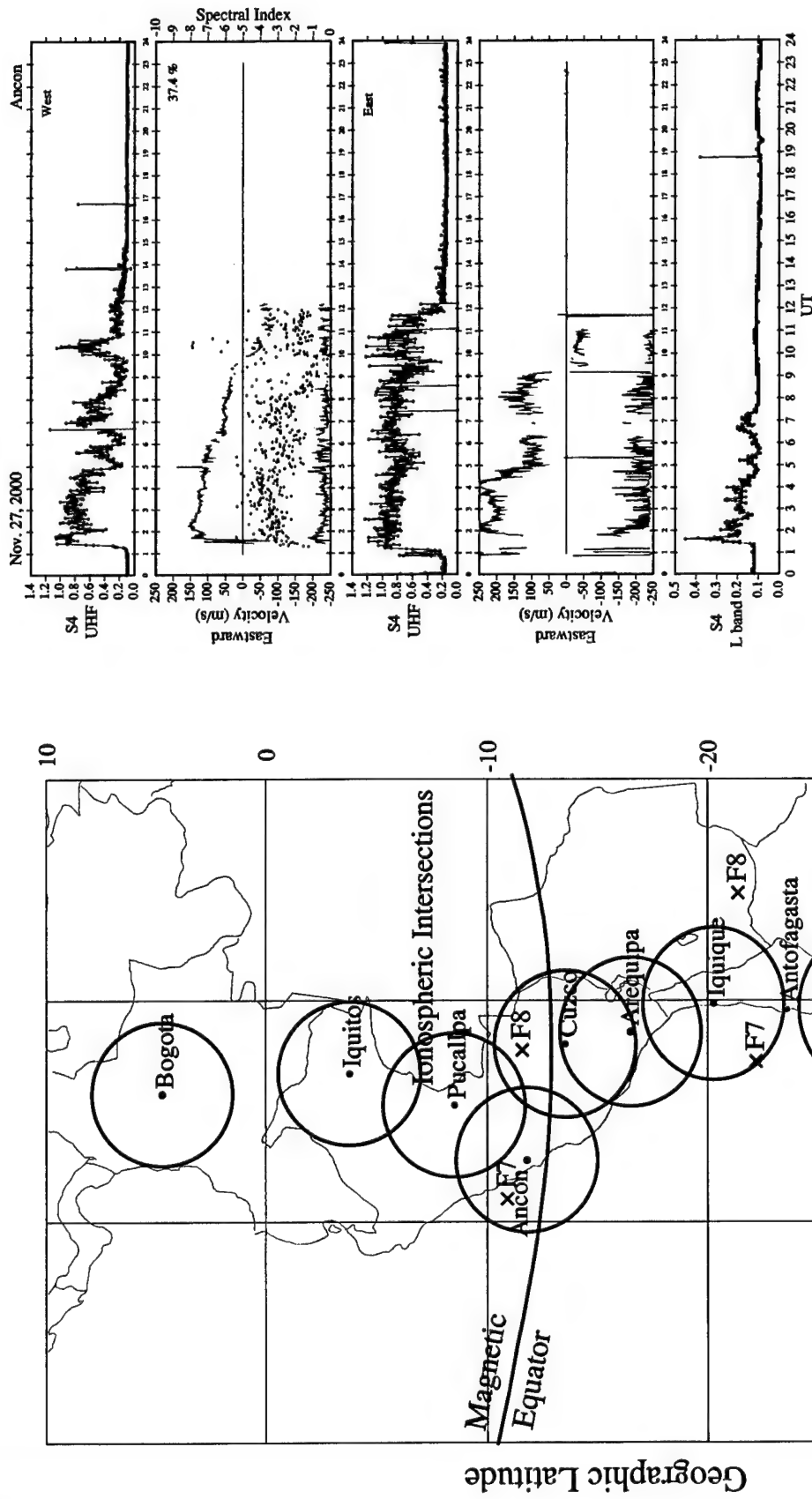


Figure 2

Figure 3

Figure 1

100%
80%
60%
40%
20%

2000

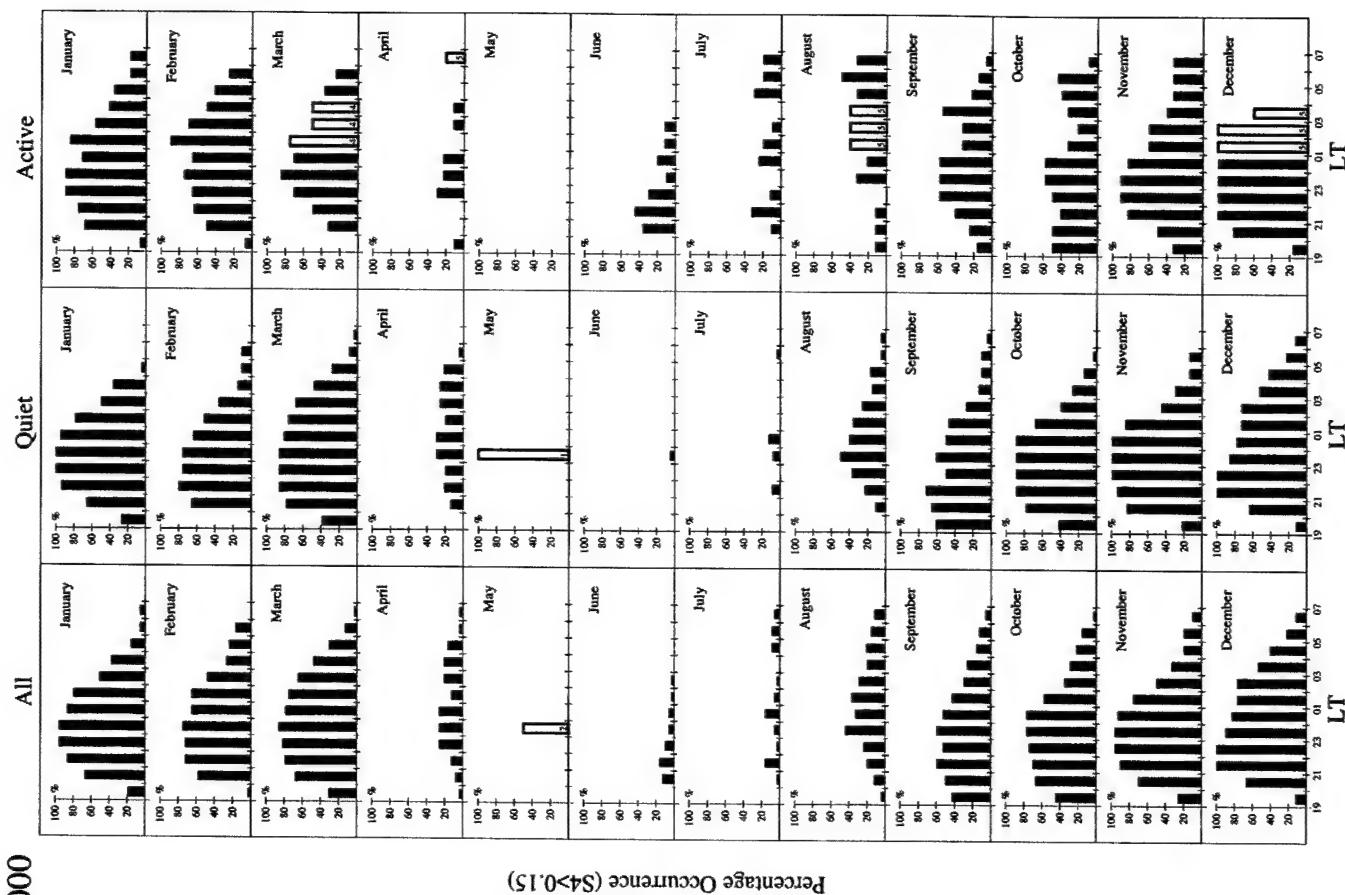


Figure 5

100%
80%
60%
40%
20%

1995

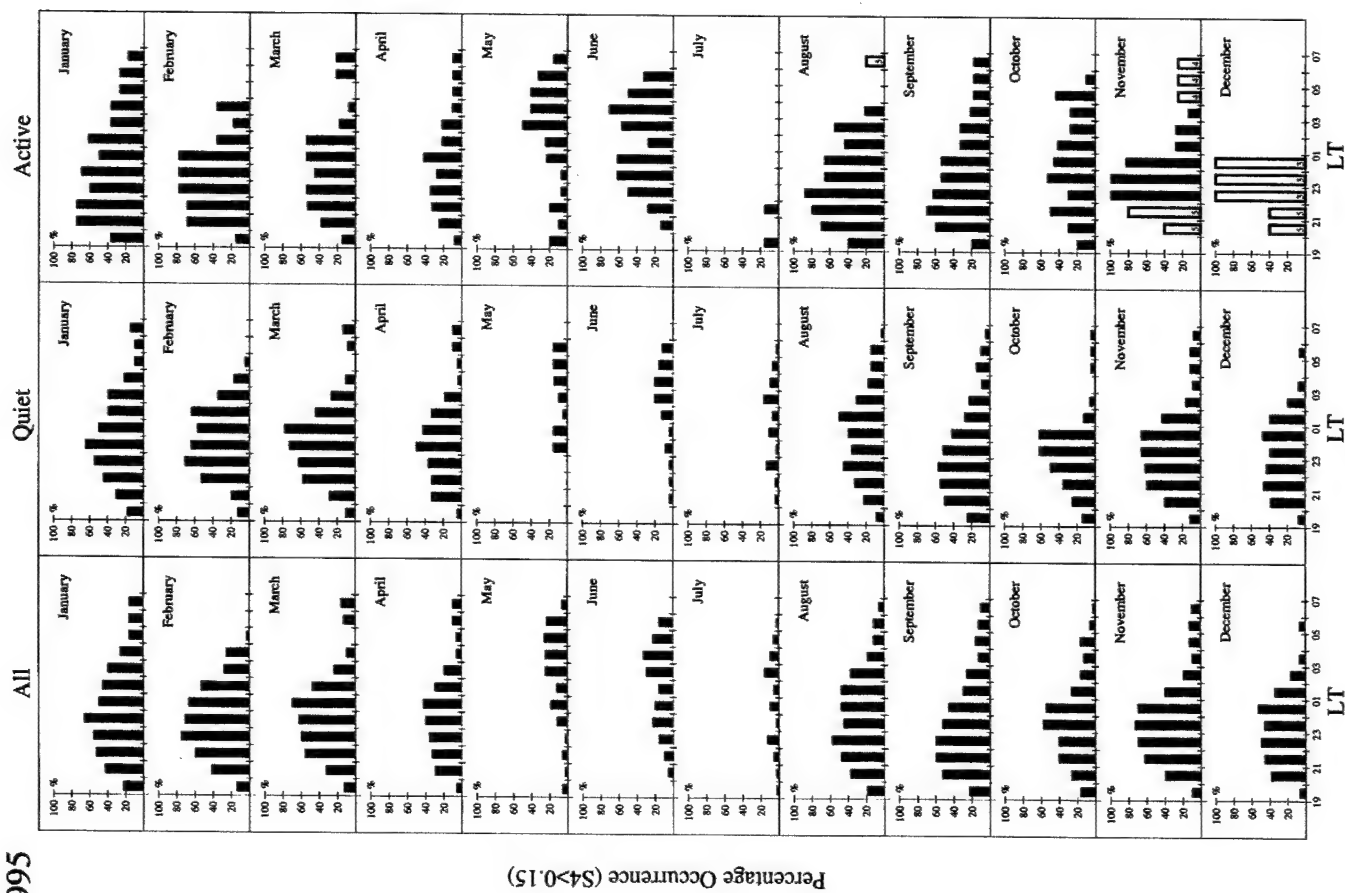


Figure 4

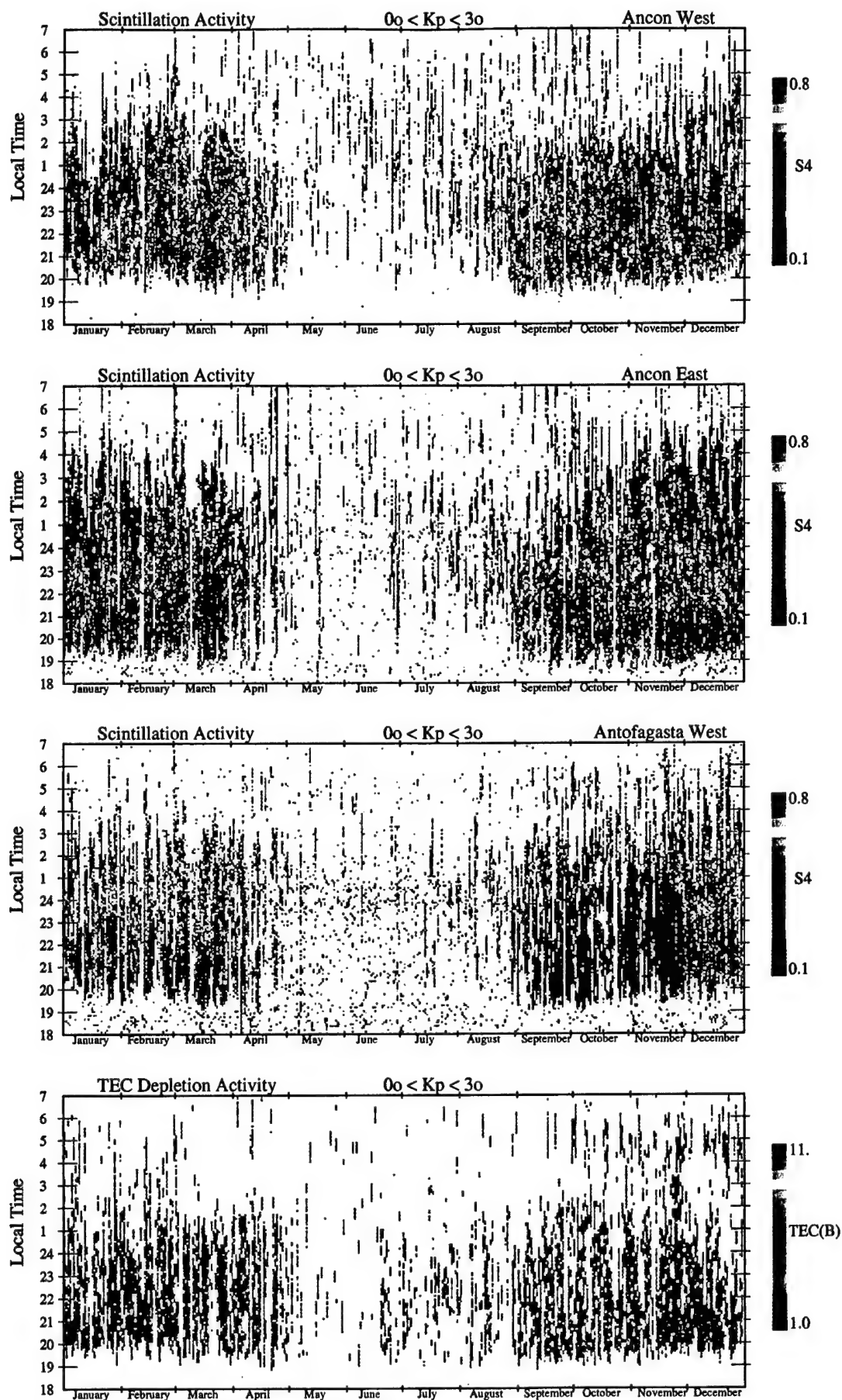


Figure 6

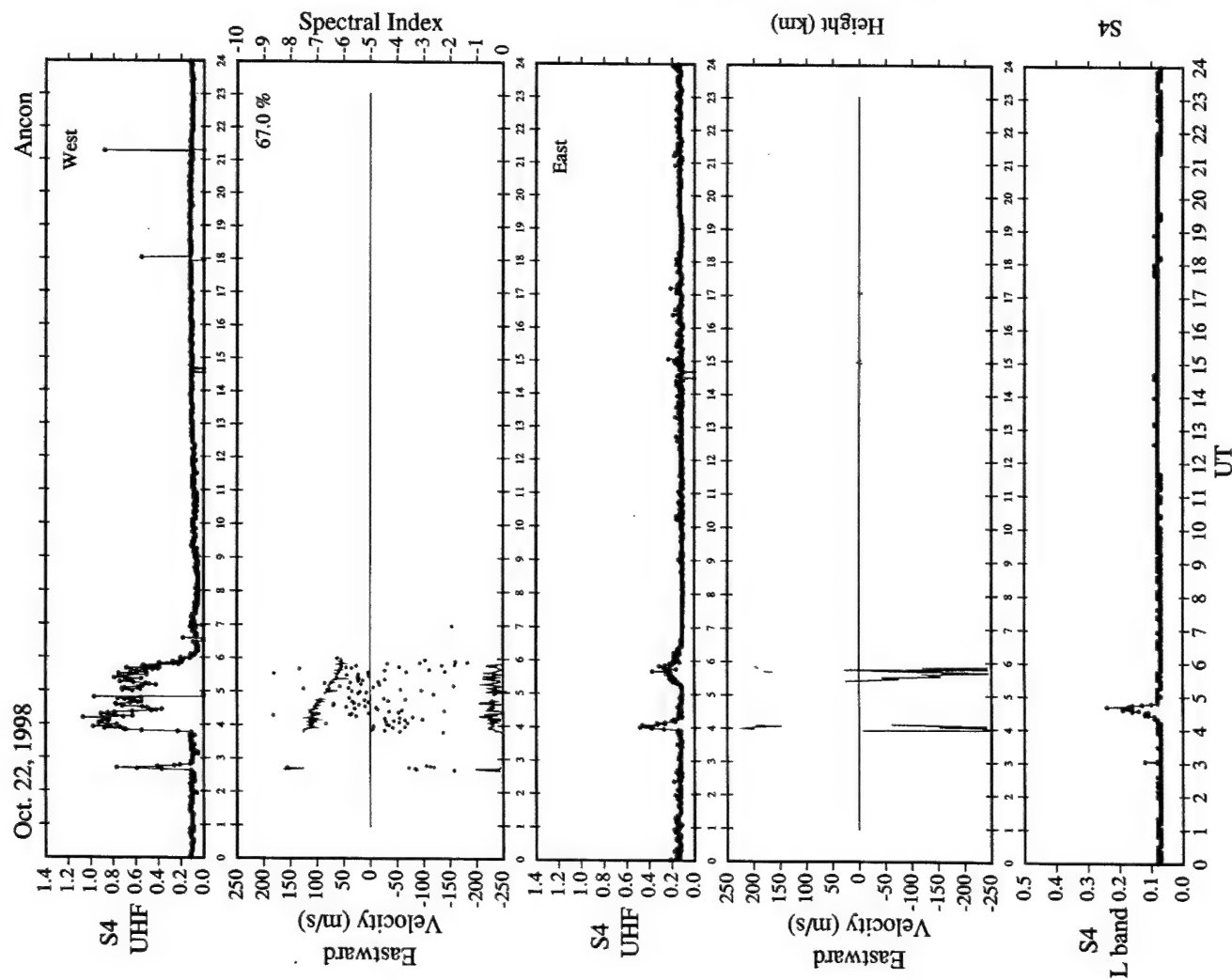


Figure 7

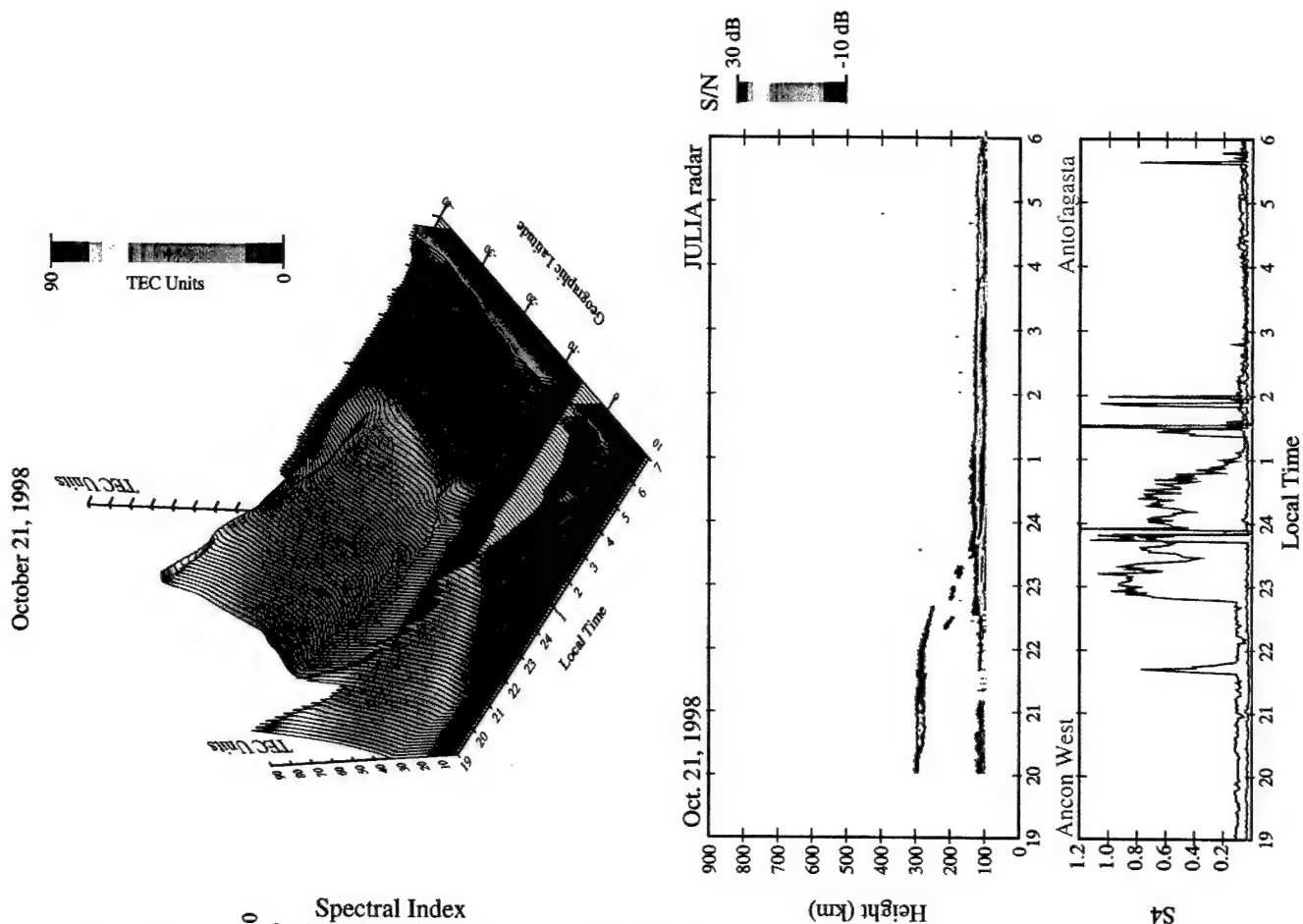


Figure 8

Correlative study of neutral winds and scintillation drifts measured near the magnetic equator

C. E. Valladares,¹ J. W. Meriwether,² R. Sheehan,¹ and M. A. Biondi³

Received 9 February 2001; revised 3 October 2001; accepted 7 December 2001; published XX Month 2002.

[1] Measurements of the thermospheric neutral wind at Arequipa, Peru, and observations of the drift of the irregularities at Ancon, Peru, are used to study the coupling that exists between ions and neutrals at equatorial latitudes and the variability of this coupling as a function of the occurrence of scintillations. This study is based on data collected at the Arequipa and Ancon stations between 1996 and 1998. Our comparative analysis indicates that the relative wind-drift values vary depending on season and the solar flux level. We found that during the equinoxes and low solar flux values, the averaged zonal drift is larger than the wind by 15 m s^{-1} , but for solar flux values above 130 units, the average wind exceeds the drift values by 10 to 20 m s^{-1} . We suggest that the occurrence of larger equinoctial drifts can be explained by the existence of altitude gradients in the zonal wind during that season. During the June solstice the zonal wind seems to exceed the irregularity drift by $\sim 10\text{--}20 \text{ m s}^{-1}$ independent of the solar flux. We also find that the meridional wind shows a modest dependence on the scintillation activity during the June solstice. During scintillation events and between 2000 and 2400 LT the averaged meridional wind observed to the south and north of Arequipa exceeds their corresponding no-scintillation values by 20 m s^{-1} . We present likely explanations of this effect. **INDEX TERMS:** 2415 Ionosphere: Equatorial ionosphere; 2437 Ionosphere: Ionospheric dynamics; 2439 Ionosphere: Ionospheric irregularities; 2427 Ionosphere: Ionosphere/atmosphere interactions (0335); **KEYWORDS:** scintillations, thermospheric wind, irregularity drift, electrodynamics

1. Introduction

[2] Recent studies of equatorial electrodynamics and of spread *F* phenomena have directed attention to the day-to-day variability (weather) of the equatorial thermosphere-ionosphere system, to the strength of the coupling of ions and neutrals in this system, and to the question of how well forecasting the appearance of equatorial spread *F* (ESF) can be achieved given limited access to *F* region parameters by existing ground-based instruments [Basu *et al.*, 1996; Fejer *et al.*, 1999]. Equatorial electrodynamics and the frequency of occurrence of spread *F* accompanied by scintillation activity at UHF frequencies are closely linked. At equatorial latitudes, mostly during quiet conditions, the neutral wind is the main driving force of plasma motion. By producing polarization electric fields through the combined action of the *E* and the *F* region dynamos [Rishbeth, 1971a, 1971b], the flow of air from the afternoon pressure bulge transports the equatorial plasma across and along field lines, while changing the altitude of the *F* region peak and the symmetry of the ionospheric density horizontal distribution with respect to the magnetic equator. These two effects make the nighttime *F* layer more or less unstable to the development of the Rayleigh-Taylor instability (RTI). It has long been considered that the equatorial ionosphere is unstable to the RTI mechanism [Dungey, 1956; Woodman and La Hoz, 1976; Kelley *et al.*, 1976; McClure *et al.*, 1977].

[3] An important feature of equatorial vertical drift morphology is the phenomenon called the pre-reversal enhancement (PRE) [Woodman, 1970]. The full development of the PRE has been associated with the sunset decay of the highly conductive *E* layer [Farley *et al.*, 1986] and the reversal of the zonal thermospheric wind from a westward to an eastward direction [Crain *et al.*, 1993]. Basu *et al.* [1996] presented the day-to-day variability of the PRE observed during an extended campaign in South America to suggest that the appearance of a well-developed PRE precedes the onset of ESF. More recently, Fejer *et al.* [1999] have indicated that the magnitude of the vertical plasma drift may constitute the only observable that is required to predict the onset of ESF.

[4] A major question in understanding the several processes that are interlinked with one another in the development of ESF is how the magnitude of the PRE responsible for the rise of the *F* region plasma at evening twilight may be related to the magnitude and direction of the thermospheric wind. The recent work of Fesen [1996] has demonstrated the significant effect on equatorial thermospheric dynamics resulting from the penetration of the *F* region by the semidiurnal and diurnal tidal components. The role of such tidal activity is particularly marked in regard to the phenomena of the midnight temperature maximum and the brightness wave [Colerico *et al.*, 1996] seen in the nighttime equatorial airglow.

[5] This paper presents data collected by two instruments: (1) a Fabry-Perot interferometer (FPI) located at Arequipa, Peru (16.5°S , 71.4°W , 3.5°S dip latitude) and (2) a spaced-receiver scintillation interferometer (SRSI) deployed at Ancon, Peru (11.79°S , 77.18°W , 0.9°N dip latitude). Both instruments are currently operating unmanned under the auspices of the CEDAR NSF initiative. The measurements to be discussed here represent the first substantial set of concurrent observations of the neutral wind and the drift of equatorial *F* region irregularities. Two previous investigations based upon short campaign measurements extending over 2 weeks have compared the zonal neutral winds and the *F* region drift of the

¹Institute for Scientific Research, Boston College, Newton Center, Massachusetts, USA.

²Department of Physics and Astronomy, Clemson University, Clemson, South Carolina, USA.

³Department of Physics and Astronomy, University of Pittsburgh, Pittsburgh, Pennsylvania, USA.

irregularities [Basu *et al.*, 1991, 1996]. The first paper presented observations of scintillation drifts obtained at Huancayo and zonal neutral winds measured at Arequipa. Basu *et al.* [1991] concluded that scintillation activity was correlated with a well-developed polarization electric field, which leads to a horizontal drift of the F region ions equal to that of the neutrals. The second paper presented comparisons of the first set of scintillation drift measurements for the Ancon SRSI with the Arequipa FPI measurements of neutral winds and noted that the day-to-day variability of the zonal thermospheric wind might potentially explain the day-to-day variability of ESF development. The lack of a large number of comparative measurements over an extended period made this conclusion rather tentative. Another study, conducted by Biondi *et al.* [1988], compared the Fabry-Perot neutral winds and the ion drift determined by incoherent scatter techniques at Jicamarca. Two days of simultaneous data found correlated motions of the neutrals and the ionospheric plasma. The present paper extends the simultaneous FPI/SRSI measurements.

[6] Measurements of the thermospheric neutral wind and temperatures at the equatorial station of Arequipa have been conducted since 1983 over one solar cycle. The seasonal and solar cycle dependencies of both zonal and meridional components of the wind have been presented in several publications [Meriwether *et al.*, 1986; Biondi *et al.*, 1990, 1991, 1999]. Biondi *et al.* [1991] demonstrated that the seasonal variations were more pronounced than the solar cycle variations. The averaged meridional winds presented a consistent pattern of southward flows in the early evening, near zero values around midnight and then again southward in the late night. This pattern was typical during the local winter solstice months of May, June, and July. The largest value of the southward meridional wind for solar minimum conditions was $\sim 100 \text{ m s}^{-1}$, which occurred during the early evening. During increased solar activity this peak value decreased by ~ 10 to 20%. During equinoctial months, meridional winds were $\sim 0 \text{ m s}^{-1}$ throughout the night. The zonal winds were found to be almost exclusively eastward during quiet magnetic conditions. The averaged zonal winds exhibited peak values occurring near midnight that increased from $\sim 100 \text{ m s}^{-1}$ at solar minimum to ~ 150 – 175 m s^{-1} at solar maximum.

[7] More recently, Meriwether *et al.* [1996] have used FPI measurements from Arequipa to show that during solar maximum, the zonal wind is often significantly weaker and the temperature is elevated over the Andes compared to over the Pacific Ocean. The authors suggested that viscous dissipation of waves propagating from below the thermosphere was the causative mechanism of the localized thermospheric heating. A more recent publication [Meriwether *et al.*, 1997] has reinforced the idea of an orographic source as the source of additional energy at longitudes over the Andes.

[8] Throughout this paper we use the term scintillation as synonymous with ESF, although we know that this is not completely accurate. Equatorial spread F encompasses a whole array of disturbances that an unstable ionosphere produces for the transmission of radio waves. At equatorial latitudes, plasma turbulence can exist within plasma depletions, which are often called "bubbles" [Woodman and LaHoz, 1976]. There also exist bottomside and bottom-type layers [Hysell and Burcham, 1998], and volumes containing bottomside sinusoids [Valladares *et al.*, 1983]. Scintillation is the name given to the fading of EM waves (mainly in the UHF and L band range) when signals pass through a turbulent plasma media. For the fading to occur it is necessary that irregularities of scale ~ 0.1 – 1 km be present within the usually much larger sized turbulent eddy.

[9] The goals of this paper are the following: (1) to examine, by means of case studies and statistical analysis, the climatology of the zonal and meridional components of the thermospheric wind during scintillation periods and (2) to estimate the degree of

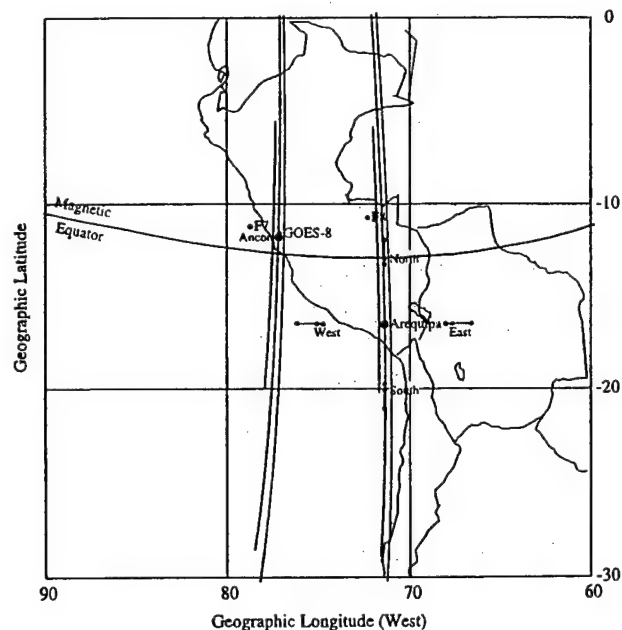


Figure 1. Geometry of the ionospheric and thermospheric observations that operate continuously at Ancon and Arequipa. The large dots indicate the locations of the spaced-receiver scintillation interferometer (SRSI) at Ancon and the Fabry-Perot interferometer (FPI) at Arequipa. The dots labeled F7, GOES 8, and F8 indicate the respective 350-km intersection points for the ray path from Ancon looking west, looking to the GOES 8 satellite, and looking east. The dumbbells indicate the horizontal extent of the 630-nm emission between altitudes of 210 and 280 km observed by the FPI for the four cardinal directions, with the internal dots indicating the emission centroids.

coupling that exists between the ions and neutrals during the nighttime hours.

2. FPI and Scintillation Instrumentation

[10] The Arequipa FPI measures nighttime thermospheric winds and temperatures by observing the Doppler shift and spectral broadening of the O I 630.0-nm nightglow emissions. Near the equator at solar minimum the half intensity points of the emitting layer extend over about two scale heights, with the emission centroid at $\sim 255 \text{ km}$ [Meriwether *et al.*, 1997]. The altitude of the emission centroid varies between 250 and 285 km, depending on the height of the F region and the season of the year. The 630-nm airglow signal detected by the Arequipa FPI instrument is increased by a factor of ~ 4 through the use of a multiaperture mask [Biondi *et al.*, 1985]. The FPI is refractive index tuned over one free spectral range ($\sim 0.02 \text{ nm}$) by changing the density of argon gas between the plates with a volume changer. The instrument collects a sufficient number of counts after a few minutes of integration to yield measurements of winds and temperature with typical 1-sigma uncertainties of 15 m s^{-1} and $\sim 45 \text{ K}$. The Arequipa FPI usually operates automatically throughout the month, except for a 5-day period centered on the full moon. However, at Arequipa, clear night skies occur regularly only from late March to late October. The night sky for the rest of the year is generally partly cloudy to overcast. Further details regarding the FPI instrument are presented by Biondi *et al.* [1985] and Meriwether *et al.*, [1997].

[11] Figure 1 shows (1) the locations of the FPI at Arequipa and the SRSI at Ancon (heavy dots), (2) the extension of three field lines with corresponding apex altitudes at 300, 450, and 600 km (light

lines), and (3) the latitudinal or longitudinal regions of the airglow observed in determining the averaged Doppler shift in the zonal and meridional directions (bars with dots). The FPI's pointing head is also programmed to observe the 630-nm nightglow layer in the zenith to provide a zero velocity reference for the line-of-sight wind determinations on the assumption that the vertical wind component averaged over one night of observations is small ($\sim 0 \text{ m s}^{-1}$).

[12] At the present time, the Ancon scintillation system receives UHF and L band signals from three geostationary satellites located at 100°W , 75°W , and 20°W longitudes. The system initially consisted of three UHF antennas placed in a magnetic east-west alignment, and a 10-m dish used for L band scintillations. In April 1996 the system was modified to accommodate another baseline consisting of two antennas pointing at 25° elevation to another satellite located at 20°W . Figure 1 displays the geographic locations of the ionospheric intersection point for both baselines and the L band system.

[13] The computer program that controls and processes the data was also upgraded to run in the more robust Labview software environment using a Pentium PC computer. A Linux PC was also incorporated into the system to establish communications, via modem, to a central computer in Lima. This scheme offers near real-time access, via Internet, to selected parameters that can be observed as the experiment progresses.

3. Case Study Comparison of Neutral Wind and Scintillation Drift

[14] Concurrent measurements of scintillation drifts and thermospheric winds have been carried out in the Peru sector since May 1994, when the Ancon SRSI started operations [Basu *et al.*, 1996]. Our study is based on the data collected between the years of 1996 and 1998. Our decision on limiting the database to these years was made because the online software of the SRSI system was not fully calibrated to extract the characteristic velocity (see discussion below about this term). Moreover, the FPI data for the years of 1994 and 1995 required additional processing to remove OH contamination [Meriwether *et al.*, 1997], and, for the purpose of this study, we chose to put aside these results to avoid possible confusion of the statistics developed from the comparison of the zonal neutral winds with the ion drifts.

[15] Before presenting data from the FPI and the scintillation systems, we indicate several sources of error or discrepancies that may exist in measurements from these types of instruments. The scintillation technique measures the transport velocity of 1-km scale irregularities in a plane that is parallel to the antenna layout (magnetic east west) and perpendicular to the local magnetic field line. The field line perpendicularity is the result of the extended elongation of the irregularities in the field line direction. Ideally, the satellite should be located immediately overhead the receiving station in order to measure the east-west horizontal motion of the patch of irregularities. In practice, however, the ray path between the satellite and the receivers will be at an elevation angle, θ , that is less than 90° . At Ancon, the direction to the western satellite is $\sim 65^\circ$ over the horizon. This introduces a component of the vertical ion drift in the "zonal ion drift" measurements. Since the vertical drift of the equatorial plasma is typically of order 10 m s^{-1} and rarely exceeds 50 m s^{-1} , this relatively small velocity should not significantly alter our measurements of the zonal drifts. However, during magnetically disturbed conditions, plasma bubbles can accelerate from the bottomside and reach supersonic upward speeds in these upward motions. Values as large as 2 km s^{-1} have been reported by Hanson *et al.* [1997] based on in situ measurements by the plasma drift meter instrument mounted on the DE 2 satellite. The 1-km scale irregularities, which are embedded within the large-scale bubbles, may also contain a very significant fraction of this large plasma motion. The new real-time program that controls the spaced receiver instrument is also able to provide

the characteristic random velocity V_c . This term gives a measure of the amount of signal decorrelation that exists at two spaced receivers [Vacchione *et al.*, 1987]. The signal decorrelation is produced by quick temporal or spatial changes in the diffraction pattern caused by the turbulent media. It has been noticed that during the early development of a plasma bubble, when its rising motion is the largest and the plasma turbulence is strongest, the level of V_c exceeds 50 m/s. However, it is much smaller at other times. Consequently, the scintillation technique is able to indicate when a fast, upward moving bubble crosses the ray path and makes it possible to discard such values.

[16] A second source of error is the fact that the scintillation technique measures the speed of $\sim 1\text{-km}$ scale irregularities. This may not be exactly equal to the plasma drift because inside a large bubble a substantial polarization electric field can be created near the walls, which makes the scintillation drift somewhat different than the $\mathbf{E} \times \mathbf{B}$ plasma drift for such bubble events.

[17] Third, there is typically a difference in altitude of approximately one scale height between the two instrument observing volumes. The scintillation drift represents the motion of the irregularities at the height of the peak density of the F region. This peak is near 350-km altitude during weak solar activity and will typically be a few tens of kilometers higher for more active periods. The altitude of the line of sight averaged Doppler shift measured by the FPI at Arequipa lies within the bottomside of the F layer; the altitude of the centroid of 630-nm emission varies between 250 and 285 km [Meriwether *et al.*, 1997]. If the wind has a gradient in latitude [Raghavarao *et al.*, 1991] or altitude [Biondi *et al.*, 1999], then a neutral wind measurement at Arequipa may underestimate the actual peak value of the wind by 5 to 10% at the location of the drift measurement. Recently, Biondi *et al.* [1999] has found indirect evidence that suggests the possible existence of a modest vertical gradient in the zonal wind.

[18] We also note that the volumes probed by the scintillation technique and the FPI are not well colocated. The F region examined by the scintillation drift receivers and the thermospheric volume probed by the FPI are separated by $\sim 250 \text{ km}$ in longitude and $\sim 400 \text{ km}$ in latitude.

[19] Operations of the Fabry-Perot instrument are conducted automatically with cloud cover information provided through examination of the images collected by the Boston University (BU) imager system [Colerico *et al.*, 1996]. The FPI results obtained during periods of cloudiness seen in the BU images are discarded. Because the BU imager did not always operate continuously throughout the month, there were times during which FPI observations were obtained without any imager data as to the extent of sky cloudiness. However, our experience has been that for periods of overcast the FPI signals are weak and the apparent Doppler shifts show a large variability. These events are identified easily and discarded. FPI observations for the more marginal situations near the vernal or austral equinoxes were included in our statistical study but excluded in any specific case study comparison. Because the skies are generally clear during the local winter months of May to August, we included these results for which there were no BU 630 nm images in our case studies.

3.1. Scintillation Drift Case Events

[20] Figure 2 shows a set of nearly continuous scintillation drifts measured at Ancon for six nights in September and October 1997. Except for the data of 17/18 September 1997, all other plots of Figure 2 correspond to times of quiet magnetic conditions. Previous measurements of the zonal drift using the incoherent scatter technique [Fejer *et al.*, 1991] or the space receiver technique [Valladares *et al.*, 1996] have indicated that during the early evening the zonal drift becomes eastward and increases. It attains a peak value between 2100 and 2300 local time (LT), and then decreases and reverses during the early morning hours. The equatorial zonal drifts show a great deal of day-to-day variability as seen in the September 1997 data. For example, on 17/18

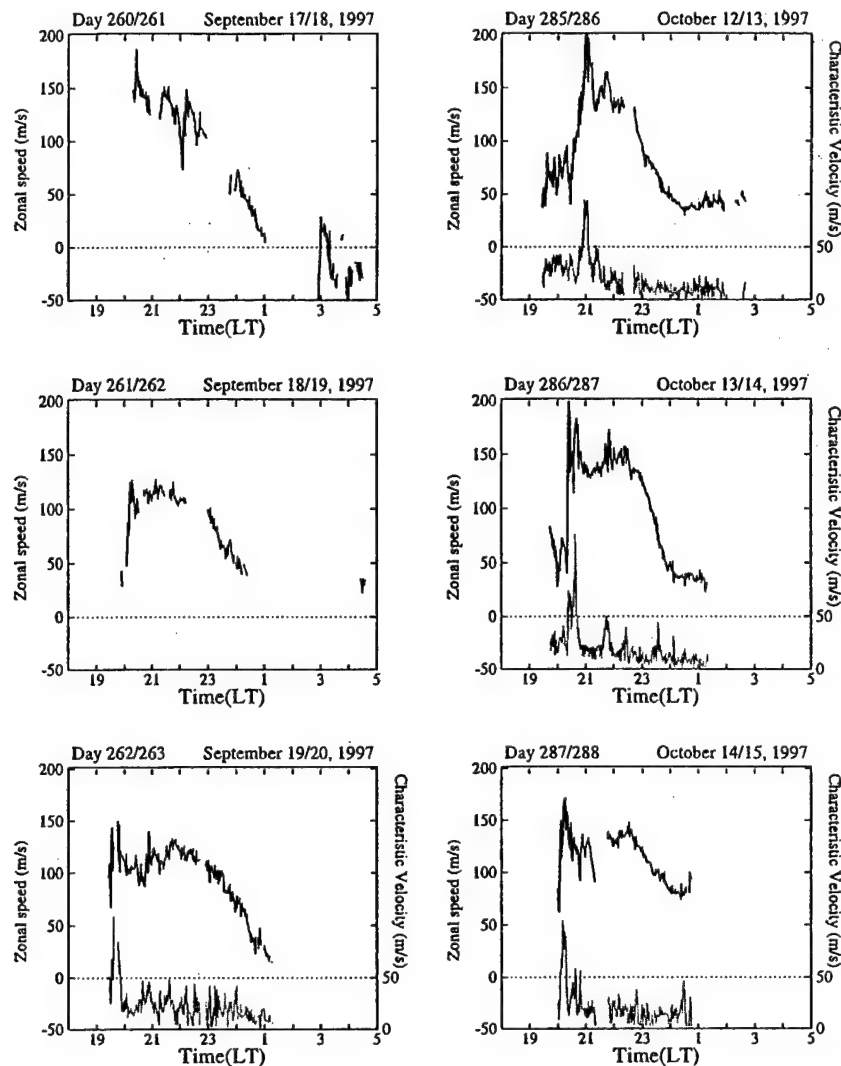


Figure 2. The temporal variation of the scintillation zonal drift (eastward positive) measured at Ancon, Peru, on 6 days during the months of September and October 1997. The gray line at the bottom of some panels displays the characteristic velocity. See text for details.

September the peak value was 150 m s^{-1} , on 18/19 September, 100 m s^{-1} , and on 19/20 September started with a value close to 100 m s^{-1} and then increased to 135 m s^{-1} . On 17/18 September 1997, when the K_p index was 5^0 , the zonal drift increased rapidly in the early evening hours, reached a maximum eastward value of 150 m s^{-1} , then decayed to near zero at 0100 LT and reversed at 0310 LT.

[21] The second trace (gray line), shown in some of the frames, is the characteristic velocity V_c . During a typical night V_c is usually well below 50 m s^{-1} , except when the turbulence of the plasma or the upward velocity is large [Battacharyya *et al.*, 1992]. In these cases, as seen in the plots corresponding to 12/13, 13/14, and 14/15 October 1997, the scintillation drifts show large positive or negative spikes and at the same time V_c rises for few minutes above 50 m s^{-1} . As described above, it is quite possible that these spikes correspond to large vertical velocities or shears within the plasma bubbles and are not a zonal $\mathbf{E} \times \mathbf{B}$ drift. As a corollary, we conclude that the V_c parameter can be used to exclude non- $\mathbf{E} \times \mathbf{B}$ drifts by noting when V_c is larger than 50 m s^{-1} . This is a property of our new analysis program that we have exploited.

3.2. Neutral Wind Events During Periods of No Scintillation

[22] Figure 3 shows values of the zonal neutral wind measured at Arequipa on four nights during equinoctial months in

1996 and 1997. The equinoxes are periods when the scintillation activity is strong in the American sector. However, on these specific days, no scintillation events were detected at Ancon. Only a short segment of scintillation appeared in the early morning hours on 23/24 April 1996 (seen on the lower left panel). Each measurement of the zonal neutral wind is plotted with its error bar and a letter (W or E) to indicate the pointing direction of the FPI at the time of the measurement. Similar to the drift measurements, the zonal wind displays a large day-to-day variability in their peak values, time of the peak, width, and rate of decay. The peak value of the winds can be as high as 175 m s^{-1} (23/24 April 1996), or as low as 125 m s^{-1} (19/20 April 1996). On many occasions the zonal winds show a good correlation (equal sign and similar magnitude) in their west and east observations (23/24 April 1996), implying a large degree of longitudinal coherence. At other times the FPI winds show a zonal spatial gradient, which may be an indication of the passage of gravity waves. Also, not all the daily neutral wind patterns exhibit as smooth a growth and decay as the climatological patterns published by Biondi *et al.* [1999] suggest. Instead, as shown on 4/5 and 5/6 October 1996, the zonal wind can decrease in the early evening and then rapidly increase. Such short-term decrease-increase signatures were seen near 1900 LT. It is interesting that on 19/20 April 1996 a magneti-

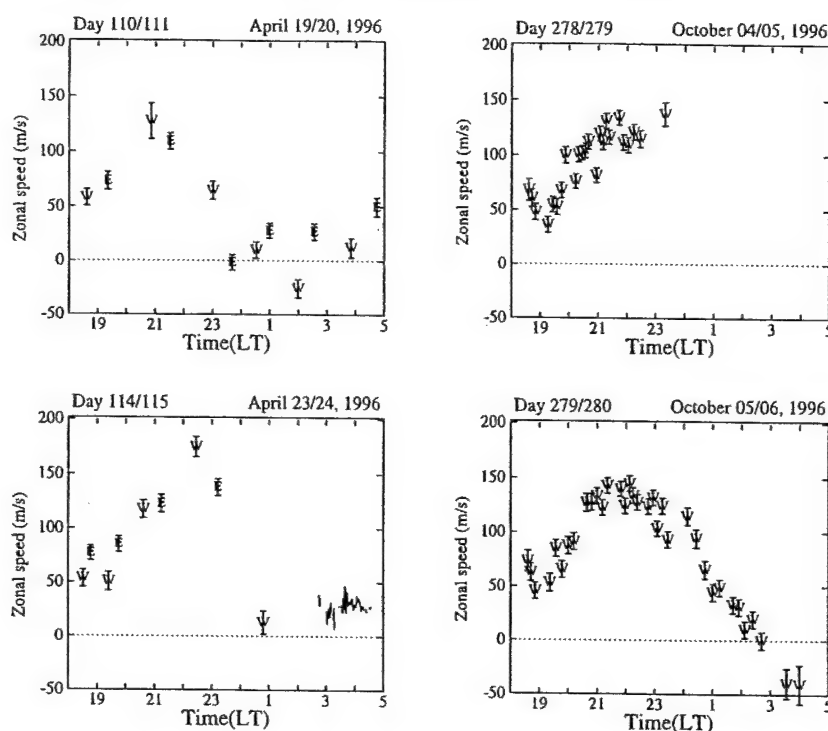


Figure 3. The temporal variation of the zonal neutral winds (eastward positive) measured on four equinoctial nights of 1996. The letters (E) and (W) indicate the observation direction at the time of the measurement. The error bars are also displayed on top of each letter.

cally disturbed day ($K_p = 4^-$, 4^0), the zonal wind diminishes from 130 m s^{-1} eastward at 2100 LT to $\sim 0 \text{ m s}^{-1}$ westward near 2400 LT. This westward wind value is very reminiscent of the scintillation drifts observed during high K_p values [Valladares *et al.*, 1996].

3.3. Simultaneous Observations of Drifts and Winds

[23] Figures 4, 5, 6, and 7 show several events in which there are concurrent measurements of the neutral winds and the scintillation drifts. Figure 4 shows selected examples obtained during the vernal equinoxes of 1997 and 1998. Two prominent features of these plots are the resemblance that exists between the scintillation drifts and the thermospheric winds, and the longitudinal coherence of the zonal winds. The longitudinal separation between the regions under observation to the east and the west is $\sim 800 \text{ km}$, implying a lack of a gradient over a distance of at least 800 km for the zonal wind. The wind-drift agreement is more evident in the data on 26/27 August 1997, 16/17 October 1998, and September 15/16, 1998. These 3 days qualify as quiet days ($\Sigma K_p < 20$). For the quiet day of 14/15 August 1997, differences of $25\text{--}50 \text{ m s}^{-1}$ are evident. On this day, there exists also a difference between the zonal winds looking to the east and west at 2400 LT. Some velocity spikes are sometimes seen in the scintillation drifts as on 14/15 August 1997 and 15/16 September 1998. Understandingly, no similar excursions in the neutral winds were seen because of the much coarser temporal resolution of the FPI instrument and because of the likely association of the spikes with rapidly upward drifting bubbles. The negative spikes, such as the ones at 2220 LT on 14/15 August 1997 and at 1940 LT on 15/16 September 1998 correlate with increased values of V_c .

[24] While Figure 4 introduced events of near-zero drift-wind difference; Figures 5, 6, and 7 present more uncommon cases in which the wind-drift difference is $>50 \text{ m s}^{-1}$ or were obtained in seasons not reported before. Figure 5 shows the scintillation drifts and the zonal winds for two nights during the local autumnal

equinoxes of 1996. During this season, there is a reasonable agreement between the winds and drifts. In one of the examples (20/21 April 1996), there are drift spikes exceeding 50 m s^{-1} . Not surprisingly, this day is magnetically disturbed, with K_p values $>4^-$. As shown by the gray line in the plot, the large drift values coincide with V_c larger than 50 m s^{-1} .

[25] Figure 6 shows simultaneous drifts and winds measured on two nights during the June solstice. It is known that the scintillation activity is weakest during local winter in the American sector. It occurs only on 10% of the nights, generally after midnight, with a preference for moderate or active magnetic conditions, and in short temporal patches. As seen in the plots, the variability of the wind is increased relative to the observations presented in Figures 3 and 4. Also, the difference in the neutral wind speeds between the east and west directions is significant in several instances.

[26] In Figure 5 we presented two cases where, for 1–2 hours, the wind was equal or larger than the drift. In Figure 7 we present six events in which the FPI wind exceeds the scintillation drift for many hours and in some intervals by ~ 50 to 100 m s^{-1} . Most of the nights in Figure 7 (except for 29/30 October 1997) show peak wind values close to 200 m s^{-1} ; this is almost twice the average value of the zonal wind for the years analyzed here. The magnetic activity prevailing during these measurements was quiet to moderate with the K_p index varying between 0^0 and 3^+ . The plots corresponding to 30/31 August 1996, 21/22 September 1998, and 28/29 September 1998 and up to some extent 29/30 October 1997 show a pattern in which the drift curve follows the variation of the wind values with an almost constant difference between them. This signature was commonly observed during most of the nights when wind and drifts were simultaneously measured and gives credence to the good quality of the data. The other two frames, corresponding to 1/2 September 1997 and 5/6 September 1997, present a large difference in the early hours of the evening when the winds exceeded the drifts by near 100 m s^{-1} . This large discrepancy may indicate a lack of coupling between

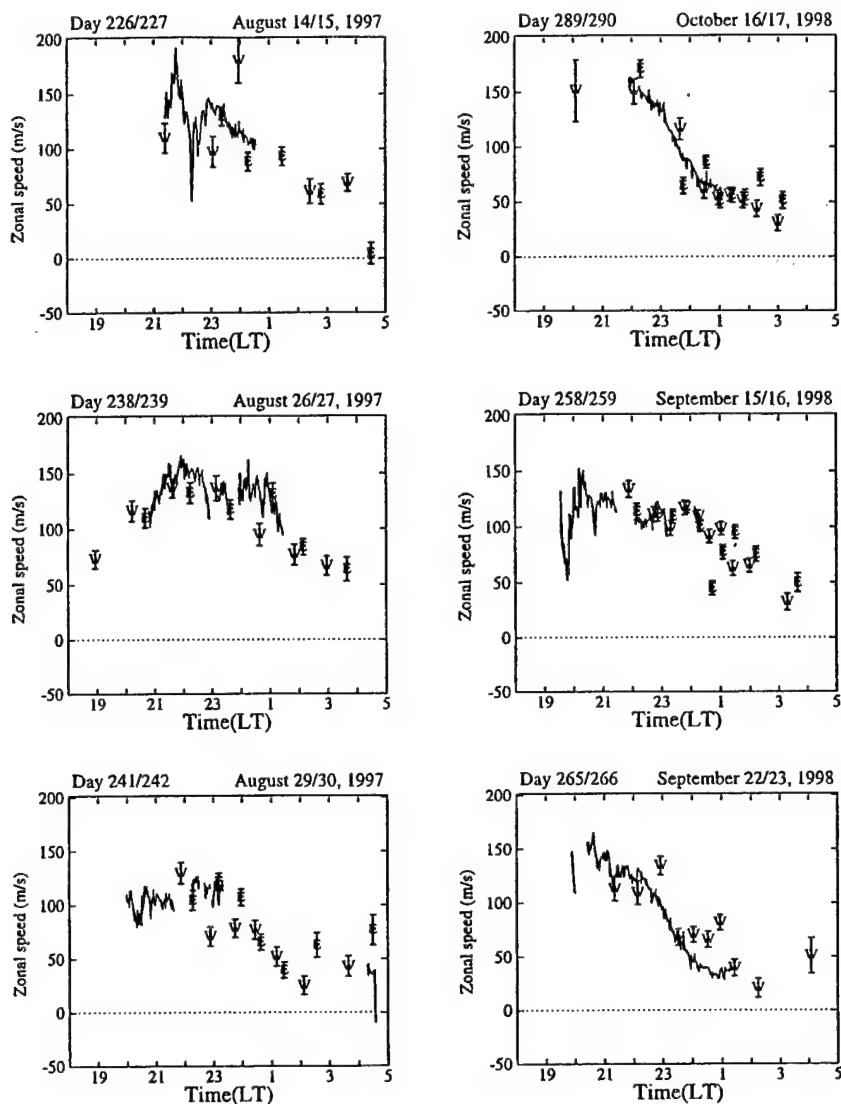


Figure 4. The temporal variation of the scintillation drifts (solid lines) and the neutral winds (symbols E and W, with error bars) measured simultaneously on six nights of the vernal equinox of 1997 and 1998. Note the very good agreement in the values of both data sets.

the neutral and the ions. More about this can be found in the discussion section.

4. Statistical Comparison of Neutral Winds and Scintillation Drifts

[27] This section presents the results of a statistical analysis that provided the climatology of the zonal scintillation drifts and the

thermospheric winds. We have applied a multivariate regression analysis [Biondi *et al.*, 1999] to both the scintillation drifts and the FPI wind data sets and obtained the dependence of these parameters on the solar flux intensity and the local time. We also calculated average values of the wind for periods of scintillation and no scintillation. We know that by calculating their statistical average we may also remove the day-to-day variability of the wind, which we believe is associated with the onset of the irregularities.

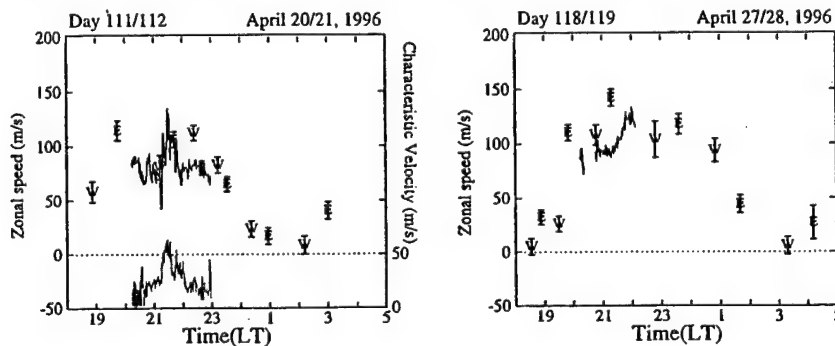


Figure 5. Same format as in Figure 4, but for two nights of the local autumnal equinox of 1996.

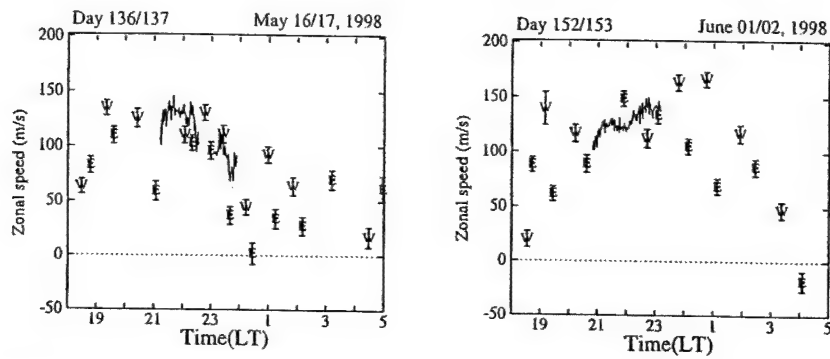


Figure 6. Same format as in Figure 4 but for two nights of the June solstice of 1998.

We found only a modest difference between the averaged morphologies of both components of the wind when they were sorted according to the presence or absence of scintillations. The 3 years considered in our statistical study correspond to the low and ascending phases of the solar cycle. Between 1996 and 1998, the solar flux varied between 67 and $170 \times 10^{-22} \text{ W m}^{-2} \text{ Hz}^{-1}$. We note that the number of nights considered in our statistical analysis

is relatively small, introducing an inherent statistical uncertainty of order 20 m s^{-1} .

4.1. Climatology of the Coupling Between Neutrals and Plasma

[28] Figure 8 shows the dependence of the irregularity drift and the neutral wind on the local time and the solar flux for the

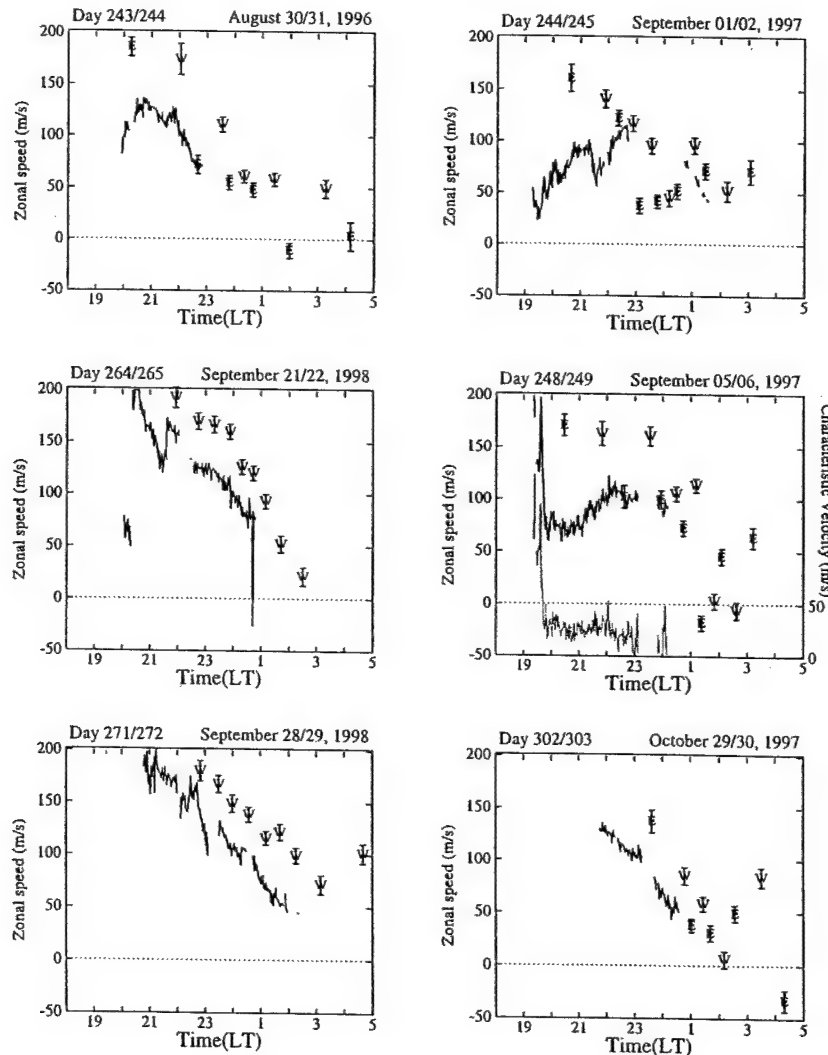


Figure 7. Same format as in Figure 4, but for six nights when the ionospheric plasma motion and the speed of the neutrals were significantly different.

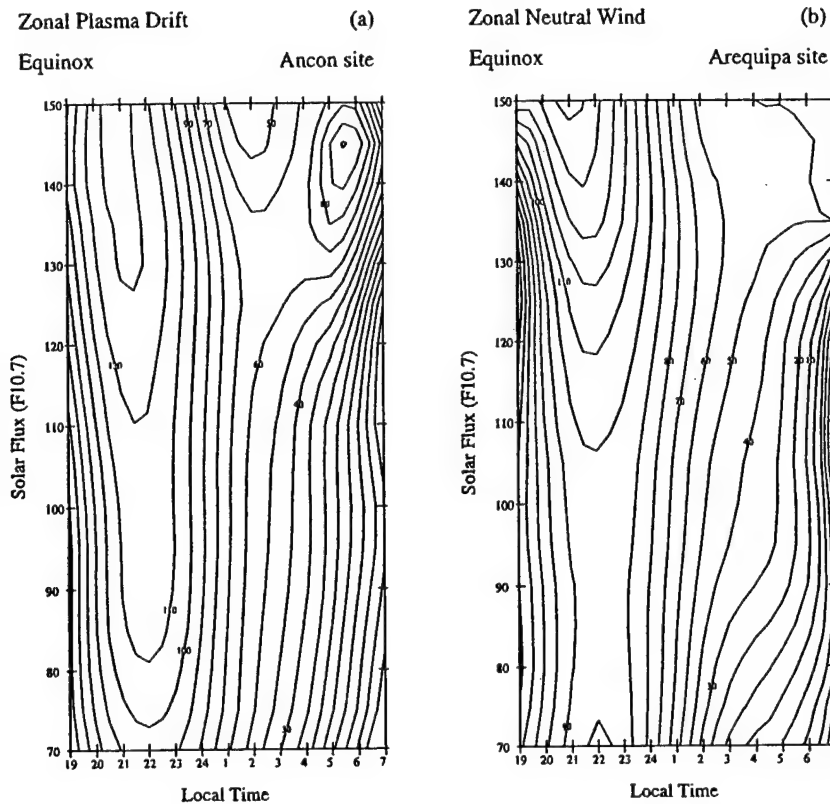


Figure 8. Zonal scintillation drift and zonal thermospheric neutral wind contours obtained by the regression analysis of the data for the equinox periods (March, April, September, and October) of 1996, 1997, and 1998. The dark trace represents a 100 m s^{-1} velocity.

equinoctial months of March, April, September, and October. Figure 9 shows similar variations for the solstitial months of May, June, July, and August. The local time variation of both parameters is quite typical; they increase in the early evening, reach a peak at 2200 LT, and slowly decrease afterward. (Note the heavy line that is used to delineate the 100 m s^{-1} contour.) For the first 5 years of operations of the Ancon SRSI (1994 through 1999), we have systematically reviewed the real-time data of scintillation and drifts. The “quick” format plots that were obtained online reveal that the peak of the nighttime eastward velocity varies proportionally with the intensity of the solar flux. Figure 8a corroborates this statement. Not surprisingly, the peak of the nighttime zonal wind, which is the driver of the nighttime plasma motion at equatorial latitudes, also shows a similar direct proportionality with the solar flux level.

[29] Recently, *Biondi et al.* [1999] have presented the variation of the thermospheric winds measured at Arequipa and Arecibo as a function of solar flux and LT. Arequipa’s zonal winds (see their Figure 7) were collected in the previous solar cycle. Although their database extended from 1983 to 1990 and ours is restricted to 1996, 1997, and 1998, the agreement between their Figure 7 and our Figure 8b is very good. In both the peak of the zonal wind occurs at 2200 LT for all values of the solar flux, and the 100 m s^{-1} contour (heavy line) first appears at a solar flux level between 100 and 110.

[30] The prominent feature of Figures 8a and 8b is the fact that in the premidnight period, the scintillation drifts are larger than the zonal winds during low levels of solar flux. This can be seen by comparing the locations of the heavy line contour (corresponding to 100 m s^{-1}) in both panels. Figure 8 indicates that when the solar flux is below $125 \times 10^{-22} \text{ W m}^{-2}$, the drifts are larger than the winds, but for values above ~ 140 , the winds exceed the drifts. This result is somewhat unexpected and may imply the existence of a

gradient of the thermospheric wind either in altitude or in latitude. A relatively small difference, probably 20 m s^{-1} , over the latitudinal spacing between Arequipa and Ancon could easily explain the presumed “overdeveloped” scintillation drift found in the scintillation data.

[31] Contrary to the comparative behavior of the winds and drifts for the equinoxes, the wind–drift comparisons of Figures 9a and 9b shows that the premidnight wind values always exceed the drift values during the winter solstice. This relationship is independent of the level of the solar flux during the epoch of low solar flux activity that has been considered in our statistical analysis. The wind’s maximum is also broader than the drift’s, and the wind contours are further apart, indicating a weaker temporal variation for the winds.

4.2. Climatology of the Meridional Neutral Winds as a Function of Scintillation Activity

[32] Figures 10 and 11 show the meridional component of the thermospheric wind binned as a function of season, scintillation activity and observation directions (north or south). Each individual measurement is represented by a small dot and the half-hour mean average is displayed by the solid line. A salient feature in the average wind values is the roughly constant difference between the meridional winds measured to the north and to the south. For example, the north observations of Figure 11a are near zero between 2000 and 2400 LT. At these times the corresponding south values (Figure 11d) approach 40 m s^{-1} . The north values of Figure 10c are -30 m s^{-1} ; the corresponding south values of Figure 10d show near zero wind values after 2200 LT. As explained more extensively in the Discussion section, we believe this persistent difference (wind convergence) implies a latitudinal variability of the meridional wind that exists between the thermospheric volumes observed by the FPI to the north or the south

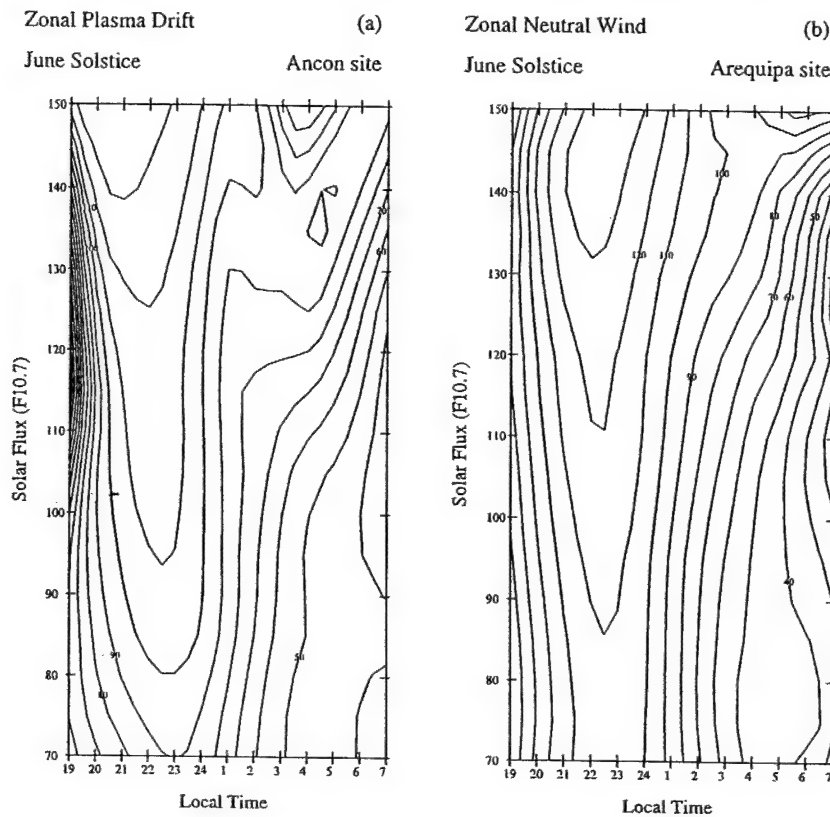


Figure 9. Zonal drift and zonal wind contours calculated using the regression analysis for the local winter solstice (May, June, July, and August).

(8° difference in Figure 1). The presence or absence of scintillations also reveals a subtle but interesting effect that occurs during the June solstice (Figures 10a–10d). Figure 10a shows that at 1900 LT the average meridional wind is -45 m s^{-1} , becomes near zero at 2100 LT and then decreases reaching -25 m s^{-1} at 2400 LT. Figure 10b (southward direction) shows an initial meridional wind of -75 m s^{-1} that also decays to zero at 2100 LT, becoming positive afterward. In the case of no scintillations the north-south relation varies quite noticeably. The wind to the north (Figure 10c) is about -42 m s^{-1} at 1900 LT and remains almost unchanged throughout the night. The wind to the south (Figure 10d) starts near -42 m s^{-1} , but rapidly decreases toward zero values (by 2200 LT) and remains near zero. Thus the average meridional winds for scintillation events are less negative, and in some case positive, than their corresponding winds for no scintillation cases. This difference is more significant between 2000 and 2400 LT. There is considerable scatter in the plots of Figure 10 ($\sigma = 15 \text{ m s}^{-1}$), and several counterexamples have been observed. Nevertheless, we find that the meridional wind climatology presents different characteristics for scintillation versus no-scintillation cases that may have some bearing on the onset of scintillation activity or alternatively be a consequence of the development of plasma bubbles and scintillations.

5. Discussion

[33] Comparisons of the plasma drift and neutral wind velocities for the years 1996, 1997, and 1998 have revealed that most often the scintillation drifts and the FPI winds are in good agreement as seen in Figure 4. Both the amplitude and the nighttime trend were almost equal 26/27 August 1997, 15/16 September 1998, 22/23 September 1998, and 16/17 October 1998 (Figure 4). However, on very few occasions the wind and the drift curves differed significantly. These are a small number of cases and no statistical

conclusion should be drawn from here. The wind-drift difference sometimes was constant and lasted for several hours, as shown in Figure 7 for 21/22 September 1998 and 28/29 September 1998, or varied, as on 1/2 September 1997 and 5/6 September 1997. The near constant wind and drift difference presented in Figure 7 indicates that even under conditions of incomplete ion-neutral coupling the neutrals can control the motion of the ions from the early evening up to the late night hours. It is known that during the late part of the night, the effect of the *F* region dynamo decreases when the *F* region conductivity becomes comparable to the *E* region conductivity [Crain *et al.*, 1993]. Under these circumstances the ions may not follow the motion of the neutrals, or their velocities may decay more rapidly than the wind. This effect is not apparent in the data of Figure 7.

[34] From Figure 8 it is somewhat surprising to find that during the equinoxes, when the occurrence frequency of scintillations maximizes, in the pre-midnight hours the mean plasma drift exceeds the averaged neutral velocities when the solar flux is below 130 units. This trend reverses for solar flux levels larger than 130.

[35] Other studies have also reported a value of the ionospheric drifts larger than the neutral winds. Coley *et al.* [1994] conducted a systematic comparison of plasma drifts and neutral winds, collected by the DE 2 satellite. Coley *et al.* used data from the ion drift meter and the wind and temperature spectrometer to show that during the period between 2200 and 0500 LT and at latitudes near the dip equator, the ion drift was larger than the neutral velocity. These authors explained their results, suggesting that an additional polarization electric field could be generated by an altitude gradient of the zonal neutral wind in the 100–200 altitude region.

[36] Basu *et al.* [1996] examined concurrent measurements of scintillation drifts and thermospheric winds during a campaign period in 1994. Their observations near sunset indicated large values of the zonal wind during nights of spread *F* compared to

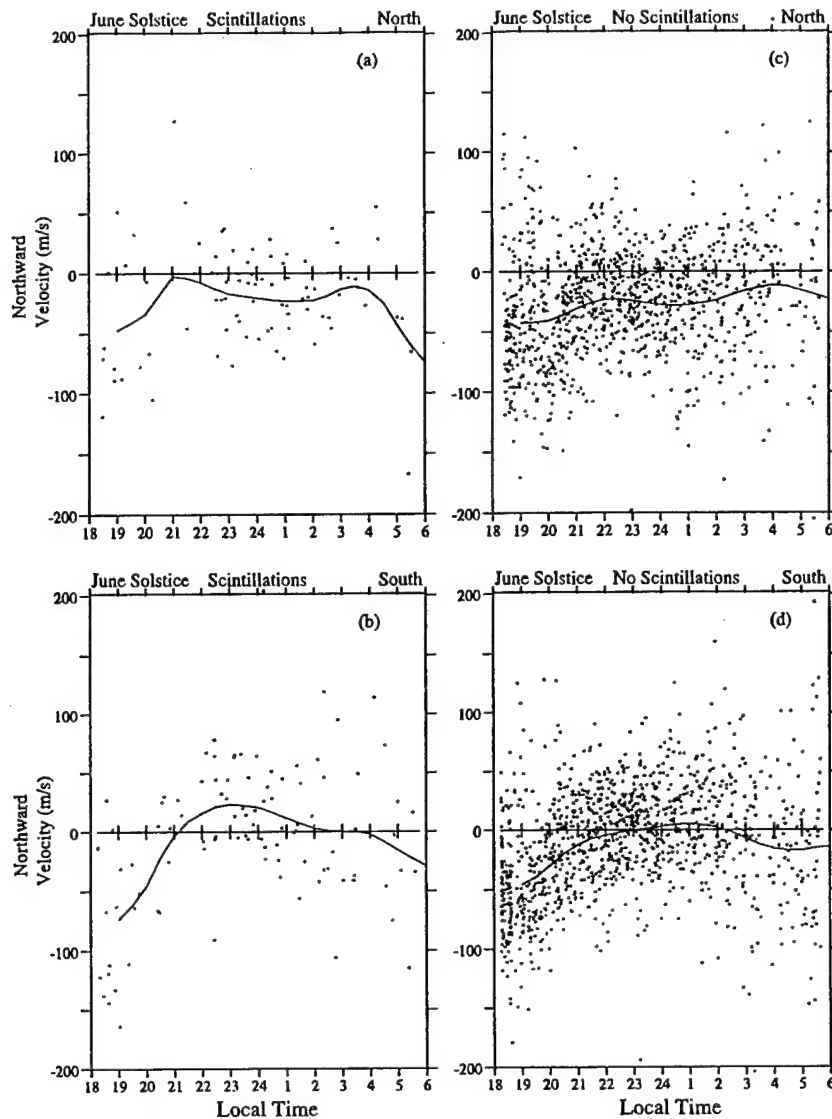


Figure 10. Meridional thermospheric wind (northward positive) measured at Arequipa during the June solstice and displayed according to the observation direction at the time of operation and the presence/absence of scintillations. The smooth curves are fitted to the half-hour mean averages.

smaller winds on other nights of non spread F condition. *Basu et al.* [1996] also conducted simultaneous measurements of the scintillation drifts at two different latitudes. In addition to the receivers at Ancon, located near the magnetic equator, they installed another system at Agua Verde at 11° magnetic latitude. The drift measurements at the two sites differed, implying a latitudinal gradient of the wind at F region altitudes.

[37] *Anderson and Mendillo* [1983] used a model of the equatorial ionosphere to demonstrate that the westward tilting of the plasma plumes was produced by an altitude decrease of the eastward plasma drift. These authors suggested that the plasma flow gradient was a result of a zonal wind pattern of decreasing speed at increasing distances from the equator. *Raghavarao et al.* [1991] presented zonal wind data measured by the DE 2 satellite when crossing the dip equator, which exhibited a broad maximum centered at the magnetic equator and a minimum at the location of the anomalies. The wind was higher near the equator and decreased by 100 m s^{-1} at both sides toward the poles. A decrease of 50 m s^{-1} was seen even at 12° away from the equator in agreement with the suggestion made by *Anderson and Mendillo* [1983]. *Raghavarao et al.* [1991] explained that the latitudinal distribution of the zonal

wind was the result of encountering more dense plasma at the anomalies, which produce a higher ion-drag on the neutrals, and a weaker ionosphere near the equator. Therefore, from the experimental and modeling points of view there is supporting evidence that there exists a latitudinal gradient in the zonal wind in the F layer. The fact that we measured drifts larger than the thermospheric wind points also to the existence of a steep latitudinal variability of the neutral wind, or alternatively, the penetration of electric fields originating at higher latitudes.

[38] As described above, the scintillation and the FPI measurements do not correspond to volumes that are collocated; there is a displacement of 50–100 km in altitude, 4° in latitude, and few hundred km in longitude. *Anderson and Mendillo* [1983] and *Anderson et al.* [1987] showed that the drift is related to an integrated conductivity, while the wind could be more localized depending on the thermospheric tides, heat sources, and to a lesser degree, interaction with the local ionosphere. Wind-drift differences like the ones encountered on 21/22 September 1998 and 28/29 September 1998 could be explained by the existence of sharp gradients in altitude/latitude and longitude. However, on others days (1/2 September 1997 and 5/6 September 1998) the

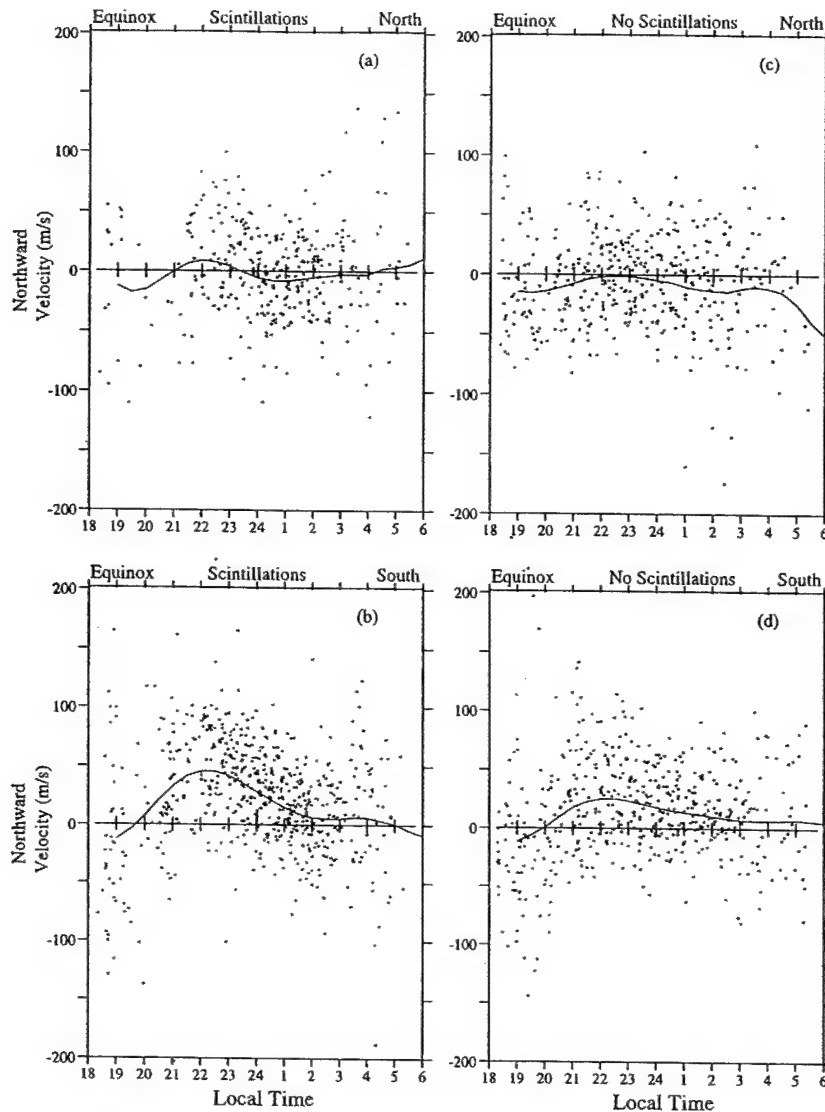


Figure 11. Same as Figure 10, but corresponding to the equinoxes.

wind-drift differences were of order 100 m s^{-1} , with the winds exceeding the drifts. We believe that for these events, penetrating electric fields extending from high to low latitudes may play a role in creating a larger downward electric field [Fejer *et al.*, 1979; Spiro *et al.*, 1988; Sastri *et al.*, 1993]. We have seen on other days (e.g., 20/21 April 1996 of Figure 5) that the zonal wind hardly reaches a peak magnitude of 100 m s^{-1} . The wind seems reduced throughout the night. This significantly reduced wind can be attributed to the presence of a disturbed dynamo.

[39] In the cases presented in Figure 7, we observed several occasions when the wind exceeded the drifts. While it is undeniable that a latitudinal gradient of the wind can explain the smaller drifts, an underlying conductive *E* layer persisting after sunset could also produce smaller drifts by partially shorting out the polarization *E* field. However, the fact that the measured wind-drift difference remains almost constant for many hours would require the persistence of the *E* region during the night. This weak *E* region should be able to damp the growth of the Rayleigh-Taylor instability and consequently inhibit the occurrence of scintillation, which did not occur.

[40] A wind distribution of large eastward values near the magnetic equator, where the ion drag is reduced, and much smaller wind values near the latitudes of both anomalies (see, for example,

Figure 6 of Richmond [1995]) could well produce the signature seen in our measurements. Figure 8 suggests that the ion drifts were slightly larger than the neutral winds during solar minimum conditions. During these conditions the ionosphere should be located at lower altitudes and able to exert a higher ion drag effect than during solar maximum conditions. For the solar-moderate epoch we observed almost equal wind and drift values, suggesting the absence of altitude gradients in the wind. Another common feature in the wind data is the spatial variability that accompanied the more dramatic cases in which the wind-drift difference was the largest.

5.1. Effect on Zonal Wind During Scintillation Events

[41] We have observed that, during scintillation and solar minimum conditions (e.g., solar flux levels below 120), the nighttime zonal wind presented a pattern of eastward winds sometimes increasing in magnitude shortly after sunset. The zonal wind of 1/2 June 1998 and 16/17 May 1998 (Figure 6) show this feature. Crain *et al.* [1993] showed that a west-to-east wind reversal and/or a positive altitude gradient of the zonal wind are able to increase the zonal polarization electric field (and generate a more fully devel-

oped PRE) that lifts the F layer, thereby making the F layer more unstable. It seems that for solar minimum the F layer needs a bit larger prereversal enhancement, as could be obtained by the combined action of the decay of the E region conductivity and the rapidly increasing eastward zonal wind. During solar maximum conditions, when the F region densities are higher, the conductivity gradient may be large enough to generate a significant PRE able to lift the equatorial ionosphere toward higher, more unstable altitudes. A large PRE in the vertical velocity (or an equivalent eastward electric field) is an important factor in the growth of the RTI for three reasons: (1) it lifts the F region to altitudes where the stabilizing damping collisional term is smaller; (2) it produces an eastward electric field, which is also a destabilizing term in the generalized RTI; and (3) it helps to decrease the integrated Pedersen conductivity of the field line connected E region [Hanson *et al.*, 1983, 1986].

5.2. On a Possible Association Between Meridional Winds and Scintillations

[42] We have observed that the presence/absence of scintillations produced a tenuous effect, but still identifiable, on the characteristics of the meridional wind when we obtained the statistics of the winds independently of the FPI observation directions. During no scintillation periods and the June solstice the averaged meridional winds to the north and south have both an average value of about -40 m s^{-1} in the early part of the evening ($\sim 1900 \text{ LT}$). During scintillation events and also the June solstice season, the meridional winds to the south were more negative with an average value of -75 m s^{-1} at 1900 LT compared to -40 m s^{-1} to the north. It was also observed that the average wind was less negative or even positive until 2300 LT during nights of scintillations than during nights when scintillations were absent. The statistical significance of our conclusion is reduced due to the limited number of scintillation days that were recorded during the June solstice. Between years 1996 and 1998 the Arequipa FPI measured the meridional winds on 125 nights during the June solstices. Of these, only 30 nights contained some level of scintillations. This low percentage of scintillation activity is quite common in the American sector during the June solstice.

[43] The meridional wind at F region altitudes results from and/or is modified by the action of several agents. During geomagnetically quiet conditions, local heating due to solar radiation is a principal source that prevails even near local sunset. During more disturbed conditions, however, there exists a disturbed dynamo, which is able to initiate a transequatorial meridional wind that can reach wind speeds of order 100 m s^{-1} . Fuller-Rowell *et al.* [1994, 1996] used a coupled thermosphere-ionosphere model to illustrate how the meridional wind develops after the initiation of a magnetic storm and diminishes after penetrating into the opposite hemisphere. The midnight temperature maximum (MTM) can also modify substantially the value of the meridional wind. Either of the latter two factors may reduce or even cancel the meridional wind in a region near the magnetic equator. Consequently, as can be seen by reference to Figure 1, Arequipa observations to the north ($\sim 0^\circ$ dip latitude) and to the south ($\sim 8^\circ \text{ S}$ dip latitude) could differ, depending on the importance of these mechanisms.

[44] Finally, for completeness we mention a third possibility, that our results might be a consequence of the development of a local circulation cell system as advocated by Raghavarao *et al.* [1991, 1993, 1998]. The analysis by Pant and Sridharan [2001] suggests that both chemical heating and ion drag mechanisms operating within the Appleton anomaly crests generate the dynamical forcing that produces this convective cellular activity. Raghavarao *et al.* [1998] based their supposition for this local circulation cell upon the analysis of Dynamic Explorer in situ measurements of zonal and vertical winds with a mass spectrometer. This work found an

indication of reduced zonal winds within the Appleton anomaly, upward vertical wind above the anomaly crests, and increased zonal winds and downward vertical winds at the magnetic equator. It was also noted that continuity requires increased meridional wind flow within the thermosphere from the crests of the Appleton anomaly to the equator and return meridional flow within the E region to complete the cellular circulation. During the winter solstice such winds would be difficult to detect against the background flow of air from the summer hemisphere to the winter hemisphere that is generated by the pressure gradient between the two hemispheres. During the equinoxes, because of the reduced global pressure gradient, this interhemispheric transport should be nearly zero. We note that the observed increase of equatorward winds observed to the south as compared with the north for periods of increased scintillation activity are consistent with this mechanism. A recent study based upon eight nights of simultaneous measurements made during 2 weeks in late September and early October 1997 (C. Martinis *et al.*, Zonal neutral winds at equatorial and low latitudes, submitted to *Journal of Geophysical Research*, 2001) has demonstrated a $\sim 15\text{--}20\%$ reduction in the zonal wind between Arequipa and Carmen Alto; a reduction that is consistent with the idea of a local circulation cell presented by Raghavarao *et al.* [1998].

6. Conclusions

[45] This work has led to the following conclusions:

1. The amplitudes of the scintillation zonal drifts and the thermospheric neutral winds are often in good agreement; in addition, their nighttime temporal variations correlate well. This implies that the zonal polarization electric field produced by the nighttime F region dynamo is fully developed, generating a perfect electrodynamic coupling.

2. On a few occasions, especially during low solar activity, the plasma drift is found to be larger than the zonal wind. We suggest that on these days there exists a significant vertical gradient of the horizontal wind with lower values at the bottomside of the F region, where the winds are observed, and significantly larger wind values close to the F region peak, where the scintillation drifts are measured. On very few nights did we find that the wind was substantially larger than the drift ($>100 \text{ m s}^{-1}$). We believe that on these nights the E region may be sufficient to short out some of the polarization electric field that drives the zonal plasma drift but still allow F region irregularities to develop.

3. The meridional winds measured to the north and to the south of Arequipa during the June solstice were binned independently according to the scintillation activity. The results plotted in Figure 11 show that during the equinoxes, when there is scintillation activity, the averaged meridional wind measured either to the south or north of Arequipa during the mid-evening hours is more equatorward by $20\text{--}30 \text{ m s}^{-1}$ than the wind observed during nights with no scintillation activity. Little difference in the meridional wind speeds was noted for the winter solstice period. Use of two FPI interferometers located on the same side of the magnetic equator (Arequipa, Peru, and Carmen Alto, Chile), should make it possible to provide a better determination of the latitudinal distribution of the zonal and meridional components of the neutral wind. In our future work we intend to explore the possibility that the correlation between scintillation activity and the amplitudes of the zonal and meridional components of the neutral wind is a result of the formation of a neutral wind cell as suggested by Raghavarao *et al.* [1991, 1993]. The mechanism proposed suggested that the combination of chemical and ion drag heating within the Appleton anomaly would reduce the zonal wind flow and produce upward vertical winds at the latitude of the Appleton anomaly, and downward vertical winds at the magnetic equator. Converging meridional flow from the Appleton anomalies to the magnetic equator within the thermosphere would connect these two vertical branches of the convective circulation cell. We will study this

phenomenon further in analyses of our results from Arequipa and Ancon during the solar maximum period, 2000–2001.

[46] Acknowledgments. We thank Jorge Espinoza and Ruben Villafani for their dedication in operating continuously the spaced receiver scintillation instrument at Ancon, Peru. The research at Boston College was funded by NSF grant ATM-9714804 and by Air Force Research Laboratory contract F19628-97-C-0094, at Clemson University by NSF grant ATM-9714770, and at the University of Pittsburgh by NSF grant ATM-9414403 and ATM-9906408. The Observatory of Ancon is operated by the Instituto Geofísico del Peru, Ministry of Education. Space and on-site technical support at Arequipa, Peru are provided by the National Aeronautics and Space Administration.

[47] Janet G. Luhmann thanks Donald T. Farley and another referee for their assistance in evaluating this paper.

References

- Anderson, D. N., and M. Mendillo, Ionospheric conditions affecting the evolution of equatorial plasma depletions, *Geophys. Res. Lett.*, **10**, 541, 1983.
- Anderson, D. N., R. A. Heelis, and J. P. McClure, Calculated nighttime eastward plasma drift velocities at low latitudes and their solar cycle dependence, *Ann. Geophys., Ser. A*, **5**, 435, 1987.
- Basu, S., Su. Basu, E. Kudeki, H. P. Zengingonul, M. A. Biondi, and J. W. Meriwether, Zonal irregularity drifts and neutral winds measured near the magnetic equator in Peru, *J. Atmos. Terr. Phys.*, **53**, 743, 1991.
- Basu, S., et al., Scintillations, plasma drifts, and neutral winds in the equatorial ionosphere after sunset, *J. Geophys. Res.*, **101**, 26,795, 1996.
- Bhattacharyya, A., K. C. Yeh, and S. J. Franke, Deducing turbulence parameters from transionospheric scintillation measurements, *Space Sci. Rev.*, **61**, 335, 1992.
- Biondi, M. A., D. P. Sipler, and M. Weinschenker, Multiple aperture exit plate for field-widening a Fabry-Perot interferometer, *Appl. Opt.*, **24**, 232, 1985.
- Biondi, M. A., J. W. Meriwether, B. G. Fejer, and R. Woodman, Measurements of the dynamics and coupling of the equatorial thermosphere and the F-region ionosphere in Peru, *J. Atmos. Terr. Phys.*, **50**, 937, 1988.
- Biondi, M. A., J. W. Meriwether, B. G. Fejer, and S. A. Gonzalez, Seasonal variations in the equatorial thermospheric wind measured at Arequipa, Peru, *J. Geophys. Res.*, **95**, 12,243, 1990.
- Biondi, M. A., J. W. Meriwether, B. G. Fejer, S. A. Gonzalez, and D. C. Hallenbeck, Equatorial thermospheric wind changes during the solar cycle: Measurements at Arequipa, Peru, from 1983 to 1990, *J. Geophys. Res.*, **96**, 15,917, 1991.
- Biondi, M. A., S. Y. Sazykin, B. G. Fejer, J. W. Meriwether, and C. G. Fesen, Equatorial and low latitude thermospheric winds: Measured quiet time variations with season and solar flux from 1980 to 1990, *J. Geophys. Res.*, **104**, 17,091, 1999.
- Colerico, M., M. Mendillo, D. Nottingham, J. Baumgardner, J. Meriwether, J. Mirick, B. Reinisch, J. Scali, and C. Fesen, Coordinated measurements of F-region dynamics related to the thermospheric midnight temperature maximum, *J. Geophys. Res.*, **101**, 26,783, 1996.
- Coley, W. R., R. A. Heelis, and N. W. Spencer, Comparison of low-latitude ion and neutral zonal drifts using DE 2 data, *J. Geophys. Res.*, **99**, 341, 1994.
- Crain, D. J., R. A. Heelis, G. J. Bailey, and A. D. Richmond, Low-latitude plasma drifts from a simulation of the global atmospheric dynamo, *J. Geophys. Res.*, **98**, 6039, 1993.
- Dungey, J. W., Convective diffusion in the equatorial F region, *J. Atmos. Terr. Phys.*, **9**, 304, 1956.
- Farley, D. T., E. Bonelli, B. G. Fejer, and M. F. Larsen, The prereversal enhancement of the zonal electric field in the equatorial ionosphere, *J. Geophys. Res.*, **91**, 13,723, 1986.
- Fejer, B. G., C. A. Gonzales, D. T. Farley, M. C. Kelley, and R. F. Woodman, Equatorial electric fields during magnetically disturbed conditions, 1, The effect of the interplanetary magnetic field, *J. Geophys. Res.*, **84**, 5797, 1979.
- Fejer, B. G., E. R. de Paula, S. A. Gonzalez, and R. F. Woodman, Average vertical and zonal F region plasma drifts over Jicamarca, *J. Geophys. Res.*, **96**, 13,901, 1991.
- Fejer, B. G., L. Scherliess, and E. R. de Paula, Effects of the vertical plasma drift velocity on the generation and evolution of equatorial spread F, *J. Geophys. Res.*, **104**, 19,859, 1999.
- Fesen, C. G., Simulation of the low latitude midnight temperature maximum, *J. Geophys. Res.*, **101**, 26,683, 1996.
- Fesen, C. G., G. Crowley, R. G. Roble, A. D. Richmond, and B. G. Fejer, Simulation of the pre-reversal enhancement in the low latitude vertical ion drifts, *Geophys. Res. Lett.*, **27**, 1851, 2000.
- Fuller-Rowell, T. J., M. V. Codrescu, R. J. Moffett, and S. Quegan, Response of the thermosphere and ionosphere to geomagnetic storms, *J. Geophys. Res.*, **99**, 3893, 1994.
- Fuller-Rowell, T. J., M. V. Codrescu, H. Rishbeth, R. J. Moffett, and S. Quegan, On the seasonal response of the thermosphere and ionosphere to geomagnetic storms, *J. Geophys. Res.*, **101**, 2343, 1996.
- Hanson, W. B., S. Sanatani, and T. N. L. Patterson, Influence of the E region dynamo on equatorial spread F, *J. Geophys. Res.*, **88**, 3169, 1983.
- Hanson, W. B., B. L. Cragin, and A. Dennis, The effect of vertical drift on the equatorial F-region stability, *J. Atmos. Terr. Phys.*, **48**, 205, 1986.
- Hanson, W. B., W. R. Coley, R. A. Heelis, and A. Urquhart, Fast equatorial bubbles, *J. Geophys. Res.*, **102**, 2039, 1997.
- Hedin, A. E., et al., Revised global model of thermospheric winds using satellite and ground-based observations, *J. Geophys. Res.*, **96**, 7657, 1991.
- Hysell, D. L., and J. D. Burcham, JULIA radar studies of equatorial spread F, *J. Geophys. Res.*, **103**, 29,155, 1998.
- Kelley, M. C., G. Haerendel, H. Kappler, A. Valenzuela, B. B. Balsley, D. A. Carter, W. L. Ecklund, C. W. Carlson, B. Hausler, and R. Torbet, Evidence for a Rayleigh-Taylor type instability and upwelling of depleted density regions during equatorial spread F, *Geophys. Res. Lett.*, **3**, 448, 1976.
- McClure, J. P., W. B. Hanson, and J. H. Hoffman, Plasma bubbles and irregularities in the equatorial ionosphere, *J. Geophys. Res.*, **82**, 2650, 1977.
- Meriwether, J. W., J. W. Moody, M. A. Biondi, and R. G. Roble, Optical interferometric measurements of nighttime equatorial thermospheric winds at Arequipa, Peru, *J. Geophys. Res.*, **91**, 5557, 1986.
- Meriwether, J. W., J. L. Mirick, M. A. Biondi, F. A. Herrero, and C. G. Fesen, Evidence for orographic wave heating in the equatorial thermosphere at solar maximum, *Geophys. Res. Lett.*, **23**, 2177, 1996.
- Meriwether, J. W., M. A. Biondi, F. A. Ferrero, C. G. Fesen, and D. C. Hallenbeck, Optical interferometric studies of the nighttime equatorial thermosphere: Enhanced temperatures and zonal wind gradients, *J. Geophys. Res.*, **102**, 20,041, 1997.
- Pant, T. K., and R. Sridharan, Plausible explanation for the equatorial temperature and wind anomaly (ETWA) based on chemical and dynamical processes, *J. Atmos. Sol. Terr. Phys.*, **63**, 885, 2001.
- Raghavarao, R., L. E. Wharton, N. W. Spencer, H. G. Mayr, and L. H. Brace, An equatorial temperature and wind anomaly (ETWA), *Geophys. Res. Lett.*, **18**, 1193, 1991.
- Raghavarao, R., W. R. Hoegy, N. W. Spencer, and L. E. Wharton, Neutral temperature anomaly in the equatorial thermosphere: A source of vertical winds, *Geophys. Res. Lett.*, **11**, 1023, 1993.
- Raghavarao, R., R. Suhasini, W. R. Hoegy, H. G. Mayr, and L. Wharton, Local time variation of equatorial temperature and zonal wind anomaly (ETWA), *J. Atmos. Sol. Terr. Phys.*, **60**, 631, 1998.
- Rishbeth, H., The F layer dynamo, *Planet. Space Sci.*, **19**, 263, 1971a.
- Rishbeth, H., Polarization fields produced by winds in the equatorial F region, *Planet. Space Sci.*, **19**, 357, 1971b.
- Richmond, A. D., Modeling equatorial ionospheric electric fields, *J. Atmos. Terr. Phys.*, **57**, 1103, 1995.
- Sastri, J. H., J. V. S. Visweswara Rao, and K. B. Ramesh, Penetration of polar electric fields to the nightside dip equator at times of geomagnetic sudden commencements, *J. Geophys. Res.*, **98**, 17,517, 1993.
- Spiro, R. W., R. A. Wolf, and B. G. Fejer, Penetration of high-latitude electric-field effects to low latitudes during SUNDIAL 1984, *Ann. Geophys.*, **6**, 39, 1988.
- Vacchione, J. D., S. J. Franke, and K. C. Yeh, A new analysis technique for estimating zonal irregularity drifts and variability in the equatorial F region using spaced receiver scintillation data, *Radio Sci.*, **22**, 745, 1987.
- Valladares, C. E., W. B. Hanson, J. P. McClure, and B. L. Cragin, Bottom-side sinusoidal irregularities in the equatorial F-region, *J. Geophys. Res.*, **88**, 8025, 1983.
- Valladares, C. E., R. Sheehan, S. Basu, H. Kuenzler, and J. Espinoza, The multi-instrumented studies of equatorial thermosphere aeronomy scintillation system: Climatology of zonal drifts, *J. Geophys. Res.*, **101**, 26,839, 1996.
- Woodman, R. F., Vertical drift velocities and east-west electric fields at the magnetic equator, *J. Geophys. Res.*, **75**, 6549, 1970.
- Woodman, R. F., and C. LaHoz, Radar observations of F region equatorial irregularities, *J. Geophys. Res.*, **81**, 5447, 1976.

M. A. Biondi, Department of Physics and Astronomy, University of Pittsburgh, Pittsburgh, PA 15260, USA.

J. W. Meriwether, Department of Physics and Astronomy, Clemson University, Clemson, SC 29631, USA.

R. Sheehan and C. E. Valladares, Institute for Scientific Research, Boston College, Chestnut Hill, MA 02467, USA.

Simultaneous observations of dayside aurora from Heiss Island and Ny Ålesund

C. E. Valladares,¹ J. Moen,^{2,3} P. E. Sandholt,² W. F. Denig,⁴ and O. Troshichev⁵

Received 29 July 2002; revised 24 September 2002; accepted 22 November 2002; published 27 December 2002.

[1] This paper presents the first simultaneous observation of the cusp aurora using two overlapping imagers displaced in longitude by several hundreds of km. The imagers were located at Ny Ålesund, Norway and Heiss Island, Russia. The uniqueness of the case study presented here consists of the rapid response of the entire extension of the cusp-related aurora to an unsettled IMF. At the start of the event, the IMF B_z component was equal to -5 nT. It was followed by a 10-min period of positive B_z excursions ($\sim +2$ nT), before returning to a -3 nT value. Initially, when B_z was negative, the cusp aurora was located at 73° MLAT, displayed a B_z south-type ion dispersion signature, and antisunward convection. When the IMF B_z became positive, but under a dominant B_x (-6 nT), the cusp aurora rapidly retreated poleward, and a long single band was seen extending for over 2000 km brightening from east to west. A few minutes later, still during a period of clock angle less than 120° , two bands of red emission, separated in longitude by ~ 1000 km, split from the main auroral trace and move equatorward. The data presented here suggest that during a short period of dominant $B_x < 0$ and a solar wind phase front tilted toward the northern hemisphere the whole cusp-related aurora responded rapidly to the new solar wind configuration. **INDEX TERMS:** 2704 Magnetospheric Physics: Auroral phenomena (2407); 2724 Magnetospheric Physics: Magnetopause, cusp, and boundary layers; 2437 Ionosphere: Ionospheric dynamics. **Citation:** Valladares, C. E., J. Moen, P. E. Sandholt, W. F. Denig, and O. Troshichev, Simultaneous observations of dayside aurora from Heiss Island and Ny Ålesund, *Geophys. Res. Lett.*, 29(24), 2202, doi:10.1029/2002GL016001, 2002.

1. Introduction

[2] The cusp is a funnel shaped region of the dayside high-latitude magnetosphere, resulting from the interaction between the geomagnetic field and the magnetic field of the shocked solar wind. In this region magnetosheath particles have easy access into ionospheric altitudes producing auroral displays highly dependent on the orientation of the IMF [Sandholt *et al.*, 1998a]. When the IMF has a southward direction, reconnection at locations equatorward of the cusp produce open flux tubes at the dayside magnetopause, and a

series of poleward moving auroral forms (PMAF) emerge from a steady aurora located between 70° and 74° MLAT [Sandholt *et al.*, 1996]. This type of aurora, named type 1, is observed in association with poleward decreasing ion dispersion signatures and antisunward convection. When the IMF is predominantly northward, $B_z > |B_y|$, high-latitude auroras (type 2) are seen between 75° and 78° MLAT in response to reconnection sites at locations tailward of the cusp [Øieroset *et al.*, 1997b]. The type 2 auroras are accompanied by reverse latitudinal ion dispersion signature [Woch and Lundin, 1992] and sunward convection. When the IMF is weakly northward $|B_y| > B_z$, or B_z near zero both types 1 and 2 auroras can be simultaneously present. This configuration has been called bifurcated aurora by Sandholt *et al.* [1998b]. More recently, a comprehensive study involving rocket-borne instrumentation and an incoherent radar has provided evidence that during a period of B_z north, merging in the southern hemisphere can add open fluxes in the northern hemisphere [Maynard *et al.*, 2000]. In this paper, we present auroral emissions seen by two imagers, which were located under the cusp. This unique field-of-view allows a more comprehensive view of the spatial extent of the interaction of the solar wind, magnetosphere and ionosphere.

2. Observations

[3] Several characteristics made the measurements of December 20, 1998 unique. Firstly, there were three satellites transiting the solar wind (IMP-8, WIND, and ACE). Secondly, there was an opportune crossing of the cusp aurora by a DMSP satellite. Thirdly, there was the availability of two imagers separated by ~ 800 km, both with optimum observing conditions. The IMF measured by the 3 satellites located within the solar wind was used to calculate the tilt of the phase front and the delay time between the satellite observations and the impact time with the magnetopause.

2.1. IMF Measurements

[4] Figure 1 presents the three components of the IMF measured by ACE at $(222.8, 28.7, -16.9) R_E$, the density, and velocity measured by WIND at $(38.6, -59.1, 11.5) R_E$, the epsilon parameter [Perreault and Akasofu, 1978], the clock angle derived from the B_y and B_z values recorded by ACE, and the cross-correlation function of the B_z values measured by the IMP-8 $(0.1, -36.0, -15.5) R_E$ and ACE satellites. From the given coordinates we see that IMP-8 is closest to the Earth. Then, it is expected that the IMP-8 measurement of IMF would lag the WIND and ACE values. This fact was confirmed with the cross-correlation function (bottom panel), computed using a 4-hour data segment centered at 0708 UT. This calculation gives a lead of 91 min of the ACE B_z values over the IMP-8's. Similar

¹Institute for Scientific Research, Boston College, Newton Center, Massachusetts, USA.

²Department of Physics, University of Oslo, Oslo, Norway.

³Arctic Geophysics, University Courses on Svalbard, Norway.

⁴Space Vehicles Directorate, Air Force Research Laboratory, Hanscom AFB, Massachusetts, USA.

⁵Arctic and Antarctic Research Institute, St. Petersburg, Russia.

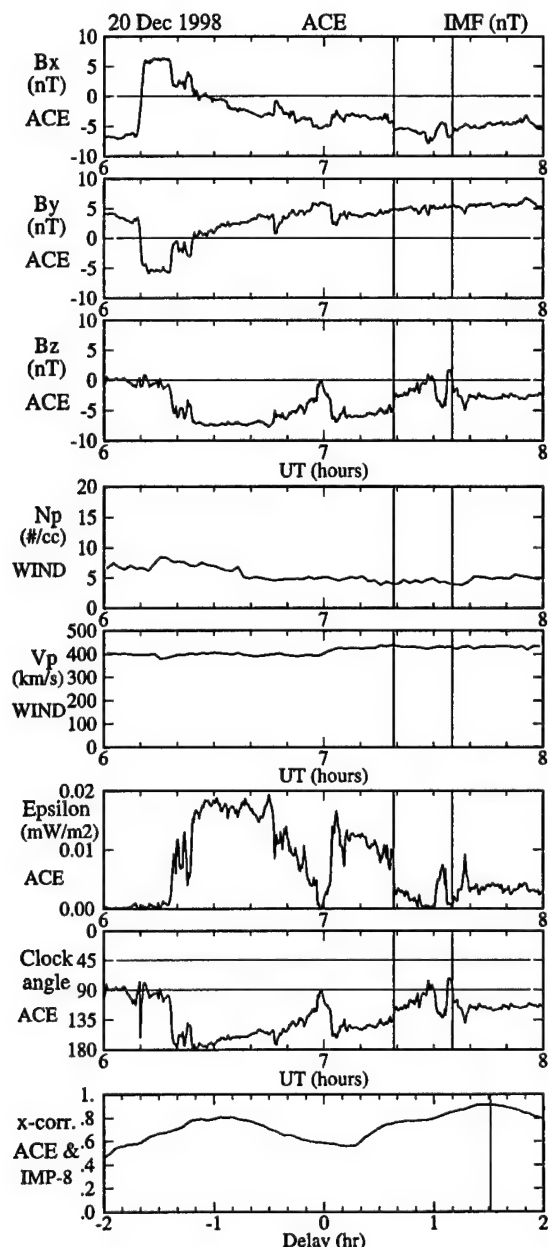


Figure 1. Solar wind parameters measured by the ACE, Wind and IMP-8 spacecraft on December 20, 1998. Top three panels show the IMF components in GSM coordinates. The solar wind density and velocity measured by WIND. Bottom three panels are the Epsilon parameter, the clock angle and the cross correlation factor of the IMF B_z values measured by ACE and IMP-8. The guidelines indicate the time of the images after the delay between each data set and IMP-8 has been incorporated.

analysis between the IMP-8 and WIND B_z values indicated a 4-min lead of WIND. We also cross-correlated the other two components of the IMF and the Z-component of the velocities measured by WIND and ACE. In all these cases, the delays were in accord with the numbers given above. The WIND and ACE parameters, plotted in Figure 1, have

been shifted in time by including their lead times with respect to the IMP-8 measurements. The vertical guidelines serve to indicate the times of the auroral measurements presented here, but shifted 11 min to compensate for the delay between the IMP-8 measurements and the response of the aurora.

[5] Figure 2 illustrates a calculation of the timing and location of the phase front (yellow plane) impacting the ecliptic plane of the magnetopause (curved black trace at $Z = 0$). The yellow line, seen at the center of the phase front plane, shows where the ecliptic intersects the plane front. Due to the nearness of IMP-8 to Earth, the IMF associated with the images shown below actually impacted the magnetopause before it was sensed by IMP-8. The phase front is defined as a surface of constant interplanetary magnetic and electric fields. This surface can be determined using the coordinates of 3 points in interplanetary space that have similar IMF values. One of these points is given by the coordinates of IMP-8 at 0729 UT. The other two points are introduced based on the locations of WIND and ACE at 0729 UT but subtracted by their time delays with respect to IMP-8. The phase front, constructed with these 3 points, is then "transported" until it becomes tangent to the magnetopause. The three plus (+) signs indicate the locations of the solar wind plasma at 0708 UT after these have been "transported" using their respective delays and the solar wind vector velocity. The three plus signs are displayed embedded within color-coded planes; however, they are also used to define the yellow plane. Due to the long delay between the ACE and IMP-8 satellites, the plasma that was detected by ACE (near the Lagrangian point) convects to a location closer to

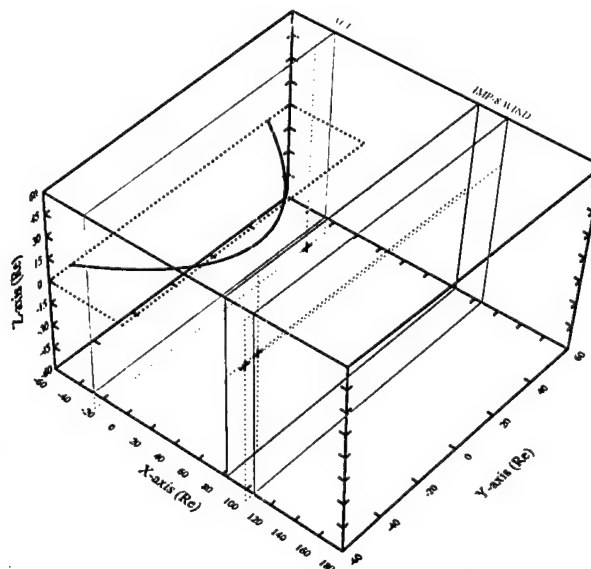


Figure 2. Three-dimensional view of the phase front of the solar wind impacting the magnetopause at 0708 UT. The yellow plane depicts the phase front and the red, blue and green planes serve to indicate the location of three points in space (crosses) used to determine the phase plane. These three planes have been "transported" from the satellite locations using the time delays and the satellite velocity.

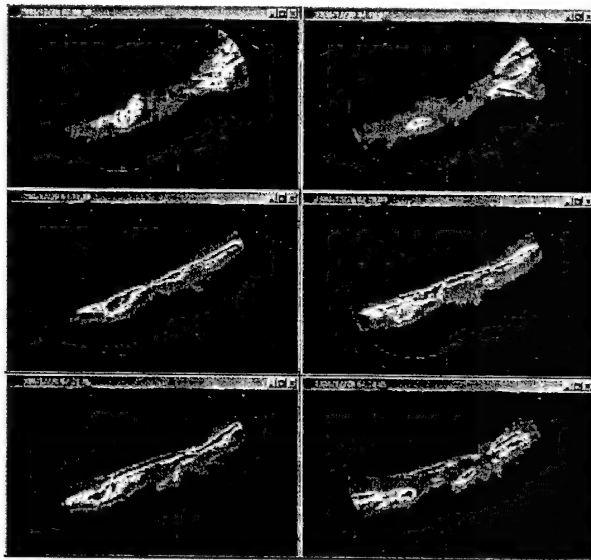


Figure 3. Images from the Ny Ålesund and Heiss Island imagers projected to 250 km altitude and merged in a common geographic frame. Notice the north-south motion of the dayside aurora and the formation of auroral forms from the main trace.

the Earth than the observations of the other two satellites. A delay between the IMP-8 measurements and the time of magnetopause impact was obtained by adjusting the time when the front plane hits the magnetopause curve. This delay was found equal to -21 min.

2.2. Auroral Measurements

[6] Figure 3 shows six pairs of 630.0 nm images from the Heiss Island and the Ny Ålesund imagers that have been merged and projected into a common geographic frame. The top left frame (0708 UT) shows the cusp aurora divided longitudinally in two broad regions. This configuration persists for few minutes until 0710 UT when the western aurora dims and the eastern side brightens. There are also three forms re-brightening near the eastern end of the aurora, which are seen to drift poleward and increase their extension toward the west. At 0714 UT the main auroral trace starts retreating poleward. However, this motion is not uniform along the east-west extension of the aurora; the westward part seems to leap poleward first. This is followed by a brightening of the red and green (data not shown) line emissions propagating westward along the newly formed aurora. The images of 0717 and 0720 UT show that the intensity at the poleward boundary of the aurora decreases sharply, and the equatorward edge presents smaller auroral features emanating from the main band. The images in the bottom panels, corresponding to 0721 and 0724 UT, show that the equatorward auroral forms continue moving equatorward and westward. These two auroral forms grow from two regions that are separated in the east-west direction by ~ 1000 km, one of them located near Ny Ålesund and the other over Heiss Island. At 0724 UT the western form, seen equatorward of the main band, continues moving westward and the eastern region displays a rayed structure. After 0726 UT (images

not shown) a more stable and typical type 1 aurora forms at the equatorward side of the arcs described above.

2.3. DMSP Observations

[7] Figure 4 shows, from top to bottom, the energy fluxes and average energy of electrons and ions (dotted), the differential number flux of the precipitating electrons and ions, and the horizontal (violet trace) and vertical (green trace) ion velocities. The top two panels of Figure 3 show the trajectory of the DMSP-F13 pass and the interval during which the satellite intersected the cusp aurora (0710:40–0712:00 UT). During this interval strong fluxes of precipitating particles are encountered with average energies of <150 eV and <2 keV for electrons and ions respectively. These values correspond to the energies of typical magnetosheath particles. Between 0711 and 0712 UT, a clear ion dispersion signature is observed with the energy of the ions decreasing with increasing latitude. Equatorward of the cusp (after 0712:10 UT), the characteristics of the precipitating particles resemble central plasma sheet particles. The convective drifts in the vicinity of the noontime cusp were strongly anti-sunward and approaching 3000 m/s.

3. Discussion and Conclusions

[8] Previous studies of dayside auroras have been limited to observations, in most cases of only a section of the cusp aurora. Here, we present a case study in which two imagers covered a ground distance of 2900 km at 80° geographic latitude and were able to map almost the whole east-west extension of cusp-related auroras. The imagers were located at Ny Ålesund (78.9°N , 11.9°E ; geomagnetic latitude 75.7° ; noon MLT 0850 UT) and Heiss Island (80.6°N , 58.1°E ; geomagnetic latitude 75.1° noon MLT 0600 UT).

[9] With 3 satellites orbiting in the solar wind we were able to determine the tilt of the phase front and the time and location at which the front surface of constant magnetic and electric fields impacted the magnetopause. One satellite

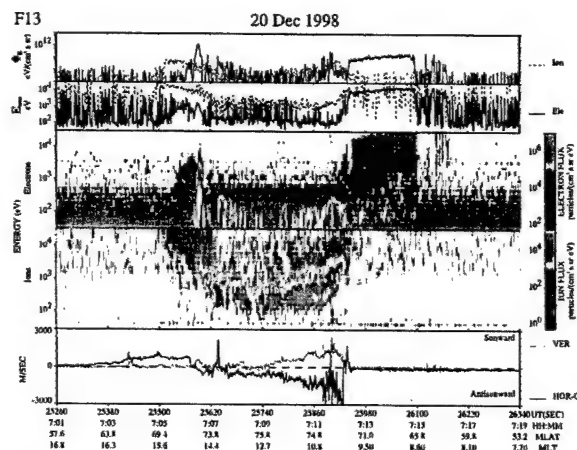


Figure 4. Particle and drift data measured by the DMSP-F13 satellite between 0701 and 0719 UT on December 20, 1998. The panels show from top to bottom the number fluxes, the average energy, the energy spectrograms for electrons and ions and cross-track horizontal and vertical ion velocities.

does not provide the tilt of the phase front and gives a coarse timing. We calculated that the IMF seen by IMP-8 at 0729 impacted the equatorial plane of the magnetopause at $X_{GSM} = (0.6, 21, 0) R_E$ at 0708 UT, or 21 min ahead of the IMP-8 observations. This time can be used to calculate more precisely the delay between the auroral observations and the IMP-8 measurements by considering the delays due to magnetosheath crossing (~ 7 min), the electron flight time from the magnetopause to the ionosphere (2 min), and the radiative lifetime of 630 nm cusp aurora (~ 1 min). Thus, a total delay of ~ 11 min is expected between the IMP-8 measurements and the auroral displays due to merging on the magnetopause northern dusk side. It is known that during $B_y > 0$ and for IMF clock angles larger than 90° , the antiparallel merging hypothesis predicts reconnection at the dusk side of the cusp in the northern hemisphere, and on the dawnside of the cusp in the southern hemisphere [Crooker, 1979]. The B_x component favors reconnection in the southern (northern) hemisphere for $B_x < 0$ ($B_x > 0$). Due to the positive tilt of the phase front, which was inclined toward the northern hemisphere, the solar wind will encounter the northern dusk merging site almost immediately after impact of the magnetopause.

[10] At the start of the observations (0708 UT) the IMF values were $(-5, +5, -5)$ nT. In addition, B_x was becoming more negative and B_z less negative. In accordance with these IMF conditions the dayside aurora was located near 73° MLAT, and presented direct ion dispersion signatures and large antisunward convection. Three auroral forms were also seen to the east of Heiss Is. resembling PMAFs. It is known that during B_y positive conditions, PMAFs are preferably seen in the pre-noon sector and moving westward [Øieroset et al., 1997a]. The auroral forms, seen here were rapidly moving poleward, increasing their extension toward the west, but located in the post-noon sector. The uncharacteristic location is probably due to a large displacement of the cusp toward dusk.

[11] At 0714 UT the IMF value was $(-6, +4, -1)$ nT. During the following 10 minutes, B_z remained above -1 , and presented short positive excursions. The dominant component was B_x , with an elevation angle of the IMF large enough to overcome the dipole tilt effect. Under these circumstances, it is common to observe a narrow dayside aurora [Sandholt et al., 2000], and the merging site poleward of the cusp. In agreement with the new IMF, both imagers showed that the dayside aurora retracted poleward, became narrower (< 100 km) and re-brightened in both 630 and 557.7 nm emissions. In addition, the aurora presented a sharp poleward boundary and other smaller auroral forms were seen departing equatorward from the main arc. Based on these features, we suggest that during this time the merging site moved to a location poleward of the cusp on lobe field lines, which were open. Due to $B_y < |B_x|$, it is also likely that the northern hemisphere merged field lines drape over the magnetopause toward the southern hemisphere [Lockwood and Moen, 1999]. By using two imagers, we were able to observe the whole extension of the cusp aurora

and report that any change in the IMF is followed quite quickly by a response of the cusp aurora in its entirety [Moen et al., 1999]. The cusp aurora, seen with both imagers, may map to an extended reconnection line located solely in the northern hemisphere. Future research based on data from our pair of imagers should enable us to test the component versus the anti-parallel merging hypothesis.

[12] **Acknowledgments.** The authors are grateful to H. C. Carlson Jr. for his advice to locate one of the imagers at Heiss Island. We thank N. Maynard for useful comments of the manuscript. We also thank Mikhail Krylov for wintering over on 1997 and 1998 and his dedication to run the imager at Heiss Island. We are grateful to Vladimir Gizler for his efforts to deploy the imager at Heiss Island. The work at Boston College was partially supported by NSF grants OPP-9708101, by Air Force Research Laboratory contract F19628-97-C-0094 and AFOSR task 2311AS. The work at the University of Oslo was supported by the Norwegian Research Council and AFOSR Task 2311AS.

References

- Crooker, N. U., Dayside merging and cusp geometry, *J. Geophys. Res.*, **84**, 951, 1979.
- Lockwood, M., and J. Moen, Reconfiguration and closure of lobe flux by reconnection during northward IMF: Possible evidence for signatures in cusp/cleft auroral emissions, *Ann. Geophys.*, **17**, 996, 1999.
- Maynard, et al., Driving dayside convection with northward IMF: Observations by a sounding rocket launched from Svalbard, *J. Geophys. Res.*, **105**, 5245, 2000.
- Moen, J., H. C. Carlson, and P. E. Sandholt, Continuous observation of cusp auroral dynamics in response to an IMF B_y polarity change, *Geophys. Res. Lett.*, **26**, 1243, 1999.
- Øieroset, M., P. E. Sandholt, H. Luhr, W. F. Denig, and T. Moretto, Auroral and geomagnetic events at cusp/mantle latitudes in the prenoon sector during positive IMF B_y conditions: Signatures of pulsed magnetopause reconnection, *J. Geophys. Res.*, **102**, 7191, 1997a.
- Øieroset, M., P. E. Sandholt, W. F. Denig, and S. W. H. Cowley, Northward interplanetary magnetic field cusp aurora and high-latitude magnetopause reconnection, *J. Geophys. Res.*, **102**, 11,349, 1997b.
- Perreault, P., and S.-I. Akasofu, A study of geomagnetic storms, *Geophys. J. R. Astr. Soc.*, **54**, 573, 1978.
- Sandholt, P. E., C. J. Farrugia, P. Stauning, S. W. H. Cowley, and T. Hansen, Cusp/cleft auroral forms and activities in relation to ionospheric convection: Responses to specific changes in solar wind and interplanetary magnetic field conditions, *J. Geophys. Res.*, **101**, 5003, 1996.
- Sandholt, P. E., C. J. Farrugia, J. Moen, and S. W. H. Cowley, Dayside auroral configurations: Responses to southward and northward rotations of the interplanetary magnetic field, *J. Geophys. Res.*, **103**, 20,279, 1998a.
- Sandholt, P. E., C. J. Farrugia, J. Moen, O. Norberg, B. Lybekk, T. Sten, and T. Hansen, A classification of dayside auroral forms and activities as a function of interplanetary magnetic field orientations, *J. Geophys. Res.*, **103**, 23,325, 1998b.
- Sandholt, P. E., C. J. Farrugia, S. W. H. Cowley, M. Lester, W. F. Denig, J.-C. Cerisier, S. E. Milan, J. Moen, E. Trondsen, and B. Lybekk, Dynamic cusp aurora and associated pulsed reverse convection during northward interplanetary magnetic field, *J. Geophys. Res.*, **105**, 12,869, 2000.
- Woch, J., and R. Lundin, Magnetosheath plasma precipitation in the polar cusp and its control by the interplanetary magnetic field, *J. Geophys. Res.*, **97**, 1421, 1992.
- W. F. Denig, Space Vehicles Directorate, Air Force Research Laboratory, 29 Randolph Rd., Hanscom AFB, MA 01731, USA.
- J. Moen and P. E. Sandholt, Department of Physics, University of Oslo, P.O. Box 1048, Blindern, N-0316, Norway. (p.e.sandholt@fys.uio.no)
- O. Troshichev, Arctic and Antarctic Research Institute, 53 Bering St., St. Petersburg, Russia. (olegtr@aar.i.nw.ru)
- C. E. Valladares, Institute for Scientific Research, Boston College, 140 Commonwealth Av. Chestnut Hill, MA 02647, USA. (valladar@bc.edu)

Multi-site observations of the association between aurora and plasma convection in the cusp/polar cap during a south-eastward ($B_y \simeq |B_z|$) IMF orientation

P. E. Sandholt¹, J. Moen¹, C. J. Farrugia², S. W. H. Cowley³, M. Lester³,
S. E. Milan³, C. Valladares⁴, W. F. Denig⁵, and S. Eriksson⁶

Short title: BURSTY BIFURCATED CUSP

¹Department of Physics, University of Oslo, Oslo, Norway

²Space Science Center, University of New Hampshire, Durham

³Department of Physics and Astronomy, University of Leicester, UK

⁴Institute for Scientific Research, Boston College, Newton Center, Mass.

⁵Space Vehicles Directorate, Air Force Research Laboratory, Hanscom AFB, Mass.

⁶Laboratory for Atmospheric and Space Physics, University of Colorado

Abstract. In a case study we demonstrate the spatiotemporal structure of aurora and plasma convection in the cusp/polar cap when the interplanetary magnetic field (IMF) $B_z < 0$ and $B_y \simeq |B_z|$ (clock angle in GSM Y-Z plane: $\simeq 135^\circ$). This IMF orientation elicited a response different from that corresponding to strongly northward and southward IMF. Our study of this “intermediate state” is based on a combination of ground observations of optical auroral emissions and ionospheric plasma convection. Utilizing all-sky cameras at Ny Ålesund, Svalbard and Heiss Island (Russian arctic), we are able to monitor the high-latitude auroral activity within the ~ 1000 -1500 MLT sector. Information on plasma convection is obtained from the SuperDARN radars, with emphasis placed on line of sight observations from the radar situated in Hankasalmi, Finland (Cutlass). A central feature of the auroral observations in the cusp/polar cap region is a ~ 30 min long sequence of four brightening events, each of which consists of latitudinally and longitudinally separated forms, which are found to be associated with pulsed ionospheric flows in merging- and lobe convection cells. The auroral/convection events may be separated into different forms/cells and phases, reflecting a spatiotemporal evolution of the reconnection process on the dayside magnetopause. The initial phase consists of a brightening in the postnoon sector (~ 1200 -1400 MLT) at $\sim 73^\circ$ MLAT, accompanied by a pulse of enhanced westward convection in the postnoon merging cell. Thereafter the event evolution comprises two phenomena which occur almost simultaneously: (1) westward expansion of the auroral brightening (equatorward boundary intensification) across noon, into the ~ 1000 -1200 MLT sector, where the plasma convection subsequently turns almost due north, in the convection throat, and where classical poleward moving auroral forms (PMAFs) are observed; and (2) auroral brightening at slightly higher latitudes ($\sim 75^\circ$ MLAT) in the postnoon lobe cell, with expansion towards noon, giving rise to a clear cusp bifurcation. The fading phase of PMAFs is

accompanied by a “patch” of enhanced (~ 1 km/s) poleward-directed merging cell convection at high latitudes ($75\text{--}82^\circ$ MLAT), i.e., more than 500 km poleward of the cusp equatorward boundary. The major aurora/convection events are recurring at $\sim 5\text{--}10$ min intervals.

Introduction

There is now increasing evidence supporting the view that plasma convection at dayside high latitudes under conditions of a dominant B_y component consists of a composite pattern of so-called merging and lobe convection cells [Reiff and Burch, 1985; Knipp *et al.*, 1993; Lu *et al.*, 1994; Weiss *et al.*, 1995; Crooker *et al.*, 1998; Weimer, 2001; Eriksson *et al.*, 2002]. While the merging cells are characterized by the transfer of magnetic flux across the open-closed field line boundary (OCFLB) in the cusp region, the lobe cells circulate plasma in the polar cap region, entirely poleward of the OCFLB. Recent case studies have documented that these two types of plasma convection are accompanied by corresponding auroral forms [Sandholt *et al.*, 1998c, b, 2001]. The aurora associated with merging cell convection is characterized by a sequence of equatorward boundary intensifications from which emanate poleward moving auroral forms (PMAFs) [Sandholt *et al.*, 1986; Fasel, 1995; Sandholt and Farrugia, 1999; Sandholt *et al.*, 2002]. The sequential behaviour is considered to reflect the pulsed (intermittent) nature of magnetic reconnection at the magnetopause [Russell and Elphic, 1978; Cowley, 1984]. The corresponding convection signature consists of pulsed flows in the cusp region ionosphere [Lockwood *et al.*, 1989; Provan *et al.*, 1999; Moen *et al.*, 2001].

Initial case studies indicate that the auroral manifestation of the composite pattern of merging and lobe cells appears in the form of two latitudinally separated forms, called types 1 and 2, forming a so-called bifurcated cusp [Sandholt *et al.*, 1998c, 2001], which corresponds to a double cusp in particle precipitation data [Wing *et al.*, 2001; Sandholt *et al.*, 2002]. The detailed 2-D association between aurora and convection in this configuration is not well known at present. This association is the topic of the present paper.

The importance of B_y for lobe reconnection and the resulting convection cells confined entirely to the polar cap has been highlighted for a purely positive IMF B_y in magnetohydrodynamic (MHD) studies by e.g. Crooker *et al.* [1998] and White *et al.* [1998]. The former study indicated that the IMF B_y and B_x components

are more important controlling factors than IMF B_z . Moreover, the Alfvén Mach number seemed to control the relative strengths of the model lobe cell circulation relative to the normal dayside two-cell convection pattern. The larger the Alfvén Mach number, the weaker the lobe cell strength.

Recently, a few observations of B_y -dominant IMF reconnection have been presented. *Marcucci et al.* [2000] reported an indirect observation of a long reconnection event detected by the Equator-S spacecraft for a dawn magnetopause skimming orbit near the equatorial plane during a predominantly dawnward directed IMF with a southward B_z component. *Popescu et al.* [2001] presented Interball Tail data of a reconnection event, also during mainly dawnward IMF, at the high-latitude dawnside flank with a sunward-flowing plasma layer adjacent to the plasma mantle that lasted for many hours. The question of sub-Alfvénic versus super-Alfvénic flow regimes along the magnetopause and the stability of the reconnection site have been addressed in a few publications. Adopting the antiparallel merging hypothesis to study the magnetopause location of quasi-steady and transient reconnection at the magnetopause *Rodger et al.* [2000] concluded that the condition of fields being within 10° of pure antiparallel alignment is met within a sub-Alfvénic region at the dusk (dawn) high-latitude northern hemisphere flank for an IMF of equal magnitudes of a positive (negative) B_y and negative B_z .

Lobe cell convection during $|B_y| > |B_z|$ IMF conditions is characterized by sunward (zonal) polar cap convection in the postnoon (prenoon) sector for $B_y > 0$ (< 0) [*Reiff and Burch*, 1985; *Lu et al.*, 1994; *Eriksson et al.*, 2002]. According to these studies lobe cell convection is present for both positive and negative B_z polarity so long as $|B_y| \geq |B_z|$. Furthermore, in their recent case study based on data from the FAST satellite, *Eriksson et al.* [2002] show that the zone of sunward (zonal) lobe cell convection is accompanied by a patch of precipitating magnetosheath plasma with the presence of strong field-aligned currents (of opposite polarity) at its northern and southern boundaries, within the 79° - 82° MLAT/1300-1400 MLT sector ($B_y > 0$) in the summer hemisphere (see

their Plate 3). In this study we are taking advantage of the ability of ground based observations to reveal the spatiotemporal variability of auroral precipitation and convection referring to the same sector/phenomenon. However, our observations are performed in the winter hemisphere.

At present there is an ongoing debate about where reconnection takes place at the magnetopause during strong IMF B_y conditions. One view is that reconnection in such cases can occur where there is antiparallel components in the external, magnetosheath magnetic field and the Earth's field [Gonzalez and Mozer, 1974; Cowley, 1981; Sonnerup, 1984; Taguchi *et al.*, 1993; Kawano and Russell, 1997; Siscoe *et al.*, 2001]. According to this view, reconnection can take place over large areas of the dayside magnetopause, i.e., along a tilted reconnection line traversing the subsolar region and extending to high latitudes in both hemispheres. In the antiparallel model, on the other hand, reconnection is restricted to high latitudes during B_y -dominated IMF conditions [Crooker, 1979; Luhmann *et al.*, 1984; Rodger *et al.*, 2000; Coleman *et al.*, 2001]. Auroral observations of relevance to this issue is reported in this paper.

By combining observations from two similar all-sky imagers with partly overlapping fields of view in the east-west direction, we have been able to study the 2-D evolution of auroral forms in the cusp region, around magnetic noon, and in the postnoon sector of the polar cap. The continuous ground-based monitoring by this technique allows us in this case study to demonstrate the detailed spatiotemporal evolution of auroral precipitation and plasma convection when the latter consists of a composite pattern of merging and lobe cells, during a long interval of $B_y > 0$ and $B_z < 0$ conditions.

The detailed observations of the evolution of the auroral events, including poleward moving/expanding auroral forms (PMAFs), are placed in the proper context of large-scale plasma convection at high temporal and spatial resolution. First of all we demonstrate a close association between the sequence of auroral brightenings/PMAFs and pulsed ionospheric flows [Provan *et al.*, 1999; Greenwald

et al., 1999; *Provan et al.*, 2002]. Each episode of enhanced merging cell convection may be divided in two phases, i.e., i) enhanced westward convection at the cusp equatorward boundary, followed by, ii) a “patch” of strong (~ 1 km/s), poleward convection at high latitudes, > 500 km poleward of the cusp equatorward boundary. The corresponding phases of cusp auroral activity are: i) equatorward boundary intensification (initial appearance in the postnoon sector followed by rapid expansion across noon) and ii) poleward moving/expanding auroral form in the 1000-1200 MLT sector.

We note that ion flow velocities are observed to increase poleward of the cusp during these poleward propagating events. Phases i) and ii) of the ionospheric auroral-convection events are considered to be manifestations of bursty/pulsed dayside magnetopause reconnection and the subsequent tailward motion of reconnected field lines. The high-latitude, phase ii) observations appears as the recently reconnected field lines are being pulled antisunward by the magnetosheath flow. The observed flow excitation in this phase is in agreement with the previous observations/interpretations reported by e.g. *Sandholt et al.* [1993] and *Provan et al.* [2002]. PMAFs are found to be tracers of electron precipitation along poleward moving flux tubes in the convection throat which are present during a ~ 5 min long phase following the initial equatorward boundary intensification.

The presence of a stepped cusp particle precipitation observed by polar orbiting, low-altitude spacecraft [*Escoubet et al.*, 1992] during an interval of sequential auroral brightenings/PMAFs, an association first documented by *Yeoman et al.* [1997] and *Farrugia et al.* [1998], is confirmed in this study. In the present case the cusp was observed to be permeated by thin filaments of electron precipitation containing a rather broad energy spectrum (~ 30 eV-1 keV; average energy 200 eV). The latter is consistent with the long auroral rays which are so typical in the cusp region.

Data presentation

Figure 1.

Figure 1 shows interplanetary magnetic field and plasma data observed by the IMP8 spacecraft during the interval 0600-1100 UT on January 14, 1999. At 0800 UT IMP8 was located at $(-1.9, -33.6, -9.4)R_E$, i.e., the spacecraft was in the solar wind near the dawn terminator. B_y was strongly positive (10-15 nT) throughout, except for three brief excursions to zero or slightly negative between 0920-1000 UT. B_x was negative. We note the southward (at 0750 UT) and northward turnings at 0954 UT, marked by the first and third vertical guidelines. The same major features are observed from spacecraft ACE, located at $(233, 36, 8)R_E$. The mentioned rapid and strong northward turning was recorded by ACE at 0840 UT, i.e., 74 min earlier than IMP8. Both spacecraft recorded a solar wind bulk speed of 420-430 kms^{-1} and density (dynamic pressure) of 10 cm^{-3} (4 nPa). The ground magnetic effect of the northward turning at 0954 UT (IMP8 time) is clearly observed in the local magnetograms from the Svalbard IMAGE stations at 1000 UT. The propagation delay from IMP8 to the ground is about 5-10 min in this case. We shall be concerned with the auroral activity in the cusp region during the interval 0810-0850 UT, when the IMF is characterized by a negative (-10 nT) B_z component and a positive (10 nT) B_y component. This is the interval between the first two vertical guidelines in Figure 1. The clock angle (polar angle of the IMF vector projected into the GSM Y-Z plane) is $\sim 135^\circ$.

Figure 2.

Figure 2 shows the observation geometry at ~ 0835 UT superposed on a schematic convection pattern consisting of merging (M) and lobe (L) cells. Arrowed meridional line and circle mark the fields of view (FOV) of the meridian scanning photometer (MSP) and the all-sky camera, respectively, in Ny Ålesund, Svalbard (76.1°MLAT). The FOV of the all-sky camera at Heiss Island, located ~ 700 km to the east of Svalbard is marked by the second circle (to the left).

Hatched areas mark two latitudinally and longitudinally separated cusp-type auroral forms, labelled 1 and 2. Strong red line emission in the type 1 cusp aurora in the convection throat in the 1000-1130 MLT sector during 0836-0838 UT is

marked by cross-hatching. The westward expansion of the type 2 form into the eastern part of the field of view at Ny Ålesund during 0833-0835 UT, as well as the poleward expansion of type 1 auroras during 0835-0838 UT, are indicated. Regions of strong backscatter along beams 4, 9, and 14 of the CUTLASS Finland HF radar are marked by bars along the respective antenna beams.

Figure 3.

Figure 3 shows MSP observations of the auroral emission lines at 630.0 nm (panel a) and 557.7 nm (panel b) taken at Ny Ålesund (76.1°MLAT) during the interval 0800-0900 UT (1100-1200 MLT) on January 14, 1999. Line of sight intensities are colour-coded according to the scales at the bottom of each panel. The MSP FOV for the red line emission (at 0830 UT/~1130 MLT) is indicated in Figure 2. The auroral equatorward boundary is located well to the south of Ny Ålesund and is moving slightly equatorward during the interval shown. We focus on the four strong brightening events (red) recorded during 0820-0850 UT (0825, 0835, 0841/42, and 0849 UT). Three of these events show a characteristic poleward expansion of luminosity. Each event consists of the following substructure, when moving from lower to higher latitude (from bottom to top in the MSP panels): 1) green line enhancements near the southern horizon, at 70°-80°SZ (south of zenith) (the corresponding red line emission is very weak), 2) strong brightening of a band located at at ~40-60°SZ appearing in both emission lines, often in the form of two subsequent brightenings, 3) one or two “re-brightenings” closer to the zenith (30°-0°SZ), related to the poleward expansion of luminosity. As we shall see below, the “re-brightening” phenomenon can be the result of the expansion of type 2 events into the MSP FOV, from the east (postnoon) side. The events typically recur at 5-10 min intervals. The 2-D evolution of the activity in the interval 0830-0838 UT will be shown below, revealing that the type 2 auroral brightening/expansion events are accompanied by zonal flow towards noon from dusk, in the polar cap.

Figure 4.

In order to illustrate the transition in auroral emission along the Ny Ålesund meridian which took place at 0855-0900 UT (1200 MLT) we show in Figure 4 a red line plot for the interval 0800-1000 UT. The aurora along the Ny Ålesund meridian

changed latitudinal position and character when the local meridian rotated with the Earth into the postnoon sector. After 0900 UT the aurora is located further to the south and the poleward moving forms are not such a dominant feature as in the interval 0800-0900 UT.

Figure 5.

Figure 5 shows an all-sky image sequence of the 630.0 nm aurora observed at Ny Ålesund during the interval 0831-0839 UT. The Ny Ålesund all-sky camera FOV for the red line emission (at ~0830 UT) is indicated in Figure 2. This sequence shows the 2-D evolution of one of the four major auroral events recorded by the MSP plot during the interval 0825-0850 UT (Figure 3). Two features are clearly manifest: 1) the appearance of a bright form (rayed band) in the eastern part of the FOV at ~0832 UT (type 2 aurora), which expands westward and poleward, reaching the MSP meridian at ~0836 UT, and fade out during 0836-38 UT, 2) brightening in the south-western part of the FOV during 0834-37 UT (type 1 aurora; marked as cross-hatched area in Figure 2). The latter appears as a red line intensification at 45°SZ-60°SZ in Figure 3.

Figure 6.

A closer view of the evolution of the auroral activity in the 1200-1500 MLT sector during the interval 0830-0838 UT is provided by the image sequence shown in Figure 6, obtained from the Russian station Heiss Island (HI), located at 80.6° N; 58.1° E (75.2° MLAT). This location is ~700 km to the east of Ny Ålesund. The approximate FOV of this camera (at 630.0 nm) is indicated in Figure 2. The center of the FOV of the HI camera is located at the eastern boundary of the Ny Ålesund camera. The HI camera therefore effectively extends the FOV in the eastward direction to include (in our case) the ~1300-1500 MLT sector.

The initial brightening, located in the ~1300-1500 MLT sector, is seen in the third (0831:38 UT) image in Figure 6. The brightening continues in the next image (0832:46 UT). This is followed by a clear auroral bifurcation which is evident in the 0833:56 UT image and onwards, characterized by a type 1 aurora in the south-western part of the HI FOV and the type 2 form expanding westward across the whole FOV further north. The western boundary of the type 2 event

expanded westward from Heiss Island (center of the FOV) to Svalbard during the interval 0832-35 UT. Thus, this form entered the FOV of the Ny Ålesund meridian scanner, slightly south of the zenith, at 0835 UT. The fading phase of this event is represented by the lower row of pictures in Figure 6, covering the interval 0836:17-0838:40 UT. Main features of the auroral activity during the interval 0833-0838 UT are schematically summarized in Figure 2.

Figure 7.

Figure 7 shows line of sight ion drift velocities obtained by beams 4 (upper panel), 9 (middle), and 14 (bottom) of the Cutlass Finland HF radar during the interval 0800-0900 UT on January 14, 1999. The fields of view of these radar beams are indicated in Figure 2. The four auroral brightening events observed by the Ny Ålesund MSP during the interval 0825-0850 UT, seen in Figure 3, are marked by vertical dashed guidelines. Strong line of sight flows away from the radar (red) are recorded in both the upper (beam 4) and middle (beam 9) panels after 0825 UT. The equatorward boundary of the region of enhanced backscatter in beam 9 (the beam located closest to the MSP FOV) migrated equatorward from 75° to 72° MLAT during 0800-0850 UT, and then expanded down to 70° MLAT by 0900 UT. This backscatter boundary and its motion correspond closely with the equatorward boundary of the type 1 cusp aurora (see Figure 3). A pulsed nature of the away (antisunward) flow, roughly corresponding to the auroral brightenings marked by the vertical guidelines, is seen in beams 4 and 9.

The easternmost beam (14; bottom panel) shows four patches of line of sight flows toward the radar (green and blue), within 73 - 78° MLAT, during 0820-0850 UT. These events are centered at the times of the marked auroral events. At this point we note that the CUTLASS beam 14 overlaps with the eastern part of the Ny Ålesund all sky camera field of view and the western part of the Heiss island camera field of view. The initial phase of these radar events (within 73 - 75° MLAT), representing westward convection (also containing an equatorward component), corresponds to the initial auroral brightening in the same region. We also note in the beam 14 data the presence of transient events of away flow (red) at the

equatorward boundary of the region of backscatter at the time of the type 1 auroral brightening events (the vertical lines). There are some spurious positive (blue) Doppler shift echoes mixed in with the general negative (red) Doppler shift flow.

Returning to the 0832-0838 UT event, we observe the following association between aurora and ion drift. At 0835 UT (second vertical guideline in Figure 7) beam 14 recorded away (line of sight) flow (red) at 73°MLAT, near the equatorward boundary of the (type 1) aurora in the 1200-1300 MLT sector, and toward flow (blue) between 75°-78°MLAT, in the region of the type 2 expansion event (see Figure 6 and Figure 2). This association of aurora-convection is seen in most events. We also notice that each individual patch of toward (blue) flow typically expands poleward during the event (see for example the interval 0832-38 UT). Each event (blue patch) is associated with auroral forms (type 2) expanding towards Svalbard, from the eastern (postnoon) side. The aurora corresponding to the 0832-0838 UT event is shown in Figures 5 and 6.

Figure 8.

The spatial structure of the convection pattern and its evolution during the interval 0832-0842 UT are shown in Figure 8. The coordinate system is magnetic local time (MLT) and magnetic latitude (MLAT). To construct the 2-D flow pattern from the radar line of sight velocities, we employ the analysis technique developed by *Ruohoniemi and Baker [1998]* (see also *Greenwald et al. [1995]*). This technique determines the solution for the distribution of electrostatic potential expressed as a series expansion in spherical harmonics (in our case of order 10), constrained by the line of sight measurements of the radars. Contours of the electrostatic potential so derived are superimposed, which in effect represent convection flow streamlines. In regions where no radar backscatter is present the potential solution is driven by a statistical convection model, which may not accurately reflect the instantaneous flows occurring in the ionosphere. However, in regions where backscatter is present, and so constrains the solution, the contours represent a flow pattern that accurately reflects the line-of-sight measurements.

From Figure 8 we note the following three features of the evolution of the event:

(1) The initial (0832-0834 UT) westward convection in the 1200-1400 MLT/ ~ 73 - 75° MLAT sector which is accompanied by a clear local auroral brightening (see Figure 6). (2) The strong (red) poleward flow in the 1000-1130 MLT/ 73° - 78° MLAT sector during 0834-0838 UT. The corresponding aurora consists of an equatorward boundary intensification (EBI) at $\sim 73^\circ$ from which emanates a poleward moving auroral form (PMAF). These observations strongly indicate that there is a close association between the auroral phenomenon (EBI-PMAF) (see Figure 3) and enhanced poleward flow in the convection throat. The brightest type 1 aurora during 0834-0839 UT is confined to the western side of the Ny Ålesund meridian, as is seen in Figure 5. (3) The westward convection in the lobe cell (blue) in the postnoon sector (1200-1500 MLT/ ~ 75 - 77° MLAT) during 0834-38 UT (Figure 8). This is accompanied by the westward expansion of the type 2 aurora (Figure 6). The spatial relationship between the two auroral forms (called types 1 and 2) and the convection pattern at this time is illustrated in Figure 9. We note that the sunward flow in the postnoon sector (blue), containing an equatorward component, is in accordance with the MHD modelling work by *Crooker et al.* [1998] (see their Figure 3).

Figure 9.

The detailed association between aurora and convection for 0836 UT (in MLT/MLAT coordinates) is illustrated in Figure 10. The two auroral forms labelled 1 and 2 in Figure 9 are easily identified. The aurora seen in the postnoon sector (1230-1430 MLT), well separated from the type 2 form, on its equatorward side (within ~ 72 - 74° MLAT), is accompanied by northwestward convection in the merging cell. The latitudinal gap between this form (type 1) and the type 2 aurora also represents the separation between the merging and lobe convection cells. Poleward moving auroral forms are localized in the convection throat in the 1000-1200 MLT/ 73 - 77° MLAT sector.

Figure 10.

The evolution of the convection during the interval 0836-0838 UT is illustrated in Figure 11. We note the patch of strong poleward ion drift (red vectors) in the 75 - 82° MLAT/1000-1200 MLT range. The bright cusp aurora in this local time

sector (1000-1200 MLT) is shown in Figure 5.

Figure 11.

The association between plasma convection, particle precipitation and auroral forms during one of the events is indicated in Figure 12. The figure shows the convection pattern for 0838-0840 UT with the trajectory of spacecraft DMSP F14 during 0836-0842 UT and the approximate field of view of the MSP in Ny Ålesund marked by dark blue symbols. Precipitating protons with energy-latitude dispersion typical of the cusp-mantle region during southward IMF conditions (energy increasing with decreasing latitude) was recorded from F14 in the sector marked by red double-headed line (during 0839:00-0840:20 UT). In this same sector the ion driftmeter onboard the spacecraft recorded strong, westward ion drift, i.e., a classical convection channel, after exiting a region of near zero drift in the direction normal to the S/C trajectory (during 0836-0838 UT). The spacecraft skimmed the boundary of the lobe cell during ~0835-0838:30 UT. The strong sunward/equatorward convection within 0835-0837 UT is one manifestation of the lobe cell. The latitudinal sector of the auroral brightening (equatorward boundary intensification) at ~0840 UT, as recorded by the MSP in Ny Ålesund (Figure 3), is marked by red double-headed line along the MSP FOV.

Figure 12.

At 0840 UT the poleward boundary of the previous auroral brightening/poleward expanding event had reached well beyond the latitude of Ny Ålesund (marked by isolated solid dot in the figure). At this time Ny Ålesund is located near the western boundary of the region of enhanced (> 800 m/s) poleward ion drift in the convection throat. This data set demonstrates i) that the poleward part of the cusp aurora, appearing as a classical PMAF, is expanding poleward in the direction of plasma convection in the throat region, ii) the episode of enhanced convection (0832-0840 UT) may be divided in two phases (enhanced westward convection at the cusp equatorward boundary followed by a poleward propagating patch of strong, poleward convection) corresponding to two phases of the cusp auroral activity (equatorward boundary intensification followed by a poleward moving/expanding form), iii) the fading phase of one event (0838-0840 UT) overlaps

with the initial phase of the next event, and iv) the patch of enhanced poleward ion drift is located within $75\text{--}82^\circ\text{MLAT}$, i.e., it extends beyond the poleward boundary of the PMAFs in the fading phase.

Figure 13.

Figure 13 shows the DMSP F14 data obtained during the pass indicated in Figure 12. A clear staircase cusp with three ion energy steps was recorded during the interval 0839:00–0840:30 UT. Low-energy cutoffs in these three steps are observed at 150 eV, 500 eV, and 2 keV (see panel 4). Thus, these steps are very similar to those reported by *Escoubet et al.* [1992], which were interpreted in terms of a pulsed magnetopause reconnection process and the associated poleward/tailward motion of a series of discrete, open flux tubes, which is due to the coupling to the solar wind. Within the regime of the stepped cusp ($\sim 71.5\text{--}74.0^\circ\text{MLAT}/\sim 12.0\text{--}13.5\text{MLT}$) there is highly structured electron precipitation characterized by latitudinally separated filaments containing a broad energy spectrum, extending to relatively high energies (600 eV and occasionally above 1 keV; see panel 3), a channel of strong westward (antisunward) convection (panel 5), and strong magnetic deflections (bottom panel). The average energy of the electrons in the cusp is 200 eV. The magnetic deflections indicate the presence of pairs of up- and down-flowing field-aligned currents showing the same electrodynamic properties as those reported by *Sandholt et al.* [1989] and *Lockwood et al.* [2001].

A different regime of ion dispersion was observed during 0835–0839 UT, in the $16.9\text{--}13.5\text{ MLT}/73\text{--}75^\circ\text{MLAT}$ sector. During the 0835–0837 UT part of this sector the cross-track ion drift (blue) has a clear equatorward component, in contrast to the later traversal through the stepped cusp. This is consistent with the lobe cell recorded by the SuperDARN radar (Figure 12). The first part of the pass (0833–0835 UT) shows the traversal of the dusk sector of the auroral oval and its plasma sheet precipitation.

Figure 14.

Figure 14 shows the evolution of the convection pattern (SuperDARN vector plots) for the interval 0846–0850 UT, covering the last major “midday auroral breakup event”/PMAF in the sequence illustrated in Figure 3. The field of view

(FOV) of the meridian scanning photometer (MSP) in Ny Ålesund is marked in panels C and D. As in the previous case the convection event starts with enhanced westward flow at the cusp equatorward boundary, accompanied by auroral brightening, during 0844-0846 UT. This is followed by a swing to more poleward convection (in the convection throat) and associated poleward expanding aurora in the later phase of the event (0848-0850 UT). The latitudinal span of the aurora at this time is marked by a bar along the MSP FOV in panel D of Figure 14. As in the previous event, the “patch” of enhanced convection, marked by red vectors, extends to higher latitudes than the PMAF, well beyond 80°MLAT. The 0848-0850 UT panel shows the strongest flow within 77-82°MLAT, when the cusp equatorward boundary was located at $\sim 72\text{--}73^\circ\text{MLAT}$.

Figure 15.

Figure 15 shows X-component magnetograms from the IMAGE (International Monitor for Auroral Geomagnetic Effects) stations on Svalbard and in Scandinavia (see <http://www.geo.fmi.fi/image/>). The data are 10 s resolution. For each trace, the average over the whole interval has been subtracted from the raw readings.

The four events of type 1 auroral brightenings and associated away (antisunward/poleward) ion drift are marked by vertical full lines (event onsets) at 0825, 0835, 0841, and 0848 UT. We can see that the auroral and the radar events are accompanied by clear events of positive X deflection at stations HOP-HOR-LYR-NAL, spanning the latitude range 72°-76°MLAT. This is the latitudinal band of the type 1 cusp aurora (see Figure 2). The dash-dot line at 1000 UT marks the abrupt recovery after the strongly negative deflection (convection bay) at cusp latitudes during the interval 0900-1000 UT. This is a clear signature of the convection response to the rapid northward turning of the IMF recorded by IMP8 at 0954 UT (see Figure 1).

In this paper we focus on the auroral activity which occurred during the interval 0825-0850 UT (associated with the four positive X-deflections marked by the vertical lines), before the negative convection bay during 0855-1000 UT. The onset of the latter convection bay was accompanied by a marked equatorward

displacement of the aurora along the Ny Ålesund meridian to $\sim 70\text{--}72^\circ\text{MLAT}$ (see Figure 4 and further comments below).

Discussion

The basis for this study is a detailed description of the 2-D structure/evolution of a sequence of auroral activations in the cusp/polar cap and the association with plasma convection observed during a 30 min interval on January 14, 1999. The main features of the aurora-convection observations during two individual events in the sequence are shown in Figures 10 and 14 and schematically summarized in Figure 2.

These events occurred when the interplanetary magnetic field (IMF) was relatively stable and characterized by strong B_y (10 nT) and B_z (-10 nT) components (clock angle $\simeq 135^\circ$). During the interval under study (0825-0855 UT) the cusp equatorward boundary migrated slowly equatorward (see Figure 3) within the latitude range $73^\circ\text{--}75^\circ\text{MLAT}$. At the end of this interval (~ 0855 UT) a reconfiguration occurred in aurora and plasma convection, resulting in a substantial lowering of the latitudinal position of the cusp/cleft aurora, approaching the boundary of the field of view at $\sim 70\text{--}72^\circ\text{MLAT}$, and the activation of a strong magnetic convection bay at these latitudes. The latter state lasted until a strong IMF northward turning which arrived at the magnetopause just before 1000 UT. One reason for the transition at 0855-0900 UT is a gradual southward rotation of the IMF from the state $|B_y| \geq |B_z|$ to the state $|B_y| < |B_z|$ (IMF clock angle increasing from below to above 135°), which was recorded by spacecraft IMP8 at ~ 0840 UT (Figure 1). Related to this we note that it has been documented previously that during large, continuous southward IMF rotations a greater qualitative change in the convection pattern occur at $|B_y| \simeq |B_z|$ (clock angle $\simeq 135^\circ$) than at the transition through $B_z = 0$ [Knipp *et al.*, 1993] (see also Freeman *et al.* [1993] and Huang *et al.* [2000]). The corresponding change in auroral configuration at midday (meridian scanning photometer data only) and associated

ground magnetic deflection, very similar to that which occurred in the present case, is seen in the two case studies reported by *Sandholt and Farrugia* [1999].

The events we study here belong to an interval characterized by IMF $B_y \simeq |B_z|$. They appear as a sequence of brightening events which involve latitudinally and longitudinally separated cusp-type auroral forms. Individual events in the sequence consists of (1) initial brightening, accompanied by westward convection in the postnoon sector (1200-1500 MLT/ ~ 73 - 75° MLAT), followed by (2) rapid westward expansion into the prenoon sector, appearing as equatorward boundary intensification/poleward expansion in the MSP records at Ny Ålesund, in the 1000-1200 MLT sector, as well as (3) a brightening form expanding westward (towards noon) in the 1200-1500 MLT sector ($B_y > 0$), at ~ 75 - 77° MLAT. While the auroral phenomena (1) and (2) are accompanied by bursts of enhanced westward and poleward convection in the merging cell, the type 2 auroral events are found to be related to lobe cell convection (see also *Sandholt et al.* [1998a, 2001]). We find that each type 2 auroral event is accompanied by a ~ 5 min long event of zonal (westward) convection in the postnoon sector (~ 1400 - 1700 MLT), at polar cap latitudes ($\sim 75^\circ$ MLAT; see Figures 9 and 12). The close association in space between the auroral forms and the composite convection pattern, consisting of merging and lobe cells, during a long sequence of auroral events was indicated in *Sandholt et al.* [2001]. However in that case the optical field of view was limited to a single meridian (the Ny Ålesund MSP meridian). In this case we demonstrated the detailed temporal-spatial evolution of the auroral forms by applying observations from two all-sky cameras with partly overlapping fields of view. This extended instrumentation was particularly appropriate for demonstrating the evolution of the type 1 and 2 auroral events. Furthermore, in the present case the FOV of the Cutlass Finland radar (see Figure 2) was ideally located for monitoring the temporal evolution of the convection pattern on the dayside.

The main thrust of this paper is therefore the demonstration of the 2-D morphology and dynamics of the interrelated activations of latitudinally and

longitudinally separated auroral forms in the cusp/polar cap, and the association with a composite pattern of merging and lobe convection cells [Reiff and Burch, 1985]. Combining the present results with those reported in Sandholt *et al.* [2001] we find that this auroral configuration/convection pattern is typical for intervals of B_y -dominant IMF orientation (including the clock angle range 90° - 135°). The aurora in this case may correspond to the type of double (or bifurcated) cusp precipitation that has been reported by Wing *et al.* [2001]. The association between aurora and particle precipitation (protons and electrons) for such cases has been documented in a recent study by Sandholt *et al.* [2002].

We note that the type 1 auroral brightenings recorded by the meridian scanning photometer in Ny Ålesund are located in the convection throat in the prenoon sector (marked by cross-hatching in Figure 2) during the prevailing $B_y > 0$ and $B_x < 0$ conditions, which is in agreement with the results of Maynard *et al.* [2001] (concerning the plasma configuration see also Neudegg *et al.* [2001], and the pulsed ionospheric flows (PIFs) statistics of Provan *et al.* [1999]). The auroral transition appearing in the MSP records at ~ 0900 UT/1200 MLT (Figure 4), when the PMAF sequence is replaced by an aurora at lower latitude, took place when the Ny Ålesund MSP moved out of the convection throat (with poleward convection), into the postnoon sector, where the local convection is more zonal (westward return flow in the postnoon sector) (see Figure 9). Here it is also shown that the type 1 auroral activations (near the cusp equatorward boundary) and subsequent poleward expansions (PMAFs) are accompanied by episodes of enhanced westward flow followed by swings to antisunward (poleward) drift in the convection throat (Figures 7, 9, 11 and 14) and X-component magnetic deflection (Figure 15) at cusp latitudes. The convection enhancements evolve with time towards higher latitudes in the cusp/mantle region (Figures 9, 11 and 14). The latter is in agreement with previous radar observations of enhanced poleward flow poleward of the cusp which has been attributed to a transient increase in dayside reconnection [Greenwald *et al.*, 1999]. The pulsed nature of the type 1 cusp

aurora is clearly demonstrated in Figure 3. We have documented the one-to-one association between the auroral and convection events.

One important feature in the data set deserves a further comment. That is the bursts of westward convection appearing as toward flow (blue) in beam 14 of the CUTLASS radar in the 1200-1400 MLT/ 73-75°MLAT sector in the early phase of the events described above. We note that the flow is not always strictly westward, i.e., an equatorward component may be present at times (see also *Neudegg et al.* [2001]). However, the occasional presence of an equatorward flow component could be an artefact. Clear examples are represented by the intervals 0832-0834 UT (see Figures 7 and 8) and 0844-0846 UT (Figure 14). The aurora corresponding to the former event is seen in the lower section of the Heiss Island images in Figure 6. The phenomenon also appears to be present in the form of initial brightenings seen in the MSP plot in Figure 3 during the intervals 0832-0834 and 0844-0846 UT. Referring back to the schematical illustration in Figure 2, this aurora-convection feature in our data set is manifest in the region of the single-hatched region south of 75°MLAT in the ~1200-1400 MLT sector and along the most equatorward bar marked along antenna beam 14. In our view this phenomenon is well explained by the model of the initial ionospheric flow response to flux transfer events during $B_y > 0$ conditions, as illustrated schematically in Figure 4 of *Milan et al.* [2000] (see also *Cowley* [1998]).

Figure 16.

The evolution of the present aurora-convection events may be explained in terms of a wave-like propagation of reconnection events on the dayside magnetopause, much in the way as was explained in recent studies by *Milan et al.* [2000] and *Sandholt et al.* [2001]. The upper panel of Figure 16 shows a tilted reconnection line on the magnetopause for IMF $B_y > 0$ conditions (IMF clock angle $\sim 135^\circ$) and field lines just inside the magnetopause which are tilted over in the direction of IMF B_y (see *Cowley et al.* [1991]). The northern cusp, displaced into the post-noon sector, is thus connected with the southern cusp which is displaced pre-noon. This is the sense of displacement of the main cusp as

determined by *Newell et al.* [1989] from DMSP particle precipitation data. A burst of magnetopause reconnection starting at noon (component reconnection in the subsolar region) will first map into the post-noon sector in the northern hemisphere, followed by propagation away from this centre both west and east, towards higher latitudes. In the ionosphere the westward (dawnward) propagation/expansion at the magnetopause (in the southern hemisphere) results in an auroral transient propagating at lower latitudes around noon from post-noon to pre-noon at the equatorward edge of the merging cell. The eastward (duskward) propagation to higher latitudes at the magnetopause eventually produces the type 2 auroral form, which will also propagate westward towards noon in the lobe cell due to field tension (curvature force). This evolution of the ionospheric events is indicated in the lower panel of Figure 16. The two open arrows mark westward surges of the type 1 and 2 auroras. Thus, our interpretation of the auroral data is that the reconnection signature starts in the ionosphere post-noon (due to field line tilting), and then propagates in both directions, east to give the type 2 aurora eventually, and west to give the westward propagation across noon of the type 1 aurora. The latter auroral expansion from postnoon to prenoon, which is often observed (see e.g. *Sandholt et al.* [1998c], their Plate 2), is in our view in good agreement with presence of a tilted X-line in the subsolar region, which is based on the component reconnection model (see Introduction).

Related to the above interpretation we note that a combined ground-satellite data study of plasma convection and particle precipitation during similar IMF conditions as in the present case has been reported by *Coleman et al.* [2001]. Their data set was found to be consistent with antiparallel, steady state merging, as described by *Crooker* [1979] and *Luhmann et al.* [1984]. That interpretation is based on the observation of certain convection vortices involving strong equatorward flow at cusp latitudes at noon, and an ion dispersion signature consistent with steady state reconnection. In their view, the cusp is spatially bifurcated due to two spatially separated reconnection sites on the magnetopause. We find that

the auroral evolution (activation sequence) reported here, characterized by rapid auroral expansion across noon, as described above, is consistent with the presence of component reconnection in the subsolar region. This scenario is also supported by the ionospheric ion flow at noon, which is mainly westward, and definitely turns northwestward in the later phase of each event. Furthermore, the clearly stepped (or staircase) cusp, in combination with the optical data (a clear sequence of brightening/expansion events), lead us to interpret our observations in terms of a bursty reconnection process. We note, however, that in order to completely resolve the component versus antiparallel reconnection issue we need to examine more examples.

In the configuration indicated in Figure 16, characteristic of IMF $B_y > 0$ conditions, poleward moving auroral forms (PMAFs) are expected to occur in the region where the merging cell flow turns poleward in the ~ 1000 -1200 MLT sector, which is in very good agreement with the observation in our case as well as the previously reported observations. We point out the association between classical PMAFs, i.e., those emanating from cusp equatorward boundary intensifications (EBIs) and fading out ~ 500 km further north, and the poleward ion flow in the convection throat. Thus, we conclude that these poleward moving/expanding forms (Figure 3) represent a low-altitude signature of the evolution of plasma transfer/precipitation along reconnected field lines in the cusp/mantle regime/convection throat during ~ 5 -10 min long intervals following the initial EBIs. The “patch” of enhanced (~ 1 km/s) poleward convection, observed within a latitude range located ~ 500 -1000 km poleward of the cusp equatorward boundary in the late phase of the PMAFs, is then related to the addition of new open flux to the high-latitude boundary layer (mantle/lobe), as described by *Cowley and Lockwood* [1992], and the associated solar wind-magnetosphere dynamo action ($\vec{j} \cdot \vec{E} < 0$) taking place there [*Siscoe et al.*, 1991]. It has been previously documented that the fading phase of PMAFs occur within the regime of mantle precipitation [*Sandholt et al.*, 1993]. Steady-state aspects of the high-latitude

dynamo process for the actual IMF orientation (IMF $B_y > 0$) are discussed by e.g. *Taguchi et al.* [1993]. Our aurora-convection results are in good agreement with the recent study of *Provan et al.* [2002] showing that the high-latitude pulsed ionospheric flows are observed within the regime of mantle precipitation and can be considered as “fossilized signatures of dayside reconnection, observed as the field lines are being pulled antisunward by the magnetosheath flow.”

From the reported observations we may consider the partitioning of the total polar cap potential drop ($\Phi_{PC} = 80\text{--}90$ kV) among the merging and lobe convection cells, in line with the discussion in *Crooker et al.* [1998]. In the case discussed by *Crooker et al.* [1998], for an IMF pointing due west (clock angle = 90°), the merging and lobe cells contributed 65 and 25 kV, respectively. In the present case we estimate from the potential contour plots in Figures 9 and 11 that the merging and lobe cells contributed ~ 60 and 20 kV, respectively.

We note that many of the apparent “rebrightenings” at high latitudes of poleward moving auroral forms (PMAFs) in meridian scanning photometer (MSP) records [*Sandholt et al.*, 1986; *Fasel*, 1995] may be due to type 2 auroral forms expanding into the MSP field of view from the side, as exemplified by the 0835 UT case in the present study. Other, more spectacular examples of such “rebrightening” events, which occurred during similar IMF conditions as in the present case (or slightly lower clock angles), are seen in Plates 1 and 2 in *Sandholt et al.* [1998c, a, 2001] (see also *Øieroset et al.* [1997]). An interesting observation to note, which is in accordance with the present interpretation, is that these “rebrightenings”/bifurcations disappeared when the IMF clock angle increased above $\sim 135^\circ$. So, the disappearance of the PMAF/“rebrightening” phenomenon in the MSP records at 0900 UT/1200 MLT in the present case may be due to a combination of two effects, one being a spatial and the other a temporal structure: i) the MSP moved out of the convection throat, and ii) the IMF rotated further south (beyond 135° clock angle), giving rise to a reconfiguration of the convection pattern, which approached a more symmetrical two-cell configuration (see *Huang*

et al. [2000]). If we then briefly return to the auroral condition at 0800-0815 UT (Figure 3), when IMF B_z was close to zero (clock angle $\sim 90^\circ$), the highest-latitude form represents the type 2 aurora and the lobe cell when its focus was located closer to midday and at higher latitude, in agreement with the results of *Huang et al.* [2000].

Finally, we point out that the rather broad energy spectrum (~ 30 -600 eV; occasionally reaching above 1keV) of the highly structured electron precipitation (latitudinally separated current filaments) permeating the cusp region (see Figure 13) is consistent with the presence of long auroral rays, spanning much of the altitude range ~ 120 -400 km, which is so characteristic for this locale.

Acknowledgments. We thank Bjørn Lybekk and Espen Trondsen for technical assistance during the collection and with the presentation of the optical data. The IMAGE magnetometer data used in this paper were collected as a German-Finnish-Polish-Norwegian project conducted by the Technical University of Braunschweig and the Finnish Meteorological Institute. The auroral observation program on Svalbard is supported by the Norwegian Research Council, AFOSR Task 2311AS, and the Norwegian Polar Research Institute. The CUTLASS radar is funded by the Particle Physics and Astronomy Research Council on grant PPA/R/R/1997/00256. SWHC and SEM are supported by PPARC Senior Fellowship PPA/N/S/2000/00197. CJF is supported by NASA grant NAG 5-2834 and NASA Living with a Star Grant Nag 5-10883.

References

- Coleman, I. J., G. Chisham, M. Pinnock, and M. P. Freeman, An ionospheric convection signature of antiparallel reconnection, *J. Geophys. Res.*, **106**, 28,995, 2001.
- Cowley, S. W. H., Magnetospheric asymmetries associated with the Y-component of the IMF, *Planet. Space Sci.*, **29**, 79, 1981.
- Cowley, S. W. H., Solar wind control of magnetospheric convection, in *Achievements of the International Magnetospheric Study (IMS)*, no. SP-217 in ESA Special Publ., pp. 483–494, ESA (European Space Agency), Noordwijk, The Netherlands, 1984.
- Cowley, S. W. H., Excitation of flow in the Earth's magnetosphere-ionosphere system: Observations by incoherent-scatter radar, in *Polar Cap Boundary Phenomena*, edited by J. Moen, A. Egeland, and M. Lockwood, vol. 509 of *NATO ASI Series C*, pp. 127–140, Kluwer Academic Publishers, Dordrecht, Holland, 1998.
- Cowley, S. W. H., and M. Lockwood, Excitation and decay of solar wind-driven flows in the magnetosphere-ionosphere system, *Ann. Geophys.*, **10**, 103, 1992.
- Cowley, S. W. H., J. P. Morelli, and M. Lockwood, Dependence of convective flows and particle precipitation in the high-latitude dayside ionosphere on the X and Y components of the interplanetary magnetic field, *J. Geophys. Res.*, **96**, 5557, 1991.
- Crooker, N. U., J. G. Lyon, and J. A. Fedder, MHD model merging with IMF B_y : Lobe cells, sunward polar cap convection, and overdraped lobes, *J. Geophys. Res.*, **103**, 9143, 1998.
- Crooker, U., N. Dayside merging and cusp geometry, *J. Geophys. Res.*, **84**, 951, 1979.
- Eriksson, S., J. W. Bonnell, L. G. Blomberg, R. E. Ergun, G. T. Marklund, and C. W. Carlson, Lobe cell convection and field-aligned currents poleward of the Region 1 current system, *J. Geophys. Res.*, 2002, in press.
- Escoubet, C. P., M. F. Smith, S. F. Fung, P. C. Anderson, R. A. Hoffman, E. M. Basinska, and J. M. Bosqued, Staircase ion signature in the polar cusp: A case study, *Geophys. Res. Lett.*, **19**, 1735, 1992.
- Farrugia, C. J., P. E. Sandholt, W. F. Denig, and R. B. Torbert, Observation of a correspondence between poleward-moving auroral forms and stepped cusp ion precipitation, *J. Geophys. Res.*, **103**, 9309, 1998.

- Fasel, G., Dayside poleward moving auroral forms: A statistical study, *J. Geophys. Res.*, **100**, 11,891, 1995.
- Freeman, M. P., C. J. Farrugia, M. R. Burlaga, L. F. Hairston, M. E. Greenspan, J. M. Ruohoniemi, and R. P. Lepping, The interaction of a magnetic cloud with the Earth: Ionospheric convection in the northern and southern hemispheres for a wide range of quasi-steady interplanetary magnetic field conditions, *J. Geophys. Res.*, **98**, 7633–7655, 1993.
- Gonzalez, W. D., and F. Mozer, A quantitative model for the potential resulting from reconnection with an arbitrary interplanetary magnetic field, *J. Geophys. Res.*, **79**, 4186, 1974.
- Greenwald, R. A., J. M. Ruohoniemi, K. Baker, W. A. Bristow, G. J. Sofko, J. P. Villain, M. Lester, and J. Slavin, Convective response to a transient increase in dayside reconnection, *J. Geophys. Res.*, **104**, 10,007, 1999.
- Greenwald, R. A., et al., DARN/SUPERDARN, *Space Sci. Rev.*, **71**, 761, 1995.
- Huang, C.-S., D. Murr, G. J. Sofko, W. J. Hughes, and T. Moretto, Ionospheric convection response to changes of interplanetary magnetic field B_z component during strong B_y component, *J. Geophys. Res.*, **105**, 5231, 2000.
- Kawano, H., and C. Russell, Survey of flux transfer events observed with the ISEE 1 spacecraft: Dependence on the interplanetary magnetic field, *J. Geophys. Res.*, **102**, 11,307, 1997.
- Knipp, D. J., et al., Ionospheric convection response to slow, strong variations in a northward interplanetary magnetic field: A case study for January 14, 1988, *J. Geophys. Res.*, **98**, 19,273, 1993.
- Lockwood, M., P. E. Sandholt, S. W. H. Cowley, and T. Oguti, Interplanetary magnetic field control of dayside auroral activity and the transfer of momentum across the dayside magnetopause, *Planet. Space Sci.*, **37**, 1347, 1989.
- Lockwood, M., S. E. Milan, T. Onsager, C. H. Perry, J. A. Scudder, C. T. Russell, and M. Brittnacher, Cusp ion steps, field-aligned currents and poleward moving auroral forms, *J. Geophys. Res.*, **106**, 29,555, 2001.

- Lu, G., et al., Interhemispheric asymmetry of the high-latitude ionospheric convection pattern, *J. Geophys. Res.*, *99*, 6491–6510, 1994.
- Luhmann, J. G., R. J. Walker, C. T. Russell, N. U. Crooker, J. R. Spreiter, and S. S. Stahara, Patterns of potential magnetic field merging sites on the dayside magnetopause, *J. Geophys. Res.*, *89*, 1739, 1984.
- Marcucci, M. F., et al., Evidence for interplanetary magnetic field B_y controlled large-scale reconnection at the dayside magnetopause, *J. Geophys. Res.*, *105*, 27,497, 2000.
- Maynard, N. C., W. J. Burke, P. E. Sandholt, J. Moen, D. M. Ober, M. Lester, D. R. Weimer, and A. Egeland, Observations of simultaneous effects of merging in both hemispheres, *J. Geophys. Res.*, *106*, 2001, 24551.
- Milan, S., M. Lester, S. W. H. Cowley, and M. Brittnacher, Convection and auroral response to a southward turning of the IMF: Polar UVI, CUTLASS and IMAGE signatures of transient flux transfer at the magnetopause, *J. Geophys. Res.*, *105*, 15 741, 2000.
- Moen, J., A. P. van Eyken, and H. C. Carlson, EISCAT Svalbard Radar observations of ionospheric plasma dynamics in relation to dayside auroral transients, *J. Geophys. Res.*, *106*, 21,453, 2001.
- Neudegg, D. A., et al., The UV aurora and ionospheric flows during flux transfer events, *Ann. Geophys.*, *19*, 179, 2001.
- Newell, P. T., C.-I. Meng, D. Sibeck, and R. Lepping, Some low-altitude cusp dependencies on the interplanetary magnetic field, *J. Geophys. Res.*, *94*, 8921, 1989.
- Øieroset, M., P. E. Sandholt, H. Luhr, W. Denig, and T. Moretto, Auroral and geomagnetic events at cusp/mantle latitudes in the prenoon sector during positive IMF B_y conditions: Signatures of pulsed magnetopause reconnection, *J. Geophys. Res.*, *102*, 7191, 1997.
- Popescu, D., J.-A. Sauvaud, A. Fedorov, E. Budnik, H. Stenuit, and T. Moreau, Evidence for a sunward flowing plasma layer adjacent to the tail high-latitude magnetopause during dawnward directed interplanetary field, *J. Geophys. Res.*, *106*, 29,479, 2001.
- Provan, G., T. K. Yeoman, and S. W. H. Cowley, The influence of the IMF B_y component

- on the location of pulsed flows in the dayside ionosphere observed by an HF radar, *Geophys. Res. Lett.*, *26*, 521, 1999.
- Provan, G., S. E. Milan, M. Lester, T. K. Yeoman, and H. Khan, Simultaneous observations of the ionospheric footprint of flux transfer events and dispersed ion signatures, *Ann. Geophys.*, *20*, 281, 2002.
- Reiff, P. H., and J. L. Burch, IMF B_y -dependent dayside plasma flow and Birkeland currents in the dayside magnetosphere, 2, A global model for northward and southward IMF, *J. Geophys. Res.*, *90*, 1595, 1985.
- Rodger, A. S., I. J. Coleman, and M. Pinnock, Some comments on transient and steady-state reconnection at the dayside magnetopause, *Geophys. Res. Lett.*, *27*, 1359, 2000.
- Ruohoniemi, J. M., and K. B. Baker, Large-scale imaging of high-latitude convection with Super Dual Auroral Radar Network HF radar observations, *J. Geophys. Res.*, *103*, 20,797, 1998.
- Russell, C. T., and R. C. Elphic, Initial ISEE magnetometer results: Magnetopause observations, *Space Sci. Rev.*, *22*, 681, 1978.
- Sandholt, P. E., and C. J. Farrugia, On the dynamic cusp aurora and IMF B_y , *J. Geophys. Res.*, *104*, 12,461, 1999.
- Sandholt, P. E., C. S. Deehr, A. Egeland, B. Lybekk, R. Viereck, and G. J. Romick, Signatures in the dayside aurora of plasma transfer from the magnetosheath, *J. Geophys. Res.*, *91*, 10,063, 1986.
- Sandholt, P. E., B. Jacobsen, B. Lybekk, A. Egeland, P. F. Bythrow, and D. A. Hardy, Electrodynamics of the polar cusp ionosphere: A case study, *J. Geophys. Res.*, *94*, 6713, 1989.
- Sandholt, P. E., J. Moen, A. Rudland, D. Opsvik, W. F. Denig, and T. Hansen, Auroral event sequences at the dayside polar cap boundary for positive and negative interplanetary magnetic field B_y , *J. Geophys. Res.*, *98*, 7737, 1993.
- Sandholt, P. E., C. J. Farrugia, and S. W. H. Cowley, Pulsating cusp aurora for northward IMF, *J. Geophys. Res.*, *103*, 26,507, 1998a.

- Sandholt, P. E., C. J. Farrugia, J. Moen, and S. W. H. Cowley, Dayside auroral configurations: Responses to southward and northward rotations of the interplanetary magnetic field, *J. Geophys. Res.*, *103*, 20,279, 1998b.
- Sandholt, P. E., C. J. Farrugia, J. Moen, S. W. H. Cowley, and B. Lybekk, Dynamics of the aurora and associated convection currents during a cusp bifurcation event, *Geophys. Res. Lett.*, *25*, 4313, 1998c.
- Sandholt, P. E., C. J. Farrugia, S. W. H. Cowley, and M. Lester, Dayside auroral bifurcation sequence during B_y -dominated interplanetary magnetic field: Relationship with merging and lobe convection cells, *J. Geophys. Res.*, *106*, 15,429, 2001.
- Sandholt, P. E., W. F. Denig, C. J. Farrugia, B. Lybekk, and T. E., Auroral structure at the cusp equatorward boundary: Relationship with the electron edge of low-latitude boundary layer precipitation, *J. Geophys. Res.*, p. in press, 2002.
- Siscoe, G. L., W. Lotko, and B. U. O. Sonnerup, A high-latitude, low-latitude boundary layer model of the convection current system, *J. Geophys. Res.*, *96*, 3487, 1991.
- Siscoe, G. L., G. M. Erickson, B. U. O. Sonnerup, N. C. Maynard, K. D. Siebert, D. R. Weimer, and W. W. White, Global role of E_{\parallel} in magnetopause reconnection: An explicit demonstration, *J. Geophys. Res.*, *106*, 13,015, 2001.
- Sonnerup, B. U. O., Magnetic field line reconnection at the magnetopause: An overview, in *Magnetic reconnection in Space and Laboratory Plasmas*, edited by E. W. Hones, vol. 30 of *Geophysical Monograph*, pp. 92-103, AGU, Washington, D. C., 1984.
- Taguchi, S., M. Sugiura, J. D. Winningham, and J. Slavin, Characterization of the IMF B_y -dependent field-aligned currents in the cleft region based on DE 2 observations, *J. Geophys. Res.*, *98*, 1393, 1993.
- Weimer, D. R., Maps of ionospheric field-aligned currents as a function of the interplanetary magnetic field derived from Dynamics Explorer 2 data, *J. Geophys. Res.*, *106*, 12,889, 2001.
- Weiss, L. A., P. H. Reiff, E. J. Weber, H. C. Carlson, M. Lockwood, and W. K. Peterson, Flow-aligned jets in the magnetospheric cusp: Results from the geospace environment modeling pilot program, *J. Geophys. Res.*, *100*, 7 649, 1995.

- White, W., G. L. Siscoe, G. M. Erickson, Z. Kaymaz, N. C. Maynard, K. D. Siebert, B. U. O. Sonnerup, and D. R. Weimer, The magnetospheric sash and the cross-tails, *Geophys. Res. Lett.*, *25*, 1605, 1998.
- Wing, S., P. T. Newell, and J. M. Ruohoniemi, Double cusp: Model prediction and observational verification, *J. Geophys. Res.*, *106*, 25571.
- Yeoman, T. K., M. Lester, S. W. H. Cowley, S. E. Milan, J. Moen, and P. E. Sandholt, Simultaneous observations of the cusp in optical, DMSP and HF radar data, *Geophys. Res. Lett.*, *24*, 2251, 1997.

S. W. H. Cowley, M. Lester and S. E. Milan, Department of Physics and Astronomy, University of Leicester, Leicester LE1 7RH, United Kingdom.
(e-mail:swhc1@ion.le.ac.uk)

W. F. Denig, Space Vehicles Directorate, Air Force Research Laboratory, Mass.

S. Eriksson, Laboratory for Atmospheric and Space Physics University of Colorado, 1234 Innovation Drive, Boulder, CO. 80303

C. J. Farrugia, Space Science Center, University of New Hampshire, Durham, NH 03824. (e-mail:FERRUGIA@unhed2.sr.unh.edu)

J. Moen and P. E. Sandholt, Department of Physics, University of Oslo, P. O. Box 1048, Blindern, N-0316, Norway. (e-mail:p.e.sandholt@fys.uio.no).

C. Valladares, Institute for Scientific Research, Boston College, Newton Center, MA, USA

Received

This manuscript was prepared with AGU's \LaTeX macros v4, with the extension package 'AGU++' by P. W. Daly, version 1.5f from 1998/07/16.

Figure Captions

Figure 1. Interplanetary magnetic field (IMF) and solar wind plasma data obtained from spacecraft IMP8 during the interval 0600-1100 UT on January 14, 1999. Panels from top to bottom show proton density, bulk speed, proton temperature, dynamic pressure, field intensity, and GSM X, Y, and Z components, and the clock angle. IMF regimes are marked by vertical guidelines (see text).

Figure 2. Schematic overview of the observations of aurora (hatched areas) and convection (with merging (M) and lobe (L) cells), representing the interval 0833-0838 UT on Jan. 14, 1999. The coordinate system is magnetic local time (MLT)/ magnetic latitude (MLAT). Approximate fields of view of auroral all-sky imagers at Ny Ålesund, Svalbard and Heiss Island, Russia, are marked by circles. Arrowed meridional line indicate the field of view of the meridian scanning photometer (MSP) in Ny Ålesund (76.1°MLAT). Beams 4, 9, and 14 of the CUTLASS Finland radar are indicated as well as different auroral forms.

Figure 3. Meridian scanning photometer line of sight intensities versus zenith angle, at 630.0 nm (a) and 557.7 nm (b), for the interval 0800-0900 UT on January 14, 1999. Intensities are colour-coded according to the scale at the bottom.

Figure 4. Meridian scanning photometer line of sight intensities versus zenith angle, at 630.0 nm, for the interval 0800-1000 UT on January 14, 1999. Intensities are colour-coded according to the scale at the bottom.

Figure 5. Ny Ålesund all-sky camera images at 630.0 nm taken at 0831:31; 0832:31; 0833:31; 0834:03; 0835:31; 0836:31, 0837:31, 0838:31, and 0839:31 UT. Each image is projected to an altitude of 250 km and shown on the background of a geographic coordinate system. The 70° and 80° latitude circle and meridians separated by 10° are shown.

Figure 6. Heiss Island all-sky camera images at 630.0 nm taken at 0829:19; 0830:29; 0831:38; 0832:46; 0833:56; 0835:05; 0836:17; 0837:28; and 0838:40 UT, projected to an altitude of 250 km and shown on the background of a geographic coordinate system. Same format as in Figure 5.

Figure 7. Line of sight ion drift velocities as a function of magnetic latitude and time, obtained from beams 4, 9, and 14 of the CUTLASS HF radar during 0800-0900 UT. Velocities are colour-coded according to the scales to the right. Four successive auroral brightening events are marked by vertical guidelines at 0825, 0835, 0841, and 0848 UT.

Figure 8. Cutlass spatial plot of line of sight velocities from all 14 beams for the interval 0832-0842 UT. Velocities are color coded according to the scale to the right. Superimposed are plasma flow streamlines. The coordinate system is MLT/MLAT. 12 MLT is at the top. Latitude circles at 60, 70, and 80° MLAT are shown.

Figure 9. SuperDARN vector plot for the center time of the main event under study (0834-0836 UT) in MLT/MLAT coordinates. Ion drift vectors are plotted in MLT/MLAT coordinates. Fields of view of the optical instruments in Ny Ålesund and at Heiss Island are indicated by circles and arrowed meridional line. The latter marks the FOV of the MSP in Ny Ålesund. The locations of auroral forms called types 1 and 2 are indicated.

Figure 10. SuperDARN streamline plot with the 630.0 nm aurora superimposed for 0836 UT. The aurora is obtained from all-sky imagers at Heiss Island, Russia and Ny Ålesund, Svalbard. The red line emission is projected to an altitude of 250 km. The coordinate system is MLT/MLAT.

Figure 11. SuperDARN vector plot for the interval 0836-0838 UT. Same format as in the previous figure.

Figure 12. SuperDARN vector plot for the interval 0838-0840 UT. Same format as in the previous figure. The trajectory of spacecraft DMSP F14 during the interval 0836-0842 UT is inserted as well as the field of view of the MSP in Ny Ålesund (meridional double-arrowed line).

Figure 13. Particle spectrograms, ionospheric ion drift and magnetic deflections obtained from spacecraft DMSP F14 during the interval 0833-0842 UT on January 14, 1999. Panels 1 and 2 show differential particle flux (electrons and ions) and average energy, respectively. Panels 3 and 4 show color coded particle spectrograms for electrons and ions, respectively. Panel 5 show ion drift in the horizontal (cross track; violet) and vertical (upward; green) directions. Panel 6 shows the horizontal magnetic field deflection components along (DB_Y) and normal (DB_Z) to the satellite track.

Figure 14. Panels A, B, C, and D show SuperDARN vector plots for the intervals 0842-0844, 0844-0846, 0846-0848, and 0848-0850 UT, respectively. Same format as in the previous figure. The MSP field of view and the approximate latitudinal extent of the aurora are marked by double-arrowed meridional line and bars, respectively, in panels C and D.

Figure 15. Magnetometer data from the IMAGE chain of magnetometers in Svalbard and Scandinavia. Panels from top to bottom show X-component traces from stations Ny Ålesund (NAL; 76.1°MLAT; optical site), Longyearbyen (LYR; 75.1°MLAT), Hornsund (HOR; 74.0°MLAT), Hopen (HOP; 72.9°MLAT), Bear Island (BJN; 71.3°MLAT), Sørøya (SOR; 67.3°MLAT), Kilpisjärvi (KIL; 65.9°MLAT), Pello (PEL; 63.6°MLAT), and Lycksele (LYC; 61.4°MLAT).

Figure 16. The upper panel shows a schematical illustration of magnetic field lines just inside the magnetopause which are tilted over in the direction of IMF B_y . Reconnection line is marked by dashed tilted line. North is up and the dawn side is to the left. The lower panel shows the corresponding convection pattern with cusp auroral precipitations. 1200 MLT is up and the dusk side is to the left. Open arrows mark the westward expansions of the two components of the bifurcated cusp aurora associated with activations of merging and lobe convection cells. The ionospheric footprint of the merging line is marked by dashed curved line. The dotted line marks the open-closed field line boundary.

IMP8 January 14, 1999 (GSM)

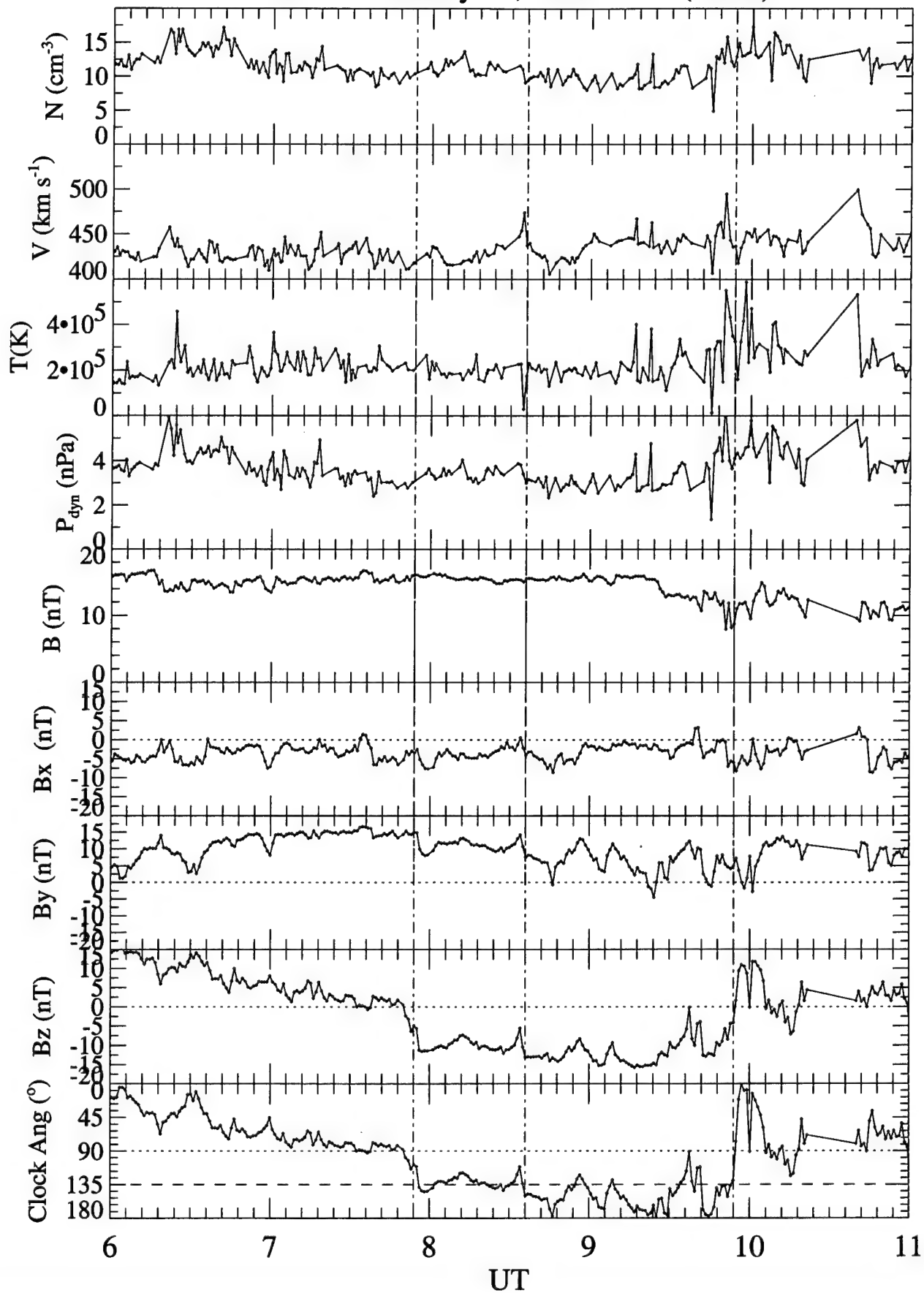


Figure 1

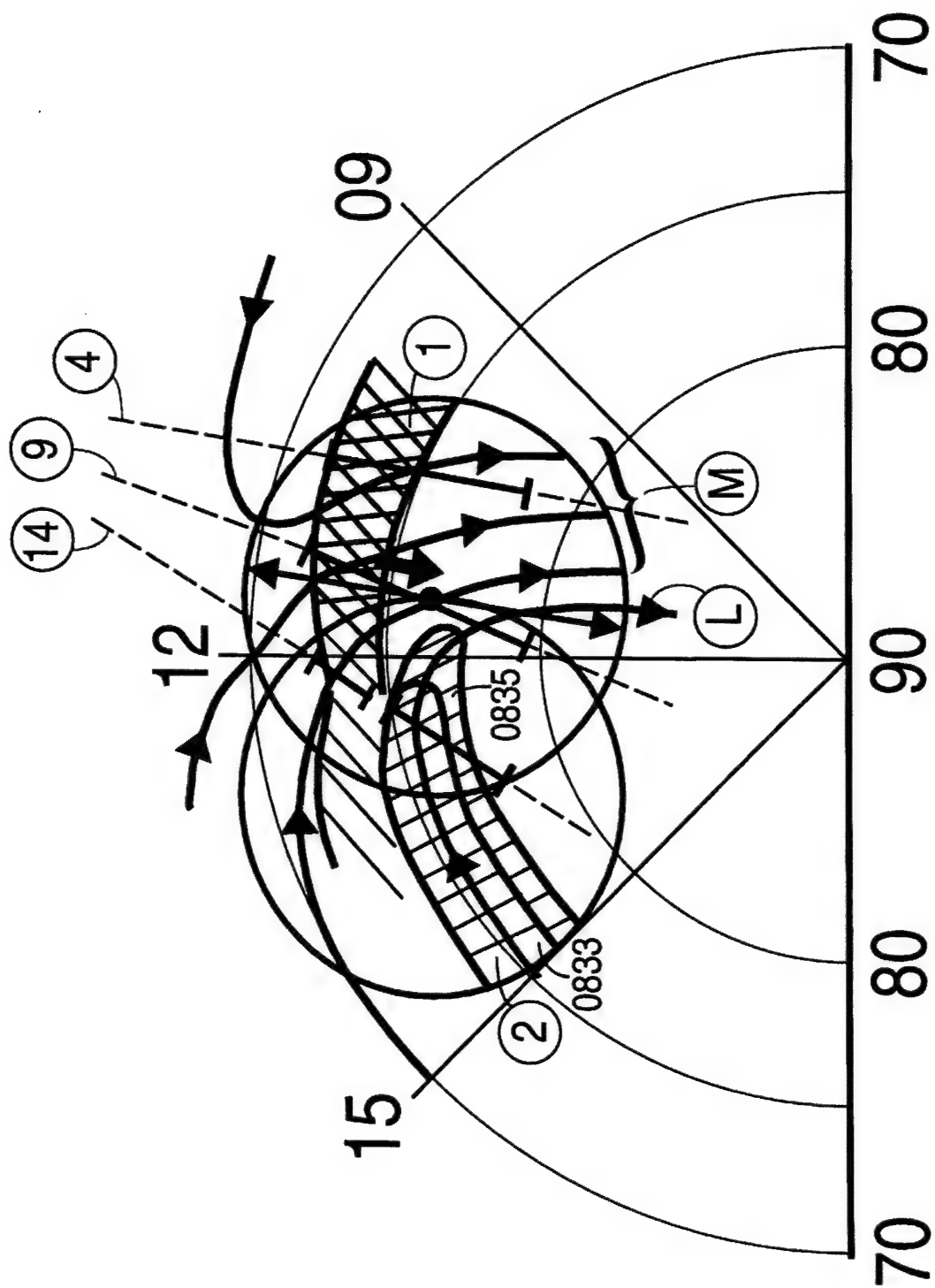
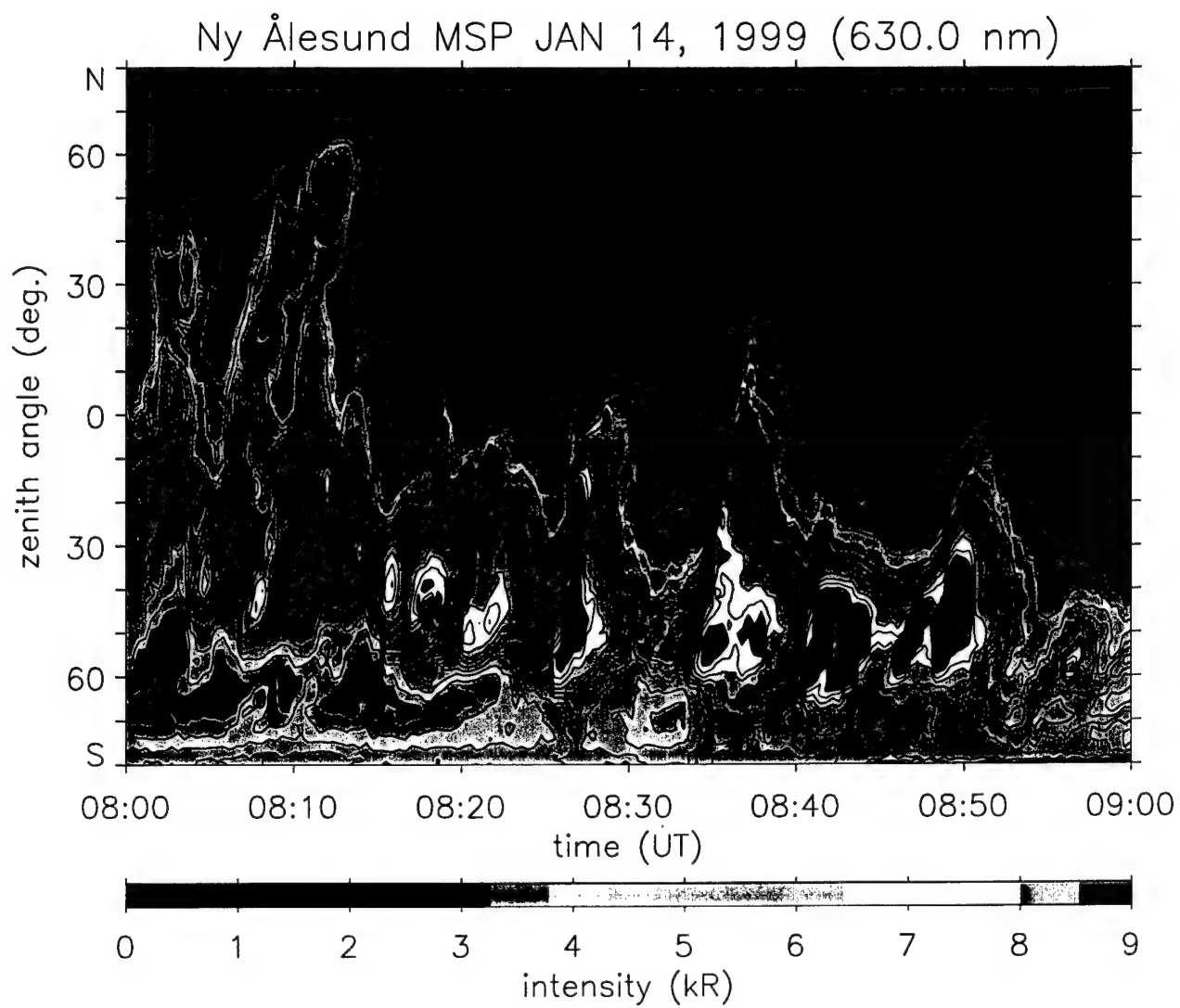


Figure 2



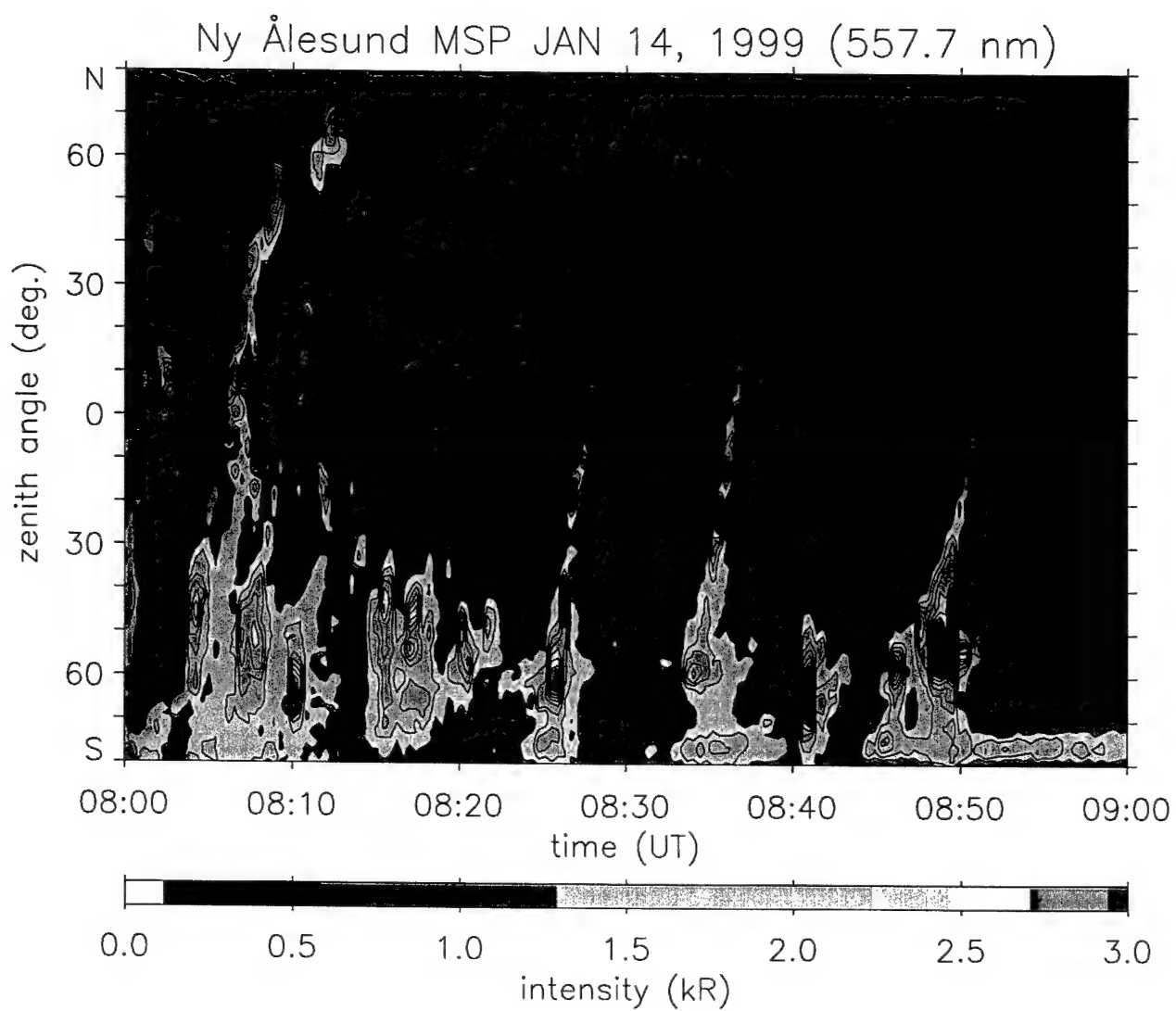
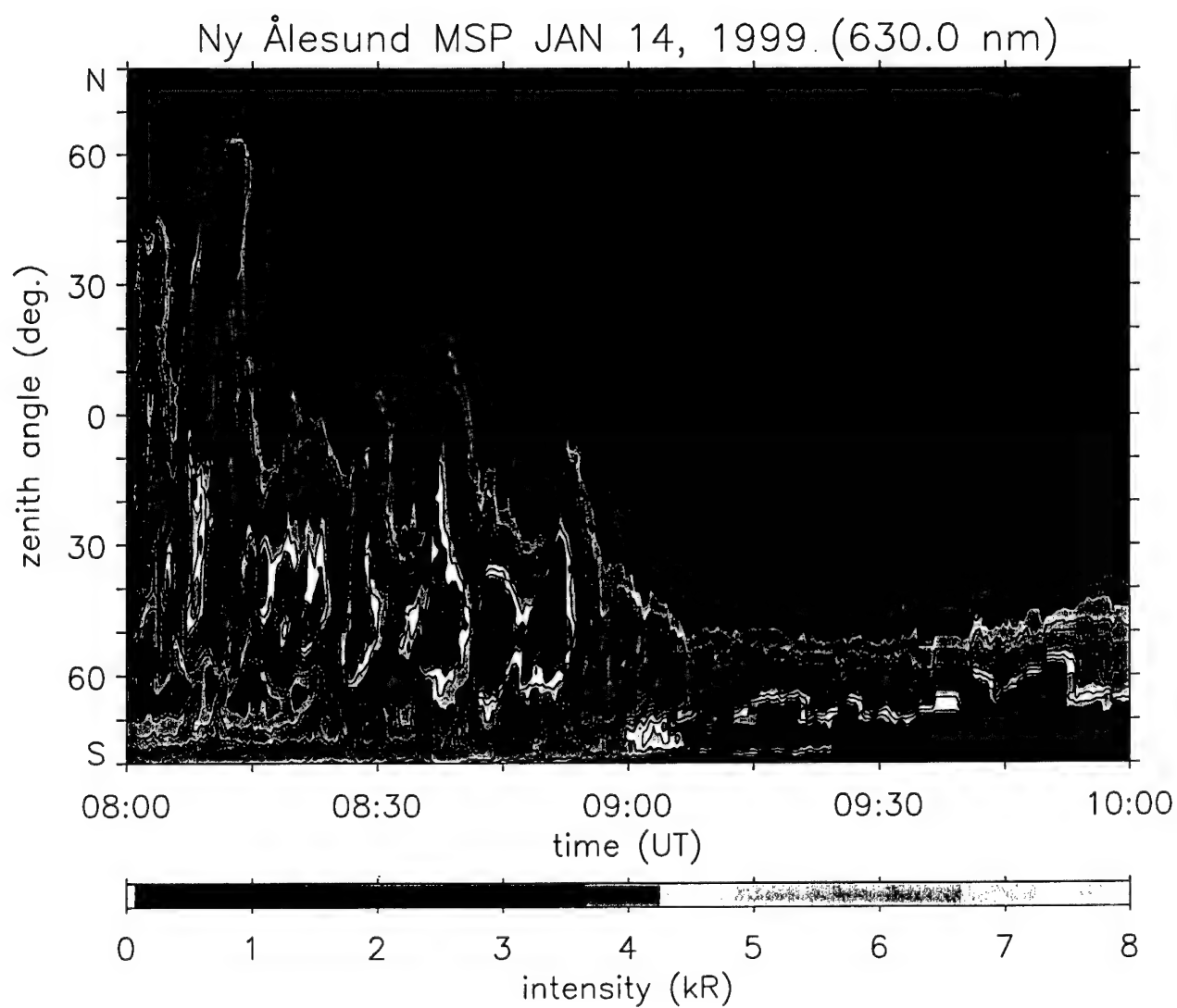


Figure 3b



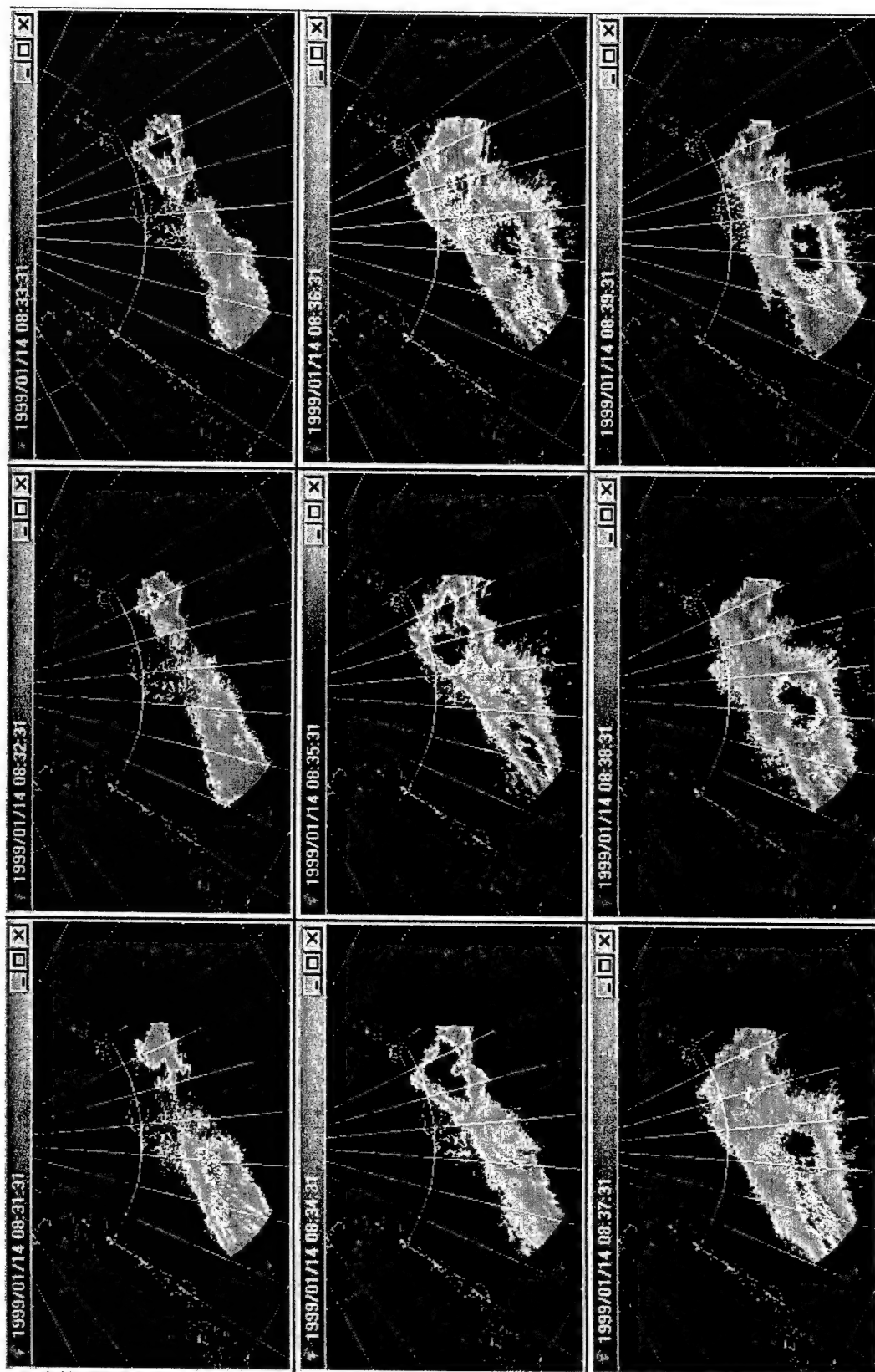
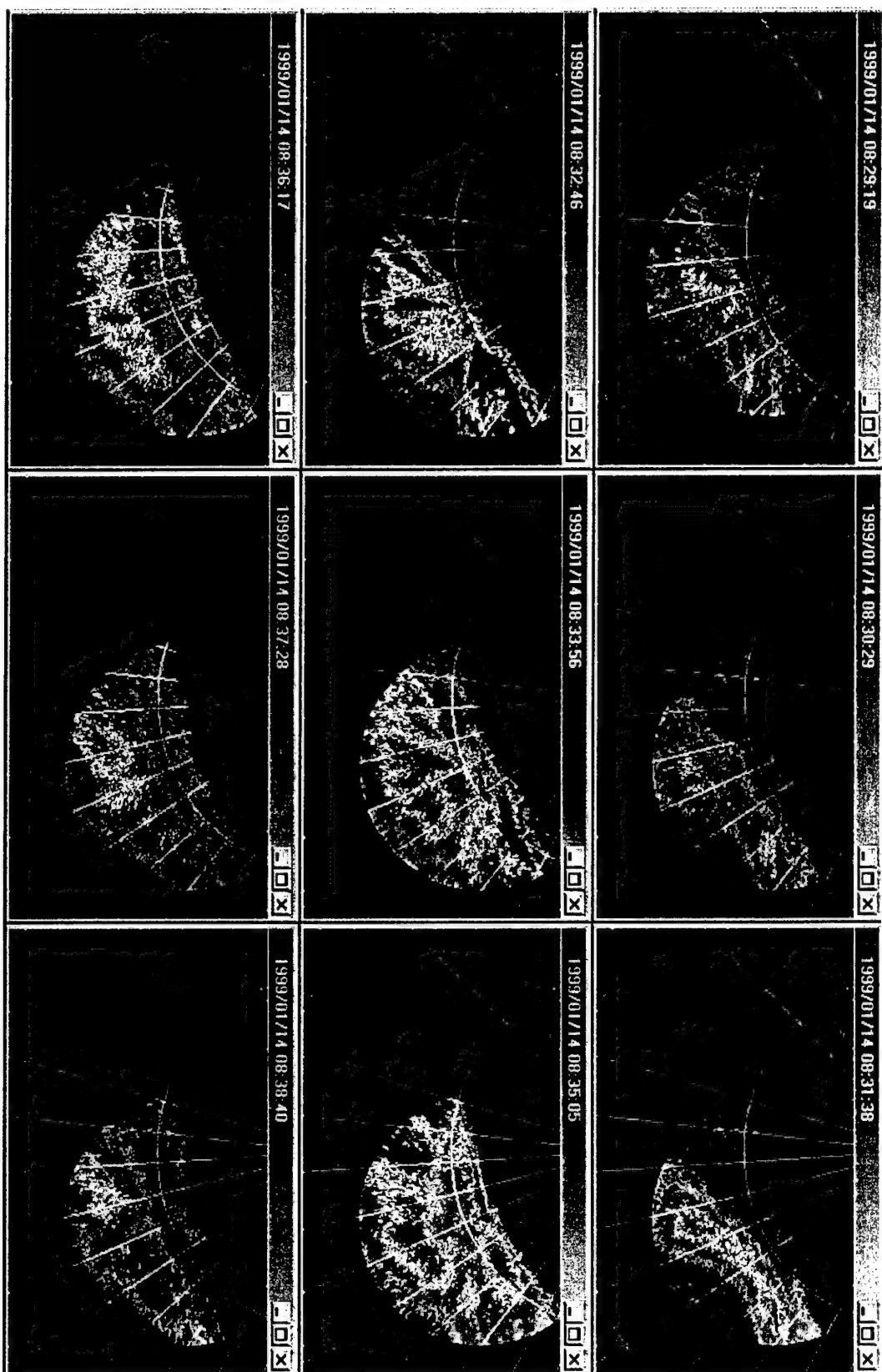


Figure 5

2

• 1 • 3

Figure 9



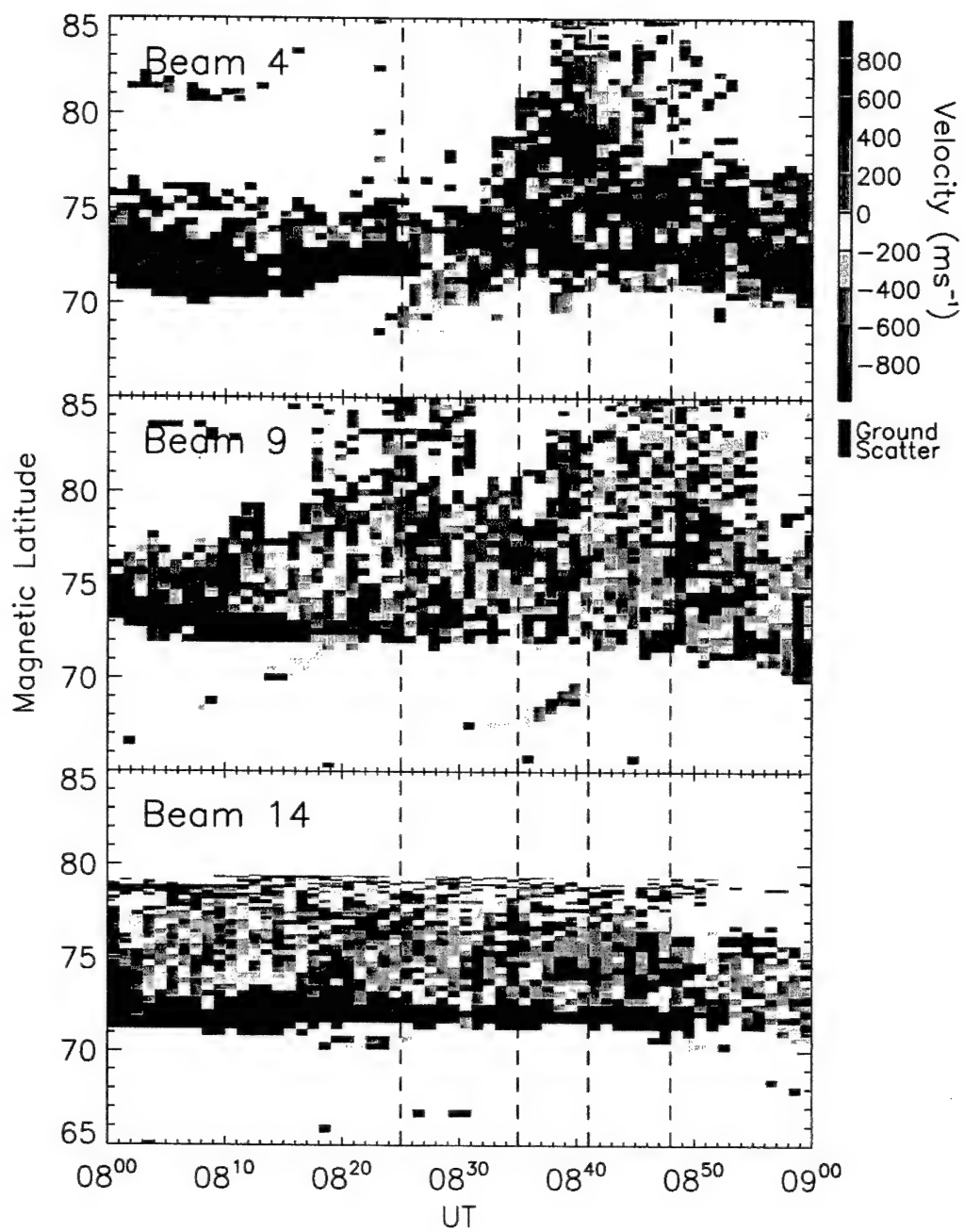


Figure 7

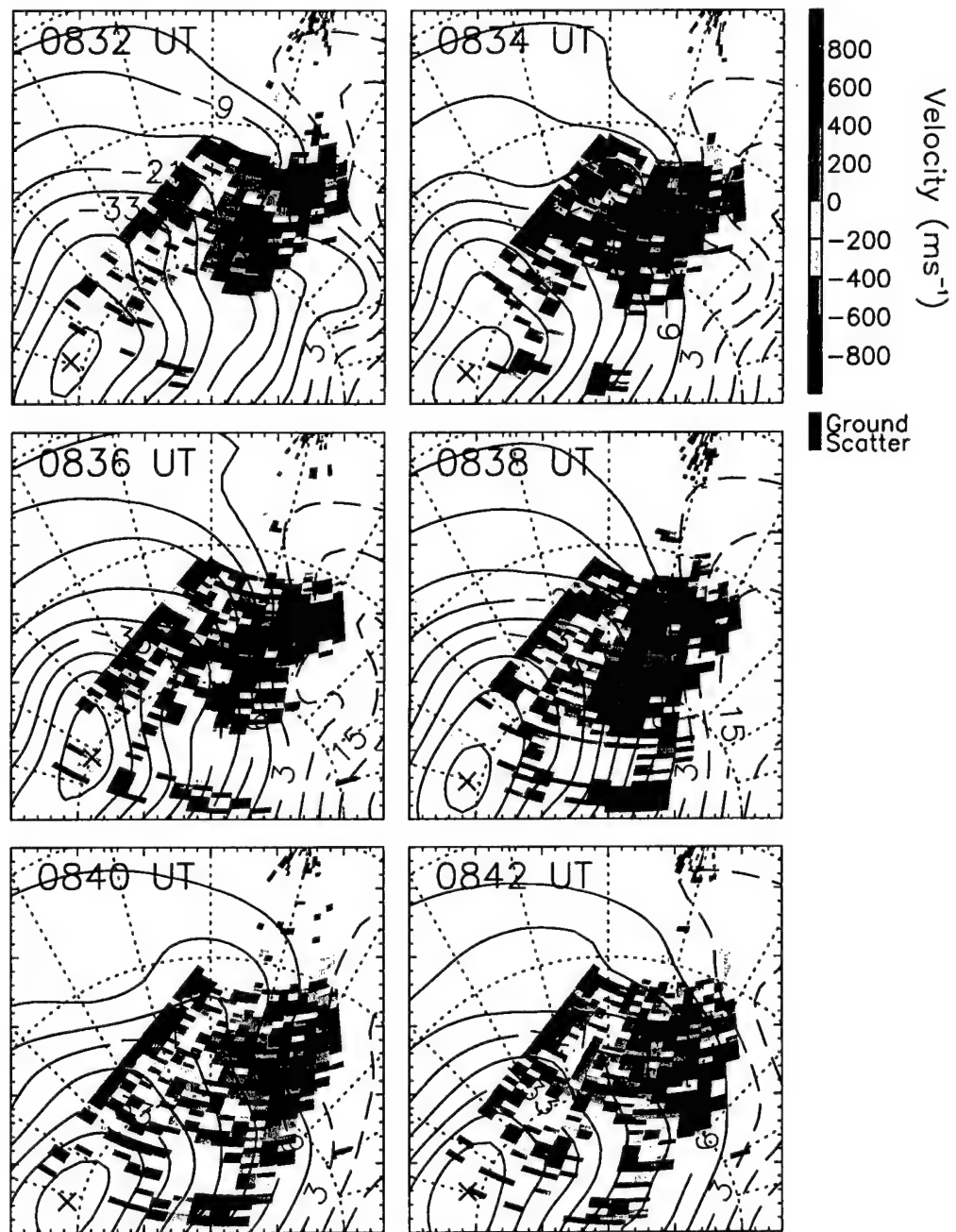
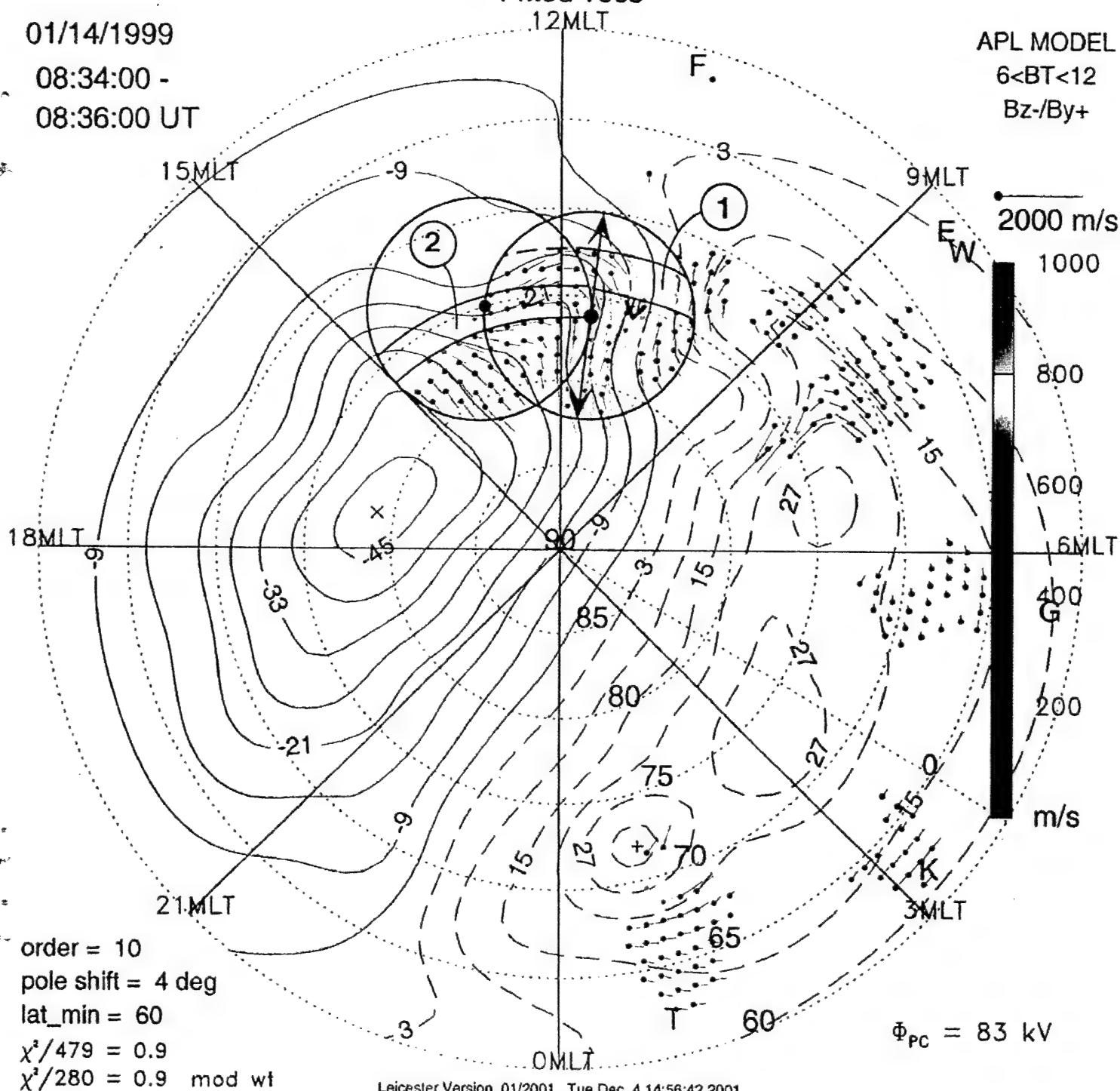


Figure 8

01/14/1999
08:34:00 -
08:36:00 UT

Fitted vecs

APL MODEL
6<BT<12
Bz-/By+



14 January 1999

0836 UT

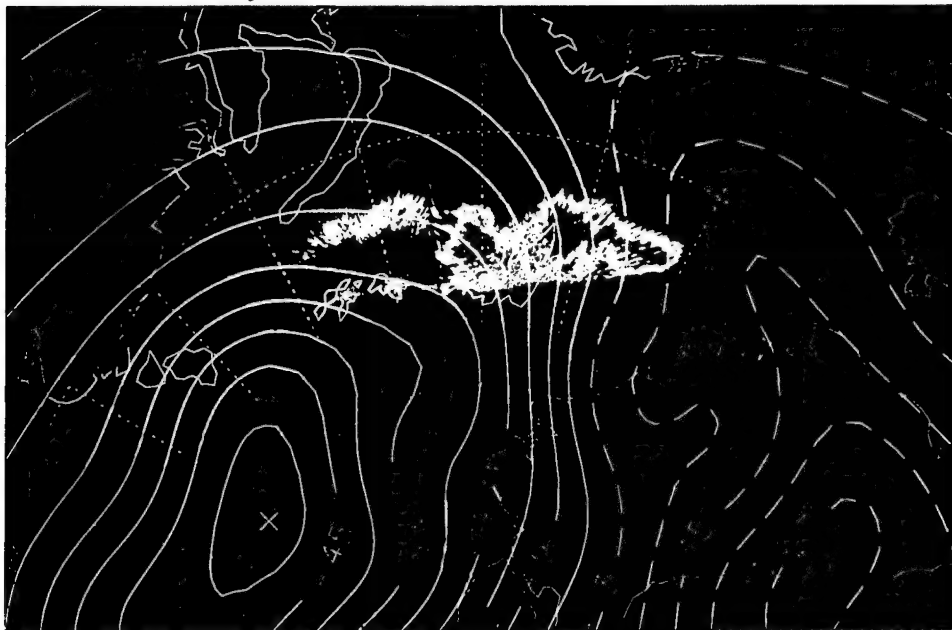


Figure 10

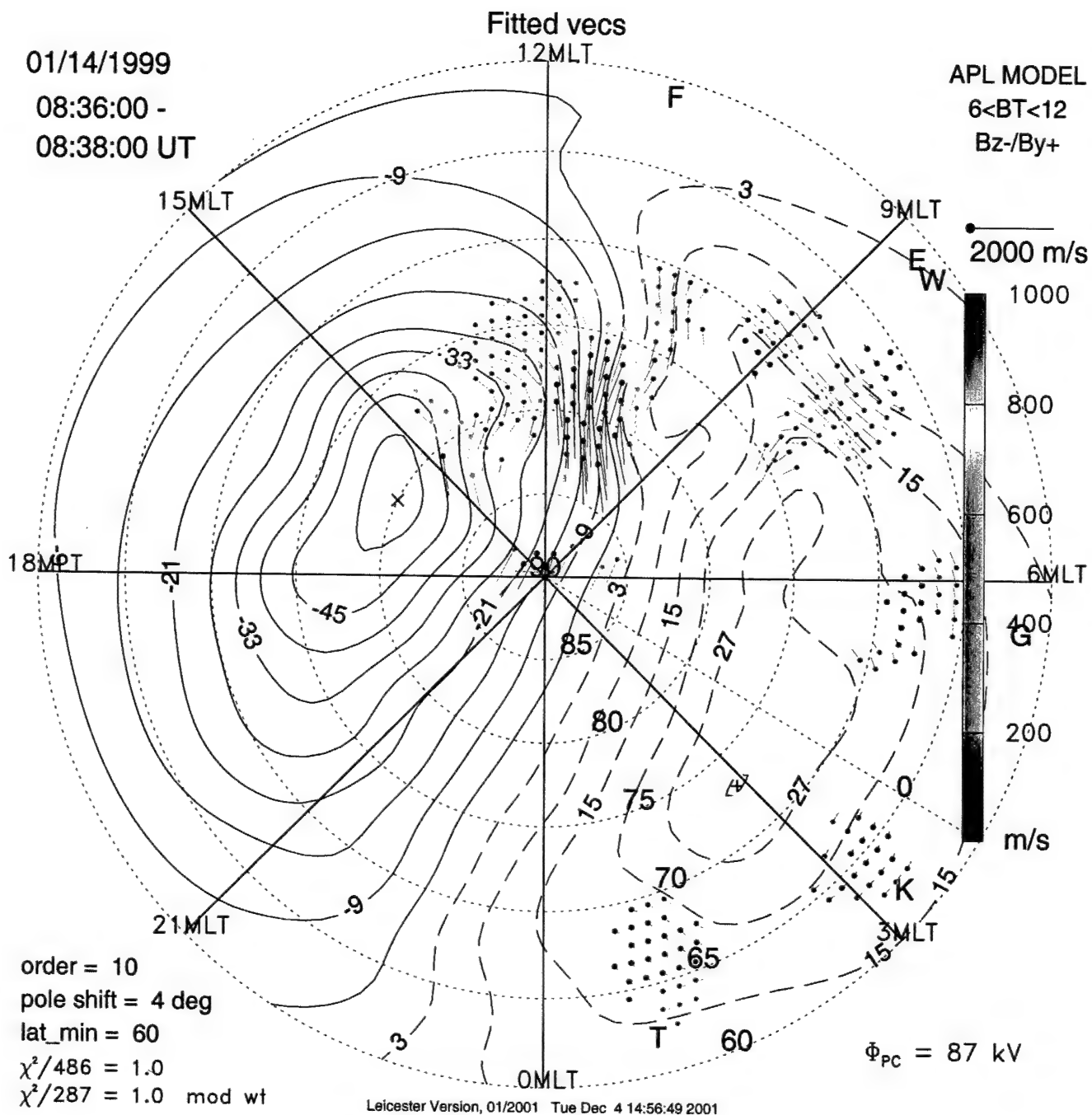


Figure 11

Fitted vecs **F14**
...12MLT

APL MODEL
6<BT<12
Bz-/By+

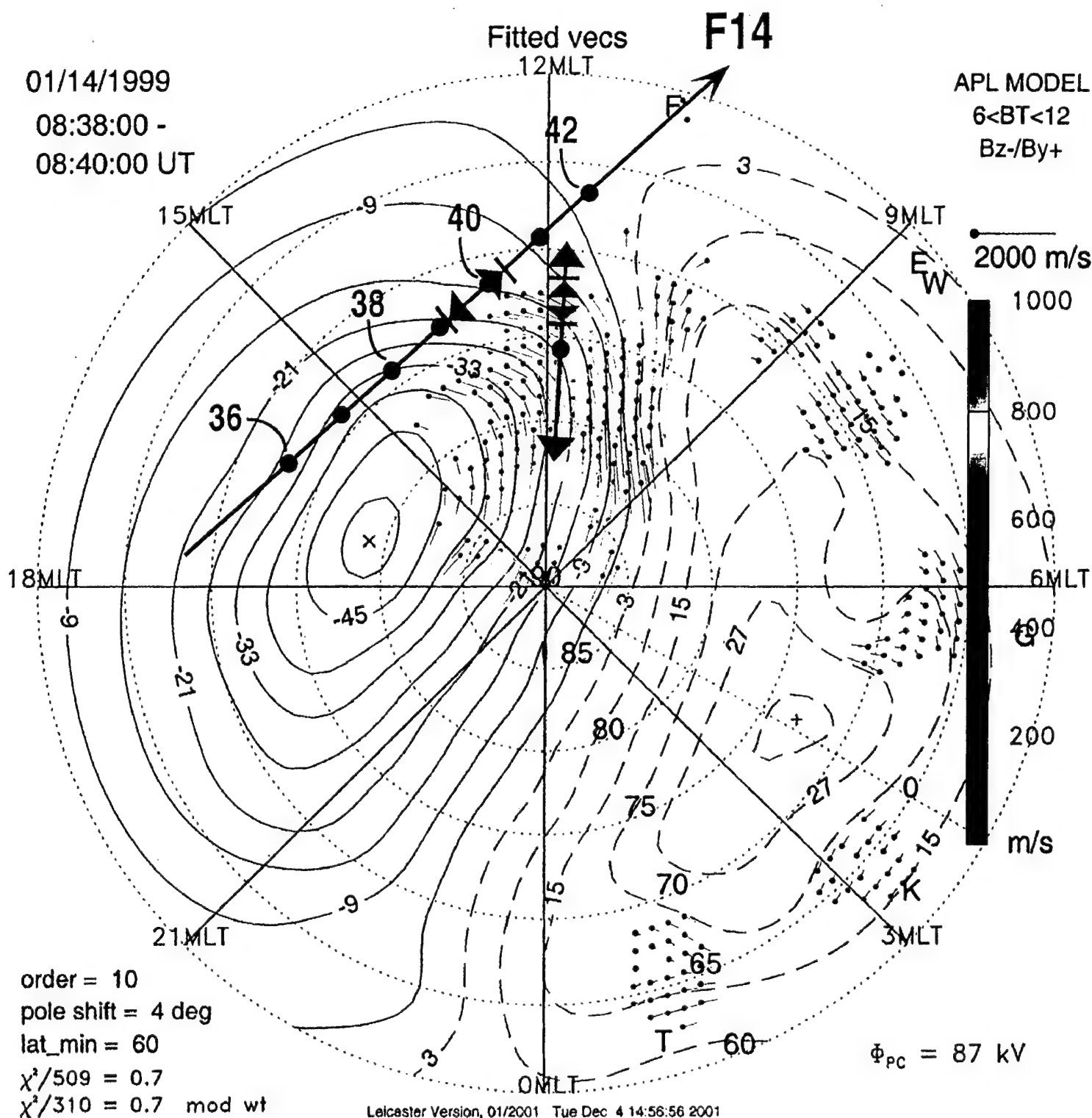


Figure 12

F14

14 Jan 1999

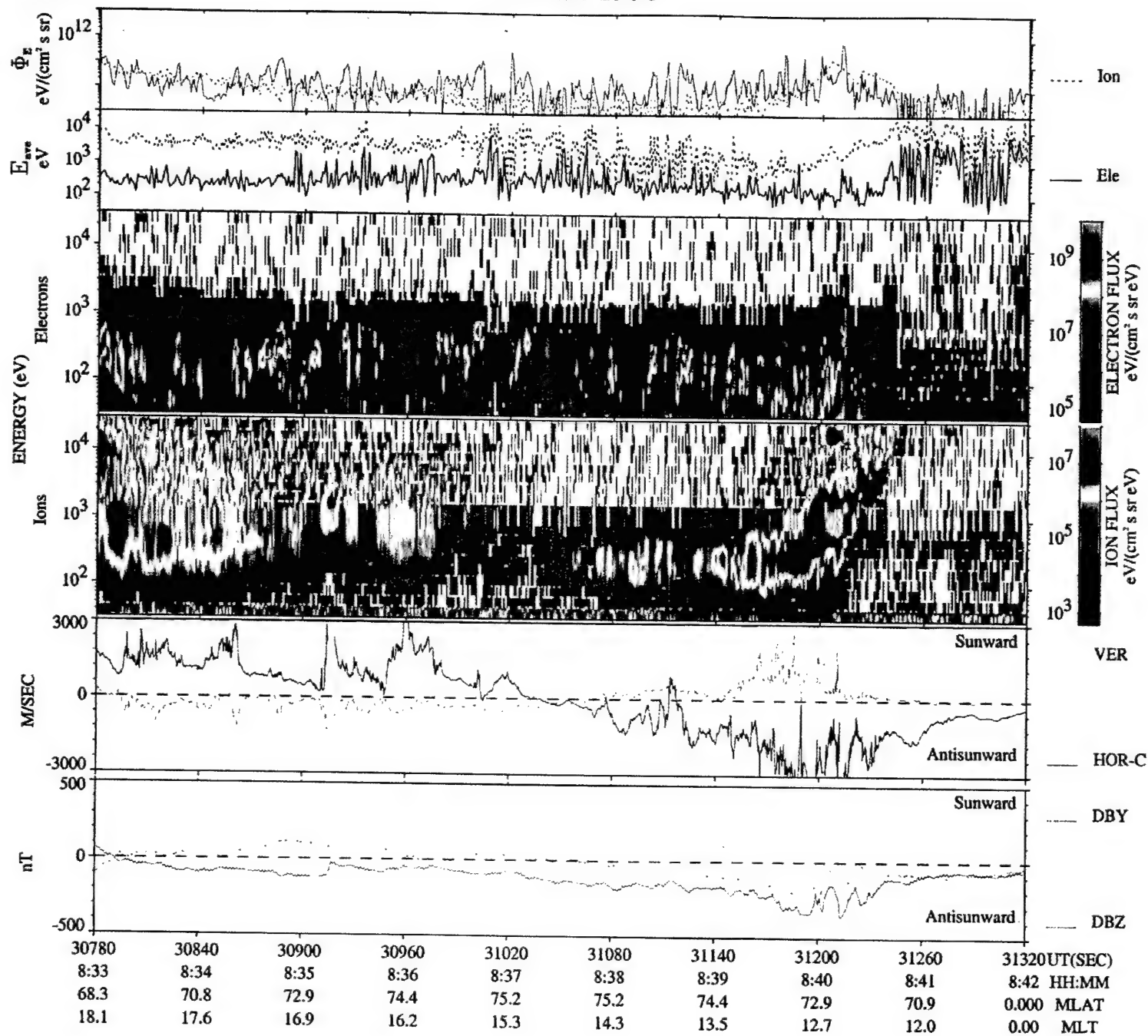
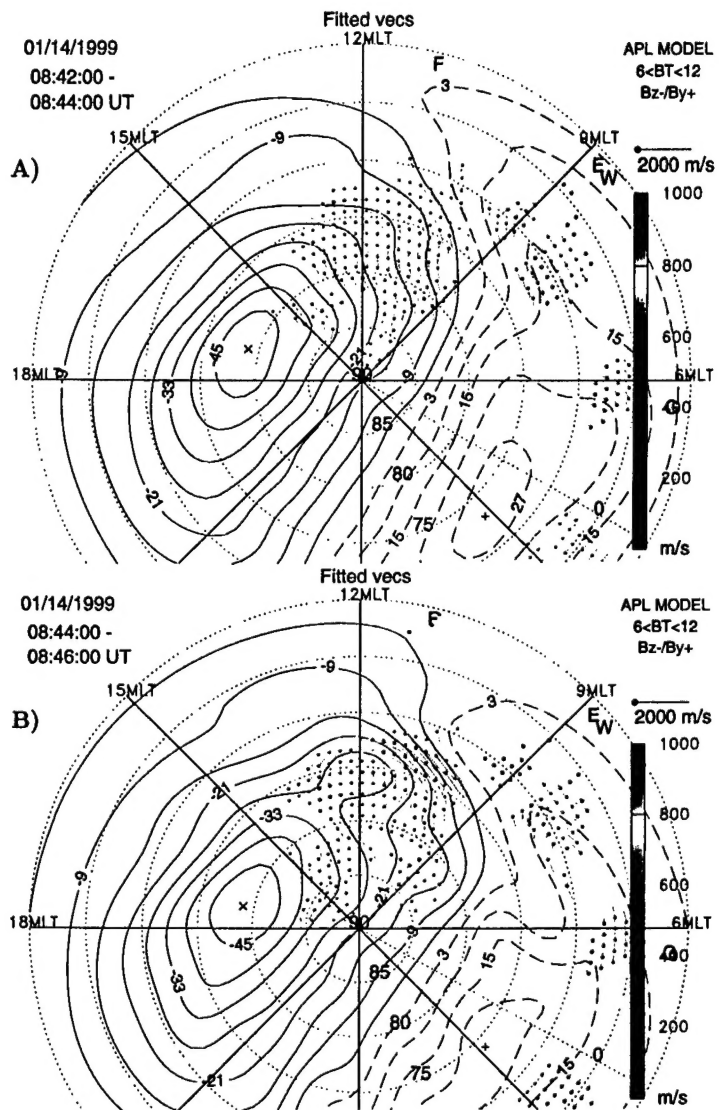


Figure 13



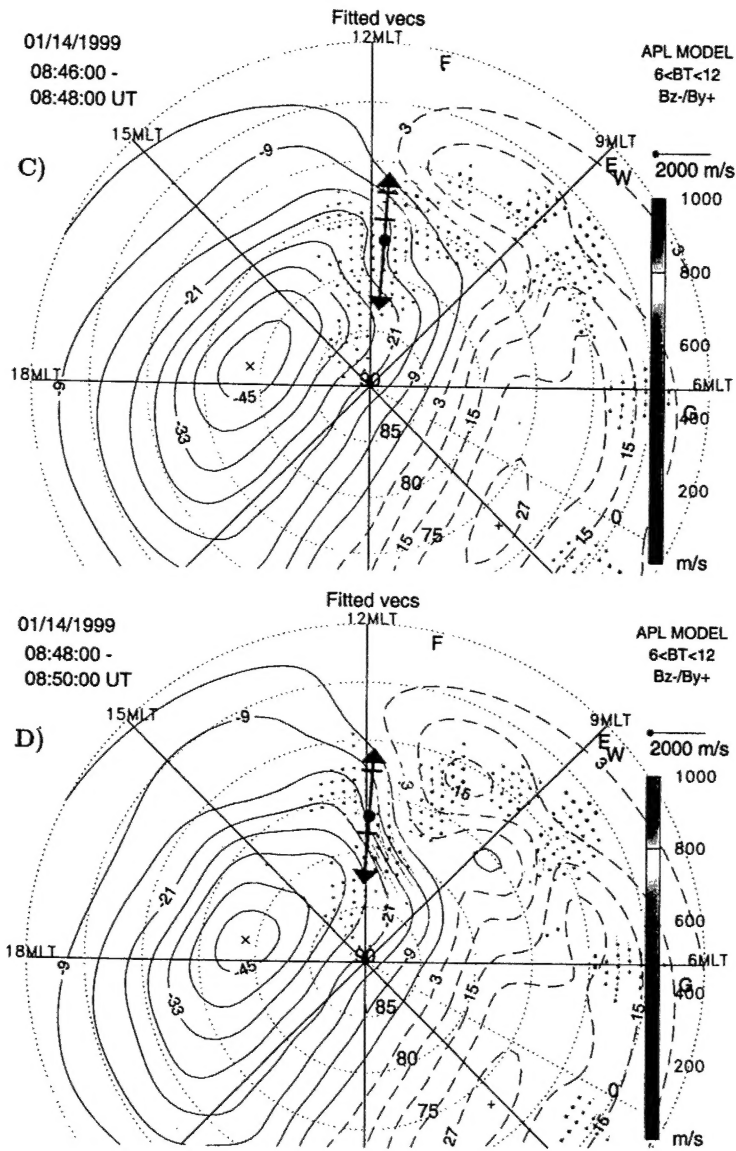
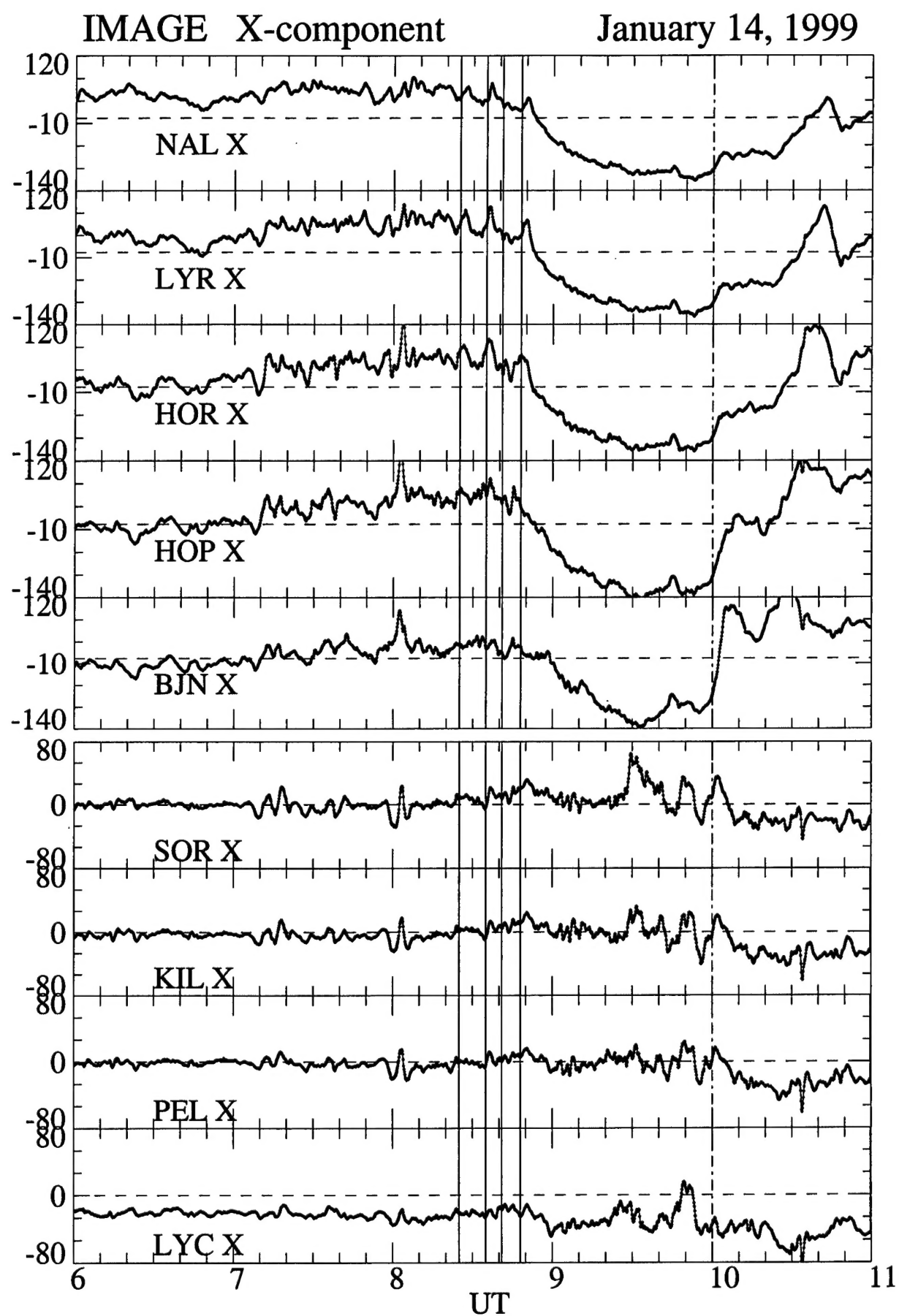


Figure 14 (Panels C and D)



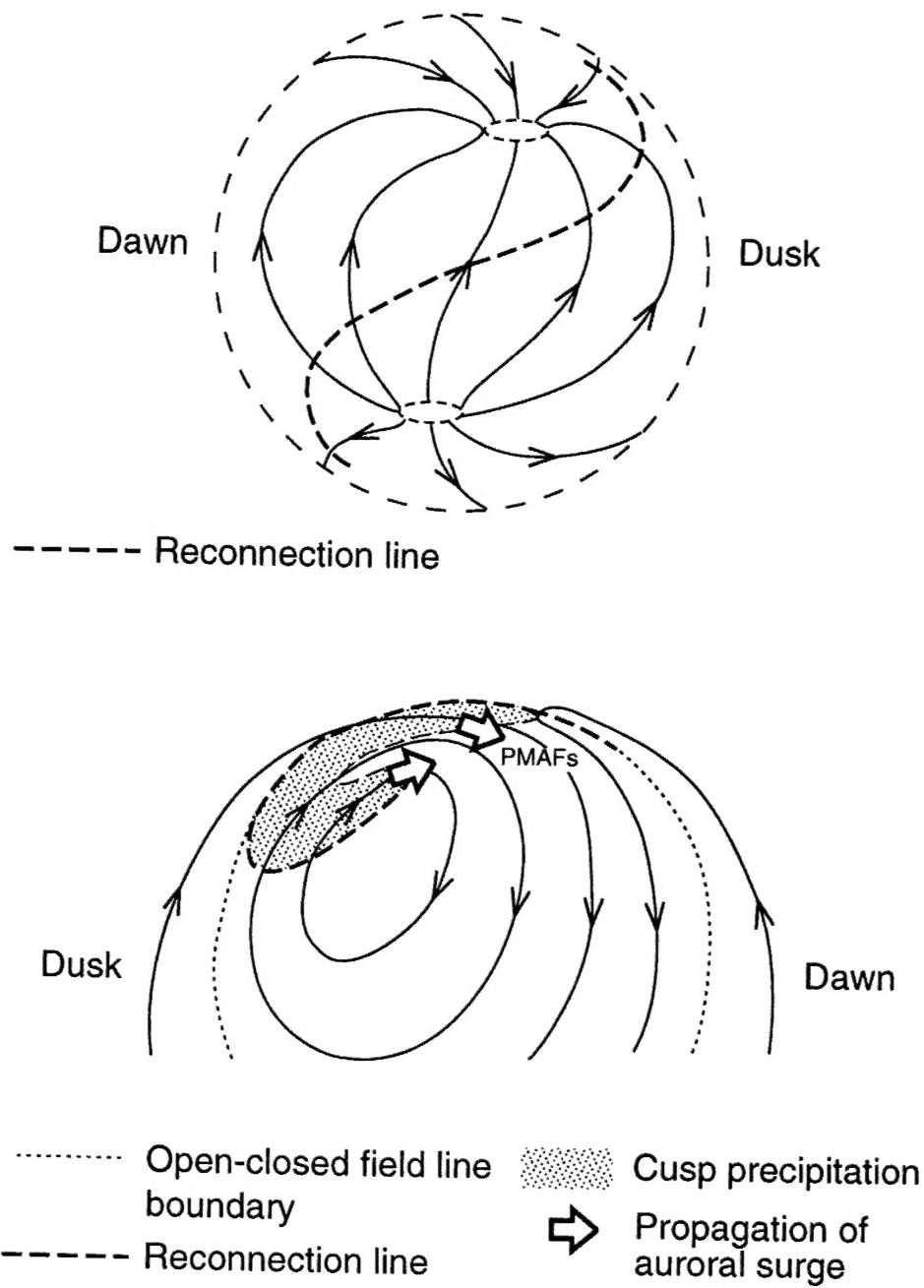


Figure 16